

**MHD experiments on quasi two-dimensional and
three-dimensional liquid metal flows**

RICO KLEIN

**A thesis submitted in partial fulfilment
of the University's requirements
for the Degree of Doctor of Philosophy**

JUNE 2010

Coventry University

Declaration

The work submitted in this dissertation describes the research performed by me at the University of Ilmenau and the Coventry University. I declare that it is the result of my own investigation, except where otherwise stated. I further certify that the material contained herein has not been substantially used in any other submission for an academic award or other qualification.

This dissertation contains approximately 40.000 words and 50 figures.

Abstract

This dissertation reported an experimental answer to the long-standing question of how three-dimensionality appears in wall-bounded magnetohydrodynamic flows and presented also an experimental study on the transition to turbulence in a confined, mostly quasi two-dimensional flow. Accordingly, it was shown the analysis of a vortex array with susceptibility to three-dimensionality, enclosed in a cubic container and a mostly, quasi two-dimensional vortex pair confined by the walls of a shallow, cylindrical container.

Both containers were hermetically filled by a liquid metal fluid and subject to a constant, homogeneous magnetic field. The flow forcing was made by injecting constant electric current from one wall that intersects magnetic field lines (*Hartmann* wall). Flow characteristics and the presence of three-dimensionality were monitored by measuring electric potentials on either *Hartmann* walls that confined the liquid metal.

A form of three-dimensionality termed as *weak* appeared through differential rotation along the axis of individual vortices, while a *strong* form manifested itself in vortices that do not extend from one to the other *Hartmann* wall. In the cubic container, this resulted into an array of novel, spectacular flow structures that were both steady and strongly three-dimensional, and, yielded to a frequency-selective breakdown of quasi two-dimensionality in chaotic and turbulent flow regimes.

The mostly quasi two-dimensional flow in the shallow, cylindrical container was shown to undergo a sequence of supercritical bifurcations to turbulence triggered by boundary layer separations from the circular wall. For very high forcing, the flow reached a turbulent regime where the dissipation increased drastically. This was related to a possible transition from a laminar to a turbulent *Hartmann* layer.

Acknowledgments

I'm grateful to my research supervisor Dr. Alban Pothérat for the excellent guidance and support of this dissertation. I strongly benefited from our scientific collaboration over the last years at Ilmenau University (Germany) and Coventry University (United Kingdom). Also, thanks to Dr. Alban Pothérat my work was funded from the Deutsche Forschergruppengemeinschaft (grant No. PO1210/4-1).

I further acknowledge the important support and many helpful technical advices provided by the Electroheat group over the first three years of my work at Ilmenau University. This group also lent me their superconducting magnet which I strongly needed for my experimental work. In this context too, I am thankful to Artjom Alferenok from Moscow Power Engineering Institute who helped me performing part of the measurements during his stay at Ilmenau University.

I owe my deepest gratitude to Sebastian Berkes from the company *neuroConn* for his excellent technical assistance when setting up the high-precision amplifier system used for my experimental measurements. On the basis of his vast experience in the field of electronics this system could be perfectly adapted to the experimental conditions at the laboratory.

I thank my supervisor for having given me the opportunity to spend two years of my research at Coventry University. As a member of the magnetohydrodynamic (MHD) group headed by Prof. Sergei Molokov I benefited from many useful discussions with local experts working on the field of MHD. During my stay in England I could also massively improve my expertise in MHD and my skills in writing publications.

I express my gratitude to my beloved parents and my sister for their moral support at all the time and their technical assistance over some weekends to mount part of the experimental set-up. Special thanks go to my lovely sister who caricatured the *Giraffe*-like structures presented thereafter in this dissertation. Finally, I offer my regards and blessings to all of those who helped me in any respect during the completion of this dissertation.

Contents

Declaration	I
Abstract	II
Acknowledgments	III
General introduction	1
1. Introduction	7
1.1. Basic equations	7
1.1.1. Equations of electromagnetism	7
1.1.2. Equations of low-Rm MHD	10
1.2. Some important results of liquid metal MHD	13
1.2.1. Effect of the <i>Lorentz</i> force	13
1.2.2. The <i>Hartman</i> layer	16
1.2.3. <i>Shallow water</i> liquid metal MHD	21
1.3. Turbulence	29
1.3.1. Hydrodynamic turbulence	29
1.3.2. Magnetohydrodynamic (MHD) turbulence	32
2. Experimental setups	43
2.1. Construction elements	43
2.1.1. Choice of liquid metal	43
2.1.2. Magnetic field systems	45
2.1.3. Flow forcing - constant electric current injection	46
2.2. Measurement techniques	54
2.2.1. Set-up of the electric potential measurement system	54
2.2.2. Electric potentials measured at Hartmann walls	55
2.2.3. Measurement of three-dimensionality	57
2.2.4. Electric potentials measured at the parallel wall	58
2.3. Source of errors when measuring electric potentials	60
2.3.1. Effect of thermoelectricity	60
2.3.2. Inhomogeneity of the magnetic field	62

2.4. Experiment on a confined electrically driven vortex pair	63
2.4.1. Experimental set-up and measurement technique	63
2.5. Experiment on the appearance of three-dimensionality	67
2.5.1. Design container	67
2.5.2. Filling with liquid metal	68
2.5.3. Installation inside the superconducting magnet	69
2.5.4. Experimental set-up and measurement techniques	70
2.6. Experimental procedure	74
3. Experiment on a confined electrically driven vortex pair	77
3.1. Introduction	77
3.2. General aspects of the flow	80
3.3. Scaling laws in observed flow regimes	89
3.4. Analysis of the bifurcations	90
3.5. Appearance of three-dimensionality	93
3.6. <i>Hartmann</i> layer friction	96
3.7. Conclusion	98
4. Experiment on the appearance of three-dimensionality	103
4.1. Introduction	103
4.2. Observed flow states	105
4.2.1. Flow states forced through 10×10 electrodes ($L_i = 0.01\text{m}$)	105
4.2.2. Flow states forced through 4×4 electrodes ($L_i = 0.03\text{m}$)	114
4.3. Appearance of three-dimensionality in chaotic and turbulent flow regimes	119
4.3.1. Quantities that characterize the appearance of three-dimensionality	119
4.3.2. Appearance of three-dimensionality	121
4.4. Frequency-selective strong three-dimensionality	124
4.5. Conclusion	126
General conclusion	129
Appendix	141
A. Influence of noise on signal correlations	143
B. Determination of the cutoff frequency f_c	147
C. Article: Experiment on a confined electrically driven vortex pair	153
D. Article: Appearance of three-dimensionality in wall-bounded MHD flows	169

List of Figures

1.1.	Effect of the <i>Lorentz</i> force on a planar flow	13
1.2.	Effect of the <i>Lorentz</i> force on a vortex.	14
1.3.	Schematic illustration of the <i>Hartmann</i> layer.	17
1.4.	Schematic illustration of a quasi two-dimensional flow that shows too flow quantities used to describe the flow by the SM82 model ([64]).	22
1.5.	Profile of the azimuthal velocity component $u_\theta(r)$ for an isolated, electrically driven vortex.	25
1.6.	Effect of <i>Ekman</i> pumping.	27
1.7.	Double energy cascade in continuously forced two-dimensional turbulence [32].	31
1.8.	Sketch of the Joule cone in Fourier space. It progressively opens and separates modes dissipated by Joule dissipation from those that contain mostly the kinetic energy in a turbulent MHD flow.	33
1.9.	Sketch of the Joule cone in Fourier space in a quasi-steady equilibrium state where energy is transferred from energy-containing modes into the Joule cone at its edge, to compensate Joule dissipation induced by current eddies at the vortice's extremities ([4]).	35
1.10.	Characteristic of the energy spectrum $E(k)$ in hydrodynamic and magnetohydrodynamic turbulence.	35
1.11.	Sketch of the Joule cone in Fourier space for turbulent, magnetohydrodynamic flows bounded by <i>Hartmann</i> walls with a discrete spectrum for modes along the magnetic field lines ([64]).	38
2.1.	Sketches of magnet systems used in the experiments. The magnetic field is generated either by permanent magnets or by electric current circulating in the superconducting coil of a Cryogen-Free magnet.	45
2.2.	Signal contamination induced by the cooling system of the Cryogen-Free magnet.	46
2.3.	Simplified electric circuit for flow forcing through one electric current injection electrode.	47
2.4.	Schematic representation of the experimental set-up to measure the contact resistance between the liquid metal and different metallic electrodes.	48

2.5. Measured contact resistance between liquid metal and injection electrodes for both copper and CrNi electrodes.	49
2.6. Control of the electric flow forcing. Constant resistances with $R = 2\Omega$ are implemented in each electric circuit to compensate erratic variations of contact resistances and to provide an uniform forcing.	49
2.7. Variability of the flow forcing geometry.	50
2.8. Cooling system that evacuates the heat generated by resistances with $R = 2\Omega$ into flowing cold water.	51
2.9. Design of the switchboard. The switchboard is used to control the geometry of the electric flow forcing and connects electric current injection electrodes to either the positive or negative pol of the DC power supply.	52
2.10. Electric current switchboard system. This system is made to combine all important elements of the flow forcing into one single unit.	53
2.11. Measurement system with simplified sketch representing the principle of measuring and recording electric potentials.	55
2.12. Principle of <i>Electric potential velocimetry</i> . Velocities just outside the <i>Hartmann</i> layer are obtained from electric potentials measured at the <i>Hartmann</i> wall.	56
2.13. The effect of thermoelectricity in the experiment and sketch of an experiment purpose built to measure the <i>Seebeck</i> coefficient of the liquid metal. .	61
2.14. Sketch of the experiment to study the transition to turbulence in a confined, mostly quasi two-dimensional flow. The flow in a shallow, cylindrical container filled with liquid metal is electrically driven through two injecting electrodes that are embedded in one <i>Hartmann</i> wall.	64
2.15. Photograph showing the liquid metal filled, cylindrical container installed in the centre of the gap spanned by two identical sets of permanent magnets. .	65
2.16. Photographs of the bottom plate of the shallow, cylindrical container showing the injection electrodes and electric potential probes to respectively force and measure the flow.	65
2.17. Schematic illustration of the experiment purpose built to study the appearance of three-dimensionality in wall-bounded magnetohydrodynamic flows. Particular emphasis is put on its modular design consisting of a cubic frame with interchangeable side plates.	68
2.18. Photographs of the electronic boards that are embedded in the side plates and contain the injection electrodes and potential probes to respectively force and measure the flow in the cubic, liquid metal filled container. . . .	69
2.19. Manufacturing of the side plates.	69
2.20. Hermetic filling of the cubic container with liquid metal alloy GaInSn. . . .	70

2.21. Experiment on the appearance of three-dimensionality in wall-bounded magnetohydrodynamic flows installed inside the superconducting magnet..	71
2.22. Sketch of the experiment to study the appearance of three-dimensionality in wall-bounded magnetohydrodynamic flows.	73
 3.1. Experimentally obtained stability diagram showing critical Reynolds numbers <i>vs.</i> <i>Hartmann</i> number to distinguish flow regimes observed in the shallow, cylindrical container.	80
3.2. Experimentally obtained, time averaged velocity profiles and profiles of RMS of velocity fluctuations along the diameter of the cylindrical container in different flow regimes.	81
3.3. Evolution of both the location of the maximum velocity in the velocity profile along the diameter and the angle where the boundary layer separates from the circular wall in different flow regimes.	82
3.4. Experimentally obtained, time averaged velocity profiles along the circular wall of the cylindrical container. The angle where the boundary layer separates from this wall is indicated too.	82
3.5. Numerically obtained snapshots of equilibrium and quasi-equilibrium states in identified flow regimes. Related numerical simulations have been done by [28] and their outcomes are used as a qualitative comparison to experimental findings.	84
3.6. Time averaged velocity profiles and profiles of RMS of velocity fluctuations along the diameter of the cylindrical container in different flow regimes, obtained numerically from [28]	85
3.7. [28]'s schematic representation of the analogy between steady flows with boundary layer separation inside and around a cylinder container.	85
3.8. Experimentally obtained time series of electric potential in the periodic and the two base frequency flow regime.	86
3.9. Typical frequency spectra obtained from times series of measured electric potential in related flow regimes.	86
3.10. Analysis of the bifurcations observed at the transition to the periodic and the two base frequency flow regime. The analysis is based on time series of measured electric potential.	90
3.11. Appearance of three-dimensionality in the mostly, quasi two-dimensional flow in the cylindrical container. The presence of weak and strong three-dimensionality is quantified by correlations of electric potential gradients.	94
3.12. Possible transition from a laminar to a turbulent <i>Hartmann</i> layer. Experimentally observed, extra dissipation in the flow points to a brutal change in the <i>Hartmann</i> layer friction.	96

4.1. Phase diagram giving critical <i>Reynolds</i> numbers <i>vs.</i> <i>Hartmann</i> numbers Ha and snapshots of iso-electric-potential lines for flows forced through 10×10 injection electrodes in the experiment on the appearance of three-dimensionality. A region of strong (high Ha) and weak (low Ha) electromagnetic effects clearly stands out.	106
4.2. Typical time series of recorded electric potential obtained for high Ha, showing periodic oscillations with one fundamental frequency at the destabilisation of the 10×10 vortex array and chaotic behaviour at higher forcing.	107
4.3. Ha <i>vs.</i> fundamental frequency that represents the periodic oscillation in times series of measured electric potential at the destabilisation of the 10×10 vortex array	107
4.4. Time averaged profiles of electric potential gradients measured along the centerline at bottom and top <i>Hartmann</i> wall of the cubic container, for high values of Ha. Related profiles are almost identical indicating quasi two-dimensionality in corresponding flow regimes.	108
4.5. Phase diagram giving critical <i>Reynolds</i> numbers <i>vs.</i> <i>Hartmann</i> numbers Ha for flows forced through 10×10 injection electrodes and for low Ha. Corresponding snapshots of iso-electric-potential lines show the appearance of weak and strong three-dimensionality.	110
4.6. Time averaged profiles of electric potential gradients measured along the centerline at bottom and top <i>Hartmann</i> wall of the cubic container, for low values of Ha. Related profiles are clearly different indicating the presence of three-dimensionality in corresponding flow regimes.	111
4.7. Caricature of strongly three-dimensional and steady flow structures that appear for lowest values of Ha= 1822. The caricature illustrates <i>Giraffe</i> -like flow structures.	113
4.8. Phase diagram giving critical <i>Reynolds</i> numbers <i>vs.</i> <i>Hartmann</i> numbers Ha and snapshots of iso-electric-potential lines for flows forced through 4×4 injection electrodes in the experiment on the appearance of three-dimensionality. This case exhibits flow states that are similar to the 10×10 forcing geometry, but peculiar flow states too when Ha is very high.	115
4.9. Typical spectra of recorded electric potential at critical <i>Reynolds</i> numbers and obtained for different <i>Hartmann</i> numbers.	117
4.10. Spatially averaged correlations plotted with respect to the distance to an injection electrode. Related plots show that the flow forcing mechanism intrinsically induces three-dimensionality in the vicinity of individual injection electrodes.	120

4.11. Appearance of three-dimensionality in chaotic and turbulent flow regimes quantified by plotting spatially averaged correlations <i>vs.</i> the true interaction parameter. Snapshots of iso-electric-potential lines and related power density spectra respectively visualise the presence of three-dimensionality and identify a <i>cutoff</i> frequency that separates the quasi-two-dimensional from the three-dimensional part of the frequency spectrum.	122
4.12. <i>Cutoff</i> frequency <i>vs.</i> true interaction parameter	125
B.1. Determination of the <i>cutoff</i> frequency for a small value of the true interaction parameter characterising a strongly three-dimensional flow.	148
B.2. Determination of the <i>cutoff</i> frequency for a high value of the true interaction parameter characterising a mostly quasi-two-dimensional flow.	149

List of Tables

2.1.	Physical properties of different electric conductors as well as related typical joule times τ_j and <i>Hartmann</i> numbers Ha.	44
2.2.	Contact resistance between liquid metal GaInSn and electric current injection electrodes made from copper or CrNi.	48
2.3.	Typical values of the <i>Hartmann</i> number Ha and <i>Hartmann</i> friction time τ_H in the experiment on the transition to turbulence in a confined, mostly quasi two-dimensional flow.	66
2.4.	Typical values of <i>Hartmann</i> number Ha, <i>Hartmann</i> friction time τ_H and two-dimensionalisation time τ_{2D} in the experiment on the appearance of three-dimensionality.	72

General introduction

When a strong magnetic field is applied to an electrically conducting fluid, inertia induced variations of physical quantities are damped along it by the *Lorentz* force so that the flow tends to two-dimensionality ([64]). In such magnetohydrodynamic (MHD) flows the fluid moves only in the plane orthogonal to the magnetic field, except in thin *Hartmann* boundary layers. Those shape along walls that are transverse to the magnetic field lines (*Hartmann* walls) and confine the fluid, thus letting the flow assume a quasi two-dimensional state. The "two-dimensionalisation" effect in MHD problems and its consequences on wall-bounded MHD flows as well as the question how and when these flows are affected by inertia induced three-dimensionality is of primary importance in a great variety of fundamental and practical applications:

Fundamentally, this is relevant to other flows with tendency to two-dimensionality, such as rotating or stratified flows like they appear in rather large scales in geophysics and astrophysics. Tornados for example, are such large scale, almost column-like air rotations in the atmosphere. Although very devastating, they are spectacular and interesting flow structures too. Their appearance triggered by stratifying of cold and dry air above warm and moist air is a complex process where the propagation of inertial waves along the tornado's rotation favours two-dimensionality.

In practical situations like in coolant blankets (or heat exchangers) of fusion reactors the above fundamental physics of MHD bears critical consequences too. The coolant, typically liquid lithium, is used to evacuate the heat generated by the nuclear fusion. A strong, toroidal magnetic field used to confine the electrically conducting deuterium-tritium plasma also penetrates the blankets so that the coolant flow intrinsically tends to two-dimensionality. However, to enhance the heat transport and therefore the efficiency of the energy production process, three-dimensional flows in the coolant are preferable to two-dimensional ones so that substantial knowledge about these flows is required when designing effective coolant channels.

Fundamental MHD effects are also important in industrial processes like continuous steel casting where they help to improve the quality of the final good (steel slabs). The steel solidification starts in so-called moulds where the application of strong magnetic fields is essential to damp and control the flow of hot, liquid steel precisely. By contrast, at the process level where steel slabs are solidified from outside, but still liquid inside, magnetic fields are used to stir the remaining liquid steel and to favour its homogeneous mixing before its solidification.

Studying fundamental MHD effects in flows at the laboratory scale therefore helps both to understand natural large scale phenomena like tornados and to improve MHD appli-

cations in practical situations. In such laboratory scale configurations is the feedback reaction of the flow onto the imposed magnetic field neglected so that the related non-dimensional magnetic *Reynolds* number Rm is smaller than unity (Sec. 1.1). In the frame of this dissertation we designed and performed two important MHD experiments at the fundamental level to address the above key issues. To be more precisely, we study the transition to turbulence induced by boundary layer separation in quasi two-dimensional flows in a small scale experiment, and, point out the mechanisms that govern the appearance of three-dimensionality in wall-bounded MHD flows in both steady and unsteady flow regimes in a large scale experiment. It should however be stressed that the small scale experiment has not been designed to discover interesting physical effects *a priori*, but to test the elements of the bigger experiment.

To this day, the mechanisms that favour two-dimensionality in MHD flows are fairly well understood. Most studies of the breakdown of two-dimensionality however have focused either on strictly two-dimensional vortices [74, 71], or on single vortices or vortex pairs [65, 28]. The mechanisms that ignite three-dimensionality in more complex, wall-bounded flows, where boundary layers that develop along the walls preclude strict two-dimensionality, pose an open question. To answer this question we perform the large scale experiment on the appearance of three-dimensionality. The related initial objectives and the work plan of this dissertation have been scheduled accordingly:

- Design and test of an purpose-built experiment to study the appearance of three-dimensionality in MHD flows in the presence of walls

A MHD experiment in the spirit of [62]'s experiment on quasi two-dimensional turbulence is to design and to built from scratch using sophisticated manufacturing techniques. The flow forcing is to arrange by injecting DC electric current into liquid metal, through a square array of electrodes embedded in one *Hartmann* wall [62]. Electric potential is to measure locally on two identical sets of electric potential probes positioned on either *Hartmann* walls that confine the liquid metal. Major components of the experimental set-up have to be tested carefully in pre-experiments, to obtain a high precision flow measurement and flow forcing system and to select appropriate materials. Furthermore, the experiment should be made of modular elements, firstly to reduce development costs and time and secondly, to put experimenter in the position to modify it easily.

- Performance of laboratory experiments

Flows in steady and unsteady regimes are to be generated by varying the intensity and the geometry of the flow forcing as well as the strength of the imposed

magnetic field. Related flow states are to monitor by recording time-series of electric potentials measured at either *Hartmann* walls.

- Signal processing

Quasi two-dimensional and three-dimensional flow states are to identify in steady and unsteady flow regimes by comparing sets of electric potentials obtained at opposite *Hartmann* walls. When and under which form three-dimensionality appears in related flows is to determine, and to quantify in the space of non-dimensional parameters by calculating correlations between pairs of recorded electric potentials obtained along the same magnetic field line.

The design of this large scale experiment was purposely chosen such that it follows that of [62] in which a quasi two-dimensional flow was produced by applying a constant homogeneous magnetic field across a square, shallow container made of electrically insulating walls and filled with liquid metal. Unlike [62]'s earlier experiment though, our liquid metal container is made not shallow, but cubic to favour the appearance of inertia induced three-dimensionality. In other words it means firstly that, when imposing strong magnetic fields, it is possible to reproduce some elementary properties of the quasi two-dimensional flow that [62] observed in his shallow experiment. And secondly, when imposed magnetic fields are moderate, it allows us to examine the actual limit of quasi two-dimensionality when three-dimensional inertial effects become more important.

The dissertation is organised in four chapters and corresponding subsequent sections. In the first part of Chapter 1 we recall the basics of MHD equations and important MHD results like the effect of the *Lorentz* force or the properties of the *Hartmann* layer. The second part of this chapter is devoted to fundamentals of hydrodynamic (non-MHD) and MHD turbulence to review some of their major characteristics. The principle of the flow forcing and the electric potential measurements is presented in Chapter 2. In this chapter we describe too the construction elements and the design of our small and large scale experiment. It should however be stressed that this part of the dissertation, though most time consuming, is described rather briefly, in favour of the presentation of our novel experimental findings discussed in chapter 3 and chapter 4, also published in [28] and [29] respectively. We conclude the manuscript by reviewing and summarising the main objectives and results of this dissertation.

Lastly we would like to mention some financial aspects related to the development of both experiments. Experimental costs often increase with experimental precision and reliability, but are of course limited by a certain financial budget. In order not to exceed the budget limit, but still to obtain excellent experimental data, it was in some cases necessary

to perform intensive negotiations with companies that supplied us with equipment like the high-precision amplifier system (Sec. 2.2.1). This last remark may not be of scientific interest, though important in our opinion as it gives small inside in the complexity of work that we faced when building our experiments.

Chapter 1

Introduction

1. Introduction

1.1. Basic equations

This section is dedicated to the basics of Magnetohydrodynamics (MHD) and provides the reader with the fundamental equations, characteristic time scales and dimensionless groups. MHD combines both the field of electrodynamics and the field of fluid mechanics in the sense that the *Maxwell's* equations that govern electromagnetic quantities are applied to a moving liquid conductor with electric conductivity σ .

1.1.1. Equations of electromagnetism

Electric conductors used in our experiments are liquid metals with electric conductivity σ of the order of 10^6 S/m. Values of σ of this order imply that displacement currents are negligible which simplifies the classical *Maxwell's* equations. Those are:

Gauss' law: Free and bound charges in the space generate the electric field \mathbf{E} .

$$\nabla \cdot \mathbf{E} = \frac{\rho_e}{\epsilon_0}. \quad (1.1)$$

where ρ_e is the electric charge density and ϵ_0 permittivity of free space.

Gauss' law for magnetism: Magnetic fields \mathbf{B} are solenoidal and magnetic monopoles do not exist.

$$\nabla \cdot \mathbf{B} = 0. \quad (1.2)$$

The Faraday's law of induction: The electric field \mathbf{E} is generated in a conductor either due to a time varying magnetic field $\mathbf{B}(t)$ or due to the conductor's motion across the field \mathbf{B} .

$$\nabla \times \mathbf{E} = -\frac{\partial \mathbf{B}}{\partial t}. \quad (1.3)$$

The Ampére's law: The magnetic field \mathbf{B} is induced when the electric current with current density \mathbf{J} flows within the conductor.

$$\nabla \times \mathbf{B} = \mu_0 \mathbf{J}. \quad (1.4)$$

where $\mu_0 = 4\pi \cdot 10^{-7} Vs/(Am)$ is a constant and denotes the permeability of free space. In addition to the *Maxwell* equations there are the following important equations:

Charge or electric current conservation: This relation is found when applying $\nabla \cdot (\cdot)$ to either side of (1.4) and balances the flux of current density which goes into and out of a conductor element.

$$\nabla \cdot \mathbf{J} = 0. \quad (1.5)$$

Ohm's law: The electric current density in the conductor results from the electric field $\mathbf{E} = -\nabla\Phi$ and the motion of the conductor inside the magnetic field \mathbf{B} ($\nabla\Phi$ is the gradient of the electric potential ϕ).

$$\mathbf{J} = \sigma(-\nabla\Phi + \mathbf{u} \times \mathbf{B}). \quad (1.6)$$

where σ is the electric conductivity.

The Lorentz F force: This force acts on the conductor when it is subject to the magnetic field \mathbf{B} and the electric current density \mathbf{J} flows inside.

$$\mathbf{F} = \mathbf{J} \times \mathbf{B}. \quad (1.7)$$

In liquid metal MHD, the *Lorentz* force is the most important force acting on electric charges as the electrostatic force or *Coulomb* force which is related to the electric field \mathbf{E} is negligible (see *e.g.* [12]).

When taking the curl of *Ohm's law* (1.6) and combining it with *Ampére's law* (1.4) and *Faraday's law* (1.3) it yields to the advection-diffusion or induction equation for the magnetic field \mathbf{B} . This equation expresses the relation between the velocity \mathbf{u} of the moving electric conductor and \mathbf{B} as follows:

$$\frac{\partial \mathbf{B}}{\partial t} = \nabla \times (\mathbf{u} \times \mathbf{B}) + \lambda \nabla^2 \mathbf{B}. \quad (1.8)$$

$\lambda = (\mu_0\sigma)^{-1}$ is the magnetic diffusivity. When using dimensional analysis one finds that the first and the second term of (1.8) are of order of $BUL^{-1} = B\tau_a^{-1}$ and $B\lambda L^{-2} = B\tau_d^{-1}$ respectively. τ_a and τ_d are characteristic time scales for the effect of magnetic field advection and diffusion respectively for a conductor that moves with a typical velocity U over a typical distance L . Whether the effect of magnetic field diffusion or advection is dominant can be estimated by the ratio τ_a/τ_d which is known as the *magnetic Reynold's number*:

$$\text{Rm} = \mu_0\sigma UL. \quad (1.9)$$

Rm can be also obtained when writing (1.8) in dimensionless form using the scalings $\mathbf{u}^* = \mathbf{u}U^{-1}$, $\nabla^* = \nabla L$, $t^* = t(U/L)$ and $\mathbf{B}^* = \mathbf{B}B^{-1}$. It yields:

$$\frac{\partial \mathbf{B}^*}{\partial t^*} = \nabla^* \times (\mathbf{u}^* \times \mathbf{B}^*) + \frac{1}{\text{Rm}} \nabla^{*2} \mathbf{B}^*. \quad (1.10)$$

The significance of Rm becomes even more apparent when considering the induced magnetic field \mathbf{b}_i that Ampère's law (1.4) relates to the current density \mathbf{J} (note that we use here the specific notation \mathbf{b}_i instead of the rather general notation \mathbf{B} as in (1.4)):

$$\nabla \times \mathbf{b}_i = \mu_0 \mathbf{J}. \quad (1.11)$$

Assuming that \mathbf{J} was induced inside a moving electric conductor that crosses a constant, externally imposed magnetic field \mathbf{B}_0 it is of the order of $\simeq \sigma UB_0$ (1.6). Using this and applying dimensional analysis to (1.11) it yields:

$$\frac{b_i}{L} \simeq \mu_0\sigma UB_0 \rightarrow \frac{b_i}{B_0} \simeq \mu_0\sigma UL = \text{Rm}. \quad (1.12)$$

where b_i is a typical value of the induced field \mathbf{b}_i . The above relations show that Rm may also be interpreted as the ratio between the strength of the induced magnetic field \mathbf{b}_i and the externally imposed, constant magnetic field \mathbf{B}_0 .

In liquid metal MHD one usually studies problems where $\text{Rm} \ll 1$ which implies that $B_0 \gg b_i$. Using the vector identity $\nabla \times (\mathbf{u} \times \mathbf{B}) = (\mathbf{B} \cdot \nabla) \mathbf{u} - (\mathbf{u} \cdot \nabla) \mathbf{B}$ and $\mathbf{B} = \mathbf{B}_0 + \mathbf{b}_i$ for the total magnetic field that penetrates the electric conductor (1.10) can be approximated by:

$$\frac{\partial \mathbf{b}_i^*}{\partial t^*} = (\mathbf{B}_0^* \cdot \nabla^*) \mathbf{u}^* + \frac{1}{\text{Rm}} \nabla^{*2} \mathbf{b}_i^*. \quad (1.13)$$

This indicates that in the limit of $\text{Rm} \ll 1$, the induced field \mathbf{b}_i diffuses inside the conductor almost instantaneously which justifies the assumption $\partial_t \mathbf{b}_i \simeq 0$, referred to as

[56]’s *quasi-static approximation*. Thus, we have:

$$(\mathbf{B}_0^* \cdot \nabla^*) \mathbf{u}^* = -\frac{1}{\text{Rm}} \nabla^{*2} \mathbf{b}_i^*. \quad (1.14)$$

The *magnetic Reynold’s* number can also have values $\text{Rm} > 1$ in liquid metal MHD. Given that the permeability μ_0 is of order $\sim 10^{-6} N/A^{-2}$ and the conductivity σ for a typical liquid metal is of order $\sim 10^6 (\Omega m)^{-1}$, $\text{Rm} > 1$ when $UL > 1 m^2/s$. In this context, the authors of ([58]) demonstrate a nice experimental work on a rapidly rotating spherical *Couette* flow where several types of magneto-inertial waves have been identified.

1.1.2. Equations of low-Rm MHD

In our study we are interested in liquid metal flows with velocity field \mathbf{u} that satisfy the incompressibility condition. This yields to the equation for mass conservation:

$$\nabla \cdot \mathbf{u} = 0. \quad (1.15)$$

The motion of a fluid element that progresses through a fluid with density ρ and viscosity ν is described by the *Navier-Stokes* equation. When studying MHD problems, the *Lorentz* force $\mathbf{J} \times \mathbf{B}$ affects its motion and has to be included in this equation as follows:

$$\frac{\partial \mathbf{u}}{\partial t} = -(\mathbf{u} \cdot \nabla) \mathbf{u} - \frac{1}{\rho} \nabla p + \nu \nabla^2 \mathbf{u} + \frac{1}{\rho} \mathbf{J} \times \mathbf{B} + \frac{1}{\rho} \mathbf{G}. \quad (1.16)$$

where ∇p is the pressure gradient and \mathbf{G} is some externally imposed force which drives the flow. Using dimensional analysis one finds that the first two terms on the right hand side of (1.16) are of order of $U^2 L^{-1} = U \tau_U^{-1}$, the third term of order of $U \nu L^{-2} = U \tau_\nu^{-1}$ and the *Lorentz* force term of order of $U \sigma B^2 \rho^{-1} = U \tau_j^{-1}$ (note that U and L is a typical velocity and distance respectively and recall that \mathbf{J} is of the order of $\asymp \sigma U B$ according to (1.6)).

The characteristic time τ_U relates to the effect of inertia that causes the advection of a perturbation \mathbf{u}' through an initial steady velocity field \mathbf{U}_0 within the flow field $\mathbf{u} = \mathbf{U}_0 + \mathbf{u}'$. On the other hand, by the effect of viscosity, \mathbf{u}' diffuses into the flow field in the time τ_ν . The relative importance of the two effects is measured by the *Reynold’s* number Re that is found, when taking the ratio τ_ν / τ_U :

$$\text{Re} = \frac{UL}{\nu}. \quad (1.17)$$

The *Lorentz* force operates at the joule time τ_j while competing with inertial forces that acts at the times scale τ_U . The ratio τ_U/τ_j brings us to another important parameter in MHD that is referred to as the *Stuart* number or Interaction parameter N which expresses as:

$$N = \frac{\sigma B^2 L}{\rho U}. \quad (1.18)$$

Finally, the ratio τ_ν/τ_j measures the relative strength of *Lorentz* to viscous forces as follows:

$$\text{Ha}^2 = \frac{L^2 B^2 \sigma}{\nu \rho} = \text{Re } N. \quad (1.19)$$

where Ha is the *Hartmann* number. Both forces are of the same order of magnitude when $\text{Ha}^2 \sim 1$. This provides a length scale δ , which is commonly known as a measure of the *Hartmann* layer size in liquid metal MHD:

$$\delta = \frac{1}{B} \sqrt{\frac{\nu \rho}{\sigma}} = \frac{L}{\text{Ha}}. \quad (1.20)$$

Replacing dimensional quantities in (1.16) by their dimensionless counterparts which are $\mathbf{u}^* = \mathbf{u}U^{-1}$, $\nabla^* = \nabla L$, $t^* = t(U/L)$, $\mathbf{B}^* = \mathbf{B}B^{-1}$, $p^* = p(\rho U^2)^{-1}$, $\mathbf{J}^* = \mathbf{J}(\sigma UB)^{-1}$, the *Reynolds* number Re and the interaction parameter N are recovered in the dimensionless form of (1.16) as follows:

$$\frac{\partial \mathbf{u}^*}{\partial t^*} + (\mathbf{u}^* \cdot \nabla^*) \mathbf{u}^* = -\nabla p^* + \frac{1}{\text{Re}} \nabla^{*2} \mathbf{u}^* + N(\mathbf{J}^* \times \mathbf{B}^*). \quad (1.21)$$

Combining the vector identity $\nabla(\mathbf{B}^2/2) = (\mathbf{B} \cdot \nabla)\mathbf{B} + \mathbf{B} \times \nabla \times \mathbf{B}$ with *Ampère's law* (1.4) splits the *Lorentz* force in (1.16) into a irrotational and a rotational part as follows:

$$\mathbf{J} \times \mathbf{B} = (\mathbf{B} \cdot \nabla)(\mathbf{B}/\mu_0) - \nabla(\mathbf{B}^2/2\mu_0) \quad (1.22)$$

The irrotational part (second term on the right) can be interpreted as a magnetic pressure. It adds to the pressure p in (1.16) such that $p' = p + \mathbf{B}^2/2\mu_0$. In the limit of magnetic *Reynolds* number $\text{Rm} \ll 1$ and assuming that $\mathbf{G} = 0$ this yields into a further important representation of the motion equation (1.16):

$$\frac{\partial \mathbf{u}}{\partial t} + (\mathbf{u} \cdot \nabla) \mathbf{u} = -\frac{1}{\rho} \nabla p' + \nu \nabla^2 \mathbf{u} + \frac{1}{\mu_0 \rho} (\mathbf{B}_0 \cdot \nabla) \mathbf{b}_i. \quad (1.23)$$

recalling that \mathbf{B}_0 and \mathbf{b}_i is the externally imposed and induced magnetic field respectively.

The energy equation in MHD is obtained when taking the scalar product of (1.16) with \mathbf{u} . Given that magnetic energy related to the induced magnetic field \mathbf{b}_i is negligible when $Rm \ll 1$, it reads:

$$\frac{\partial}{\partial t} \left(\frac{\mathbf{u}^2}{2} \right) = -\frac{1}{\rho} \nabla \cdot (p\mathbf{u}) - \nabla \cdot \left[\left(\frac{1}{2} \mathbf{u}^2 \right) \mathbf{u} \right] + \nabla \cdot (\Phi \mathbf{J}) - \frac{1}{\rho \sigma} \mathbf{J}^2 - \nu \nabla \mathbf{u} \cdot \nabla \mathbf{u}. \quad (1.24)$$

When integrating the above equation over the volume V the first and second term relate to the rate of transport of energy across the surface that bounds the volume (see [13] for more details). Both terms vanish if the volume is confined by walls were the velocity is zero. Likewise disappears the volume integral of $\rho \nabla \cdot (\Phi \mathbf{J})$ for electric insulating walls. This implies for the fall of the global mechanical energy in MHD, E :

$$\frac{dE}{dt} = \frac{d}{dt} \int_V \frac{\rho \mathbf{u}^2}{2} dV = -D_J - \epsilon. \quad (1.25)$$

where $D_J = \int_V \frac{\mathbf{J}^2}{\sigma} dV$ and $\epsilon = 2\rho\nu \int_V S_{ij}S_{ij} dV$ relate to Joule dissipation and viscous dissipation respectively.

1.2. Some important results of liquid metal MHD

In this section we present fundamental findings in liquid metal magnetohydrodynamics (MHD) which are important to this work. We first explain the effect of the *Lorentz* force and then describe more specific MHD problems such as the *Hartmann* layer or the "two-dimensional" SM82-model.

1.2.1. Effect of the Lorentz force

The effect of the *Lorentz* force plays a leading role in liquid metal MHD. It operates over the joule time $\tau_j = \rho(\sigma B^2)^{-1}$ and affects a fluid flow in damping velocity variations along the lines of an imposed magnetic field \mathbf{B} . This may be clarified in the following where it is assumed that viscous and inertial effects are negligible:

$$N \gg 1 \text{ and } \text{Re} \gg 1 \quad (1.26)$$

Fig. 1.1 illustrates schematically two adjacent fluid layers, that move one above each other with velocity difference $\delta\mathbf{u}$ along the field \mathbf{B} and don not feel the effect of walls. In each

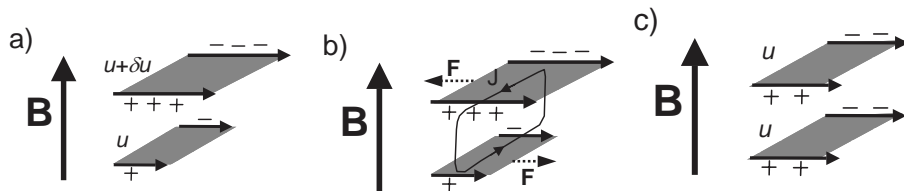


Figure 1.1.: Effect of the *Lorentz* force: planar flow a) $t = 0$, b) $t < \tau_j$, c) $t > \tau_j$

layer, the fluid motion induces an electromotive field $\mathbf{u} \times \mathbf{B}$ proportional to the velocity (Fig. 1.1a). Accordingly, an horizontal electric potential gradient $\nabla\Phi$ establishes opposing $\mathbf{u} \times \mathbf{B}$. To compensate the variation of $\nabla\Phi$ along \mathbf{B} , an electric current loop $\mathbf{J} = \sigma\mathbf{u} \times \mathbf{B}$ develops and causes the *Lorentz* forces $\mathbf{F} = \mathbf{J} \times \mathbf{B}$. As illustrated in Fig. 1.1b the *Lorentz* force acts either against or in flow direction smoothing out velocity variations $\delta\mathbf{u}$ along the magnetic field \mathbf{B} (Fig. 1.1c).

More complicate flow structures like vortices are affected by the *Lorentz* force likewise. Velocity variations along \mathbf{B} cause poloidal eddy currents densities \mathbf{J} as schematically shown in Fig. 1.2a for one vortex that spins with the velocity $\mathbf{u} = (0, U\mathbf{e}_\theta, 0)$. Assuming \mathbf{J} is invariant along e_θ and electric current loops exists only in the r-z plane, current conservation (1.5) implies that \mathbf{J} can be expressed by means of a scalar stream function Ψ_i satisfying a *Poisson* equation (see [12]):

$$\mathbf{J} = \nabla\Psi_i \times \mathbf{e}_\theta, \quad \nabla \times \mathbf{J} = -(\nabla^2\Psi_i)\mathbf{e}_\theta. \quad (1.27)$$

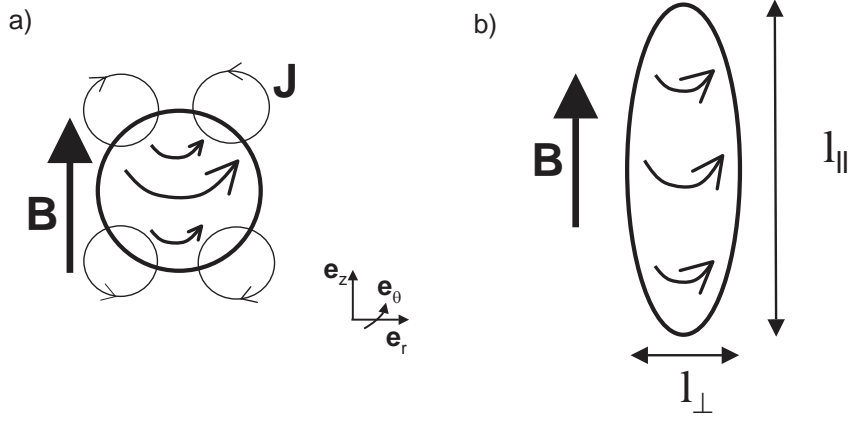


Figure 1.2.: Effect of the *Lorentz* force on a vortex. a) $t = 0$, b) $t < \tau_j$, c) $t > \tau_j$

with $\mathbf{J} = (-\partial\Psi/\partial z, 0, \partial\Psi/\partial r)$ and $\nabla^2\Psi = \partial_z J_r - \partial_r J_z$. Taking the curl of (1.6) yields to *Ohm's law* in the form:

$$\nabla \times \mathbf{J} = \sigma \nabla \times (\mathbf{u} \times \mathbf{B}) = \sigma (\mathbf{B} \cdot \nabla) \mathbf{u} = \sigma B_z \frac{\partial \mathbf{u}}{\partial z}. \quad (1.28)$$

This combines with (1.27) into:

$$-(\nabla^2\Psi_i) \mathbf{e}_\theta = \sigma B_0 \frac{\partial \mathbf{u}}{\partial z}. \quad (1.29)$$

and therefore relates the electric current density \mathbf{J} to the flow field \mathbf{u} . Given that $\mathbf{B} = B_0 \mathbf{e}_z$ and using (1.27) yields for the *Lorentz* force:

$$\mathbf{F} = \frac{1}{\rho} (\nabla\Psi_i \times \mathbf{e}_\theta) \times \mathbf{B} = \frac{B_0}{\rho} \frac{\partial\Psi_i}{\partial z} \mathbf{e}_\theta. \quad (1.30)$$

which implies that the *Lorentz* force acts in azimuthal direction. One way to demonstrate its influence on the vortex evolution is to consider the vortex as a single Fourier mode in the Fourier-space. This implies that each quantity \mathbf{u} , Ψ_i and \mathbf{F} may be expressed as:

$$\mathbf{u} = \hat{\mathbf{u}} e^{j\mathbf{k}\cdot\mathbf{x}}, \quad \Psi_i = \hat{\Psi}_i e^{j\mathbf{k}\cdot\mathbf{x}}, \quad \mathbf{F} = \hat{\mathbf{F}} e^{j\mathbf{k}\cdot\mathbf{x}} \quad (1.31)$$

where $\mathbf{k} = (k_\perp, 0, k_\parallel)$ is the wave vector with the component perpendicular to the magnetic field \mathbf{B} , k_\perp and in the direction of \mathbf{B} , k_\parallel . Both k_\perp and k_\parallel are related to the corresponding vortex length scales $l_\parallel \simeq 1/k_\parallel$ and $l_\perp \simeq 1/k_\perp$ respectively. Substituting \mathbf{u} , Ψ , and \mathbf{F} in equations (1.29) and (1.30) by expressions (1.31) leads to:

$$-(k_\perp^2 + k_\parallel^2) \hat{\Psi} = \sigma B_0 k_\parallel \hat{\mathbf{u}} \quad \text{and} \quad \hat{\mathbf{F}} = \frac{B_0}{\rho} k_\parallel \hat{\Psi}. \quad (1.32)$$

Combining both expressions in (1.32) yields for the rotational part of the *Lorentz* force in Fourier-space:

$$\hat{\mathbf{F}} = -\frac{\sigma B_0^2}{\rho} \frac{k_{\parallel}^2}{k_{\perp}^2 + k_{\parallel}^2} \hat{\mathbf{u}} = -\frac{1}{\tau_j} \cos^2 \theta \hat{\mathbf{u}}, \quad \text{where } \theta = (\mathbf{k}, \mathbf{B}). \quad (1.33)$$

The minus sign clearly shows that the *Lorentz* force damps the vortex. This damping effect is felt by wave vectors k_{\parallel} as $\theta = 0$ but leaves wave vectors k_{\perp} unaffected as $\theta = \pi/2$. For the physical space this implies that $l_{\parallel} \simeq 1/k_{\parallel}$ increases but $l_{\perp} \simeq 1/k_{\perp}$ remains constant. In other words, the vortex elongates along \mathbf{B} while its anisotropy increases.

[64] showed further that this phenomena could be interpreted as a pseudo-diffusion of momentum along the magnetic field lines. Indeed, they showed that the rotational part of the *Lorentz* force take the general form (for boundary conditions where the *Laplacian* operator is invertible):

$$\mathbf{F} = -\frac{1}{\tau_j} \nabla^{-2} \left(\frac{\partial^2 \mathbf{u}}{\partial z^2} \right) \quad (1.34)$$

For an anisotropic vortex such that $l_{\parallel} \gg l_{\perp}$ the above relation can be approximated:

$$\mathbf{F} \sim -\frac{l_{\perp}^2}{\tau_j} \partial z^2 \mathbf{u} \quad (1.35)$$

where $-l_{\perp}/\tau_j$ is the corresponding diffusion coefficient. Under the sole action of the *Lorentz* force \mathbf{F} , the velocity field evolves as:

$$\partial_t \mathbf{u} \sim -\frac{l_{\perp}^2}{\tau_j} \partial_{zz}^2 \mathbf{u}. \quad (1.36)$$

so the vortex elongates according to:

$$l_{\parallel} \sim l_{\perp} \sqrt{\frac{t}{\tau_j}} \quad (1.37)$$

Over time scales $\tau_j < t < \tau_U$ with $\tau_U = l_{\perp}/U$, this process is linear as dominated by the *Lorentz* force and the length l_{\perp} can be assumed constant. However, toward the end of this linear phase when t becomes of the order of τ_U , non-linear inertial effects are of the same order like the *Lorentz* force. Following [64], this implies that the vortex has reached its "final" anisotropic state that satisfies:

$$\frac{l_{\parallel}}{l_{\perp}} \sim \frac{k_{\perp}}{k_{\parallel}} \simeq N^{1/2}, \quad \text{with } N = \frac{\sigma B_0^2 l_{\perp}}{\rho U} \quad (1.38)$$

[67, 68] identified, subsequent to the initially linear phase, a nonlinear phase where a constant l_\perp is no further valid. Therefore, they define the "true" interaction parameter N_t which measures the current ratio $\mathbf{F}/(\mathbf{u} \cdot \nabla)\mathbf{u}$. Assuming $\partial_z \ll \partial_\perp$ this yields to:

$$\frac{\sigma B_0^2 l_\perp}{\rho U} \left(\frac{l_\perp}{l_\parallel} \right)^2 \sim N \left(\frac{l_\perp}{l_\parallel} \right)^2 = N_t. \quad (1.39)$$

The "true" interaction parameter N_t is indeed the relevant parameter that describes the appearance of three-dimensionality in our large scale experiments (Sec. 4.3). It is built on a fixed length scale l_\parallel which corresponds to the distance $L = 0.01\text{m}$ between the two opposed *Hartmann* walls (4.3). This implies that vortices with length scales l_\perp and $l_\parallel = L$ are in a quasi two-dimensional state when the related $N_t(l_\perp, L) \gg 1$. The corresponding time scale for the vortex "two-dimensionalisation", τ_{2D} , can be obtained from (1.37) and reads:

$$\tau_{2D} = \tau_j \frac{L^2}{l_\perp^2} = \frac{\tau_U}{N_t(l_\perp, L)} \quad (1.40)$$

1.2.2. The Hartman layer

The *Hartmann* boundary layer is one of the most important elements in magnetohydrodynamics (MHD). Its existence along walls that are penetrated by a transverse magnetic field \mathbf{B} (*Hartmann* walls) has been predicted theoretically and characterised experimentally by the pioneering works of [23] and [24] respectively. In this section, we derive the main properties of the *Hartmann* layer and briefly discuss its stability.

Properties of the Hartmann layer

Consider the flow along an electrically insulating *Hartmann* wall of characteristic length L and penetrated by the magnetic field $\mathbf{B} = B_0 \mathbf{e}_z$ (Fig. 1.3). Inside the *Hartmann* layer, viscous and *Lorentz* forces are of the same order of magnitude which gives an estimate for its size δ according to $\delta = B_0^{-1}(\nu\rho/\sigma)^{1/2}$ (1.20 and note that the size of δ has been experimentally verified by [38]).

Assuming that the flow is steady ($\partial_t \mathbf{u} = 0$) and laminar, the three-dimensional velocity field \mathbf{u} within the *Hartmann* layer expresses as:

$$\mathbf{u}(x, y, z) = \mathbf{u}^c(x, y) f(z). \quad (1.41)$$

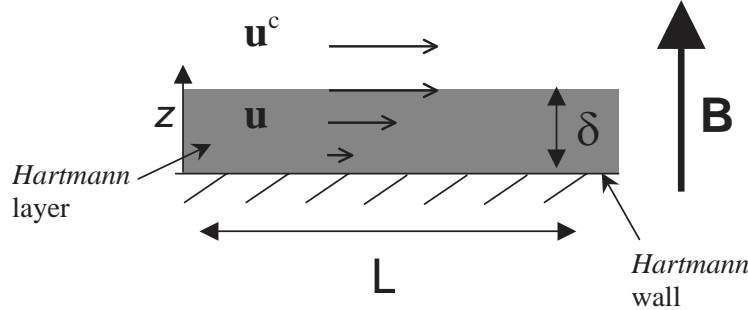


Figure 1.3.: Schematic illustration of the *Hartmann* layer. It develops along walls that are orthogonal to the magnetic field \mathbf{B} (*Hartmann* walls).

where $f(z)$ represents both the two-dimensional flow in the core (outside the *Hartmann* layer) with the velocity field $\mathbf{u}^c(x, y)$ and the velocity variations near the *Hartmann* wall inside the *Hartmann* layer. The set of equations (1.15), (1.16), (1.5) and (1.6) describe the flow. Assuming U_\perp^c and W as typical velocities at the edge of the *Hartmann* layer in transverse and vertical direction respectively and using (1.15) one finds that:

$$W \simeq \frac{U_\perp^c}{\text{Ha}}, \quad \text{with } \text{Ha} = B_0 L \sqrt{\frac{\sigma}{\rho \nu}} \quad (1.42)$$

The above relation shows that the vertical velocity component is negligible in the limit of high Ha. When comparing orders of magnitudes of the z-components of the *Navier-Stokes* equation (1.16) using the above relation it yields to:

$$\frac{\partial p}{\partial z} = \mathcal{O}(\max|\text{Ha}^{-2}, \text{Re}^{-1}|) \quad (1.43)$$

This implies that in the limit of high $\text{Ha} = LB_0\sqrt{\sigma/(\rho\nu)}$ and $\text{Re} = U_\perp^c L / \nu$ the pressure p does not vary along the direction of the magnetic field \mathbf{B} . Combining *Ohm's law* (1.6) with current conservation (1.5) yields to:

$$\nabla \cdot \mathbf{J} = \partial_{zz}^2 \Phi + \nabla_\perp^2 \Phi + \nabla \cdot (\mathbf{u} \times \mathbf{B}) = 0. \quad (1.44)$$

where the subscript (\perp) here and in the following relates to components in the horizontal plane. The first term in the above relation is of the order of $\simeq \Phi \delta^{-2}$ and the remaining two terms are both of the same order of $\simeq \Phi (\delta \text{Ha})^{-2}$. This implies that:

$$\partial_{zz}^2 \Phi = \mathcal{O}\left(\frac{1}{\text{Ha}^2}\right) \quad (1.45)$$

Integrating (1.45) across the *Hartmann* layer along \mathbf{e}_z yields:

$$\partial_z \Phi|_c - \partial_z \Phi|_w = \partial_z \Phi = \mathcal{O}\left(\frac{\delta}{\text{Ha}^2}\right) = \mathcal{O}\left(\frac{1}{\text{Ha}^3}\right) \quad (1.46)$$

where $\partial_z \Phi|_c$ and $\partial_z \Phi|_w$ are the potential gradients at the edge of the *Hartmann* layer and at the *Hartmann* wall respectively. Since the latter is insulating it requires that $\partial_z \Phi|_w = 0$ and implies that the electric potential across the *Hartmann* layer $\partial_z \Phi$ does not vary in the limit of high Ha.

The flow in the *Hartmann* layer is described by the motion equation (1.16). Assuming that $N \gg 1$ inertial effects in (1.16) are negligible. Furthermore, because of relations (1.42), (1.43) and (1.46) one needs to consider only the horizontal components of (1.16). Using (1.6) and the fact that the *Laplace* operator ∇^2 in the limit of $L \gg \delta$ can be approximated by ∂_{zz}^2 , the motion equation simplifies into (recall that $\partial_t \mathbf{u} = 0$):

$$\nu \partial_{zz}^2 \mathbf{u}_\perp - \frac{\sigma}{\rho} B_0^2 \mathbf{u}_\perp = \frac{1}{\rho} \nabla_\perp p + \frac{\sigma}{\rho} \nabla \Phi \times \mathbf{B} - \frac{1}{\rho} \mathbf{G}_\perp(x, y). \quad (1.47)$$

The external force $\mathbf{G}_\perp(x, y)$ could for instance be an horizontally imposed pressure gradient that drives the flow. All quantities on the right hand side of (1.47) are constant along \mathbf{e}_z and can be expressed by just one term $\mathbf{D}(x, y)$. This simplifies (1.47) into:

$$\partial_{zz}^2 \mathbf{u}_\perp - \frac{\sigma}{\rho \nu} B_0^2 \mathbf{u}_\perp = \frac{\mathbf{D}(x, y)}{\nu}. \quad (1.48)$$

Solving (1.48) and using the boundary conditions $\mathbf{u}_\perp(z \rightarrow \infty) = \mathbf{u}_\perp^c$ and $\mathbf{u}_\perp(z = 0) = \mathbf{0}$ one finds that the velocity field \mathbf{u}_\perp inside the *Hartmann* layer varies according to:

$$\mathbf{u}_\perp(x, y, z) = \mathbf{u}_\perp^c(x, y) \left(1 - e^{-\frac{z}{\delta}}\right), \quad \text{with } \mathbf{u}_\perp^c = -\mathbf{D}(x, y) \frac{\rho}{\sigma B_0^2} \quad (1.49)$$

Substituting \mathbf{u}_\perp by (1.49) in *Ohm's law* gives the variation of the horizontal component of the reduced electric current density inside the *Hartmann* layer, \mathbf{J}_\perp^{Ha} , as:

$$\mathbf{J}_\perp^{Ha} = \mathbf{J}_\perp^c - \mathbf{J}_\perp = \sigma \mathbf{u}_\perp^c \times \mathbf{B} \left(e^{-\frac{z}{\delta}}\right), \quad \text{with } \mathbf{J}_\perp^c = -\sigma \nabla \Phi + \sigma \mathbf{u}_\perp^c \times \mathbf{B}. \quad (1.50)$$

where \mathbf{J}_\perp^c denotes the current density outside the layer in the core flow. The term $\sigma \mathbf{u}_\perp^c \times \mathbf{B}$ in the equation on the left of (1.50) can also be seen as the electric current density \mathbf{J}_\perp^w that is found at the wall were $z = 0$. When integrating (1.50) along \mathbf{e}_z between $z = 0$

and $z \rightarrow \infty$ it yields:

$$\int_0^\infty \mathbf{J}_\perp^{Ha} dz = \mathbf{u}_\perp^c \times \mathbf{e}_z (\sigma \rho \nu)^{-1/2}. \quad (1.51)$$

This reveals one important property of the *Hartmann* layer: it demonstrates that the electric current per unit length inside the layer is proportional to the velocity field \mathbf{u}_\perp^c just outside the layer as given by [61] (also *e.g.* [42]). In other words, there is no fluid flow in the horizontal plane if no current flows inside the *Hartmann* layer.

Another important property of the *Hartmann* layer is found when combining (1.44) with (1.49) and integrating along \mathbf{e}_z between the limits $z = 0$ and $z = \infty$. This yields for the vertical component of the electric current density in the *Hartmann* layer, J_z^{Ha} :

$$J_z^{Ha} = J_z^c - J_z^w = \sigma \frac{L}{Ha} \omega_z^c B_0 + \sigma \int_0^\infty (-\nabla_\perp^2 \Phi + \omega_z^c B_0) dz. \quad (1.52)$$

where $\omega_z^c = (\nabla \times \mathbf{u}_\perp^c) \mathbf{e}_z$ is the vorticity just outside the *Hartmann* layer and J_z^c and J_z^w relate to the electric current density in the core of the flow and at the *Hartmann* wall ($z = 0$) respectively (note that $J_z^w \neq 0$ when electric current is injected at the wall (*see e.g.* [62, 63])). Electric current conservation implies that:

$$\nabla_\perp^2 \Phi = 2\omega_z^c B_0. \quad (1.53)$$

and therefore:

$$J_z^{Ha} = \sigma \frac{L}{Ha} \omega_z^c B_0. \quad (1.54)$$

The above relation shows that J_z^{Ha} is directly related to the rotation ω_z^c above the *Hartmann* layer. This rotation sets up the electric field $\nabla \Phi$ that drives in the region $z \leq \delta$ an electric current radially inward toward the rotation centre which evolves into J_z^{Ha} as required by current conservation. In other words, vorticity above the *Hartmann* layer "sucks" electric current density out of the *Hartmann* layer.

Assuming that the flow just outside the *Hartmann* layer is two-dimensional one may define $\mathbf{u}_\perp^c = \nabla \Psi \times \mathbf{e}_z$. Taking its curl one find that the scalar stream function Ψ satisfies a *Poisson* equation:

$$\nabla_\perp^2 \Psi = -\omega_z^c. \quad (1.55)$$

were ω_z^c is the vertical component of the vorticity in the core. When Ψ and Φ satisfy the same boundary condition, one may combine (1.53) with the above equation and it yields to the important relation (see *e.g.* [30]):

$$\Psi = -\frac{\Phi}{B_0}. \quad (1.56)$$

This relation is of great importance in experimental MHD as it relates the local measured electric potential to the corresponding value of the stream function.

Stability of the Hartmann layer

The state of the *Hartmann* layer, laminar or turbulent, is fundamental in many MHD flows. If laminar it possesses the properties given in Sec. 1.2.2 and exerts a linear damping on the flow (see Sec. 1.2.3). However, when the *Hartmann* layer destabilizes into a turbulent state both the global electric current circulation and the global damping of the flow are strongly affected. In other words, the flow may change completely in nature and intensity. To this end, there has been number of work, both theoretical and experimental, largely summarised in [70]’s up-to-date review. The main finding was that, in the limit of high Ha, the destabilisation of the *Hartmann* layer is controlled by the *Reynold*’s number R_h built on the *Hartmann* layer size δ :

$$R_h = \frac{U\delta}{\nu} = \frac{\text{Re}}{\text{Ha}}. \quad (1.57)$$

Following linear stability analysis, the transition to turbulence in the *Hartmann* layer occurs at critical values of R_h (*e.g.*[36]: $R_h^c \simeq 48250$) that are several orders of magnitude greater then those observed in earlier experiments on flow laminarisation in duct flows ($150 < R_h^c < 250$, *e.g* [8]). [44]’s weakly nonlinear stability analysis shows that the transition to turbulence is indeed *subcritical* and therefore, may explain this huge discrepancy between theory and experiment.

From the experimental point of view, the results of [45]’s more recent work are probably the most important ones as their experiment has been especially designed to study the laminar/turbulent transition inside the *Hartmann* layer. A fluid layer of mercury subject to a vertical magnetic field and hermetically enclosed in a cylindrical duct was set in azimuthal motion by radially injected constant electric current. In the laminar regime, the fraction of injected energy that is passed onto the flow evolves linearly with R_h , but suddenly decreases when the *Hartmann* layer becomes turbulent at the critical $R_h^c \simeq 380$. This was also confirmed numerically by [33].

Lastly, [46] showed that when the fluid rotates above the boundary layer it influences the instability threshold. In this case one addresses a combined *Boedwadt-Hartmann* layer ([11]) rather than a simple *Hartmann* layer. The former is less stable as inertial effects inside the boundary layer become important and can trigger the instability at much lower values of R_h^c than those found by [45] and [33] for a simple *Hartmann* layer.

1.2.3. Shallow water liquid metal MHD

Shallow water equations can be used to describe flows where the vertical dimension is much smaller than the typical horizontal scale and vertical velocities are small. They are derived by vertically averaging the three-dimensional *Navier-Stokes* equation to obtain a two-dimensional model.

Liquid metal MHD flows too can reach a state where vertical velocities are small and the flow moves only in the horizontal plane orthogonal to the magnetic field, except in thin *Hartmann* layers. For such quasi two-dimensional flows one is also tempted to describe the flow using two-dimensional dynamics. This is precisely what [64]'s SM82-model achieves and we shall describe it in this section. Furthermore, we explain the mechanism that drives a vortical flow in an electrically conducting fluid when electric current is injected at the physical boundaries. Finally, we briefly refer to the [54]'s PSM-model which is a refinement of the SM82-model and accounts also for weak 3D effects like *Ekman* pumping.

The SM82-model [64]

The SM82 model was developed by [64] and is based on averaging the full three-dimensional motion equation along the magnetic field lines. It results in a "two-dimensional model" which delivers quantitatively good predictions for MHD flows where:

$$N \gg 1 \quad \text{and} \quad \text{Ha} \gg 1 \tag{1.58}$$

Under these conditions, the effect of the *Lorentz* force $\mathbf{J} \times \mathbf{B}$ is to instantaneously damp velocity variations along the field direction $\mathbf{B} = B_0 \mathbf{e}_z$ (Sec. 1.2.1), except inside thin *Hartmann* layers where the effect of viscosity is of the same order as the *Lorentz* force (Sec. 1.2.2).

To recover [64]'s model one may consider the quasi two-dimensional flow in Fig. 1.4 were an incompressible, electrically conducting fluid layer of thickness a is subject to a transverse uniform magnetic field \mathbf{B} and bound by a *Hartmann* wall on either side. The

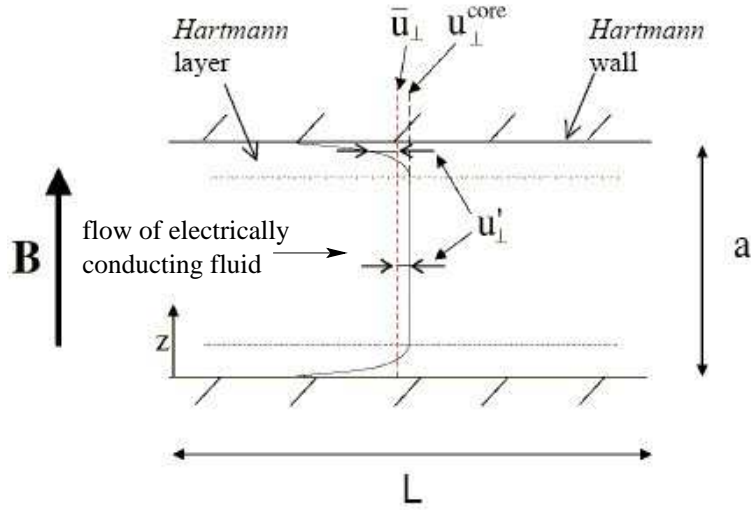


Figure 1.4.: Schematic illustration of a quasi two-dimensional flow. The term "quasi two-dimensional" reflects the flow's invariance everywhere across the fluid layer along the magnetic field \mathbf{B} , except in thin *Hartmann* layers that develop along *Hartmann* walls. Quasi two-dimensional flows can be described by the SM82-model ([64]). $\bar{\mathbf{u}}_{\perp}$ is the velocity field spatially averaged along \mathbf{B} , \mathbf{u}'_{\perp} denotes its spatial fluctuations and $\mathbf{u}^{core}_{\perp}$ is the velocity field in the core flow outside the *Hartmann* layers.

flow with the velocity field $\mathbf{u} = (\mathbf{u}_{\perp}, w\mathbf{e}_z)$ where w is small when Ha is described by the set of MHD equations (1.15), (1.16), (1.5) and (1.6). One may further define \bar{g} as the z-average of each quantity g as follows:

$$\bar{g}(x, y) = \frac{1}{a} \int_0^a g(x, y, z) dz$$

which implies that:

$$g(x, y, z) = \bar{g}(x, y) + g'(x, y, z).$$

where g' denotes the spatial fluctuation of g from its z-averaged quantity \bar{g} . The integral of (1.15) along \mathbf{e}_z between the two walls expresses as:

$$\nabla_{\perp} \cdot \int_0^a \mathbf{u}_{\perp} dz + [w]_0^a = 0 \quad (1.59)$$

where the subscript $(\cdot)_{\perp}$ stands for components orthogonal to the magnetic field \mathbf{B} . The non-slip boundary condition requires the velocity to be zero at the walls so it follows from

the above equation that the averaged velocity field $\bar{\mathbf{u}}_\perp$ is incompressible:

$$\nabla_\perp \cdot \bar{\mathbf{u}}_\perp = \mathbf{0}. \quad (1.60)$$

This further implies that $\bar{\mathbf{u}}_\perp$ can be expressed by means of a scalar stream function Ψ :

$$\bar{\mathbf{u}}_\perp = \nabla\Psi \times \mathbf{e}_z. \quad (1.61)$$

The integration of (1.16) along the field \mathbf{B} yields for the non-linear terms to:

$$\int_0^a (\bar{\mathbf{u}}_\perp + \mathbf{u}'_\perp) \cdot \nabla_\perp (\bar{\mathbf{u}}_\perp + \mathbf{u}'_\perp) = a(\bar{\mathbf{u}}_\perp \cdot \nabla_\perp \bar{\mathbf{u}}_\perp) + a(\overline{\mathbf{u}'_\perp \cdot \nabla_\perp \mathbf{u}'_\perp}). \quad (1.62)$$

For high values of Ha , the first and second term on the right hand side of the above equation are of order of $\sim \frac{\|\mathbf{u}^{core}\|^2}{L}$ and $\sim \frac{\|\mathbf{u}^{core}\|^2}{Ha^2 L}$ respectively, so the latter can be considered as negligible. The integral of the z-component of the viscous term in (1.16) provides information about the back reaction of the *Hartmann* layer onto the flow. Inside this layer, the combined effect of viscosity and *Lorenz* force imposes a friction that linearly brakes the flow according to:

$$\nu \int_0^a \partial_{zz}^2 \mathbf{u}_\perp dz = \nu \partial_z \mathbf{u}_\perp|_a - \nu \partial_z \mathbf{u}_\perp|_0 = -n\nu \frac{\text{Ha}}{a} \bar{\mathbf{u}}_\perp + \mathcal{O}\left(\frac{1}{\text{Ha}}\right). \quad (1.63)$$

In the present case, the fluid layer is bounded by a *Hartmann* layer on either side so $n = 2$ ($n = 1$ if the layer has one free surface). The integrals of the other terms in (1.16) are found readily and one can give the final z-averaged motion equation for the two-dimensional velocity field $\bar{\mathbf{u}}_\perp(x, y, t)$ as follows:

$$\partial_t \bar{\mathbf{u}}_\perp + \bar{\mathbf{u}}_\perp \cdot \nabla_\perp \bar{\mathbf{u}}_\perp + \frac{1}{\rho} \nabla \bar{p} = \nu \nabla_\perp^2 \bar{\mathbf{u}}_\perp - \frac{\bar{\mathbf{u}}_\perp}{\tau_H} + \frac{1}{\rho} \bar{\mathbf{J}}_\perp \times \mathbf{B} + \frac{1}{\rho} \bar{\mathbf{G}}. \quad (1.64)$$

with:

$$\tau_H = \frac{a^2}{2\nu} \frac{1}{\text{Ha}} = \frac{a}{2B_0} \sqrt{\frac{\rho}{\sigma\nu}}. \quad (1.65)$$

where τ_H is referred to as the *Hartmann* friction time. One way to generate a fluid motion is to inject electric current density at the boundaries (*e.g.* [62, 63, 45]). This yields to the *Lorentz* force $\bar{\mathbf{G}} = \bar{\mathbf{J}}_\perp \times \mathbf{B}$ driving the fluid. It is then customary to replace the *Lorentz* force term in (1.64) by a velocity field \mathbf{u}_0 defined as ([55]):

$$\frac{1}{\rho} B_0 \bar{\mathbf{J}}_\perp \times \mathbf{e}_z = \frac{\mathbf{u}_o}{\tau_H} \quad (1.66)$$

Implementing (1.66) into (1.64) yields:

$$\partial_t \bar{\mathbf{u}}_\perp + \bar{\mathbf{u}}_\perp \cdot \nabla_\perp \bar{\mathbf{u}}_\perp + \frac{1}{\rho} \nabla \bar{p} = \nu \nabla_\perp^2 \bar{\mathbf{u}}_\perp + \frac{(\mathbf{u}_0 - \bar{\mathbf{u}}_\perp)}{\tau_H} \quad (1.67)$$

where u_0/τ_H is the driving term that arises from current injection and $-n\bar{\mathbf{u}}_\perp/\tau_H$ represents the linear friction that the *Hartmann* layer/layers exert on the flow. With the scalings $\mathbf{u}^* = \mathbf{u}U^{-1}$, $\nabla^* = \nabla L$, $t^* = t(U/L)$ and $p^* = p(\rho U^2)^{-1}$ the SM82 model in dimensionless form is obtained and reads:

$$\partial_t^* \bar{\mathbf{u}}_\perp^* + \bar{\mathbf{u}}_\perp^* \cdot \nabla_\perp^* \bar{\mathbf{u}}_\perp^* + \nabla^* \bar{p}^* = \frac{1}{\text{Re}} \nabla_\perp^{*2} \bar{\mathbf{u}}_\perp^* + \frac{1}{R_h} (\mathbf{u}_0^* - \bar{\mathbf{u}}_\perp^*). \quad (1.68)$$

with

$$R_h = \frac{\text{Re}}{\text{Ha}} = \frac{\tau_H}{\tau_U}. \quad (1.69)$$

R_h is called the *Hartmann* friction parameter and is equivalent to the *Reynold's* number based on the Ha-layer size δ . For high Ha, R_h and not Re is the governing parameter that controls the flow dynamics. In other words, Hartmann friction and not viscous friction is the main cause of energy dissipation in the quasi-two dimensional (q2D) flow, even though they are of comparable importance in the vicinity of the walls parallel to the magnetic field.

Electrically driven flows

MHD flows experimentally studied in this work are generated by injecting constant electric current density J_w locally through point electrodes that are embedded in the *Hartmann* wall. Following [64], this imprints a vortical motion above each electrode with the velocity field $\mathbf{u}_0 = u_\theta \mathbf{e}_\theta$ that is, with respect to (1.66), related to the z-averaged electric current density $\bar{\mathbf{J}}_\perp = J_r \mathbf{e}_r$ as follows:

$$a \bar{\mathbf{J}}_\perp = -(\mathbf{u}_0 \times \mathbf{e}_z) \sqrt{\sigma \nu \rho}. \quad (1.70)$$

A typical radial profile of the azimuthal velocity $u_\theta(r)$ for a steady vortex is illustrated in Fig. 1.5. It results from the balance between electromagnetic forcing, *Hartmann* layer friction and lateral viscous friction.

u_θ increases in the vortex core in the region ($0 < r < r_0 \simeq \text{Ha}^{-1/2}$) where a viscous

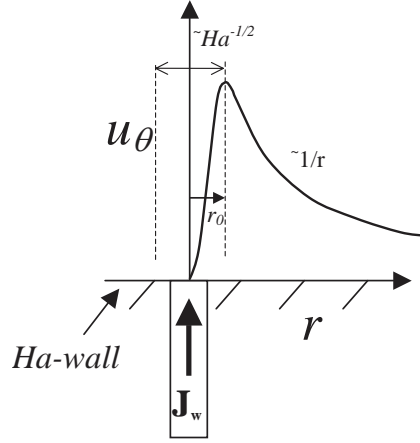


Figure 1.5.: Typical velocity profile $u_\theta(r)$ of an isolated, electrically driven vortex (see for instance [63, 54]).

shear layer of typical thickness $\text{Ha}^{-1/2}$ occurs due to the electrical nonuniformity at the boundary wall ([26]). An estimation of the shear layer size δ_s is found when comparing the orders of magnitude of the two terms on the right hand side of (1.67):

$$\frac{\|\nu \nabla_{\perp}^2 \bar{\mathbf{u}}_{\perp}\|}{\|\bar{\mathbf{u}}_{\perp}/\tau_H\|} \simeq \frac{\nu U \delta_s^{-2}}{\nu U \text{Ha}/a^2} \rightarrow \delta_s \simeq \frac{a}{\sqrt{\text{Ha}}}. \quad (1.71)$$

Outside the shear layer (in the region $r > r_0$), electric current conservation requires that the current density $\bar{\mathbf{J}}_{\perp} \sim 1/r$. It follows from (1.70) that u_θ also declines with $1/r$ as illustrated in Fig. 1.5.

According to (1.61) one may now define the scalar Ψ_0 as a stream function for \mathbf{u}_0 such that $\mathbf{u}_0 = \nabla \Psi_0 \times \mathbf{e}_z$. This combined with (1.70) expresses $\bar{\mathbf{J}}_{\perp}$ as a gradient of Ψ_0 that, using the z-averaged current conservation $\nabla_{\perp} \cdot \bar{\mathbf{J}}_{\perp} = -J_w/a$, satisfies a *Poisson* equation:

$$a \bar{\mathbf{J}}_{\perp} = \nabla \Psi_0 \sqrt{\sigma \nu \rho} \quad , \quad \nabla^2 \Psi_0 \sqrt{\sigma \nu \rho} = -J_w. \quad (1.72)$$

Integrating the above *Poisson* equation across the vortex core yields:

$$-\frac{I}{2\pi r} = \frac{\partial \Psi_0}{\partial r} \sqrt{\sigma \nu \rho}. \quad (1.73)$$

The above relation is equivalent to the radial component of $\bar{\mathbf{J}}$ in (1.72) and can be combined with (1.70). This yields to an expression for the forced velocity u_θ in the region $r \geq r_0$ depending on the injected current I and the distance r as follows:

$$u_\theta(I, r) = \frac{I}{2\pi r} \frac{1}{\sqrt{\sigma \nu \rho}} = \frac{\Gamma_0}{r}. \quad (1.74)$$

$\Gamma_0 = I/(2\pi\sqrt{\sigma\rho\nu})$ is the total circulation induced by the current injection at a single electrode and reflects the intensity of the forcing. Like the velocity $\mathbf{u}_0 = u_\theta \mathbf{e}_\theta$, it is proportional to the injected electric current I , but does not depend on the strength of the magnetic field $\mathbf{B} = B_0 \mathbf{e}_z$. The *Lorentz* force however, which is responsible for both the establishment of two-dimensionality in the core flow and this forcing, does depend on \mathbf{B} . In *strictly* quasi two dimensional flows, its strength B_0 determines only the amount of flow dissipation due to *Hartmann* friction in the *Hartmann* layer at time scale τ_H (1.66). All electric current flows now inside this very thin boundary layers and is proportional to the velocity in the core flow, independent of the magnetic field (1.51).

The flow, induced by electric current injection through point electrodes is however never strictly quasi two-dimensional. This is because of the vortex core just above the electrode where viscous effects balance the *Lorentz* force and three-dimensionality is intrinsically present (Fig. 1.5). It implies that the velocity just outside the vortex core, where $r \gtrsim r_0$, is equivalent to \mathbf{u}_0 according to (1.74), but can not reach the higher values of \mathbf{u}_0 in regions where $r < r_0$. Since the thickness of the vortex core scales with $\text{Ha}^{-1/2}$ (1.71) the forcing depends on the strength of the magnetic field B_0 , at least in the sense that it determines the velocity \mathbf{u}_0 at the edge of the vortex core. In other words, the velocity \mathbf{u}_0 outside the vortex core where the flow is strictly quasi two-dimensional does not depend on B_0 . Experimentally this has been shown by [63] where a steady isolated vortex was produced in a shallow, horizontal layer of mercury subject to uniform vertical magnetic field. Lastly it should be noted that when applied magnetic fields are moderate, the flow outside the vortex core ($r \gtrsim r_0$ in Fig. 1.5) may not be strictly quasi two-dimensional anymore but three-dimensional because of three-dimensional inertial effects. In this case, the velocity \mathbf{u}_0 is not reached in this region either and the forcing depends too on the coordinate along the direction of the magnetic field.

The velocity profile of u_θ , as schematically illustrated in Fig. 1.5, can be obtained by solving the z-averaged motion equation (1.67). [54] has shown that the resulting profile does not significantly differ from the three-dimensional solution for large Ha given by [26] and adapted to the present case by [63].

The PSM model [54]

The SM82 model delivers accurate results in the limit of high values of Ha and N to a precision of order of $\max(\text{Ha}^{-1/2}, N^{-1/2})$. Even the error because of assimilating the intrinsically three-dimensional lateral boundary layers of size $a\text{Ha}^{-1/2}$ to two-dimensional ones remains smaller than 10% as demonstrated by [54]. When however the interaction parameter N becomes moderate [64]'s approach appreciably fails as inertia in the core

flow and in the *Hartmann* layer are stronger and 3D effects appear. For instance, strong fluid rotation above the *Hartmann* layer triggers a fluid recirculation that is known as *Ekman pumping* (Fig. 1.6). More precisely, the rotation with typical velocity U_\perp sets up

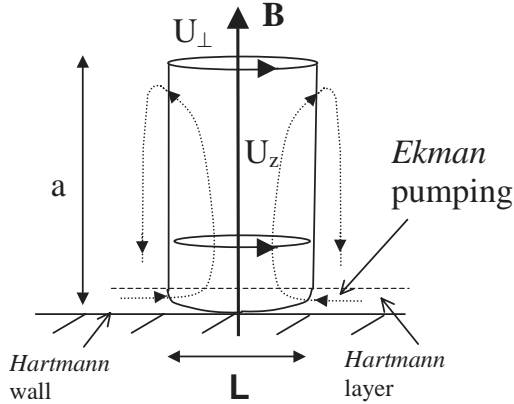


Figure 1.6.: Effect of *Ekman pumping*. *Ekman pumping* is induced by fluid rotation above the *Hartmann* layer when inertial effects in this layer become important.

a radial pressure gradient that is balanced by centrifugal forces outside the *Hartmann* layer. But the velocity and therefore the centrifugal forces drops inside the boundary layer because of viscosity. This implies that the pressure gradient dominates here and imprints a radial fluid motion of order of $\sim U_\perp/N$ ([43]). In the vicinity of the vortex axis, mass conservation pushes the fluid upwards with typical velocity U_z :

$$U_z \simeq \frac{U_\perp a}{\text{Ha} N L_\perp} \quad \text{see e.g. [43]}$$

This fluid gets released at the lateral edges of the vortex and plunges back into the boundary layer as illustrated in (Fig. 1.6) (e.g [28]).

To account for such three-dimensional effects [54] proposes a refinement of the SM82 model which is referred to as the PSM model. It expresses in dimensional form:

$$\nabla_\perp \cdot \bar{\mathbf{u}}_\perp = 0,$$

$$\partial_t \bar{\mathbf{u}}_\perp + \bar{\mathbf{u}}_\perp \cdot \nabla_\perp \bar{\mathbf{u}}_\perp + \frac{1}{\rho} \nabla \bar{p} = \nu \nabla_\perp^2 \bar{\mathbf{u}}_\perp - \frac{n \bar{\mathbf{u}}_\perp}{\tau_H} + \frac{n \alpha \tau_H}{\text{Ha}^2} \left(\frac{7}{36} \mathcal{D}_{\bar{\mathbf{u}}_\perp} + \frac{1}{8} \partial_t \right) \bar{\mathbf{u}}_\perp \cdot \nabla \bar{\mathbf{u}}_\perp \quad (1.75)$$

where $\alpha = 1 + n/\text{Ha}$ and the linear operator $\mathcal{D}_{\bar{\mathbf{u}}_\perp}$ is defined as:

$$\mathcal{D}_{\bar{\mathbf{u}}_\perp} : \mathbf{F} \longmapsto \mathcal{D}_{\bar{\mathbf{u}}_\perp} \mathbf{F} = (\bar{\mathbf{u}}_\perp \cdot \nabla_\perp) \mathbf{F} + (\mathbf{F} \cdot \nabla_\perp) \bar{\mathbf{u}}_\perp.$$

From these equations [54] obtained an expression for the velocity u_z along the magnetic field lines just at the edge of the *Hartmann* layer which reads in dimensionless form as follows:

$$u_z = -\frac{5}{6} \frac{\lambda}{\text{Ha}N} \nabla_{\perp} \cdot [(\bar{\mathbf{u}}_{\perp} \cdot \nabla_{\perp}) \bar{\mathbf{u}}_{\perp}] \nabla_{\perp} \cdot \bar{\mathbf{u}}_{\perp} = 0, \quad (1.76)$$

λ is the ratio between length scales parallel and perpendicular to the magnetic field. When interpreting our experimental results in Sec. 3.2 we benefit from [28]'s numerical outcomes obtained from simulations of the quasi two-dimensional vortex pair enclosed in the shallow cylindrical container using the PSM-model.

1.3. Turbulence

Understanding of turbulence is one of the greatest challenges offered by modern physics. Although we are here more interested in magnetohydrodynamic (MHD) turbulence where the effect of the *Lorentz* force modifies the turbulent behaviour under the condition that the magnetic *Reynolds* Rm number is small, we review in this section some major properties of both hydrodynamic turbulence (non-MHD) and MHD turbulence.

1.3.1. Hydrodynamic turbulence

3D turbulence

Turbulent flows consist of vortex structures, or modes, of different length scales l and corresponding wavenumbers $k \simeq 1/l$ as well as characteristic velocities U_l . For the case of 3D isotropic, spatially homogeneous turbulence, energy is injected at the largest turbulent structures (small k) and passed on cascade-like along the inertial range to the smallest scales (high k) where it is eventually dissipated due to the effect of viscosity. In this context, *Kolmogorov's* ([31]) theory relies on the assumption that the spectral Power Density $E(k) = de/dk \simeq U_l^2 l/2$ (where $e = \int_0^\infty E(k)dk$ is the kinetic energy of the flow per unit volume) depends on the wavenumber k and the average dissipation per unit of volume $\epsilon = \nu \|\nabla \mathbf{u}\|^2 \simeq \nu(U_l/l)^2$ only, so that:

$$E(k) = C_k \epsilon^\alpha k^\beta. \quad (1.77)$$

where C_k is a universal constant (*Kolmogorov* constant) which is approximately 1.5. The exponents α and β are found when considering the corresponding dimensional units $[E(k)] = m^3 s^{-2}$, $[k] = m^{-1}$ and $[\epsilon] = m^2 s^{-3}$. This yields to *Kolmogorov's five-third* law that reads:

$$E(k) = C_k \epsilon^{2/3} k^{-5/3} \quad \text{or} \quad E(l) = C_k \epsilon^{2/3} l^{5/3}. \quad (1.78)$$

The *five-third* law implies the large scale vortices (small wavenumbers k) in the energy spectrum (Fig. 1.10) carry much more kinetic energy in average than small scale vortices (high wavenumbers k). Furthermore, the energy content of intermediate scales k in the inertial range is determined by the power law $k^{-5/3}$.

The influence of viscosity on a vortex is measured by the corresponding *Reynold's* number Re_V that is built on the vortex velocity $U_l \simeq \sqrt{2E(l)/l} \simeq 2C_K^{1/2} \epsilon^{1/3} l^{1/3}$ and its length

scale l . It reads:

$$\text{Re}_V = (2C_k)^{1/2} \frac{\epsilon^{1/3} l^{4/3}}{\nu}. \quad (1.79)$$

When $\text{Re}_V = 1$, viscosity destroys the vortex in one vortex turn-over time $\tau_U = l/U_l$. This provides an approximation for the smallest scales l_K and associated velocity U_K (*Kolomogorov* scales):

$$l_K = \left(\frac{\nu^3}{\epsilon} \right)^{1/4} \quad \text{and} \quad U_K = (\nu \epsilon)^{1/4}. \quad \text{see e.g. [34]} \quad (1.80)$$

l_K and U_K are related to the corresponding velocity and size of the largest scales, U and L respectively, by the *Reynold's* number built on the largest scales $\text{Re} = UL/\nu$ as follows:

$$\frac{L}{l_K} \simeq \text{Re}^{3/4} \quad \text{and} \quad \frac{U}{U_K} \simeq \text{Re}^{1/4}. \quad (1.81)$$

2D turbulence

2D turbulence is of fundamental interest because of its unique turbulent phenomena that are amongst others relevant to flows in the atmospheres, oceans and all rapidly rotating flows with tendency to two-dimensionality.

In the case of continuously *forced* 2D turbulence with energy injected at wave number k_i , [32] proposes a double cascade in the energy spectrum $E(k)$ in the limit of large *Reynolds* numbers Re . For $k < k_i$ it has been found that kinetic energy $U^2/2$ is transported in reversed direction from small (high k) to large length scales (small k) so the observation was given the convenient name *inverse energy cascade*. Still, as in the 3D case, $E(k)$ depends on the wavenumber k as well as the dissipation rate ϵ and dimensional analysis yields to the same inertial range:

$$E(k) = C_{2D} \epsilon^{2/3} k^{-5/3} \quad \text{see e.g. Fig. 1.7 from [35]} \quad (1.82)$$

In the spectral region $k > k_i$, another cascade-like process has been suggested and relates to the enstrophy $\omega^2/2$, which is passed down from large (small k) to small scales (high k) along the direct *enstrophy cascade*. The corresponding spectral distribution of the enstrophy $k^2 E(k)$ and the energy $E(k)$ is likewise obtained by means of dimensional analysis and yields:

$$k^2 E(k) = C' \eta^{2/3} k^{-1} \quad \text{and} \quad E(k) = C' \eta^{2/3} k^{-3} \quad \text{see Fig. 1.7} \quad (1.83)$$

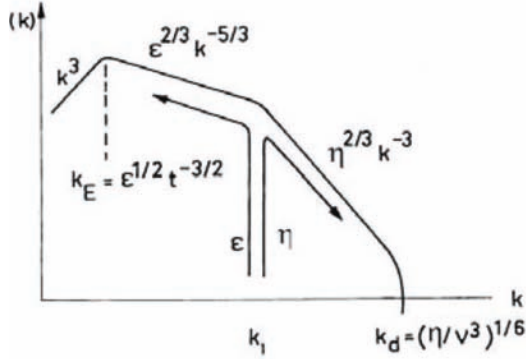


Figure 1.7.: Double energy cascade in continuously forced two-dimensional turbulence [32]. Energy $E(k)$ injected at wavenumber k_i is transported from small scales (high wavenumbers k) to large scales (small wavenumbers k) along an *inverse energy cascade* according to $E(k) \sim k^{-5/3}$ in the region $k < k_i$. In the region $k > k_i$ enstrophy is passed down from large to small scales along the direct *enstrophy cascade* which corresponds to the spectral energy distribution according to $E(k) \sim k^{-3}$. Note that the above illustration is taken from [35].

$\eta = \nu(\nabla\omega)^2$ being the dissipation rate of enstrophy (see e.g. [13]).

Experimental evidence for the built up of an *inverse energy cascade* has been found in liquid metal experiments ([62] and [17, 18]), in electromagnetically driven flows in stably stratified layers ([51]) and in flowing soap films ([57]). Amongst those, only [57] clearly observed the simultaneous existence of *inverse energy cascade enstrophy cascade*, possibly because of the high spatial resolution in their experiment.

As in the 3D case, one can find an approximate relation between the smallest and largest scales. However, in 2D it is based on grounds that the enstrophy is passed down in a cascade, instead of the energy. Combining the estimate for the vortex velocity, $U(k) \sim \sqrt{E(k)k}$, with (1.83) it yields for the *Reynolds* number built on the vortex, Re_V :

$$Re_V = \frac{\eta^{1/3}}{\nu k^2} = \frac{\eta^{1/3} l^{-2}}{\nu} \quad (1.84)$$

The smallest vortices get dissipated due to the effect of viscosity during one turnover time. For these scales it is $Re_V \simeq 1$. This implies for their approximate size l_K^{2D} and velocity U_K^{2D} :

$$l_K^{2D} = \left(\frac{\nu}{\eta^{1/3}} \right)^{1/2} \quad \text{and} \quad U_K^{2D} = (\eta^{1/3} \nu)^{1/2} \quad (1.85)$$

Eventually, one finds for the equivalent of (1.81) in two dimensions (*e.g.* [13]):

$$\frac{L}{l_K^{2D}} \simeq \text{Re}^{1/2} \quad \text{and} \quad \frac{U^{2D}}{U_K^{2D}} \simeq \text{Re}^{1/2} \quad (1.86)$$

where Re is built on the length scale and velocity of the largest scales, L^{2D} and U^{2D} respectively.

Apart from such rather heuristic approaches, [14, 48] derive an mathematically exact lower bound for the smallest length scales l_K^{2D} (or highest wave number $k_K^{2D} \simeq 1/l_K^{2D}$) in two-dimensional turbulence expressed in terms of the *Grashoff* number \mathcal{G} as follows:

$$k_K^{2D} \leq c\mathcal{G}^{1/3}(1 + \ln\mathcal{G})^{1/3} \quad (1.87)$$

where c is a constant of order 1 and \mathcal{G} expresses the ratio between the turbulent forcing and viscous friction.

1.3.2. Magnetohydrodynamic (MHD) turbulence

3D MHD Turbulence

The effect of the *Lorentz* force in MHD turbulence influences turbulent flow structures by promoting their elongation along the magnetic field lines \mathbf{B} (Sec. 1.2.1). Depending on the relative strength of the *Lorentz* force compared to inertial forces, as measured by the interaction parameter N , one should distinguish three different cases from here:

a) $N \gg 1$

When $N \gg 1$, inertial effects are small compared to the *Lorentz* force so the equation of motion can be linearised. Replacing the *Lorentz* force term in (1.23) by expression (1.34) and using *Fourier* transforms one obtains for the inviscid ($\text{Re} \gg 1$) and linearised motion equation:

$$\frac{\partial \hat{\mathbf{u}}}{\partial t} = -\frac{1}{\rho} i\mathbf{k}\hat{p}' - \frac{1}{\tau_j} (\cos^2\theta)\hat{\mathbf{u}} \quad , \text{ where } \theta = (\mathbf{k}, \mathbf{B}) \quad (1.88)$$

When taking the scalar product of the above equation with \mathbf{k} and using mass conservation in Fourier space, $\mathbf{k} \cdot \hat{\mathbf{u}} = 0$ one finds that the pressure term in (1.88) is zero. This yields to the exponentially decaying solution for $\hat{\mathbf{u}}(\mathbf{k}, t)$ according to:

$$\hat{\mathbf{u}}(\mathbf{k}, t) = \hat{\mathbf{u}}_0(\mathbf{k}, t) e^{-(t/\tau_j) \cos^2\theta}. \quad (1.89)$$

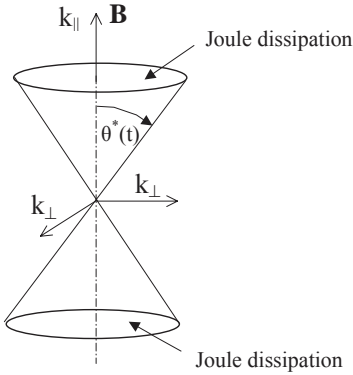


Figure 1.8.: Sketch of the Joule cone in Fourier space. $\theta^*(t)$ is the half angle of the Joule cone that progressively opens and separates modes dissipated by Joule dissipation from those that contain mostly the kinetic energy in a turbulent MHD flow.

The above equation describes the evolution of one Fourier-mode with wave vector \mathbf{k} that makes the angle θ with the magnetic field \mathbf{B} . For times $t = \tau_j$ it suggests that any turbulent mode with the angle $\theta = 0$ experiences the strongest damping or Joule dissipation, regardless its scale. Later on when $t > \tau_j$, Fourier-modes for which hold $0 < \theta < \pi/2$ also get dissipated and toward the end of the linear regime kinetic energy is contained in modes that satisfy ([66]):

$$|\cos\theta| \leq \left(\frac{t}{\tau_j}\right)^{-1/2} \quad (1.90)$$

In order to separate modes in a turbulent flow that have already lost part of their energy because of joule dissipation from those which contain mostly the kinetic energy in the Fourier-space, [41, 42] introduce the weighted and time dependent angle $\theta^*(t)$. $\theta^*(t)$ measures the half angle of the so called Joule cone (Fig. 1.8) and satisfies:

$$|\cos\theta^*(t)| \sim \left(\frac{t}{\tau_j}\right)^{-1/2} \quad (1.91)$$

In fact, $\theta^*(t)$ marks the "edge" of the Joule cone that appreciably opens when time evolves. Accordingly, the aspect ratio of each vortical structure grows at the rate (1.37) and the turbulent flow becomes anisotropic. It should be also noticed that wave vectors with $\theta = \pi/2$ remain totally unaffected by Joule dissipation. This further implies that the perpendicular length scales, $l_\perp \simeq 1/k_\perp$ can be taken as approximately invariant in this linear regime.

When studying turbulent flows in MHD one must distinguished between *freely decaying* and *forced* turbulence.

[39]’s earlier analytical work on *freely decaying* turbulence shows that the initially isotropic turbulent flow rapidly evolves into strong anisotropy in the linear phase where $\tau_j < t < \tau_U$, after a sudden magnetic field \mathbf{B} has been imposed at $t = 0$. Furthermore, [39] demonstrates that the global kinetic energy e of the turbulence decays as:

$$e \sim e_0 \left(\frac{t}{\tau_j} \right)^{-1/2} \quad (1.92)$$

It has been also predicted that the velocity component parallel to the field \mathbf{B} carries more kinetic energy than the one in the transverse plane, though both are still of the same order of magnitude. This result and the establishment of anisotropy have been later confirmed by [59]’s numerical and [4]’s experimental work on *freely decaying* MHD turbulence.

[74] numerically studies the evolution of an isotropic but *forced* homogeneous turbulence in a periodic box where the effect of physical walls onto the turbulence is excluded from the numerical simulations. For large interaction parameters such as $N = 10$, the flow rapidly transforms into a quasi two-dimensional state with a level of anisotropy approximately equal at all scales in the inertial range of the energy spectra. Furthermore, over about the first few joule times, [74] observed a stronger increase of the parallel velocity component which is in accordance with [39, 59, 4]’s observations in *freely decaying* turbulence.

b) $N \simeq 1$

When $N \simeq 1$, MHD turbulence shows the most complex behaviour. For *freely decaying* turbulence, this condition marks the end of the linear phase where the Joule cone has already sufficiently opened ($\theta^*(t)$ close to $\pi/2$) and the only part in the spectra that contains kinetic energy of the flow is located outside the Joule cone in modes with angles satisfying (1.90). Energy is now continuously ”removed” from this region and transferred into the Joule cone at its edge ($\theta^*(t)$) to compensate Joule dissipation induced by current eddies at the vortice’s extremities (Fig. 1.9). In short, a ”quasi-steady” equilibrium has been established ([4]).

The global time scales, the inertial time $\tau_U(t) = \frac{L(t)}{U(t)}$ and the Joule time τ_j , are of the same order of magnitude in this state which suggests a decay law for the global kinetic energy e of the turbulent flow according to:

$$e \simeq U^2 \sim L^2 t^{-2} \quad (1.93)$$

This law could be reasonably well confirmed by [4]’s measurements where the kinetic energy was found to follow a $t^{-1.7}$ decay.

Locally, in the spectral vicinity of the wave vector \mathbf{k} , the ”quasi-steady” equilibrium

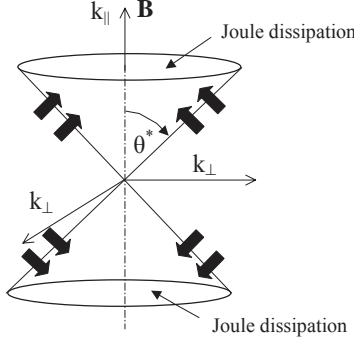


Figure 1.9.: Sketch of the Joule cone in Fourier space in a quasi-steady equilibrium state where energy is transferred from energy-containing modes into the Joule cone at its edge, to compensate Joule dissipation induced by current eddies at the vortice's extremities ([4]).

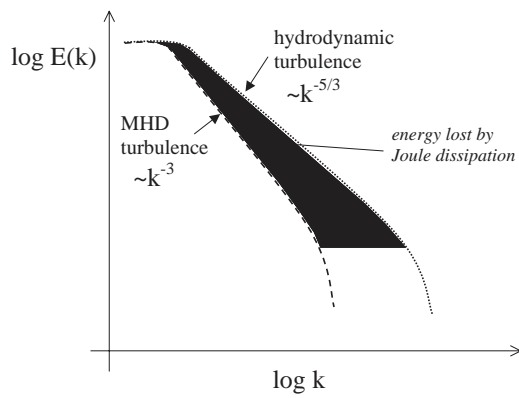


Figure 1.10.: Characteristic of the energy spectrum $E(k)$ in hydrodynamic and magnetohydrodynamic (MHD) turbulence. Turbulent eddies in MHD turbulence experience additional joule dissipation. This results in a steeper decay in the energy spectrum $E(k)$ as in hydrodynamic turbulence.

requires the equality of the energy transfer time $(U(k)k)^{-1}$ and the Joule time $\tau_j \sim t$. Assuming that both time scales are k -independent it yields to the following decay law for the energy spectra $E(k)$:

$$E(k) = k^{-3}t^{-2} \quad (1.94)$$

The experimental proof of the k^{-3} spectra for *freely decaying* turbulence is given by [4]. In this context one should stress that in [4]'s experiment the turbulence is far from being two-dimensional and, therefore, the measured k^{-3} spectra has nothing in common with the enstrophy cascade predicted by [6] for two-dimensional turbulence. The steeper slope in the energy spectra $E(k)$ in comparison with the $k^{-5/3}$ decay in classic hydrodynamic turbulence relates to the additional Joule dissipation that acts at all scales (Fig. 1.10).

[74]’s direct numerical simulations on *forced* turbulence revealed another effect when $N \simeq 1$. For $N = 0.4$, they reported intermittent behaviour consisting of quasi-two-dimensionality flow states that persists for several times τ_U , but then become interrupted by strongly three-dimensional regimes. This effect however has never been observed elsewhere than in numerical simulations with boundaries where no dissipation occurs (periodic or free-slip boundary condition).

Smallest scales for regimes where $N \gtrsim 1$ (see [53])

The smallest vortex scales in MHD turbulence, l_K^M (or highest wave numbers $k_K^M \simeq 1/l_K^M$) are like in hydrodynamic turbulence determined by the balance between inertia and viscosity. They dissipate over one turn over and mark the end of the energy spectrum $E(k)$. Considering scales in the transverse plane this implies for the *Reynolds* number based on a vortex, Re_V :

$$\text{Re}_V \simeq \frac{u_{\perp_K}^M(l_{\perp_K}^M)l_{\perp_K}^M}{\nu} = 1 \quad (1.95)$$

Following the usual assumption that anisotropy is scale-independent (*e.g.* [4]), the condition (1.37) applies also to the smallest scales. This combined with (1.95) yields to ([53]):

$$\frac{l_{\parallel_K}^M}{l_{\perp_K}^{2M}} \sim \frac{\text{Ha}}{L} \quad (1.96)$$

where L is a typical length scale of the largest scales. Following [53], the corresponding smallest scales in the transverse plane, $l_{\perp_K}^M$, and along the magnetic field \mathbf{B} , $l_{\parallel_K}^M$, can be obtained when using again (1.37) as well as the ratio $\text{Ha}^2/\text{Re} = N$. They satisfy:

$$\frac{L}{l_{\perp_K}^M} \simeq \text{Re}^{1/2} \quad \text{and} \quad \frac{L}{l_{\parallel_K}^M} \simeq \frac{\text{Re}}{\text{Ha}} \quad (1.97)$$

The *Reynolds* number Re in (1.97) is built on a typical large scale velocity U and large scale length L . It should be noticed that $l_{\parallel_K}^M$ increases with the magnetic field \mathbf{B} while $l_{\perp_K}^M$ does not depend on it. This goes along with the argument that transverse scales are not affected by the magnetic field and might also explain why $l_{\perp_K}^M$ is of the same order as l_K^{2D} in 2D turbulence.

c) $N < 1$

When $N < 1$, inertial effects are strong and the joule cone has no time to open. In short, electromagnetic effects are negligible. As consequence, [74]’s numerical simulations on

forced MHD turbulence show that the flow remains in the 3D isotropic state as in hydrodynamic turbulence. In the experiment of [4] on *freely decaying* turbulence, the authors also measured the related $k^{-5/3}$ spectra.

Quasi-2D MHD turbulence

When $N \gg 1$, 3D MHD turbulence is strongly anisotropic and can become classical two-dimensional turbulence if "put" between two transverse planes ([64]). In this case, turbulence features the properties given in Sec. 1.3.1. However, when the two planes are solid walls, velocity variations can not vanish in their vicinity because of the *Hartmann* layer (Sec. 1.2.2). In other words, the flow is quasi two-dimensional and can be described by [64]'s model (Sec. 1.2.3). [64] further shows that quasi two-dimensional turbulence may still feature the properties of classical two-dimensional turbulence, but certain conditions are required which we shall present thereafter.

A vortex can become quasi two-dimensional when its characteristic time for two-dimensionalisation $\tau_{2D} = \tau_J(L/l_\perp)^2$ is much smaller than its turnover time $\tau_U = l_\perp/U(l_\perp)$ (Sec. 1.2.1 and recall that L is the space between the solid walls and l_\perp the length scale of the vortex perpendicular to the magnetic field $\mathbf{B} = B_0\mathbf{e}_z$.) This suggests an estimate for a minimum quasi two-dimensional vortex scale in a turbulent flow, l_\perp^{q2D} (or wavenumber k_\perp^{q2D}) as follows ([64, 43]):

$$l_\perp^{q2D} \simeq \frac{1}{k_\perp^{q2D}} \gg L N^{-1/3} \quad \text{with} \quad N = \frac{\sigma B_0^2 L}{\rho U(l_\perp)} \quad (1.98)$$

When the imposed magnetic field $B_0\mathbf{e}_z$ is strong enough and all vortices satisfy the above condition the turbulent flow is quasi two-dimensional. This further implies that the dynamic of this flow is controlled by the ratio $\tau_H/\tau_U = R_h$ (Sec. 1.2.3) and two different cases should be distinguished from here .

Case 1: $\tau_U \ll \tau_H$

When $\tau_U \ll \tau_H$, *Hartmann* friction is weak. From this condition one can derive an estimate for the maximum vortex size, L_\perp^{q2D} (or minimum wavenumber K_\perp^{q2D} in the $E(k)$ -spectrum), that is not dissipated during one vortex turn over time τ_U . Following [64], it reads:

$$L_\perp^{q2D} \simeq \frac{1}{K_\perp^{q2D}} \ll L \frac{\text{Ha}}{\text{Re}} = \frac{L}{R_h} \quad \text{with} \quad \text{Re} = \frac{U(l_\perp)L}{\nu} \quad (1.99)$$

In [62, 18]’s experiment on two-dimensional turbulence conditions (1.98) and (1.99) are satisfied for a large range of wave numbers $k_\perp < k_i$ (recalling that k_i is the forcing scale, Sec. 1.3.1). Therefore, classical two-dimensional turbulence as studied by [32, 6] and characterised by an *inverse energy cascade* with the typical $k^{-5/3}$ law has been observed.

Case 2: $\tau_U \gg \tau_H$

When $\tau_U \gg \tau_H$ however, a significant part of energy is withdrawn from each turbulent scale l_\perp (or k_\perp) because of strong *Hartmann* friction inside the *Hartmann* layer. In this context, [3, 37]’s experimental studies on quasi two-dimensional MHD turbulent shear layers reported a k^{-3} spectrum like in homogeneous three-dimensional MHD turbulence (Sec. 1.3.2). The authors thought that this may point to a quasi-steady equilibrium at

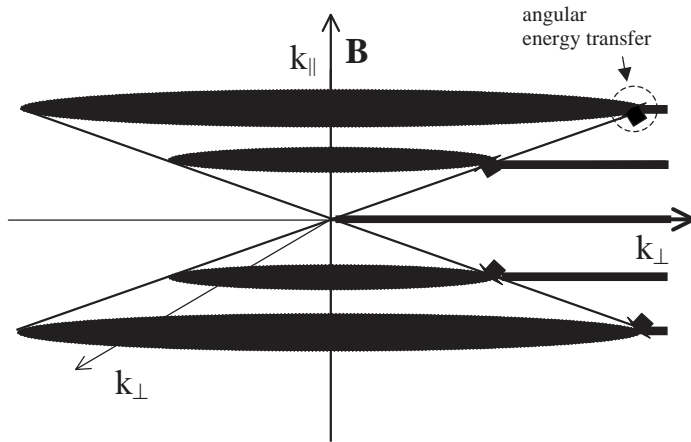


Figure 1.11.: [64]’s sketch of the Joule cone in Fourier space for turbulent, magnetohydrodynamic flows bounded by *Hartmann* walls with a discrete spectrum for parallel wave numbers k_\parallel .

each k_\perp between local inertial energy transfer and *Hartmann* friction. One may also imagine that in this regime turbulence is made of vortices with wavenumbers $K_\perp^{q2D} > k_i$. In other words, all scales $k_\perp < K_\perp^{q2D}$ are already dissipated and an *inverse energy cascade* with the $k^{-5/3}$ law can not exist.

Another important property of MHD turbulence between walls results from the *Hartmann* wall boundary condition $\mathbf{J} \cdot \mathbf{n} = 0$. [64] shows that because of this the local vorticity just at the edge of the *Hartmann* layer, ω_z^c , satisfies:

$$\frac{\partial \omega_z^c}{\partial z} = -2 \frac{a}{\text{Ha}} \nabla_\perp^2 \omega_z^c = \mathcal{O}\left(\frac{1}{\text{Ha}}\right) \quad (1.100)$$

It follows that ω_z^c varies Ha times less along the magnetic field \mathbf{B} than in the transverse plane. This result is of crucial importance as it indicates that the vortex axis in the

vicinity of the *Hartmann* walls is parallel to \mathbf{B} and vortex inclinations are possible only further out in the core flow ([64, 43]). Moreover, [64] reported that the spectrum of parallel wave numbers k_{\parallel} should be discrete which implies that angular energy transfer (due to inertial effects) from energy containing vortices to the Joule dissipation zone can only happen at these discrete levels (thick black lines in Fig. 1.11).

Chapter 2

Experimental setups

2. Experimental setups

In this chapter we describe two different experiments that we built from scratch in the frame of this work and over a period of about three years. The smaller one of these two experiments is on an electrically driven, mostly quasi two-dimensional vortex pair confined by the walls of a cylindrical container and we study the transition to turbulence induced by boundary layer separation. The larger experiment is on a square array of vortices enclosed in a cubic container and we study their breakdown to *weak* and *strong* three-dimensionality.

The cylindrical and the cubic container have electrically insulating walls and are hermetically filled with an electrically conducting fluid, in particular with a liquid metal. Both containers are placed in a uniform DC magnetic field $B_0 \mathbf{e}_z$ such that the liquid metal is confined between two corresponding *Hartmann* walls. Firstly, we present those features which both experiments have in common like for instance construction elements and measurement techniques and, secondly, describe the set-up of each experiment in more details.

2.1. Construction elements

In this section we specify the liquid metal as well as the magnetic systems that we use in our experiments and explain how we organise the flow forcing.

2.1.1. Choice of liquid metal

The eutectic alloys Galinstan and GaInSn are both made from Gallium, Indium and Tin and exhibit properties that are most appropriate in our experiments (Table 2.1). Firstly, these alloys are liquid at temperature $\theta_m < 20\text{ C}^\circ$. This property favours them against other metals like Gallium, Lithium and Sodium as experiments can be performed under room temperature and experimental costs can be saved. Secondly, although heavy metals, Galinstan and GaInSn are non-acute-toxic materials. Unlike mercury, their vapour pressure is very low so the amount of toxic vapourized metal that one might inhale and which could cause serious health problems remains negligible. Thirdly, the Galinstan and GaInSn are less reactive to other chemical elements than the eutectic alloy NaK (note that NaK is made from Sodium and Potassium). NaK for instance reacts with water to

form hydrogen which quickly inflames when getting in contact with oxygen.

Lastly one should note that the density ρ , the electric conductivity σ and the viscosity ν of Galinstan and GaInSn allows us to observe weak as well as strong electromagnetic effects depending on the strength of the imposed magnetic field $\mathbf{B} = B_0 \mathbf{e}_z$ and geometrical dimensions L (corresponding values of Joule time $\tau_j = \sigma B_0^2 / \rho$ and Hartmann number $\text{Ha} = LB_0(\sigma/(\rho\nu))^{1/2}$) are given in Table 2.1). In this context, weak (large τ_j , small Ha) means that corresponding MHD flows have the tendency to be rather three-dimensional while strong electromagnetic effects (small τ_j , high Ha) intrinsically favour their two-dimensionality. This is indeed of particular importance to this work as we are mostly interested in the physical mechanism that governs the transition between two-dimensional and three-dimensional flow regimes.

Table 2.1.: Physical properties of different electric conductors and related characteristic joule times $\tau_j = \rho/(\sigma B_0^2)$ as well as Hartmann numbers $\text{Ha} = LB_0(\sigma/(\rho\nu))^{1/2}$. Values of τ_j and Ha are given for magnetic field strengths $B_0 \in \{0.1, 5\}\text{T}$ and length scale $L = 0.1\text{m}$ which are typical values in our experiments.
Note that Galinstan can be obtained from Geratherm (Geschwenda/Germany) and GaInSn termed as MCP11 can be purchased from HEK GmbH (Lübeck/Germany).

liquid metal	melt. Temp. θ_m [C°]	Temp. θ [C°]	density ρ [kg/m³]	elect. cond. σ [S/m]	viscosity ν [m²/s]	joule time τ_j [s]		Hartmann number Ha	
						0.1T	5T	0.1T	5T
Galinstan	-19	20	6440	2.3×10^6	4×10^{-7}	0.28	1.1×10^{-4}	300	1.5×10^4
GaInSn	10.7	20	6400	3.4×10^6	4×10^{-7}	0.19	7.5×10^{-5}	360	1.8×10^4
Mercury	-38.8	20	13546	1.04×10^6	1.14×10^{-7}	1.3	5.2×10^{-4}	260	1.3×10^4
NaK	-11	100	847	2.88×10^6	5.53×10^{-7}	0.03	1.2×10^{-5}	784	3.9×10^4
Gallium	29.8	30	6093	3.85×10^6	3.1×10^{-7}	0.16	6.3×10^{-5}	450	2.2×10^4
Lithium	180	300	500	3.34×10^6	9×10^{-7}	0.02	3.9×10^{-6}	874	4.4×10^4
Sodium	98	130	922	9.34×10^6	6.5×10^{-7}	0.01	5.8×10^{-6}	1250	6.3×10^4

2.1.2. Magnetic field systems

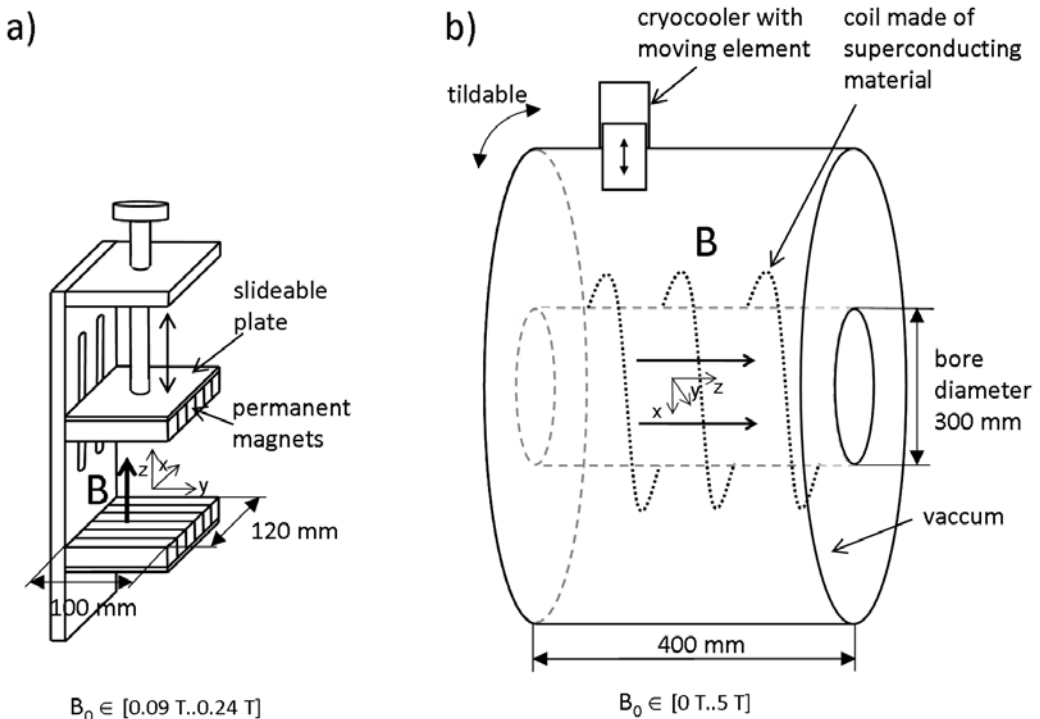


Figure 2.1.: Magnet systems: (a) different magnetic field strengths B_0 are obtained by changing the gap width between two sets of identical permanent magnets facing each other. (b) different magnetic field strengths B_0 are adjusted by varying the amount of constant electric current circulating through the coil made of superconducting material. Note that the cryocooler is a SUMITOMO RDK-408D 4K cold head which is connected to a CSW-71D compressor unit.

Both experiments, in particular the liquid metal filled containers, are subject to a constant magnetic field that is either generated by permanent magnets (Fig. 2.1a) or by a superconducting magnet (Fig. 2.1b). In the former case, two sets of 6 identical permanent neodymium-magnets are mounted on two iron plates facing each other. The magnetic field is generated in the gap between the two magnet sets and magnetic field strengths of $B_0 \in [0.09..0.24]\text{T}$ can be adjusted by moving one of the iron plates (Fig. 2.1a). The liquid metal filled container is placed inside a volume of size $40 \times 40 \times 5 \text{ mm}^3$ located in the centre of the x,y -plane with maximum deviations of the magnetic field $b\mathbf{e}_z$ of 5% along $\hat{\mathbf{e}}_y$, 3% along $\hat{\mathbf{e}}_x$ and 1 % along $\hat{\mathbf{e}}_z$.

Magnetic field strengths B_0 up to 5T and over a larger volume have been obtained thanks to a Cryogen-Free magnet (CFM) installed at the Ilmenau University. The magnetic field is generated within the bore of a superconducting coil through which constant electric current circulates almost loss-free. The bore diameter and length are 300mm and 400mm respectively as shown Fig. 2.1b and the magnetic field has a maximal deviation $b\mathbf{e}_z$ of 3% along $\hat{\mathbf{e}}_x$, $\hat{\mathbf{e}}_y$ and $\hat{\mathbf{e}}_z$, over a domain of size $100 \times 100 \times 100\text{mm}^3$ located in the bore centre.

A helium-cooled mechanical 4K cryocooler (Fig. 2.1) brings the coil temperature down to 4K which is essential to make the coil material superconducting and almost loss-free. A power supply system feeds the coil with DC electric current according to the required magnetic field strength. Once the current is set, the power supply is disconnected from the supra-conducting coil, thus avoiding any regulation-induced ripple in the field. In this so-called persistent mode, the slow-going decrease of the magnetic field due to the slight rest-dissipation of the electric current circulating inside the superconducting coil is not measurable at the timescale of the experiment.

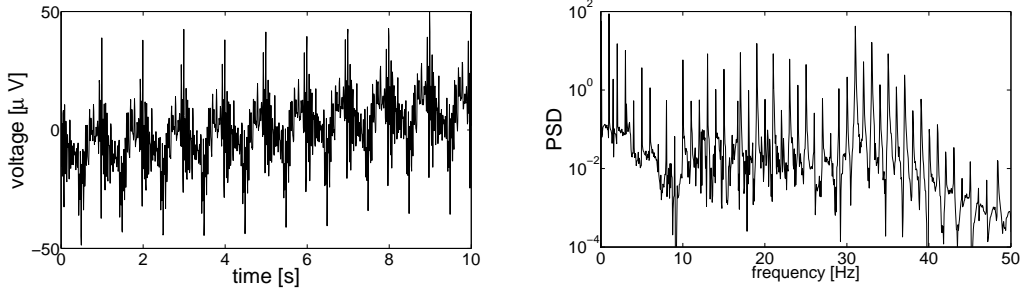


Figure 2.2.: Example of a noise contaminated signal (left) and corresponding spectrum (right) induced by the mechanical motion of the cold head attached to the superconducting magnet.

In order to keep the coil temperature constant at 4K the cooling system is supposed to work continuously by default. However, the motion of mechanical parts induces additional high-amplitude electromagnetic noise of about 1Hz and subsequent vibrations (Fig. 2.2) that contaminates the useful frequency components (typically in the range [0, 35]Hz) and spoils experimental data. The only way out of this was to switch off the cooling system when recording signals. This however limited us in recording time to at most 5min as the electric current inside the coil dissipates when the temperature reaches values > 12K.

2.1.3. Flow forcing - constant electric current injection

The flow in both experiments is driven by injecting constant electric current I through electrodes that are embedded in one of the *Hartmann* walls. The electrodes are mounted flush with the inner wall of the fluid container at their end that is in contact with the liquid metal and are connected to a well regulated DC power supply at the other end. As demonstrated in Sec. 1.2.3, such a forcing creates fluid rotation above each electrode.

Preliminary considerations

a) Choice of electrode material

The intensity of the forcing I is determined by the total electric resistance $R_{tot} = R_w + R_c + R_{LM}$. This is shown by the simplified electric circuit in Fig. 2.3 where R_w is the resistance of the electrically conducting copper wires that connect the electrodes to the power supply, R_c is the contact resistance between the electrodes surface and the liquid metal and R_{LM} is the resistance of the liquid metal. The electric resistances R_w and R_{LM}

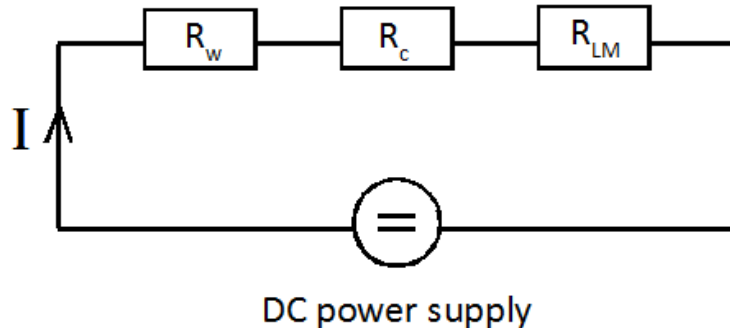


Figure 2.3.: Simplified electric circuit for flow forcing through one electric current injection electrode. R_w is the electric resistance of the copper wires in the electric circuit and R_c measures the contact resistance between injection electrode and liquid metal. The electric resistance of the latter is R_{LM} . Note that the DC power supply was either a Toellner 8852-16 or an EA-PSI 9080-300 6HE 19".

are almost constant and of the order of a few $\text{m}\Omega$ in our experiments. R_c however is subject to fluctuations that can be either of the same order of magnitude as those of R_w and R_{LM} or much higher depending on the electrode material. This makes the electric current forcing less precise and can also lead to overheating which destroys the experiment. In order to keep these effects down to a minimum by the choice of the electrode material we performed a small experimental test as shown in Fig. 2.4. In this test we measured the contact resistance for both copper and CrNi electrodes embedded in the bottom wall of a cylindrical Plexiglas container filled with GaInSn (Table 2.1). It was found that using copper electrodes in our experiments would be best as corresponding values of measured contact resistance R_c and temperature were much smaller compared with those obtained for CrNi electrodes, for all values of the electric current injected through the electrodes (Table 2.2 and Fig. 2.5). It has however been observed that the electric contact between electrode and liquid metal can also change erratically sometimes, even for copper electrodes. This probably occurs because of liquid metal oxide particles that settle down onto the electrode contact surface. This effect causes a sudden change of the contact resistance R_c which can be of the order of a few $\text{m}\Omega$ and therefore drastically affect the forcing in

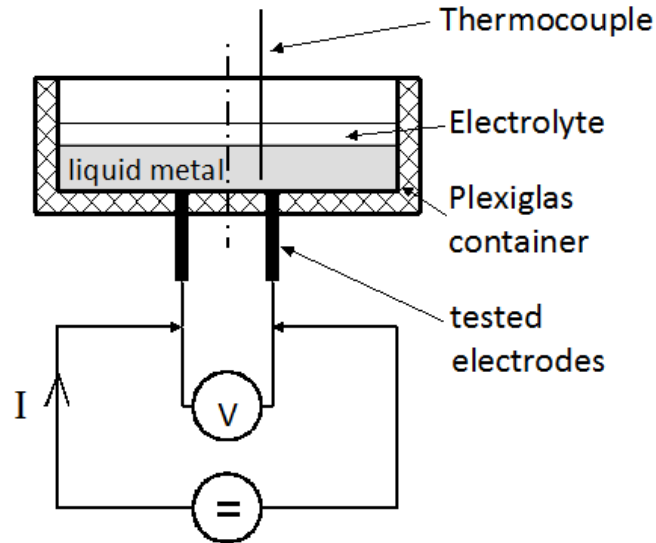


Figure 2.4.: Schematic representation of the experimental set-up to measure the contact resistance between the liquid metal and metallic electrodes made either from copper or CrNi. The contact resistance was obtained by injecting constant electric current through the metallic electrodes and measuring the related voltage drop.

Table 2.2.: Contact resistance and measured temperatures for copper and CrNi electrodes for two different injected electric currents

I [A]	copper		CrNi	
	$\langle R_c(t) \rangle$ [$m\Omega$]	Temperature [$^\circ C$]	$\langle R_c(t) \rangle$ [$m\Omega$]	Temperature [$^\circ C$]
1	3.4	22.5	270	26.9
5	4.7	25	110	70.6

the experiments.

b) Minimizing of the influence of erratic changes in R_c

The flow in our experiments is forced by injecting constant electric current through n injection electrodes with $n \in \{1, 2, 3, \dots, 100\}$, where n_p electrodes are connected to the positive and $n_m = n - n_p$ to the negative pole of the DC power supply. Particular emphasis is put to obtain a uniform forcing which implies that $n_p = n_m$ so each electrode should conduct the same amount of current into or out of the liquid metal, depending on its polarisation, either positive or negative.

For $n_p = n_m = 1$, the total current I flows through both electrodes in equal measure and fluctuations or erratic changes of the contact resistance R_c are compensated by the related

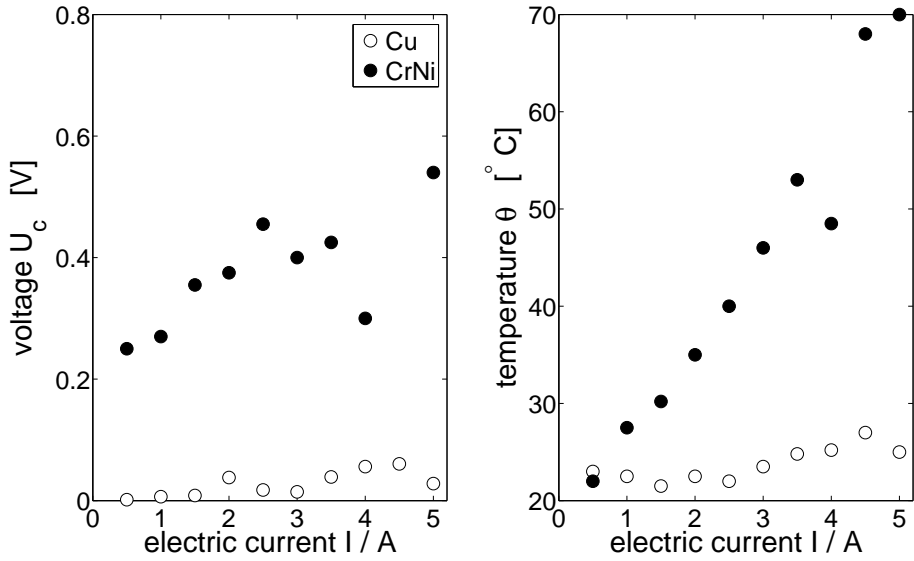


Figure 2.5.: Measured contact resistance between liquid metal and injection electrodes for both copper and CrNi electrodes and different injected electric currents I . Left: related voltage drop $U_c(I)$ over the contact surface. Right: Temperature $\theta(I)$ near the contact surface. Note that both the CrNi and the copper electrodes exhibit the same roughness at the interface between electrode surface and liquid metal.

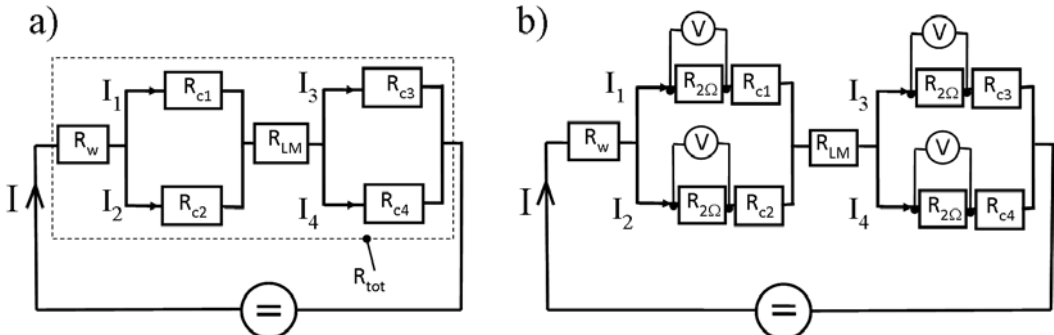


Figure 2.6.: Equivalent electric circuits for electric current forcing through $n = 4$ injection electrodes (note that $n_p = n_m = 2$). a) non-uniform forcing induced by local variations of the contact resistance R_c ($I_1 \neq I_2 \neq I_3 \neq I_4$). b) uniform forcing as controlled by constant electric resistances $R_{2Ω} \gg R_c$ ($I_1 = I_2 = I_3 = I_4$).

voltage drop over the power supply system which works in the "constant current" mode (Fig. 2.3). When however $n_p = n_m > 1$, I splits into sub-currents $I_{\{1,2,\dots,n\}}$, each of intensity that is controlled by R_c in the corresponding electric path as shown in Fig. 2.6a for $n_p = n_m = 2$. Local erratic variations of R_c can now no further be compensated by the DC power supply as it adjusts the voltage drop only over the total resistance R_{tot} (Fig. 2.6a). This leads to an irregular distribution of electric current and to an ill-controlled forcing. In order to avoid this effect in the experiment, each electric path has been extended by a

constant, ohmic resistance of $R_{2\Omega} = 2\Omega \pm 0.25\%$ (Fig. 2.6b, SRT REA 6402R \pm 0.25% / 100 W). Since $R_{2\Omega}$ is at least two orders of magnitudes higher than any other resistance in each electric circuit it determines the electric current passing through each electrode. In other words, implementing resistances $R_{2\Omega}$ makes the electric forcing uniform. The uniformity of the forcing in the experiments is verified by monitoring the voltage $U_{2\Omega}$ over resistances $R_{2\Omega}$ (Fig. 2.6b). The corresponding electric current passing through each electrode is then determined by local ratios $U_{2\Omega}/R_{2\Omega}$.

c) Geometry of the flow forcing

To allow for different forcing geometries in the experiments where $n_p = n_m > 1$ we put in each electric circuit a switcher that connects corresponding electrodes either to the positive or negative pole of the DC power supply. An example is again shown schematically

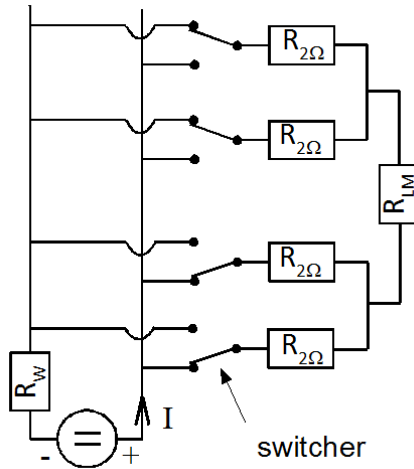


Figure 2.7.: Variability of the flow forcing geometry. Each electric circuit contains a switcher that connects electrodes to either the positive (n_p) or negative (n_m) pole of the DC power supply. The above example shows a uniform forcing with $n_p = n_m = 2$.

for $n_p = n_m = 2$ in Fig. 2.7. The electric current enters the fluid through those electrodes that are connected to the positive pole, then crosses the liquid metal of resistance R_{LM} and leaves the container through the electrodes with negative polarisation.

Current switchboard system

The current switchboard system has been built from scratch too and is used for experiments where $2 < n \leq 100$. It should provide a uniform forcing for different forcing geometries.

a) Design

The current switchboard system is made using the elements described in Sec. 2.1.3. This implies that all electric circuits that are connected to the electrodes include a $R_{2\Omega}$ resistance and a switcher. Each $R_{2\Omega}$ resistance takes a maximal power of $P_{max} = 100W$ and needs to be continuously cooled to avoid its overheating and destruction (note that this specification also limits the injected electric current per electrode to the value of $\sqrt{P_{max}/R_{2\Omega}}$). To this end, all $R_{2\Omega}$ resistances are mounted in groups of 10 to the left and right hand side of heat sinks made of aluminum cooling plates. These plates evacuate the heat generated by the $R_{2\Omega}$ resistances into streaming cold water (Fig. 2.8). According

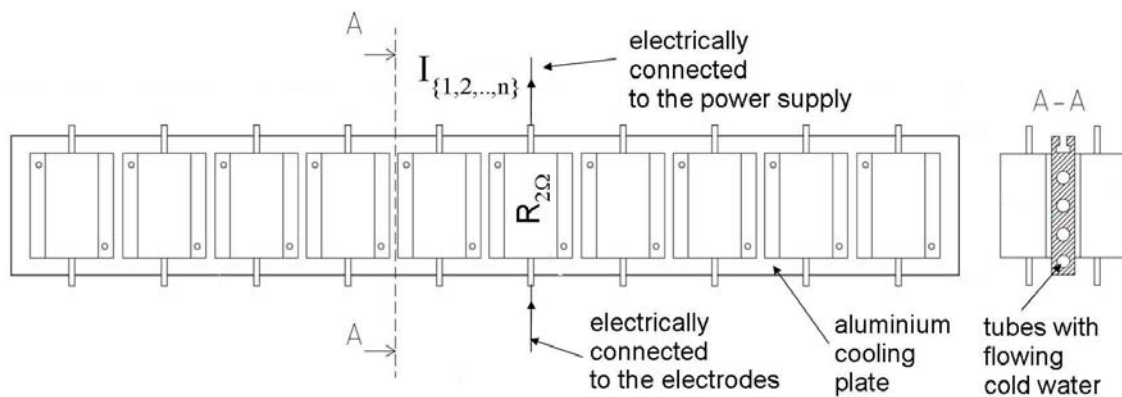


Figure 2.8.: Cooling of $R_{2\Omega}$ -resistances. Example of one aluminum cooling plate with 10 resistances $R_{2\Omega}$ mounted to either of its sides. The plate acts as a heat sink that evacuates the heat generated by the resistance $R_{2\Omega}$ into flowing cold water.

to the number of 100 maximum connected electrodes, the switchboard system contains 10 of such sets in total. They are arranged in a square lattice of 10×10 $R_{2\Omega}$ resistances as illustrated in Fig. 2.9. The switchboard shown in Fig. 2.9 is mounted above the $R_{2\Omega}$ resistances. It contains a square array of 10×10 black connectors that are plugged into a MDF panel and that are electrically connected to corresponding $R_{2\Omega}$ resistances positioned just underneath. Further 100 blue (*resp.* 100 red connectors) are inserted into the plate on either sides to the black ones and screwed in below copper bars that are connected to the positive (*resp.* negative) pole of the DC power supply (Fig. 2.9). Now, whether a single electrode is positive or negative polarised depends on the connection of "its" $R_{2\Omega}$ resistance to either a blue or a red connector on the MDF panel (note that in Fig. 2.9, this connection is made by black U-shaped connectors, however other connectors are indeed used in the experiment). The final current switchboard system as it is used in the laboratory is displayed in Fig. 2.10 (note that black cables are electrically linked to $R_{2\Omega}$ resistances and conduct the electric current to corresponding electrodes in the experiments).

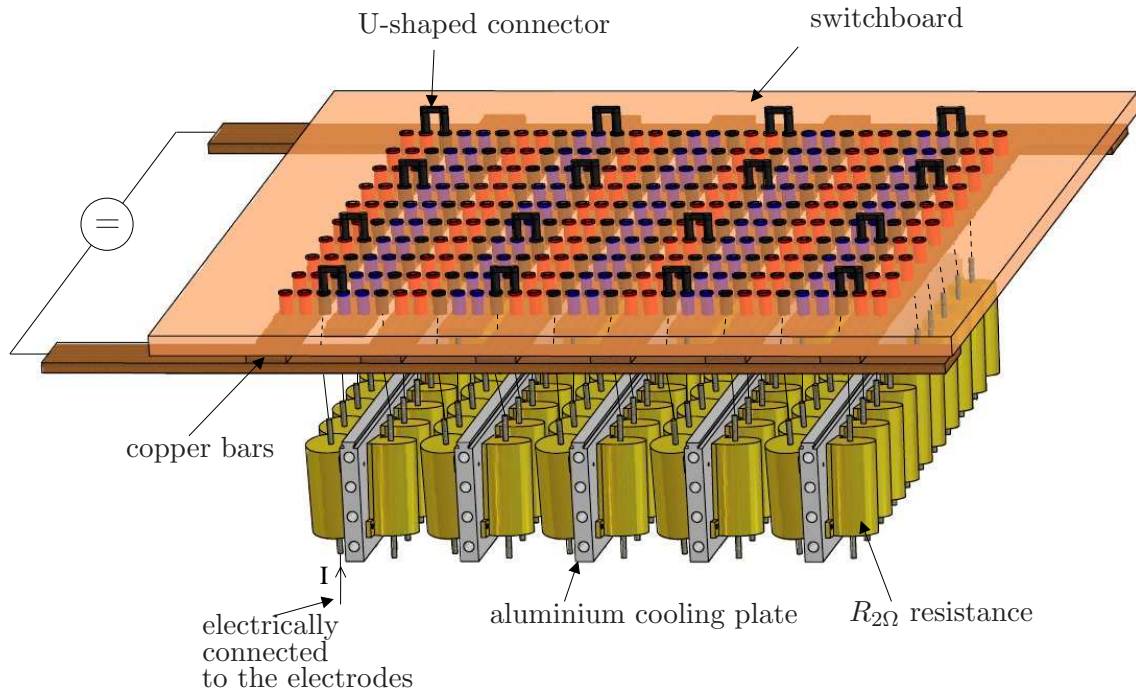


Figure 2.9.: Design of the switchboard. All electric current injection electrodes are electrically connected to one side of the 10×10 lattice made of black female-connectors plugged into the board. At the other side, also black but U-shaped male-connectors (switchers) contact them further to either the positive (*resp.* negative) pole of the DC power supply when connected to the blue (*resp.* red) female-connectors. Note that the above switchboard connections show the configuration that we use to create a flow forcing through an array of 4×4 injection electrodes.

b) Verification of uniform current distribution

In order to check the precision of the electric current switchboard system it was connected to a square lattice of 10×10 copper electrodes soldered into a copper plate of size 20×20 cm and thickness 0.5cm (electrode diameter $d_e = 2$ mm, lattice spacing 2cm). All 100 electrodes were alternatively connected to the positive or negative pole of the DC power supply so that the electric current should be homogeneously distributed inside the copper plate ($n_p = n_m$). The power supply fed the entire electric circuit with $I = 50A$ to obtain electric currents of $I/n_p = I/n_m = 1A$ per electrode. Measurements of voltage drops over corresponding $R_{2\Omega}$ resistances have shown that the current switchboard system distributes the electric current uniformly to a precision of 0.5%.

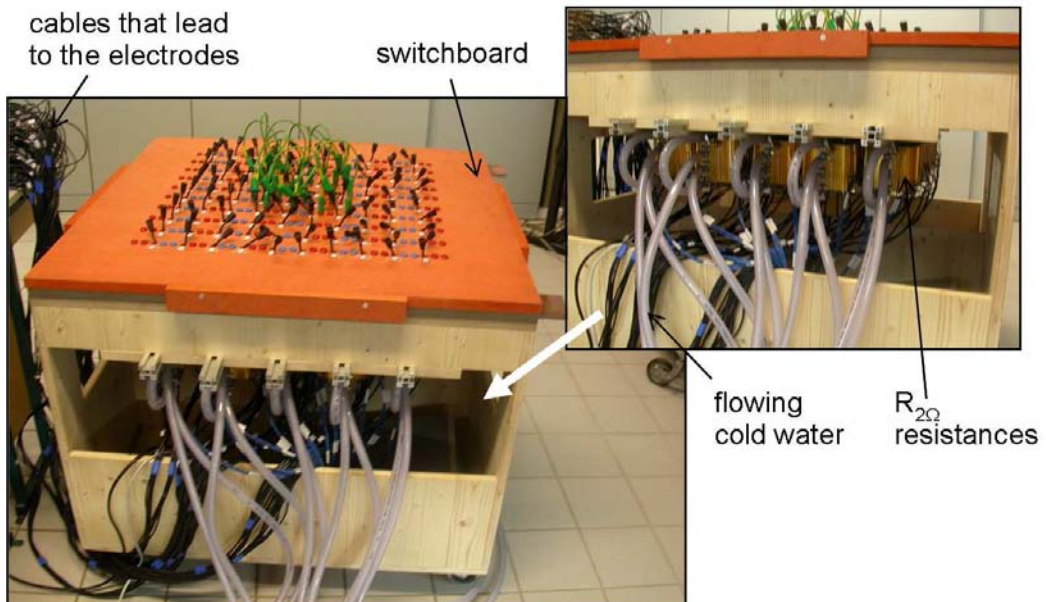


Figure 2.10.: Electric current switchboard system. Switchboard and cooling plates with resistances $R = 2\Omega$ are held by a rectangular wooden box that is equipped with wheels at the bottom which allows us to move it easily. One should notice that our current switchboard system can be used in any other MHD experiment where the flow is electrically driven and a precise control of the forcing is required. Note that the distribution of the electric current is controlled by monitoring the voltage drop over each $R_{2\Omega}$ -resistance (Sec. 2.1.3) using a Keithley 2701 data logging system.

2.2. Measurement techniques

In this section we firstly describe the set-up of the measurement system which is based on local measurements of the electric potential. Secondly we specify the conditions under which the velocity field just outside the *Hartmann* layer can be obtained from the electric potential measured at walls orthogonal to the imposed magnetic field (*Hartmann* wall) and explain how those measurements help us to identify and quantify the presence of three-dimensionality in the flow. Lastly we briefly mention the information one may draw from electric potentials obtained at walls parallel to the magnetic field.

2.2.1. Set-up of the electric potential measurement system

The electric potential ϕ is measured locally on electric potential probes that are embedded in each of the walls confining the liquid metal filled container as schematically shown in Fig. 2.11a. These walls are electronic boards of thickness 1 – 2mm and consist of either fiber-reinforced epoxy FR4 or Roger RO4003C material. They exhibit small holes with diameter 0.2mm where corresponding electric potential probes made from thin copper wires are soldered in. Again, we use copper as potential probe material to provide good electrical contact to the liquid metal.

All electric potential probes are made flush with that surface of the wall which contacts the liquid metal. In short, electric potentials are measured at the flow boundaries, thus non-intrusively. Printed electric circuits at the back side of each electronic board (illustrated thereafter in Sec. 2.4 and Sec. 2.5.1) convey all signals to connectors and further to corresponding channels of a 736-channel, single-ended and high precision, amplifier system shown on Fig. 2.11a and Fig. 2.11b. In this context, single-ended means that each electric potential is measured with respect to a reference potential which needs to be defined at one point somewhere at the edge of the liquid metal flow, for instance at one of the electric potential probes as shown in Fig. 2.11. This also implies that local electric potentials ϕ are indeed electric potential differences. Such signals can be of order of $10\mu\text{V}$ so they require amplification. For this reason, each channel of the measurement system contains a low-noise amplifier with gain factor 111 as well as a 24 bit A/D converter that digitises the signal before transmitting it to the PC where a MATLAB/SIMULINK software module controls the signal recording (Fig. 2.11). A low pass filter with cut-off frequency of 45 Hz is used to attenuate the background electronic noise of 50Hz and other high-frequency components induced by electronic equipment in the proximity of the experiments. The cut-off frequency is kept sufficiently high so that the frequencies relevant to the flow, typically in the range [0..35] Hz, remain unaffected. It should be further stressed that all 736 channels work in parallel. This allows us to simultaneously record electric potentials at different locations, at sampling frequencies $f = 2^m$ where

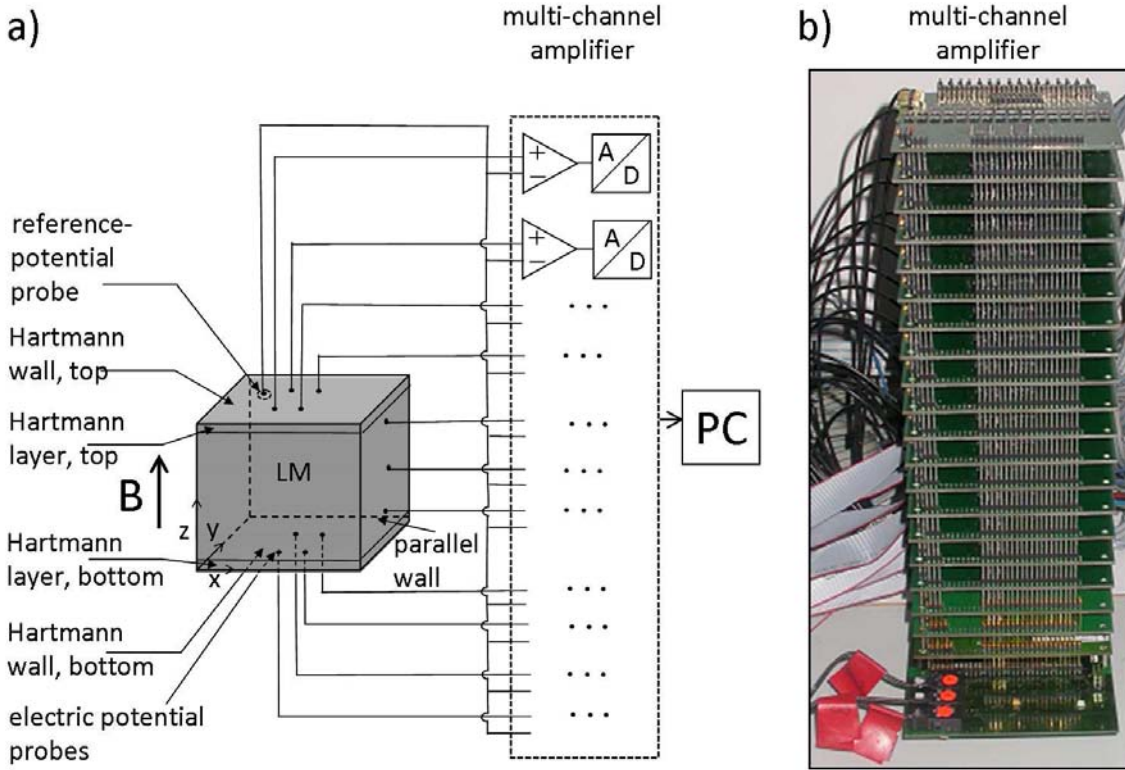


Figure 2.11.: Measurement system.(a) Simplified sketch representing the principle of measuring and recording electric potentials. Electric potential is measured locally by means of electric potential probes embedded in *Hartmann* and parallel walls. (b) Picture of one of the multi-channel amplifier-towers used in the experiment.

$m \in \{1, 2, \dots, 8\}$. In the experiments, signals are sampled with 128Hz ($m = 7$) where a peak to peak noise of about $2\mu\text{V}$ limits the precision of the measurement system.

2.2.2. Electric potentials measured at Hartmann walls

Electric potentials measured at walls that are orthogonal to the magnetic field lines $\mathbf{B} = B_0 \mathbf{e}_z$ (*Hartmann* walls) are of special importance in liquid metal MHD. Their local values ϕ_w as well as their gradients perpendicular to the magnetic field $\nabla_{\perp} \phi_w$ allow us to respectively obtain the stream function Ψ (1.56) and the velocity field $\mathbf{u}_{\perp}^c(x, y)$ at the edge of the *Hartmann* layer (recall that the superscript $(\cdot)^c$ indicates quantities measured at the interface between the *Hartmann* layer and the core of the flow, Sec. 1.2.2). This however requires the following two conditions:

- 1) The electric current density just outside the Hartmann layer \mathbf{J}_{\perp}^c is small so that Ohm's

law (1.50) can be approximated by:

$$-\nabla\phi^c + \mathbf{u}_\perp^c \times \mathbf{B} \simeq 0 \quad (2.1)$$

ϕ^c is the electric potential just outside the *Hartmann* layer. As noticed by [30] and [62], this approximation applies to quasi-2D and even to weakly 3D flows, albeit with a larger error than in quasi-2D flows.

2) The variation of the electric potential ϕ across the *Hartmann* layer is negligible. According to (1.46) this is valid in the limit of high Ha. It implies that:

$$\phi^c \simeq \phi_w \text{ and } \nabla_\perp \phi^c \simeq \nabla_\perp \phi_w \quad (2.2)$$

Combining condition 1) and 2) it leads to:

$$-\nabla\phi_w + \mathbf{u}_\perp^c \times \mathbf{B} = \mathcal{O}\left(\max\left(\frac{\delta}{\text{Ha}^2}, \frac{\|\mathbf{J}_\perp^c\|}{\sigma\|\mathbf{u}_\perp^c \times \mathbf{B}\|}\right)\right). \quad (2.3)$$

When $\delta/\text{Ha}^2 \ll 1$ and $\|\mathbf{J}_\perp^c\|/\sigma\|\mathbf{u}_\perp^c \times \mathbf{B}\| \ll 1$, the local velocity $\mathbf{u}_\perp^c(x, y)$ just at the edge of the Hartmann layer can be deduced from local electric potential differences between probes distant by Δx and Δy from one another according to (Fig. 2.12):

$$u_x^c \simeq -\frac{1}{B_0} \left(\frac{\phi_w(x, y + \Delta y) - \phi_w(x, y)}{\Delta y} \right), \quad u_y^c \simeq \frac{1}{B_0} \left(\frac{\phi_w(x + \Delta x, y) - \phi_w(x, y)}{\Delta x} \right) \quad (2.4)$$

It is also important to notice that even if the Hartmann layer becomes turbulent its thickness δ remains of the order Ha^{-1} and relations (2.4) are still valid.

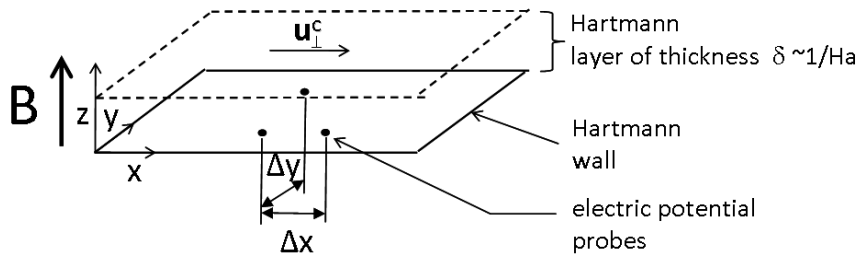


Figure 2.12.: Principle of *Electric potential velocimetry*. Velocities \mathbf{u}_\perp^c at the edge of the *Hartmann* layer can be obtained from local electric potential differences measured at the *Hartmann* wall when the core flow is quasi-2D or weakly 3D and when variations of the electric potential across the *Hartmann* layer are negligible in the limit of high Ha.

In order for three-dimensionality to spoil the validity of (2.4), the current density in the

core \mathbf{J}_\perp^c would have to be of order of $(\sigma \|\mathbf{u}_\perp^c \times \mathbf{B}\|)$. One may obtain a rough measure of the related error in (2.4) when integrating the z-component of Ohm's law (1.6) along the field lines of \mathbf{B} and across the core of a flow that is confined by two *Hartmann* walls distant by the length L . This yields to an estimate for the vertical component of the current density in the core $\|\mathbf{J}_z^c\| \simeq \sigma \Delta\phi / L$ where $\Delta\phi$ is the potential difference across the core flow. Combining this with current conservation (1.5) it provides an estimate for the horizontal current density \mathbf{J}_\perp^c in the core:

$$\|\mathbf{J}_\perp^c\| \simeq -\Delta\phi \frac{L_\perp}{L^2} \sigma. \quad (2.5)$$

where L_\perp is a typical transverse length scale. The above relation implies that the error on the calculation of the velocity because of the presence of three-dimensionality in the flow is of order of $((L_\perp/L^2)\Delta\phi/\|\mathbf{u}_\perp^c \times \mathbf{B}\|)$.

Lastly one should note that the principle of extracting flow velocities from measured electric potential differences, also referred to as "*Electric Potential Velocimetry*", is known since *Faraday*'s attempt to determine the velocity of the Thames river in London [19]. In his attempt, the field lines \mathbf{B} across the Thames flow were generated by the magnetic field induced in the earth's core. But, since his measurement instrumentation was not adequate at this time, *Faraday* failed. The measuring principle though has been applied successfully about 150 years later in magnetic flow meters [60] to measure flow rates in food and chemical industry.

2.2.3. Measurement of three-dimensionality

The presence of three-dimensionality can be identified by comparing sets of electric potential measured at both *Hartmann* walls that confine the liquid metal flow. For simplicity we denote these walls thereafter as bottom and top *Hartmann* wall, respectively positioned along the magnetic field lines $\mathbf{B} = B_0 \mathbf{e}_z$ at $z = 0$ and $z = L$. Since the electric potential does not vary across the thin *Hartmann* layer (2.2), two identical sets point to a strictly quasi-2D flow. If on the other hand these sets of measurements differ the flow is necessarily three-dimensional.

When in the state of three-dimensionality values of ϕ_w are smaller at the top wall, but lines of iso-electric-potential (thereafter: iso- ϕ_w lines) at the bottom and top *Hartmann* wall still remain topological identical, we call *weak* this manifestation of three-dimensionality as it reflect a three-dimensionality where the horizontal velocity field is of the form $\mathbf{u}_\perp(x, y, t)f(z)$ in the core flow as theoretical analysed by [54]. In other words,

flow structures are subject to differential rotation along magnetic field lines $B_0 \mathbf{e}_z$, but still extend from the bottom to the top wall, hence they are not disrupted. By contrast, flow structures that do not extend from the bottom to the top wall yield to iso- ϕ_w patterns on top and bottom that are not topologically equivalent anymore and the velocity field is no longer of the form $\mathbf{u}_\perp(x, y, t)f(z)$. Accordingly, we term this type of three-dimensionality as *strong*.

Comparing iso- ϕ_w contours at bottom and top *Hartmann* walls to distinguish between weak and strong three-dimensionality applies well to steady or slightly unsteady flows regimes, but this approach is not as revealing when the flow becomes chaotic or turbulent. In this case, the presence of weak and strong three-dimensionality is better measured by the correlation between values of time-dependent quantities $S_T(t)$ and $S_B(t)$ obtained at the same location (x, y) near the top and the bottom *Hartmann* wall respectively. In our experiments $S_T(t)$ and $S_B(t)$ are typically local electric potential gradients just outside the *Hartmann* layer. If however the flow is quasi-2D or weakly 3D and approximation (2.4) holds one could built those signal correlations on corresponding velocities just outside the *Hartmann* layer too. According to the definition of the correlations functions C_1 and C_2 given thereafter this would indeed yield to the same result:

$$C_1 = \frac{\sum_{i=0}^k S_B(t_i)S_T(t_i)}{\sqrt{\sum_{i=0}^k S_B^2(t_i)\sum_{i=0}^k S_T^2(t_i)}} \quad \text{and} \quad C_2 = \frac{\sum_{i=0}^k S_B(t_i)S_T(t_i)}{\sum_{i=0}^k S_B^2(t_i)} \quad (2.6)$$

k is the number of samples over which C_1 and C_2 are calculated. C_1 quantifies how much phase and frequency are correlated, regardless of signal amplitudes. C_2 is the more usual correlation function, that incorporates the signal amplitude. If $C_1 = C_2 = 1$ sets of measurements on the top and bottom are identical and the flow is quasi-2D. On the other hand, C_1 below 1 reflect strong three-dimensionality only, while C_2 is smaller than 1 whenever either weak or strong three-dimensionality is present. At this point it should be stressed that correlations functions C_1 and C_2 are influenced by the presence of noise, especially in flow regimes where signals are weak and the ratio $r_{S/N}$ between respectively the amplitude of the signal and the noise is small. An estimation of the corresponding error can be found in the appendix A.

2.2.4. Electric potentials measured at the parallel wall

In contrast to electric potentials measured at the *Hartmann* wall local values of ϕ_p and $\nabla\phi_p$ measured at the walls that are parallel to the imposed magnetic field \mathbf{B} can neither

be related to the stream function Ψ nor to the velocity field \mathbf{u}^c in the core flow. This is because of the complexity of those viscous shear layers or parallel layers with thickness $\delta_s \simeq \text{Ha}^{-1/2}$ that shape in the vicinity of such walls (Sec. 1.2.3). However, local potential gradients $\nabla\phi_p$ contain information about the electric current distribution near the wall which should make it possible to draw some conclusions relevant to the flow structure just outside the parallel layer in the core flow and along the magnetic field \mathbf{B} .

Local values of the electric potential have been indeed measured on potential probes embedded in parallel walls in our big experiment on the appearance of three-dimensionality (Fig. 2.22). Corresponding signals however have not been analysed in the frame of this dissertation.

2.3. Source of errors when measuring electric potentials

In this section we describe the effect of thermoelectricity and discuss its influence on locally measured electric potentials. We also explain how electric potential measurements are affected by slight inhomogeneities of the magnetic field system.

2.3.1. Effect of thermoelectricity

The effect of thermoelectricity is a direct consequence of temperature differences in electrically conducting materials. It results from the phenomenon of thermodiffusion that appears for instance as displacement of negative electric charges from the cold to the hot end of a metallic conductor, with the temperatures θ_c and θ_h respectively (*e.g.* [52]). This generates a thermoelectric voltage $V_{th}^{h/c}$ between these two ends that, according to [52], can be approximated to:

$$V_{th}^{h/c} = -\alpha(\theta_h - \theta_c) + \frac{1}{e}[\mu(\theta_h) - \mu(\theta_c)] \quad (2.7)$$

where α is the Seebeck-coefficient that depends on the material, $e = 1.6 \times 10^{-19} C$ is the elementary charge and $\mu(\theta_h)$ as well as $\mu(\theta_c)$ are chemical potentials (see *e.g.* [52] for further explanation).

The effect of thermoelectricity is used in thermocouples to measure temperatures differences (*e.g.* [52]). A thermocouple is typically made of two different metallic conductors with corresponding Seebeck-coefficients α_1 and α_2 , connected to one another at their ends. Any temperature difference $(\theta_h - \theta_c)$ between both joints induces a total thermoelectric voltage V_{th} which is the sum of both the voltage $V_{th}^{h/c}$ generated in each of the two conductors and the chemical potentials across the two joints [52]:

$$V_{th} = (\alpha_1 - \alpha_2)(\theta_h - \theta_c) \quad (2.8)$$

(notice that chemical potentials along each conductor that appear in (2.7) cancel out with those that exist across the two joints).

The above principle of a thermocouple applies also to local electric potential measurements in our experiments as shown in Fig. 2.13a. It means that a thermoelectric voltage drop V_{th} is captured in each recorded signal too, on the top of the electric potential induced by the flow. This could lead to a miss-interpretation of our experimental results so we shall estimate the influence of thermoelectricity on the electric potential measurements.

As illustrated in Fig. 2.13a, one metallic conductor is made from copper and constitutes

the electric potential probe and the reference probe. Copper has the Seebeck coefficient $\alpha_{Cu} = 7\mu V/K$ which can be obtained from thermoelectric series [20]. In other words, one

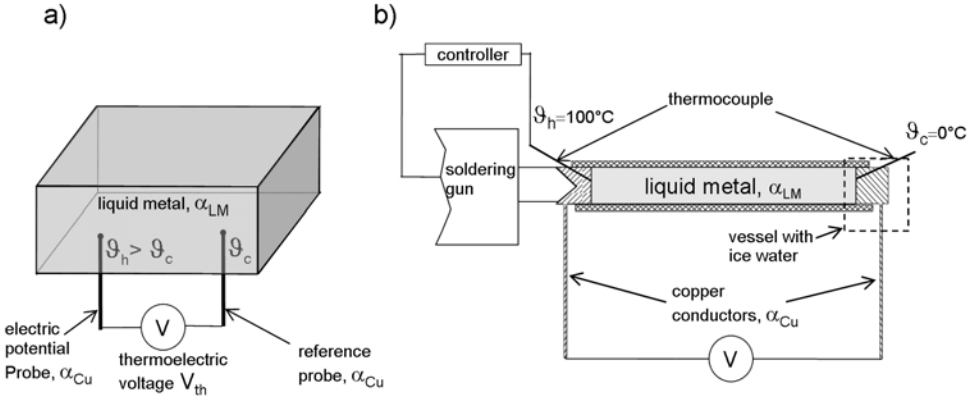


Figure 2.13.: (a) The effect of thermoelectricity in the experiment: A thermoelectric voltage drop V_{th} is induced when the temperature at the interface between potential probe and liquid metal is different to the temperature at the interface between reference potential probe and liquid metal (principle of a thermocouple). (b) Experimental setup to obtain an estimate for the *Seebeck* coefficient of GaInSn α_{LM} : The liquid metal hold inside a plastic tube (inner diameter 0.5cm) is brought to the temperatures $\theta_h = 100^\circ C$ and $\theta_c = 0^\circ C$ at its ends using a regulated soldering gun and a vessel with ice water of 0° respectively. The thermoelectric voltage drop V_{th} across the liquid metal conductor and the copper conductors electrically connected to its ends provides then an estimate for α_{LM} according to (2.8).

would measure a voltage drop of $V_{th}^{h/c} = 0.7mV$ over the two ends of a copper wire where the temperature is assumed to increase linearly from $0^\circ C$ up to $100^\circ C$ from one to the other wire end.

The Seebeck coefficient of the second conductor, here liquid metal, is denoted as α_{LM} and neither for Galinstan nor for GaInSn given by the literature, however both values should be of the same order of magnitude. To obtain an estimate for α_{LM} we set up a small test-experiment that, in fact, resembles a local thermocouple as it appears in the experiment (Fig. 2.13a), but with known temperatures $\theta_c = 0^\circ C$ and $\theta_h = 100^\circ C$ at the joints between both conductors (Fig. 2.13b). This led to a thermoelectric voltage drop of $V_{th} = 2mV$ over the entire circuit so that, according to (2.8), α_{LM} can be approximated to:

$$\alpha_{LM} \simeq -\frac{V_{th}}{100K} + \alpha_{Cu} = 5\mu V/K \quad (2.9)$$

This implies that a temperature difference of $\Delta\theta = 1K$ between a electric potential probe and the reference probe would generate a thermoelectric voltage $V_{th} \simeq 2\mu V$. In the experiments, these probes are typically distant by about 0.1m so one may indeed expect $\Delta\theta$'s

of the order of 1K. The effect of thermoelectricity may therefore limit the precision of locally measured electric potentials obtained at the *Hartmann* wall ϕ_w and parallel wall ϕ_p to $2\mu\text{V}$ or to even slightly higher values. However, since values of ϕ_w and ϕ_p are found to be typically in the range of $[10...10000]\mu\text{V}$ throughout our experiments the effect of thermoelectricity on them remains of minor relevance.

Even less affected by the effect of thermoelectricity are local gradients $\nabla_{\perp}\phi_w$, related velocities just outside the *Hartmann* layer \mathbf{u}_{\perp}^c and gradients $\nabla\phi_s$ as corresponding potential probes are usually distant by not more than 5mm. It means that their local temperatures should be almost identical. Whenever a thermoelectric voltage V_{th} is measured in signals obtained from adjacent electric potential probes, values of V_{th} captured at each probe should be about the same and cancel each other when subtracting the signals from one another.

2.3.2. Inhomogeneity of the magnetic field

The magnetic field systems presented in Sec. 2.1.2 produce magnetic fields \mathbf{B} that are slightly inhomogeneous. In order to estimate the influence of this effect on electric potential measurements on either *Hartmann* walls we restrict here to small inhomogeneities $b(x, y)\mathbf{e}_z$ along these walls so we assume that $\mathbf{B} = (B_0 + b(x, y))\mathbf{e}_z$. This implies for quasi-2D or weakly 3D flows that (2.3) can be written as follows:

$$\nabla\phi_w \simeq (\mathbf{u}_{\perp}^c \times B_0\mathbf{e}_z) \left(1 + \frac{b(x, y)}{B_0} \right) \quad (2.10)$$

We note therefore that local velocities are estimated with an error of $b(x, y)/B_0$ (values of this ratio for both magnet systems are given in Sec. 2.1.2). Furthermore, taking the vector product of either side of (2.10) with \mathbf{e}_z yields:

$$\nabla\phi_w \times \mathbf{e}_z \simeq -\mathbf{u}_{\perp}^c (B_0 + b(x, y)) \quad (2.11)$$

where ϕ_w is stream function of the field $\mathbf{u}_{\perp}^c(B_0 + b(x, y))$. Since $\nabla\phi_w \cdot \mathbf{u}_{\perp}^c = 0$, lines of constant ϕ_w (or iso- ϕ_w lines as defined in Sec. 2.2.3) still correspond to stream lines of the velocity field \mathbf{u}_{\perp} despite local magnetic field inhomogeneities $b(x, y)$. However, the value of ϕ_w along each stream line will be different to that of the stream function Ψ which is defined as $\nabla\Psi \times \mathbf{e}_z = \mathbf{u}_{\perp}$. According to (1.56) this implies that:

$$\Psi = -\frac{\phi_w}{B_0 + b(x, y)} \quad (2.12)$$

2.4. Experiment on a confined electrically driven vortex pair

In this section we describe the set-up and the measurement technique of the small scale experiment where a pair of counterrotating vortices is generated in a cylindrical container hermetically filled by liquid metal. Although parameters are chosen to favour quasi two-dimensionality, we put particular emphasis on the measure of residual three-dimensional effects and their consequences on the quasi-2D flow.

2.4.1. Experimental set-up and measurement technique

The experiment is sketched on Fig. 2.14. It is made of a closed cylindrical plexiglas container with radius $\tilde{R} = 20$ mm and height $a = 5$ mm where all walls are electrically insulating. The cylindrical cavity is hermetically filled with Galinstan that has the physical properties given in table 2.1. The top and bottom plates of thickness 1.5 mm are made of electronic board material FR4 (Fig. 2.16).

Once filled, the container is centered inside the gap between permanent magnets that create a the magnetic field \mathbf{B} pointing along \mathbf{e}_z (Sec. 2.1.2), Fig. 2.15). Magnetic fields strengths $B_0 \in \{0.09T, 0.12T, 0.19T, 0.24\}T$ are achieved by adjusting the gap width and relate to *Hartmann* numbers Ha as given in Table 2.3.

The flow is forced by injecting the total amount of constant electric current I through $n = 2n_p = 2n_m = 2$ electrodes located at $(0, d, 0)$ and $(0, -d, 0)$ and with $d = 8mm$ (Sec. 2.1.3). Both electrodes are connected to a regulated D.C. power-supply (Toellner 8852-16), providing electric currents in the range $I \in [0 - 20]A$ with a maximum output ripple $0.5 \times 10^{-3}A$. For strong magnetic fields \mathbf{B} such a forcing creates a base flow of two quasi-2D counter rotating vortices where each vortex would have a 2D circulation of $\Gamma_0 = I/(\pi n \sqrt{\sigma \rho \nu})$ according to (1.74) in Sec. 1.2.3. This suggests defining $U_0 = 2\Gamma_0/d$ as a reference velocity *a priori* along \mathbf{e}_x , at the centre between the axis of the two vortices. Expressed non-dimensionally this yields to the *Reynolds* number Re^0 :

$$Re^0 = \frac{U_0 \tilde{R}}{\nu} = \frac{I}{\pi \nu \sqrt{\sigma \rho \nu}} \frac{\tilde{R}}{d} \quad (2.13)$$

Electric potential is measured locally thanks to two symmetric sets of 56 potential probes (diameter $d_{pr} = 0.25$ mm) embedded in the top ($z = a$) and bottom ($z = 0$) *Hartmann* walls respectively at locations sketched on Fig. 2.14. The two sets are aligned exactly opposite each other along the $\hat{\mathbf{e}}_z$ axis. All signals are measured with respect to an reference probe located near the box centre and are recorded with sampling frequency 128Hz using

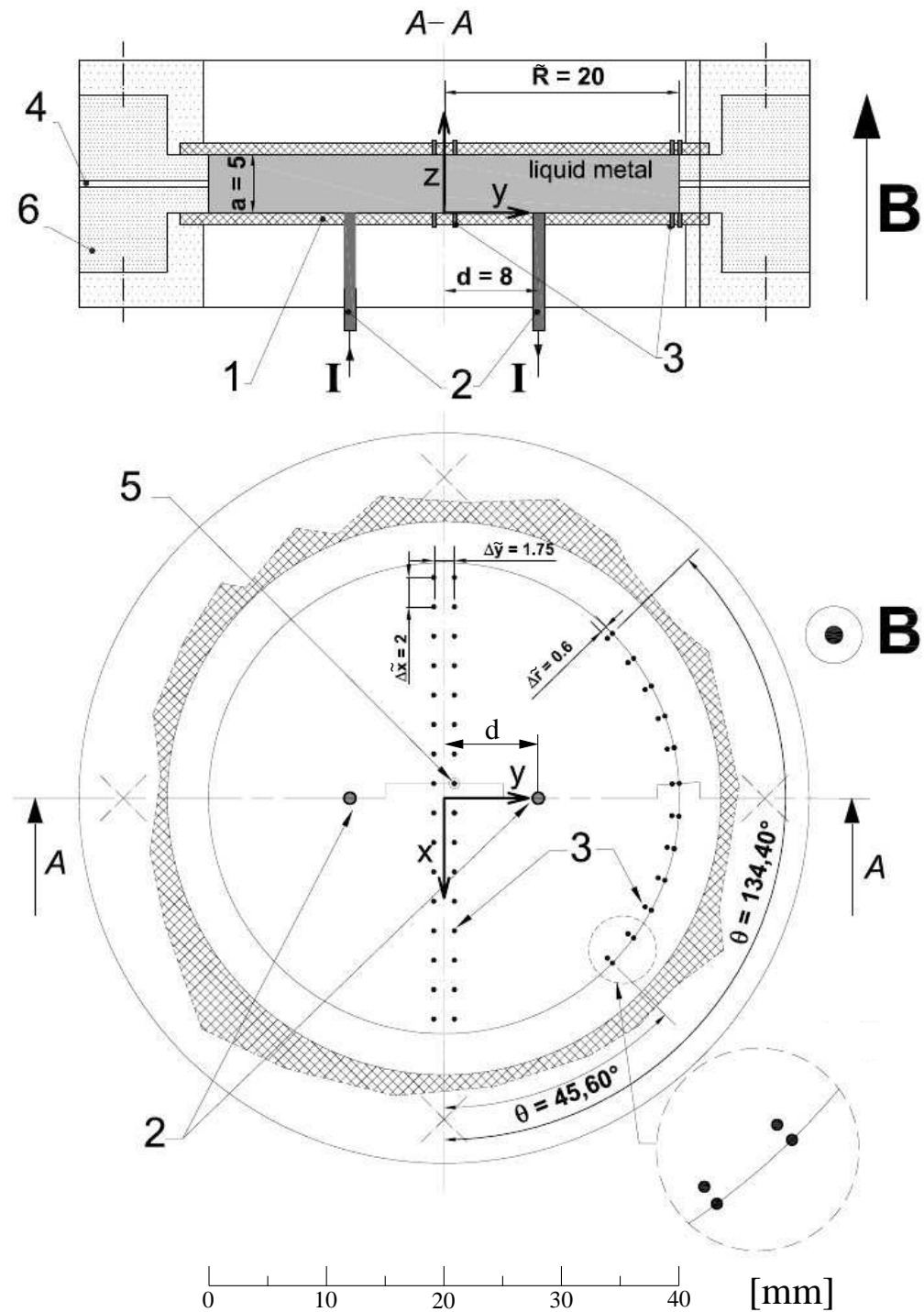


Figure 2.14.: Sketch of the experiment. top: cross section of the cylindrical container, bottom: top view of the bottom plate. (1) electric board, (2) electric current injection electrodes (diameter $d_e = 1\text{mm}$), (3) electric potential probes, (4) in-/outlet to fill cavity with Galinstan, (5) reference probe for electric potential measurements, (6) plexiglas hollow cylinder. $\Delta\tilde{x} = 2.5\text{mm}$, $\Delta\tilde{y} = 1.75\text{ mm}$ and $\Delta\tilde{r} = 0.6\text{ mm}$ are the distances between the potential probes.

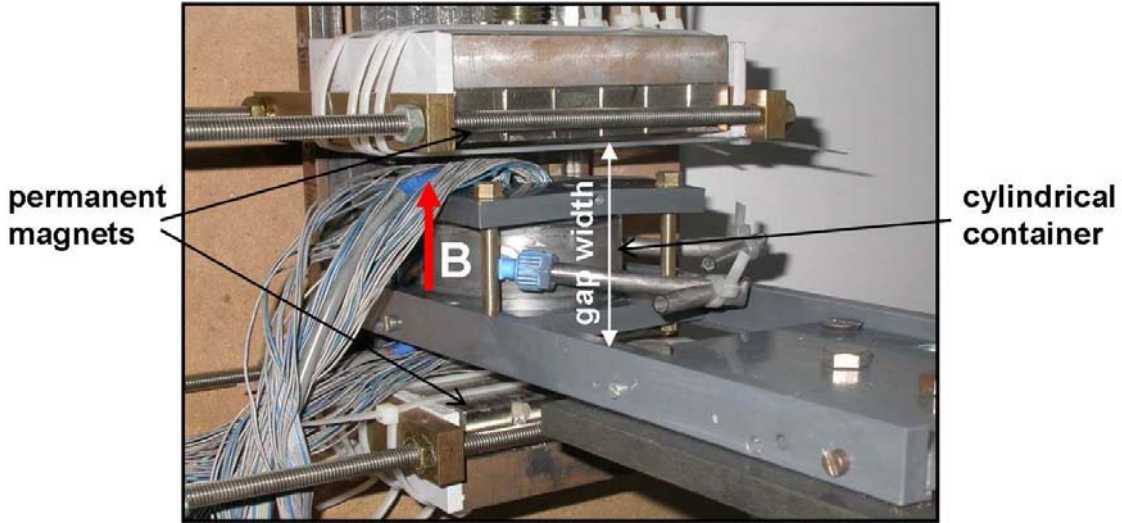


Figure 2.15.: Installation of the liquid metal filled, cylindrical container in the centre of the gap spanned by two identical sets of permanent magnets. By varying the gap width the strength of the magnetic field \mathbf{B} can be changed.

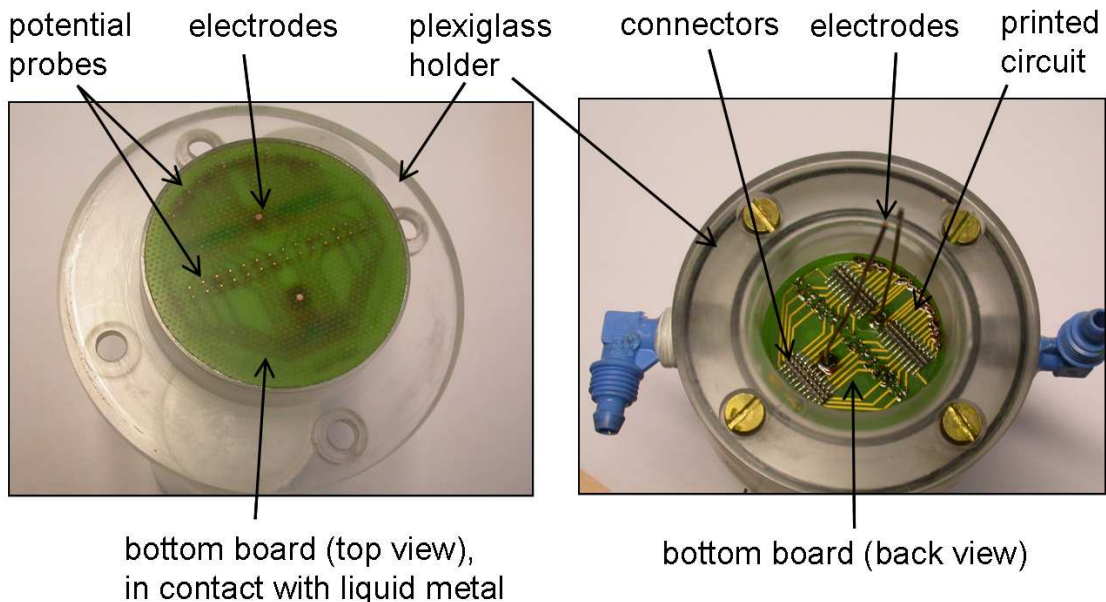


Figure 2.16.: Bottom plate made of electronic board material FR4 with embedded electric potential probes and electrodes fixed to a plexiglas holder. Left: View onto the side of the bottom plate that is in contact to the liquid metal. Potential probes as well as electrodes are mounted flush to the surface. Right: View onto the back of the board with printed electric circuits that convey all signals to connectors.

the high precision amplifier system presented in Sec. 2.2.

Since the flow is expected to be mostly quasi two-dimensional one can apply approximation (2.3) as given in Sec. 2.2. This implies that velocities just outside the *Hartmann* layer

can be extracted from measurements of the electric potential on both *Hartmann* walls using (2.4). Corresponding electric potential probes have been placed to obtain profiles of velocities \tilde{u}_x and \tilde{u}_y along the diameter $\tilde{y} = 0$ and, velocity profiles $\tilde{u}_\theta(\tilde{r}, \theta, t)$ near the side walls at $\tilde{r} = 19.7$ mm for angle $\theta \in [45.6^\circ, 134.4^\circ]$ (see Fig. 2.14 for more details).

Table 2.3.: *Hartmann* number $\text{Ha} = aB_0\sqrt{\sigma/(\rho\nu)}$ and *Hartmann* friction time $\tau_H = a^2/(2\nu\text{Ha})$ for the height of the cylindrical container $a = 5\text{mm}$ and magnetic field strengths $B_0 \in \{0.09\text{T}, 0.12\text{T}, 0.19\text{T}, 0.24\text{T}\}$.

B_0	[T]	0.09	0.12	0.19	0.24
Ha		13.5	18	28.5	36
τ_H	[s]	3.3	1.75	1.1	0.85

Furthermore, the comparison between sets of measurements obtained at $z = a$ and $z = 0$ allows us to spot residual three-dimensional effects using the elements given in Sec. 2.2.3.

2.5. Experiment on the appearance of three-dimensionality

In this section we describe the specifications of the large scale experiment that was purpose-built to study the appearance of three-dimensionality in MHD flows. The principle of our experiment follows that of [62] in which a constant homogeneous magnetic field \mathbf{B} was applied across a square, shallow container of height 0.02m filled with liquid metal mercury. In his configuration, the time scale for "two-dimensionalisation" $\tau_{2D}(l_\perp)$ for each flow structure of transverse size l_\perp was less than 10^{-2} s and much smaller than the structure's inertia $\tau_U(l_\perp)$. Accordingly, the flow was quasi two-dimensional (Sec. 1.3.2). Unlike [62]'s earlier experiment though, our container is not shallow, but cubic and with inner edge $L = 0.1$ m. For low magnetic field strengths, this favours times $\tau_{2D}(l_\perp)$ which are of the order of 1s and therefore much longer than those of [62]. When $\tau_{2D}(l_\perp)$ becomes comparable to $\tau_U(l_\perp)$ three-dimensionality in related flow structures should occur.

2.5.1. Design container

When designing the container, we aimed at having a construction that is made of modular elements. Firstly, this reduces development costs and time, and secondly, it offers far more flexibility. For instance, this allows us to easily modify the experiment when aiming at studying physical mechanism, beyond those of the present work. In this spirit, the container consists of a cubic brazen frame and plates containing elements to force or measure the flow inside the box mounted on each side (Fig. 2.17). This implies that modifications to the experiment can be done just by interchanging corresponding plates. In the present work, the two side plates across (denoted as bottom and top plate) and two side plates along the magnetic field \mathbf{B} are equipped with the elements presented in Sec. 2.1.3 and Sec. 2.2. This means that potential probes and current injection electrodes are embedded into electrically insulating electronic boards made of RO4003C material (Fig. 2.18) that, once fixed to corresponding board holders made of copper (Fig. 2.19a), constitute one of the interchangeable plates (Fig. 2.19b). We should mention that we use RO4003C as board material as it is resistant to temperatures up to 250°C. This is indeed crucial as the temperature in the vicinity of the *Hartmann* wall will reach higher values than in the core due to high current densities in the thin Hartmann layer, in particular near the electric current injection electrodes.

It is also important to notice that the brazen frame and the plates are made electrically insulating by coating them with a thin layer of black Polyamid. This layer has the thickness of about $150\mu\text{m}$ and resists temperatures up to 100°C. If for instance the walls parallel to the magnetic field lines \mathbf{B} would be electrically conducting it cannot develop an electric potential gradient at the wall that according to (2.3) balances $\mathbf{u}_\perp^c \times \mathbf{B}$. This

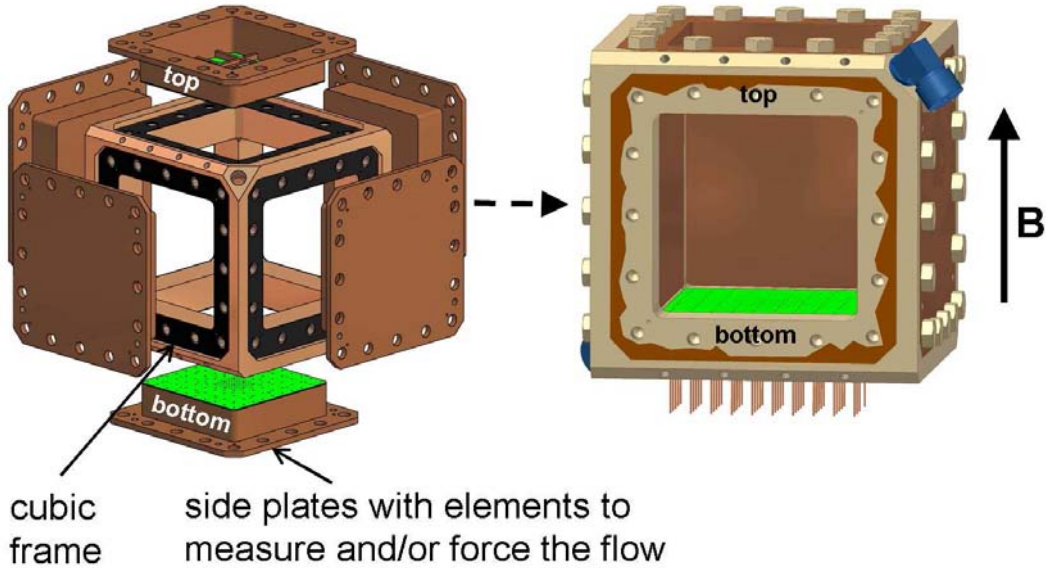


Figure 2.17.: Modular design made of a cubic frame with interchangeable side plates. When modifications on the experiment are required, those plates can be easily swapped to exchange flow forcing and flow measurement systems. Left: open container with side plates unmounted. Right: closed container where the front plate is only partly drawn to allow for a view into the container.

implies that velocities at the edge of the *Hartmann* layer cannot be extracted from electric potential measurements at the *Hartmann* wall. Furthermore, electric conductivity of the walls implies a stronger damping of the flow that appears under the form of ohmic dissipation induced by significant current densities inside the walls. The influence of this effect on flows in our experiment is indeed interesting from the physical point of view, but not part of the present work.

2.5.2. Filling with liquid metal

The liquid metal alloys GaInSn and Galinstan are both prone to quick oxidation when they come into contact with air. This results into a thin layer of liquid metal oxide that covers its surface and may deposit onto potential probes and injection electrodes when filling the container. This drastically deteriorates their electrical contact with the liquid metal and yields to unusable experimental data. Electric contact problems between liquid metal and potential probes as well as injection electrodes may also result from gas bubbles that could remain in the container after filling. Furthermore, such bubbles brutally change the electric current distribution inside the flow and, accordingly, the physics of the flow. In order to avoid these effects we firstly flush the container with inert gas argon, to press air particles out and, secondly, evacuate remaining particles of air and argon from the

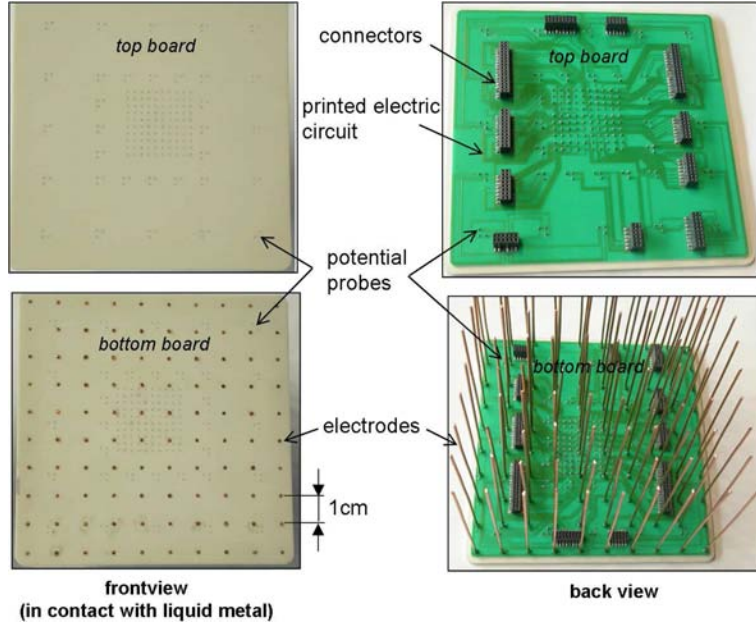


Figure 2.18.: Top and bottom plate with electrodes and potential probes that are soldered into corresponding electronic boards made from high temperature resistant roger material RO4003C . Left column: Frontview showing their side that faces the liquid metal. The set of electrodes and potential probes are made flush with the surface. Right column: Backview with printed electric circuits that transfer signals to connectors. Note that the two side plates along the magnetic field \mathbf{B} are made following the same principle.

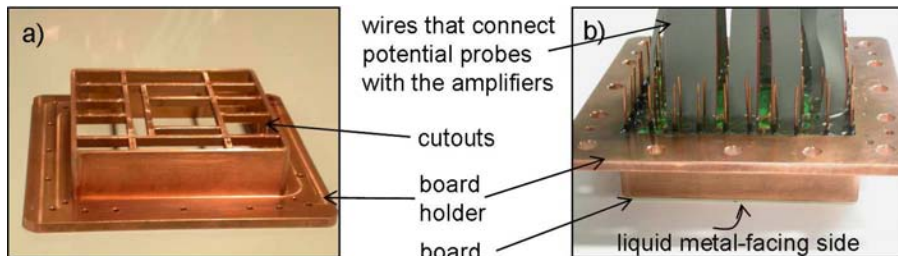


Figure 2.19.: Manufacturing of the side plates. (a) board holder made of copper with cutouts to provide a greater support surface to the board (note that wires conveying the signals to the amplifiers need to have access to the connectors attached to the back of each board (Fig. 2.18)). (b) finished side plate, here the bottom plate, with the board mounted onto the copper holder.

container up to a vacuum of order of 10^{-2}kPa .

2.5.3. Installation inside the superconducting magnet

The container has been mounted to the movable part of an aluminum rack which slides on the top of a rack that is fixed to the ground beneath the superconducting magnet (Fig. 2.21a). Once filled with liquid metal outside the magnet (Fig. 2.21b), this allows

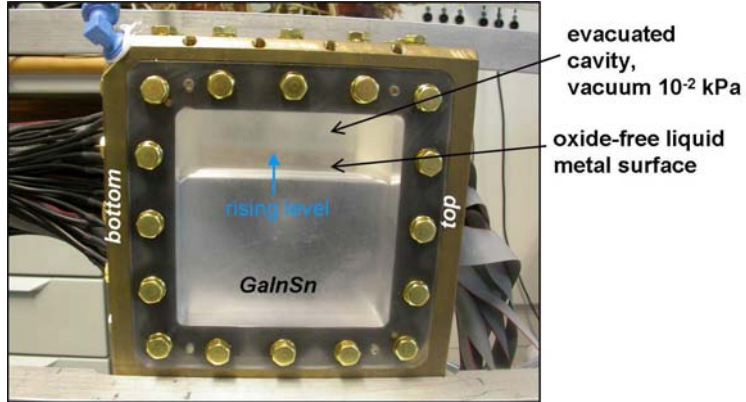


Figure 2.20.: Hermetic filling of the cubic container with liquid metal alloy GaInSn. The container's evacuation from gas particles avoids electric contact problems and remaining gas-bubbles inside the liquid metal after filling.

us to easily move the container into the magnet bore, placed at always the same position at the centre of symmetry of the magnetic field lines (Fig. 2.21c). This not only secures identical conditions between different sets of measurements, but also minimizes field inhomogeneities over the fluid domain. Furthermore, since only the cubic frame is attached to the vertical aluminum bars, side plates can be removed to clean the cavity or to replace them by other ones without changing the position of the container with respect to the aluminum rack. Lastly, this setup ensures the complete absence of mechanical contact between the magnet and the box.

2.5.4. Experimental set-up and measurement techniques

The experiment is shown on Fig. 2.22. It features a cubic container with inner edge $L = 0.1\text{m}$ where all container walls are electrically insulating. Once hermetically filled with GaInSn liquid metal (Table 2.1), the container is subject to the magnetic field $B_0\mathbf{e}_z$ shown in Fig. 2.1b (Sec. 2.1.2). Magnetic field strengths $B_0 \in [0.1, 5]\text{T}$ with corresponding *Hartmann* numbers $\text{Ha} \in [364, 18220]$ are achieved by varying the electric current that circulates inside the superconducting coil (see table 2.4 for selected values of B_0 and related Ha).

The flow entrainment relies on the same principle as in [62]'s or our small experiment (Sec. 2.4.1). This implies that uniform DC electric current I is injected at the bottom *Hartmann* wall ($z = 0$) through n injection electrodes (electrode diameter $d_e = 1\text{mm}$). In total 100 electrodes are thus mounted flush to this wall, with either $n = 100 (= 2n_p = 2n_m)$ or $n = 16 (= 2n_p = 2n_m)$ of them alternately connected to either pol of the DC power supply EA-PSI 9080-300 6HE 19' (Sec. 2.1.3). The DC power supply provides DC electric currents in the range $I \in [0 - 300]\text{A}$. This too corresponds to a forcing geometry of either a square array of 10×10 or 4×4 electrodes spaced by distances $L_i = 0.01\text{m}$ or

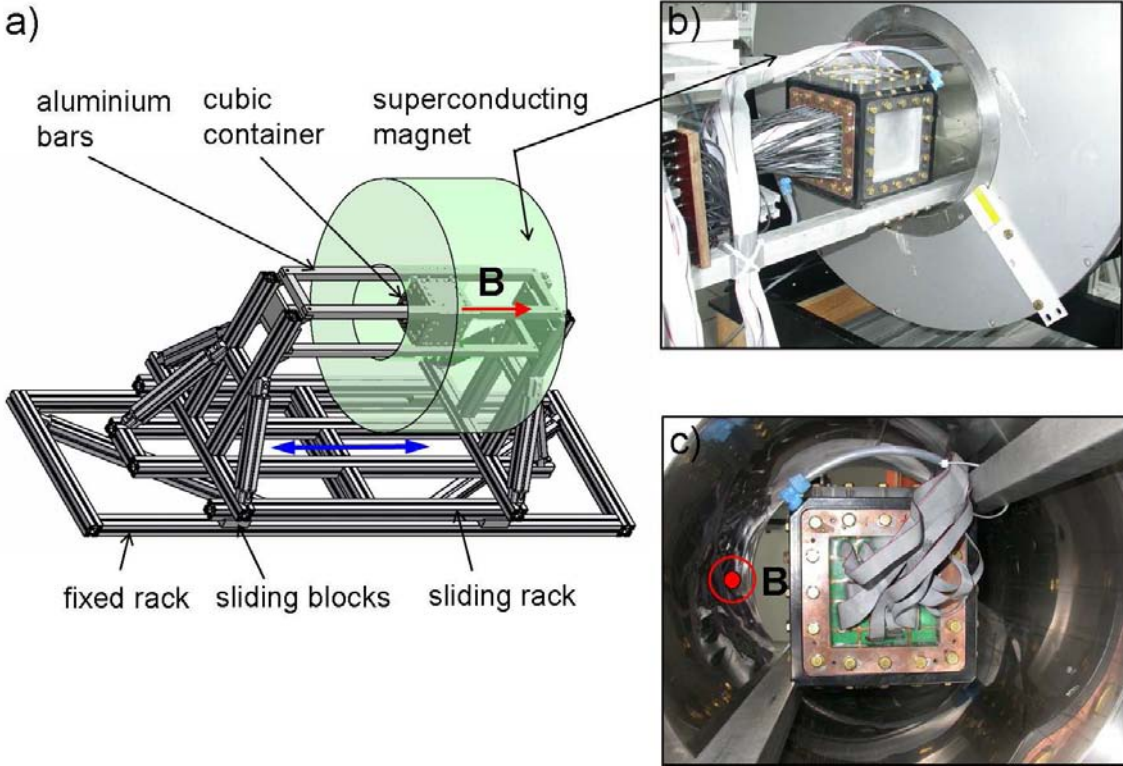


Figure 2.21.: Experiment installed inside the superconducting magnet. (a) Schematic picture of the container mounted onto an aluminum rack that have four sliding blocks to allow for its sliding along the fixed aluminum rack and brings the container always into the centre of the magnet. (b) Container outside the magnet. (c) Container in the centre of the magnet where the homogeneity of the field \mathbf{B} is best

$L_i = 0.03\text{m}$ respectively. When the imposed field \mathbf{B} is strong and the injected electric current I is weak one creates a base flow made of quasi-2D vortices spinning in alternate directions as in [62]'s experiment. Each quasi two-dimensional vortex would again have a 2D-circulation of $\Gamma_0 = I/(\pi n(\sigma\rho\nu)^{1/2})$ in absence of viscous dissipation in the vortex core (Sec. 2.4 and Sec. 1.2.3). This suggests also defining $U_0 = 2\Gamma_0/(L_i/2)$ as a reference velocity *a priori* in the centre between the axis of individual counter-rotating vortex pairs. U_0 expressed non-dimensionally yields to the corresponding *Reynolds* number Re^0 :

$$\text{Re}^0 = \frac{U_0 L_i}{\nu} = \frac{4I}{n\pi\nu(\sigma\nu\rho)^{1/2}} \quad (2.14)$$

As in [28], electric potential ϕ is measured locally in the $x-y$ plane at the bottom ($z = 0$) and top ($z = L$) *Hartmann* walls using two identical sets of 196 electric potential probes (see also Sec. 2.2 for a review of the measurement technique). These two sets are aligned exactly opposite each other along the \mathbf{e}_z axis as shown on Fig. 2.22. At the wall centre, probes are positioned in a dense 10×10 grid of spacing $\Delta x = \Delta y = 2.5\text{mm}$ to visualise the smaller vortex structures in the flow. Middle-sized vortices and vortices of the size of

Table 2.4.: Typical values of *Hartmann* number $\text{Ha} = LB_0(\sigma/(\rho\nu))^{1/2}$, *Hartmann* friction time $\tau_H = L^2/(2\nu\text{Ha})$ and two-dimensionalisation time $\tau_{2D}(L_i) = \sigma B_0^2/\rho(L/L_i)^2 = \tau_j(L/L_i)^2$ for magnetic field strengths $B_0 \in \{0.5\text{T}, 1\text{T}, 2\text{T}, 3\text{T}, 5\text{T}\}$ and electrode spacings $L_i \in \{0.01\text{m}, 0.03\text{m}\}$.

B_0	[T]	0.5	1	2	3	5
Ha		1822	3644	7290	10933	18222
τ_H	[s]	6.9	3.4	1.7	1.1	0.7
$\tau_{2D}(L_i = 0.01\text{m})$	[s]	0.8	0.2	4.6×10^{-2}	2.1×10^{-2}	7.5×10^{-3}
$\tau_{2D}(L_i = 0.03\text{m})$	[s]	8×10^{-2}	2.1×10^{-2}	5×10^{-3}	2.3×10^{-3}	8.4×10^{-4}

the box are captured by measurements on probes that are positioned in groups of always three probes (distant by $\Delta x = \Delta y = 2\text{mm}$ from one another), around the centre array and further out close to the parallel walls respectively.

Electric potential is also measured in the $y - z$ and $x - z$ plane at the wall where $x = 0$ and $y = L$ respectively, on 195 probes located as sketched in Fig. 2.22. These probes are spaced by distances $\Delta y = 4\text{mm}$ and $\Delta z = 4.6\text{mm}$ along \mathbf{e}_y and \mathbf{e}_z respectively (note that sets of probes in the $x - z$ and $y - z$ planes are arranged identically). Those measurements should shed some light on the flow structure along the magnetic field lines \mathbf{B} , but again, corresponding recorded electric potential have not been analysed in the frame of this dissertation (Sec. 2.2.4).

All electric potentials are simultaneously recorded with sampling frequency 128Hz using the high-precision signal processing amplifier system presented in Sec. 2.2. This provides both local time-dependent electric potential gradients $\nabla\phi(x, y, 0)$, $\nabla\phi(x, y, L)$, $\nabla\phi(0, y, z)$ and $\nabla\phi(x, L, z)$ and a visualisation of iso-electric-potential lines (thereafter: iso- ϕ lines) at corresponding walls. Furthermore, when the flow is quasi-2D or weakly 3D, iso- ϕ lines and potential gradients obtained at the bottom and top *Hartmann* wall can be directly related to streamlines and velocities respectively, both obtained at the edge of corresponding *Hartmann* layers (Sec. 2.2.2).

Like in our other experiment (Sec. 2.4.1), the presence of three-dimensionality in the core flow reflects on different sets of measurements obtained at top and bottom *Hartmann* walls. The form under which it appears can be identified from differences in related iso- ϕ contours as well as signal correlations (Sec. 2.2.3) .

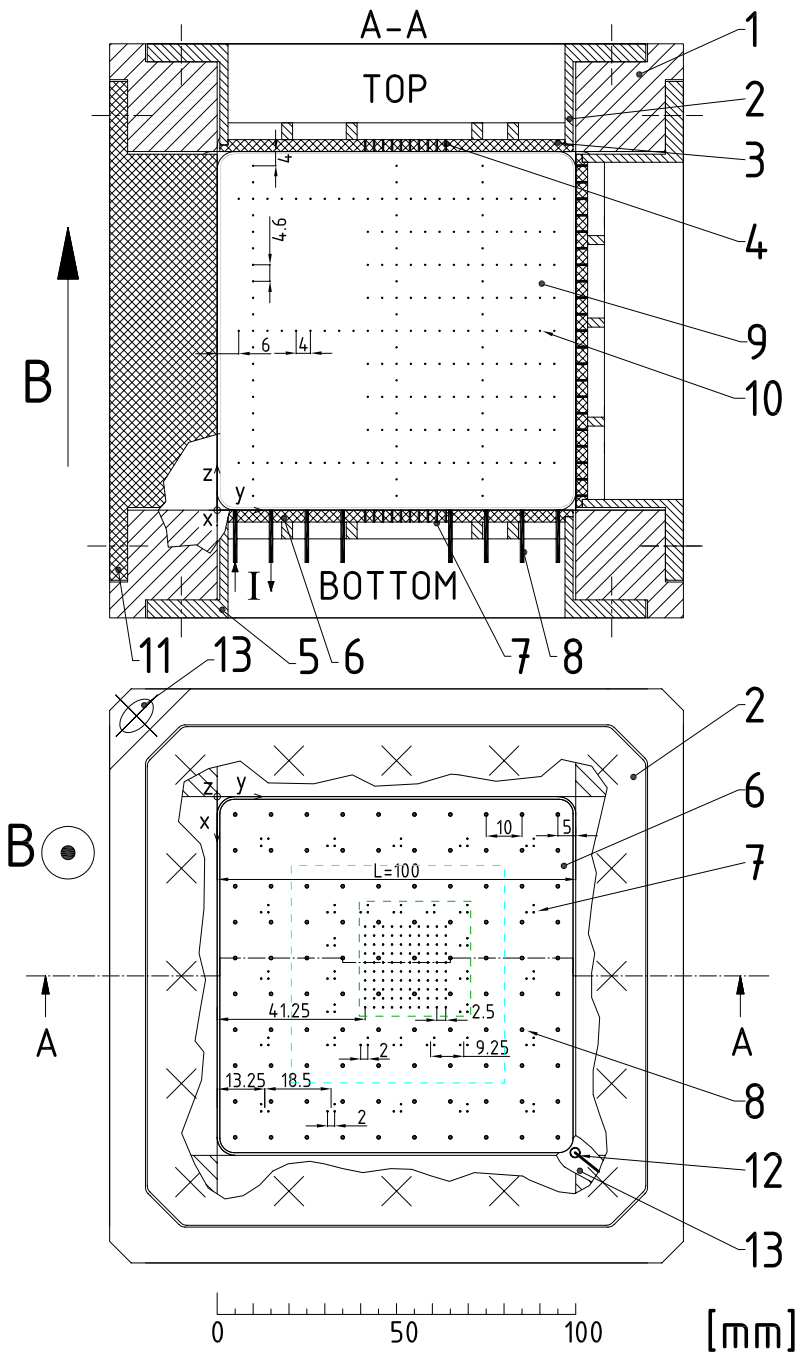


Figure 2.22.: Sketch of the cubic container. Top: cross section. Bottom: top view onto the bottom plate. (1) cubic brazen frame; (2) top-holder with top-electronic board (3) with 196 potential probes (4); (5) bottom-holder with bottom-electronic board (6) with the same set of 196 potential probes (7) as on the top and additional 100 forcing electrodes (8); (9) parallel-electronic board with 195 potential probes (10) (the same set of probes exists in the $x - z$ plane where $y = L$)); (11) side plate; (12) reference probe; (13) inlet and outlet to evacuate the container and to fill it with liquid metal. All container walls are electrically insulating, except on locations where potential probes or electrodes are embedded.

2.6. Experimental procedure

The experiments presented in previous Secs. 2.4, 2.5 are performed following the same experimental procedure. Starting at $I = 0A$, the total electric current I injected through n electrodes was increased in steps up to the maximum that is reached when either $I/n = 10A$ or $I/n = 7A$, depending on whether measurements are performed on the small or the large scale experiment (recall that in the latter the amount of current that can be injected through each electrode is limited by the $R_{2\Omega}$ -resistance). When a bifurcation is found, the step size of changing I has been reduced to obtain detailed information on the flow properties around the transition. For each corresponding forcing I measured non-dimensionally by $\text{Re}^0(I)$ we waited until the flow was fully developed before recording electric potentials over a period in the range of $[10\tau_H, 300\tau_H]$. This procedure is repeated for different values of magnetic field strength B_0 with corresponding non-dimensional Hartmann numbers Ha (Table 2.3 and Table 2.4). Ha and Re^0 are then the two control parameters in both experiments.

Chapter 3

Experiment on a confined electrically
driven vortex pair

3. Experiment on a confined electrically driven vortex pair

In this chapter we present the results obtained from the experiment on the electrically driven vortex pair confined in a shallow, cylindrical container. It should be noted that the whole content of this chapter is published in [28].

3.1. Introduction

We are interested in the transition to turbulence induced by the presence of a wall in quasi two-dimensional flows. In applications, boundaries are often responsible for the development of turbulence. Their role is for example crucial in the dynamics of wings or flying objects where boundary layer separations initiate vortex shedding and subsequent turbulent patterns that, in turn, determine lift and drag forces. The complexity of these flows makes them difficult to investigate experimentally and very costly to tackle numerically. In this regard, quasi two-dimensional flows in simpler configurations allow us to easily reproduce some elementary properties of the transitions phenomena that occur in real configurations and to understand the two-dimensional part of their dynamics. This is why a large number of studies have been dedicated to the very generic quasi two-dimensional separated flow past a circular cylinder (see [72, 73] and [40] for a review of numerical work on boundary-generated two-dimensional turbulence). These flows are, to a large extent, determined by how single vortices or vortex pairs interact with walls so it is essential to understand the dynamics of such a reduced system. There has been number of studies around this theme and one can cite two that are closest to our purpose: [63] demonstrated some elegant visualisation of the vortex/wall interaction in liquid metal Magnetohydrodynamic flows and [40] recently performed numerical simulations of a forced vortex array in a square box. They exhibit a transition to turbulence through a sequence of supercritical bifurcations that leads to a chaotic, then turbulent state, as in the case of the cylinder wake. In the work presented in this chapter we aim at reproducing such a boundary induced transition to turbulence experimentally and analyse it, by studying a forced vortex pair confined in a circular domain.

Since a purely two-dimensional flow cannot be achieved experimentally, we wish to put a particular emphasis on the measure of residual three-dimensional effects and their consequences on the quasi two-dimensional flow. To this end, we study a flow in a thin layer of liquid metal under an externally imposed, transverse magnetic field, as [63] did, using the experimental setup described in Sec. 2.4. If the transverse magnetic field is strong enough, the resulting flow is quasi two-dimensional in the sense that physical quantities don't vary across the layer except in the vicinity of the walls that confine it, where so-called Hartmann boundary layers develop because of the no slip condition (see for instance [42]). Because of this particular flow structure, several small but important laboratory Magnetohydrodynamic experiments have been built where a layer of liquid metal held between two parallel planes is used to obtain an experimental realisation of quasi two-dimensional flows. Among them, [62] has provided an experimental evidence of the two-dimensional inverse energy cascade that characterises two-dimensional turbulence. [5] experimentally and [15, 21] numerically have studied the quasi two-dimensional wake of a circular cylinder and identified the usual regimes found in the hydrodynamic case. In none of these studies, however, was the actual limit of the quasi two-dimensionality assumption examined, although more general studies have proposed theoretical scenarios for the transition between quasi two-dimensional and three-dimensional flows ([64, 10]). This question is crucial in order to quantify the relevance of Magnetohydrodynamic flows in thin layers to two-dimensional flows. We shall therefore address it by calculating the correlations between quantities measured on either side of the fluid layer, just outside of the Hartmann layers as [68] did, to measure the progressive elongation of a single pulsed vortex in a magnetic field. This will allow us to determine whether the observed flow properties are influenced by three-dimensional effects that are related to differential rotation and vortex disruption (Sec. 2.2.3).

Thereafter in Sec. 3.2, we present experimentally observed flow regimes and compare them qualitatively with flow patterns found numerically by [28]. In Sec. 3.3 we identify scaling laws for measured topological quantities against a single parameter $R_h^0 = Re_h^0/Ha$ that is known to control the dynamics in quasi two-dimensional flows (see Sec. 1.2.3). The nature of bifurcation observed at the transition between flow regimes is characterised in Sec. 3.4. Finally, we discuss the appearance of three-dimensionality and the role of the *Hartmann* layer friction in all observed flow regimes in Sec. 3.5 and Sec. 3.6 respectively.

To recall our experimental setup shown on Fig. 2.14 and described in Sec. 2.4 we shall now briefly discuss its main properties. The experiment features a horizontal shallow liquid metal layer of height $a = 5\text{mm}$ enclosed in a cylindrical container of radius $\tilde{R} = 20\text{mm}$. The liquid metal layer is penetrated by a vertical, constant magnetic field $\mathbf{B} = B_0 \mathbf{e}_z$. A pair of counterrotating vortices is generated by injecting constant electric current I from one *Hartmann* wall, through two point electrodes distant by 16mm. The magnetic

field strength B_0 and the electric current I , respectively expressed non-dimensionally as *Hartmann* number $\text{Ha} = aB_0(\sigma/(\rho\nu)^{1/2}$ and *Reynolds* number $\text{Re}^0 = I\tilde{R}/(\pi\nu d(\sigma\rho\nu)^{1/2})$, control the flow in steady and unsteady regimes. Related flow states are identified from local quantities such as velocity profiles obtained from electric potential measurements at the *Hartmann* walls (Sec. 2.2.2): along the diameter $y = 0$, and at distance 0.3mm from the circular side wall between angles $\theta = 45.6^\circ$ and $\theta = 134.4^\circ$ (see Fig. 2.14). To back our experimental analysis we also take advantage of more global representations of the flow provided by [28], who numerically simulate the mostly quasi two-dimensional flow for *Hartmann* number $\text{Ha} = 43$ using [54]'s two-dimensional model (Sec. 1.2.3).

3.2. General aspects of the flow

In this section we report observed flow regimes that occur in the mostly quasi two-dimensional flow in the cylindrical container when increasing the electric forcing from $I = 0$ (or $\text{Re}^0 = 0$). The established flow state goes through a sequence of bifurcations that appear at critical forcing measured non-dimensionally by the *Reynolds* numbers Re_{III}^0 , Re_{IV}^0 , Re_V^0 and Re_{3D}^0 .

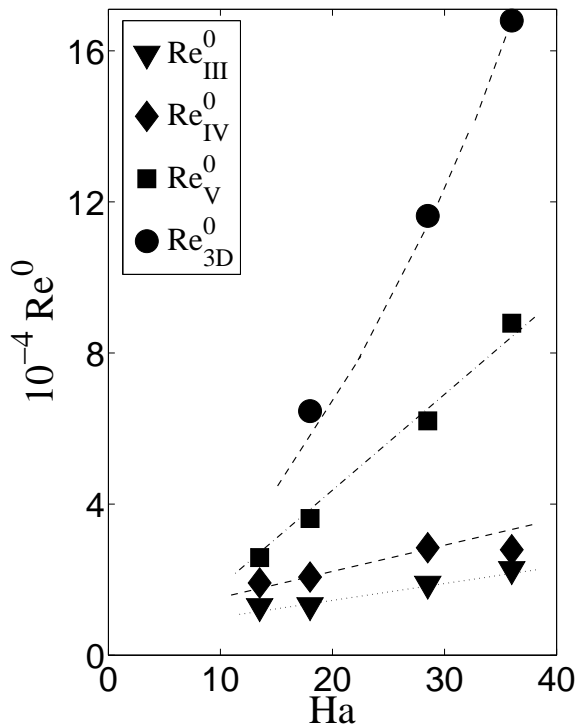


Figure 3.1.: Critical Reynolds numbers *vs.* Hartmann number. Re_{III}^0 : transition from the steady flow regime to the periodic flow regime. Re_{IV}^0 : transition from the periodic flow regime to the flow regime with two base frequencies. Re_V^0 : transition to the flow regime where the profile of u_x almost becomes symmetric again. Re_{3D}^0 : transition to three-dimensionality (see Sec. 3.5).

These critical values are in fact functions of the *Hartmann* number Ha as shown in Fig. 3.1 and corresponding flow regimes are described thereafter.

At very low forcing, such that $\text{Re}^0 < \text{Re}_{III}^0$, the flow is steady and the corresponding profile of u_x (marked by "I" in Fig. 3.2a) along the diameter $y = 0$ is almost symmetric about $x = 0$, with $u_x > 0$ everywhere. In this regime "I", the point of maximum velocity u_x^M is however located at $x^M > 0$, x^M being small and increasing with Re^0 (Fig. 3.3a).

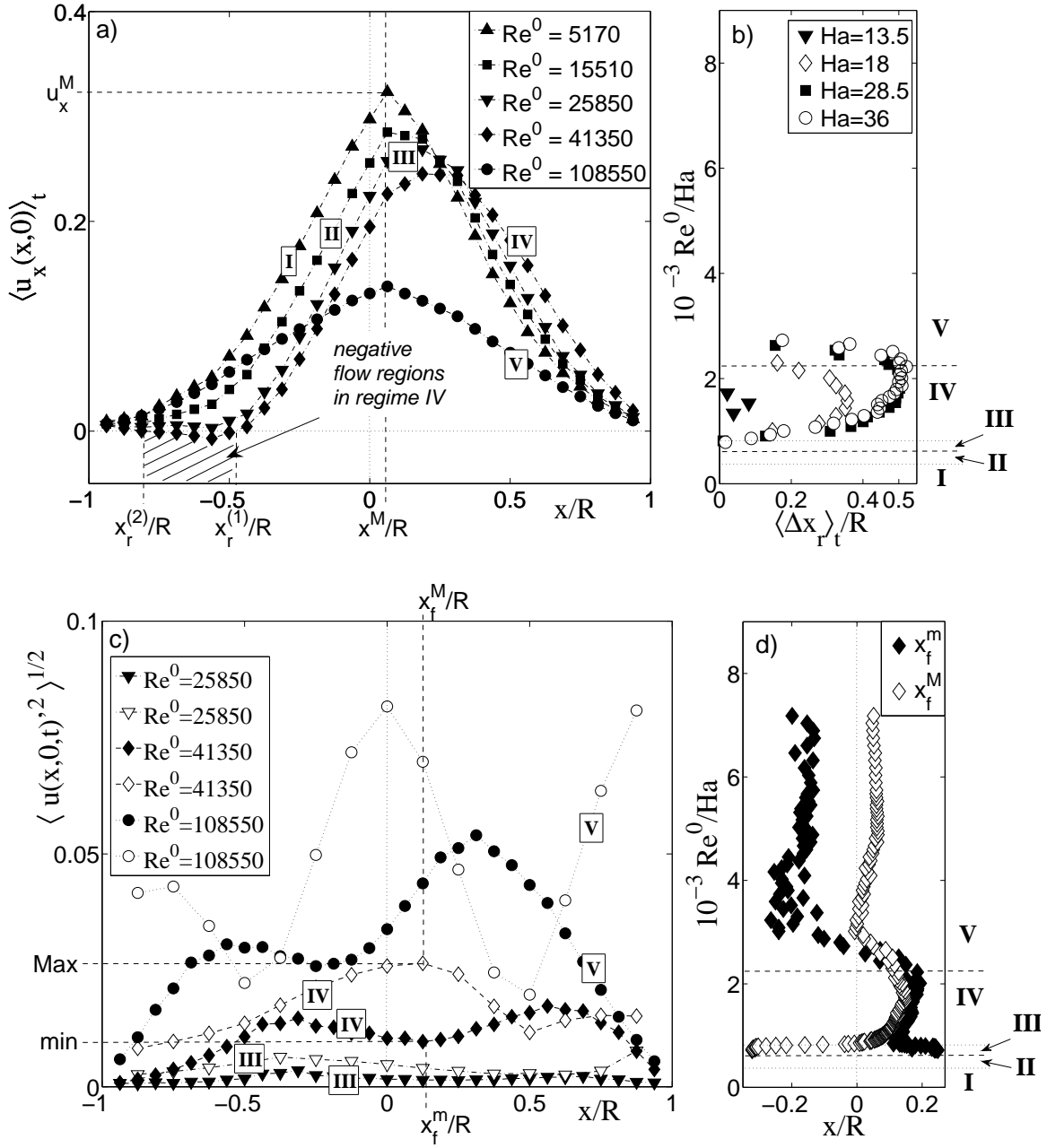


Figure 3.2.: Experimentally obtained, time averaged quantities where velocities and distances are normalized by the forcing U_0 and the cylinder radius R respectively. (a) velocity profiles $\langle u_x(x, 0) \rangle_t$ for $Ha = 36$. (b) width of recirculating region $\langle \Delta x_r \rangle_t = \langle x_r^{(1)} - x_r^{(2)} \rangle_t$ vs. Re^0 / Ha . (c) RMS of velocity fluctuations $u'(x, 0, t)$ along the diameter $y = 0$ for $Ha = 36$. Black markers: $\langle u'_x(x, 0, t)^2 \rangle_t^{1/2}$, white markers: $\langle u'_y(x, 0, t)^2 \rangle_t^{1/2}$. (d) $\langle x_f^m \rangle_t$ and $\langle x_f^M \rangle_t$ vs. Re^0 / Ha for $Ha = 36$. The corresponding flow regimes are indicated as I, II, III, IV and V.

Velocities $u_\theta(r = 0.985R, \theta, t)$, measured near the cylinder wall, are orientated anticlockwise and almost azimuthal, without any sign reversal (Fig. 3.4).

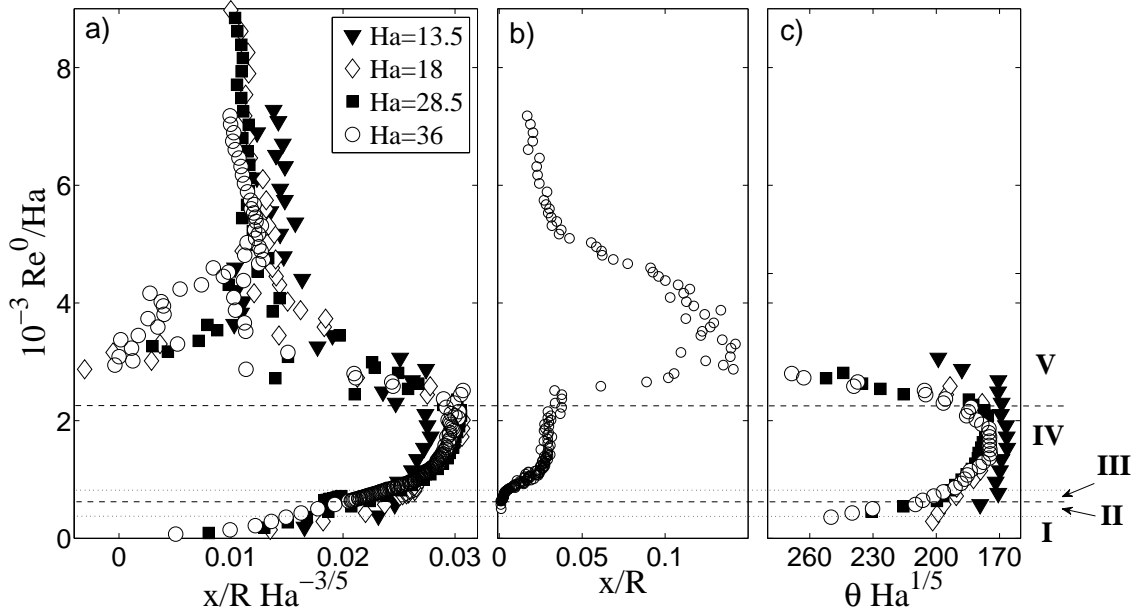


Figure 3.3.: (a) $\langle x^M \rangle_t$ vs. Re^0/Ha . (b) x_{RMS}^M vs. Re^0/Ha for $\text{Ha} = 36$. (c) $\langle \theta_{s'} \rangle_t$ vs. Re^0/Ha .

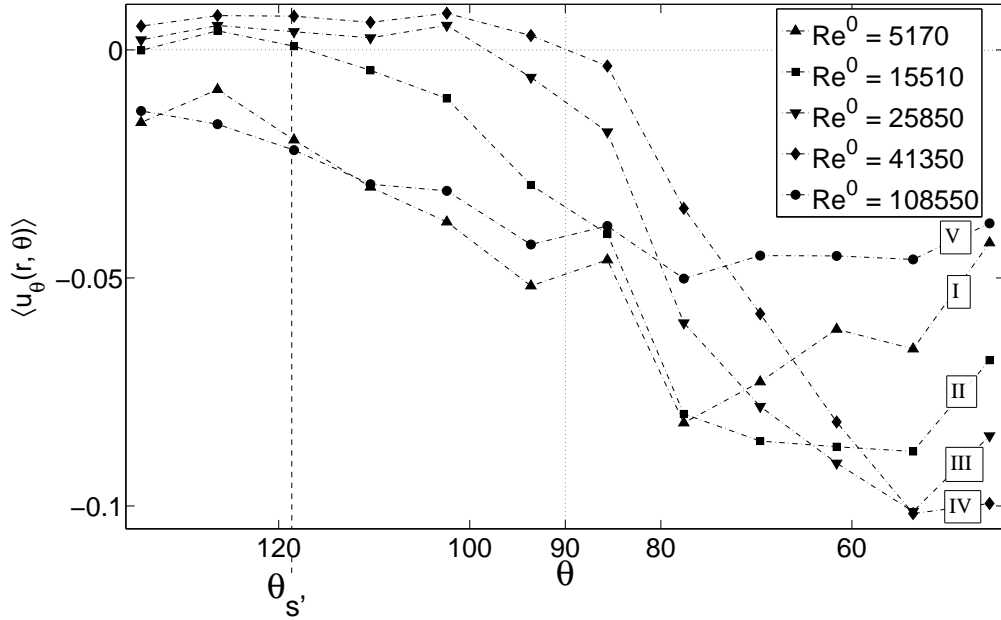


Figure 3.4.: Time averaged velocity profiles $\langle u_\theta(r = 0.985R, \theta) \rangle_t$ along the circular side wall for $\text{Ha} = 36$. Note that the precise determination of $\theta_{s'}$ is limited by the number of measurement points along the side wall and a low signal to noise ratio $r_{S/N}$.

The type of profile as shown in Fig. 3.2a in this regime is also typical from regime "I" that [28] found numerically for $\text{Ha} = 43$ (Fig. 3.6a). In this first steady regime, contours of vorticity (Fig. 3.5a) and stream lines (Fig. 3.5b) provided by the numerical simulations essentially show two steady counterrotating vortices, antisymmetric about the $\hat{\mathbf{e}}_x$ axis and

centered slightly to the right of the electrode axis. This explains therefore the location of the maximum velocity u_x^M that was found at $x^M > 0$ along the diameter $y = 0$ as it corresponds to the position of the initial vortex pair. In fact, the distance between the location of their rotation axis and the electrodes results from the balance between their mutual influence that tends to imprint a motion toward $x > 0$, and the influence of the circular wall. Furthermore, Fig. 3.5a (left) shows that each of these vortices presents a sharp vorticity maximum located away from the vortex centre that corresponds to a free shear layer in the shape of a ring.

For slightly higher values of Re^0 , but still in regimes where $\text{Re}^0 < \text{Re}_{II}^0$, the flow changes into a second steady state denoted as regime "II" where the velocity profile $u_\theta(r = 0.985R, \theta, t)$ first exhibits a change of sign at angle $\theta_{s'}$ (Fig. 3.4).

[28]'s numerical results presented Fig. 3.5b confirm that this observation can be related to the side layers that separate from the cylinder wall at angle $\theta_{s'}$ at two symmetric locations behind the initial vortices to form counterrotating recirculation regions. Interestingly, [28] points too to an apparent analogy between these regions to those which appear in duct flows past a cylindrical obstacle with an homogeneous magnetic field oriented along the cylinder axis, as studied by [15] (Fig. 3.7).

When the forcing is further increased, the flow still remains steady and $\theta_{s'}$ is displaced along the wall in clockwise direction (Fig. 3.3c). This displacement also coincides with the increase of x^M (Fig. 3.3a and Fig. 3.6a), which indicates that it is a consequence of the displacement of the initial vortex pair in the $x > 0$ direction. The zone of positive azimuthal velocity for $\theta > \theta_{s'}$ in Fig. 3.4 therefore characterises the antisymmetric counterrotating recirculation regions that appear behind each of the two initial vortices because of the separated boundary layer.

The transition into regime "III" occurs when the flow becomes unsteady at $\text{Re}^0 = \text{Re}_{III}^0$. It results into a periodic oscillation of local electric potentials $\phi(x, y, t)$ (Fig. 3.8a) which yields strong peaks with base frequency f_1 and further harmonics $2f_1$ and $3f_1$ in the frequency spectrum. Corresponding spectra, recorded from measurements on the bottom plate at $x = -0.4375R$, $y = -0.04375R$ and $z = 0$ are shown on Fig. 3.9a (note that time-dependent signals $\phi_w(x, y, z, t)$ and related power spectra taken from potential measurements at other locations yield qualitatively similar results). Accordingly, x^M and $\theta_{s'}$ obtained from velocity profiles III of u_x and u_θ in Fig. 3.2 and Fig. 3.4 respectively are time-dependent and when the forcing is intensified, $\langle x^M \rangle_t$ and the RMS of its fluctuations, $x_{RMS}^M = \langle (x^M(x, 0, t) - \langle x_M(x, 0) \rangle_t)^2 \rangle_t^{1/2}$, increases. We also found that the time-averaged angle $\langle \theta_{s'} \rangle_t$ where separation occurs is displaced along the circular wall in the $\theta < 0$ direction (see Fig. 3.3c). Having inspected time series of subsequent vorticity contours provided by numerical simulations for this regime we could attribute the transition into

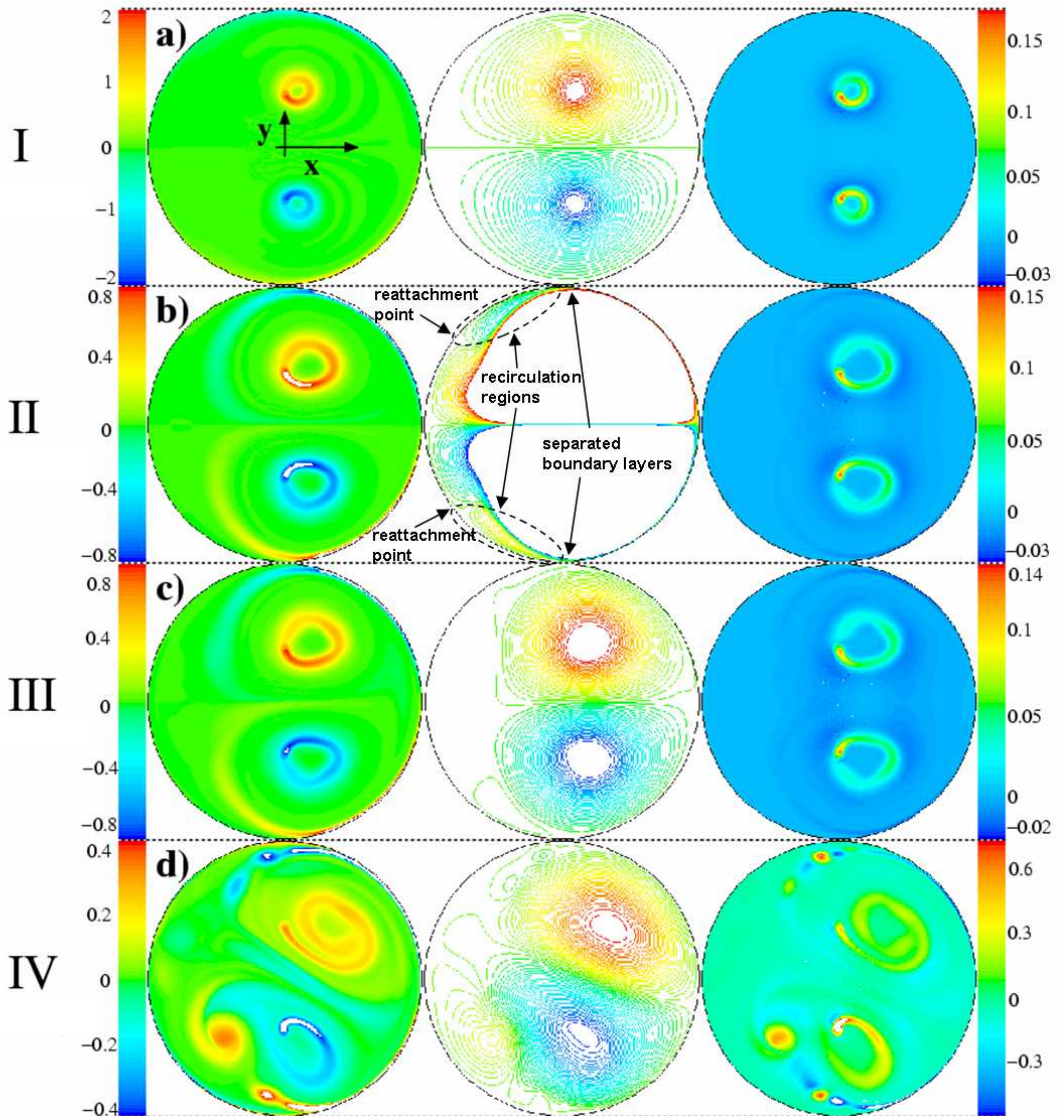


Figure 3.5.: Snapshots of equilibrium and quasi-equilibrium states in all flow regimes for $\text{Ha} = 43$ obtained from [28]'s numerical simulations that use the model of [54] (see Sec. 1.2.3). Contours of vorticity normalised by U_0/a (left column), streamlines (centre column), contours of vertical velocity as given by (1.76), normalised by U_0 (right column). (a) regime I. (b) regime II. (c) regime III. (d) regime IV.

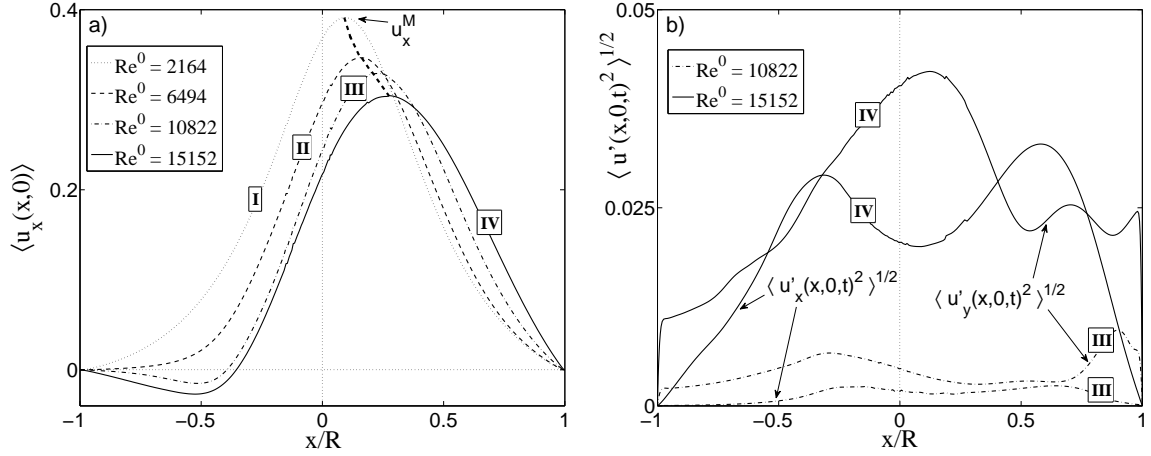


Figure 3.6.: Time averaged quantities obtained from [28]'s numerical simulations for $Ha = 43$. (a) Velocity profiles $\langle u_x(x, 0) \rangle$ (the thick dashed line indicates the shift of the vortex pair toward $x > 0$ with increasing Re^0). (b) RMS of velocity fluctuations $u'(x, 0, t)$ along the diameter $y = 0$: $\langle u'_x(x, 0, t)^2 \rangle_t^{1/2}$ and $\langle u'_y(x, 0, t)^2 \rangle_t^{1/2}$.

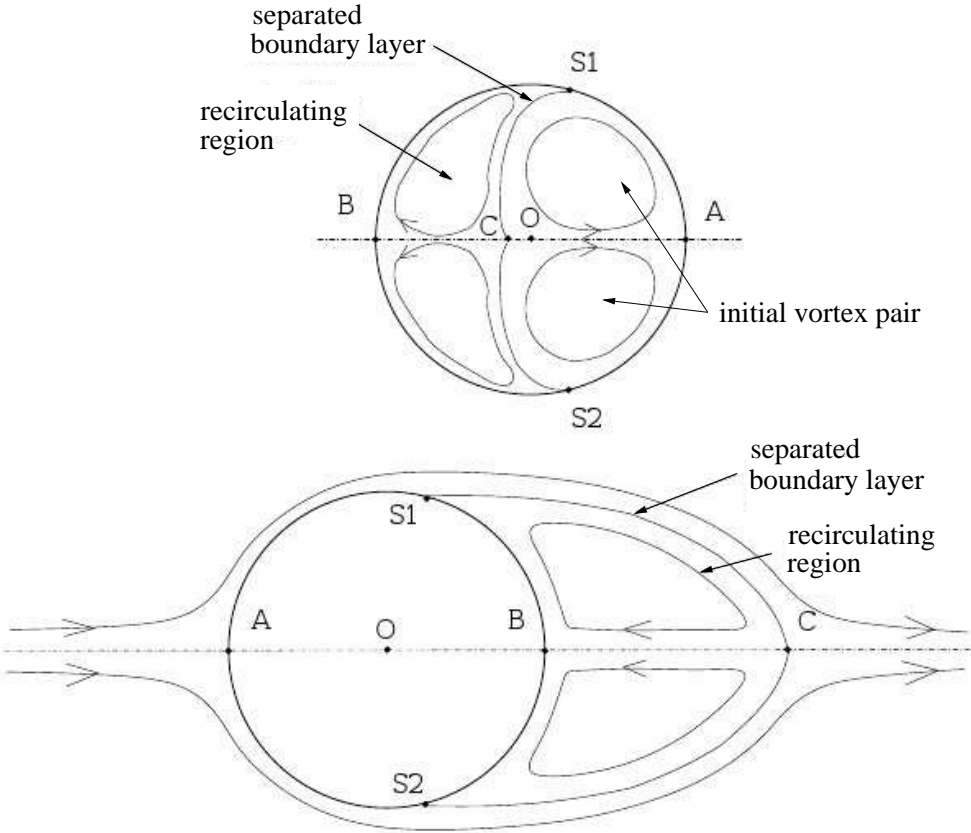


Figure 3.7.: [28]'s schematic representation of the analogy between steady flows with boundary layer separation inside (top) and around (bottom) a cylinder container. A, B and C are stagnation points, S₁ and S₂ are separation points.

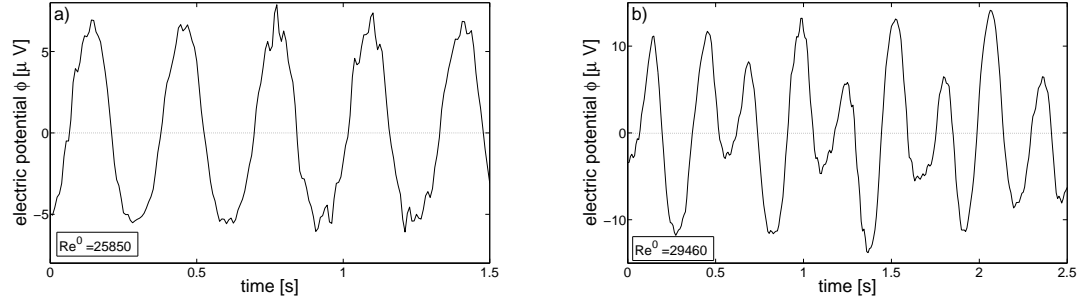


Figure 3.8.: Recorded time-dependent signal $\phi_w(x = -0.4375R, y = -0.04375R, 0, t)$ for $\text{Ha} = 36$. (a) Periodic flow regime with base frequency f_1 for $Re^0 = 25850$, regime "III". (b) Two base frequency flow with base frequencies f_1 and f_2 for $Re^0 = 29460$, regime "IV".

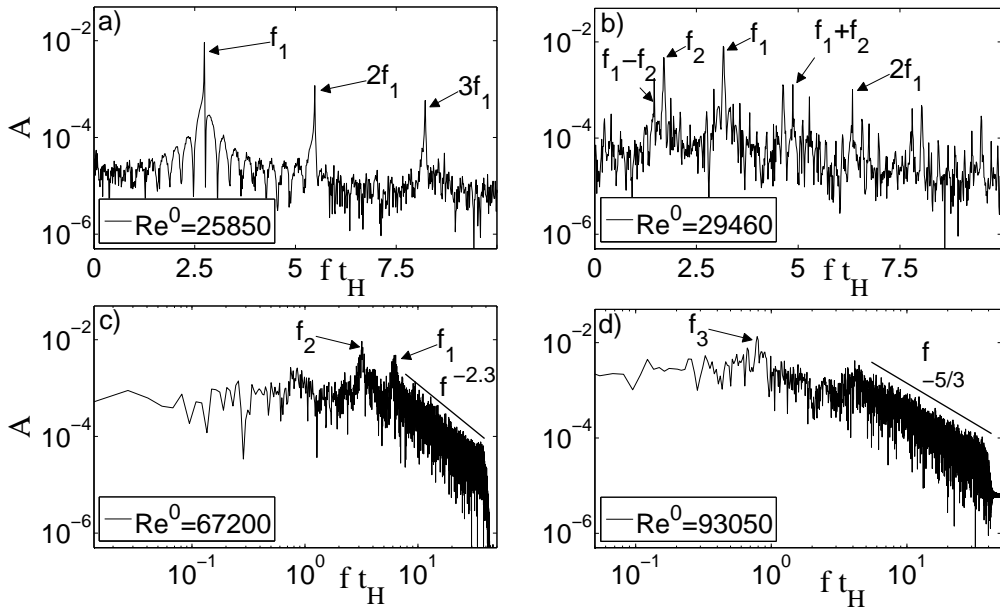


Figure 3.9.: FFT of recorded time-dependent signal $\phi(x = -0.4375R, y = -0.04375R, 0, t)$ for $\text{Ha} = 36$. (a) periodic flow (regime III). (b) two base frequency flow (regime IV). (c) chaotic/turbulent flow in flow regime IV. (d) chaotic/turbulent flow in flow regime V. Oscillation amplitudes A and frequencies f_i are normalised by $B_z U_0 a$ and the Hartmann friction time t_H^{-1} respectively.

flow regime "III" to a destabilisation of the separated boundary layers at the back of the initial vortex pair (Fig. 3.5c) shows a snapshot of this time series). The vorticity time series visualises small vortices that form in the vicinity of the locations where the boundary layer detaches from the circular wall and grow along the separated boundary layers, until they are released almost simultaneously from either side of the centerline $y = 0$ into the stream between the two electrodes. As in the experiments, this results in the appearance of a low base frequency and subsequent harmonic oscillations of the velocity

field (see [28] for detailed information). That the measurements do indeed characterize the vortex shedding regime found in the numerical simulations can be also proven by the good qualitative agreement between numerical and experimental mean velocity profiles, as well as RMS of velocity fluctuations (*resp.* Figs. 3.2a, 3.6a and Figs. 3.2c, 3.6b).

This vortex shedding also explains the presence of maxima at $x < 0$ in the profiles III of $\langle u'_x(x, 0, t)^2 \rangle^{1/2}$ and $\langle u'_y(x, 0, t)^2 \rangle^{1/2}$ plotted along the diameter $y = 0$, as they correspond to the location where the shed vortices impact onto the centerline (see Fig. 3.2c). It is also noteworthy that, as in the previous regime "II", this vortex shedding process is reminiscent to that of the Von Kàrmàn street behind a cylindrical obstacle as *e.g.* numerically studied from [15], but differs from it: at the onset of the unsteady regime "III", vortices detached from the cylinder wall are released in turn and not almost simultaneously as in the flow inside the cylindrical container. The synchronisation of this shedding is however lost at slightly higher forcing.

A further flow regime, called regime "IV" is found when $\text{Re}^0 = \text{Re}_{IV}^0$ as a second base frequency f_2 , with $f_2 < f_1$, appears in the frequency spectrum of $\phi(x, y, t)$. The spectrum is then seen to be extended as further frequency peaks occur for Re^0 slightly higher than Re_{IV}^0 (Fig. 3.9b and corresponding time-dependent signal Fig. 3.8b). This equates to a regime that [28] identified in his numerical simulations and denoted too as regime "IV" as here again, the time averaged profiles of velocity as well as RMS profiles of velocity fluctuations, obtained experimentally and numerically are in good qualitative agreement (Figs. 3.2a, 3.2b) and Figs. 3.6a, 3.6b respectively). Further in this regime, a clear maximum in the profiles of $\langle u'_y(x, 0, t)^2 \rangle^{1/2}$ appears in the region $x > 0$ at x_f^M (Fig. 3.2c), roughly at the location x^M where $u_x = u_x^M$ (recall that x^M identifies the location of the initial vortex pair along the centerline $y = 0$, *ig.* 3.2a). This can be interpreted using a series of images of vorticity contours obtained from the numerics of [28] at subsequent time steps (Fig. 3.5d for a related snapshot). They show that the above observation is related to the two initial vortices, however strongly disrupted now, starting to oscillate around the centerline $y = 0$ while exhibiting both long and short wave instabilities so the global picture becomes that of a strongly chaotic flow (Fig. 3.5d). This argument finds support as the frequency spectrum experimentally obtained in this regime shows that the amplitude of all measured frequencies raises significantly above that from previous regimes. According to [40] this indicates a transition to a spectrum with a broad continuous component, thus implying that the flow for higher forcing in regime "IV" is turbulent.

Also, since vortices that are shed into the $x < 0$ region are stronger in regime "IV" they induce a flow of negative mean velocity that occupies a region of width $\langle \Delta x_r \rangle = \langle x_r^{(1)} - x_r^{(2)} \rangle$ along the centerline as can be noticed from the velocity profile "IV" in Fig. 3.2a. When the forcing is intensified, the associated return flow extends and, therefore, $\langle \Delta x_r \rangle$ in-

creases (Fig. 3.2b). Furthermore, once sucked into the stream between the two oscillating vortices located at $x > 0$, the shed vortices are strongly squeezed and stretched which damps their fluctuations along $\hat{\mathbf{e}}_x$ and may explain the minimum in the profile "IV" of $\langle u'_x(x, 0, t)^2 \rangle^{1/2}$ at x_f^m in Fig. 3.2c. Since this stretching is directly induced by the two initial vortices, the evolution of x_f^m follows that of x_f^M with increasing forcing, until these two points clearly separate, which marks the end of regime IV.

As a last remark related to our experimental observations in this regime "IV", we should refer to similarities to the Von Kàrmà̄n street behind a cylindrical obstacle: [28] pointed out that [15] also identified the appearance of a lower base frequency in the flow regime he calls regime "IV". It corresponds to vortices that, after being detached from the duct side walls, disturb the Von Kàrmà̄n street. Further details related to similarities between the flow within and past the cylinder for flow regimes "I", "II", "III" and "IV" can be found in [28].

A last flow regime, denoted as regime "V", has been detected at $Re^0 = Re_V^0$ where all quantities are brutally altered. $\langle \Delta x_r \rangle_t$ drastically shrinks (Fig. 3.2b) and negative velocity components vanish completely along the diameter $y = 0$, resulting in a profile of $\langle u_x \rangle_t$ that is almost symmetric about $x = 0$ (Fig. 3.2a). Accordingly, the average $\langle x_M \rangle_t$ rapidly drops to the vicinity of $x = 0$ at first, increases again and then slightly decreases for higher forcing. Also, the averaged point of sign reversal along the circular wall $\langle \theta_{s'} \rangle_t$ is displaced in anticlockwise direction, thus following the displacement of $\langle x^M \rangle_t$. For $Re^0 \gg Re_V^0$ however, very strong velocity fluctuations make the detection of $\theta_{s'}(t)$ in the profile $u_\theta(r = 0.985R, \theta, t)$ impossible. The corresponding spectrum in this regime shows that the flow is turbulent, but interestingly, also reveals a new dominating base frequency f_3 that is much lower than f_2 (Fig. 3.9d).

The experimental findings in this regime can not be compared to numerical simulations as the interaction parameter N in [28]'s numerical calculations at the end of the previous regime "IV" is already close to unity which implies that [54]'s model on which they rely fails to deliver accurate results. Furthermore, the transition into regime "V" seems to be related to the transition from a laminar to a turbulent *Hartmann* layer as we will demonstrate in Sec 3.6. In this case too, [54]'s model breaks down as it can neither account for a turbulent *Hartmann* layer profile nor for the transition between a laminar and a turbulent *Hartmann* layer (see *e.g.* [28] for more information on the validity of [54]'s model).

3.3. Scaling laws in observed flow regimes

The *Reynolds* numbers Re_{III}^0 , Re_{IV}^0 and Re_V^0 , in the previous section identified as critical forcing that separates observed flow regimes, are shown on Fig. 3.1 where the evolution of corresponding points in the figure suggests that those numbers depend linearly on the *Hartmann* number Ha . This indicates that the transition between regimes is governed by a single parameter $R_h^0 = \text{Re}^0/\text{Ha}$ which is known to control quasi two-dimensional MHD flows dominated by *Hartmann* friction (Sec. 1.2.3). In order to further check this property, all Re^0 dependent quantities have been plotted against R_h^0 instead of Re^0 (see Figs. 3.2b, 3.3a and 3.3c). It clearly appears that any set of curve describing a topological quantity ($\langle x^M \rangle_t$, $\langle \theta_{s'} \rangle_t$, $\langle \Delta x_r \rangle_t$) can be merged into a single one, provided they are respectively scaled as:

$$\frac{\langle x^M \rangle_t}{\text{Ha}^{3/5}} \sim f(\text{Re}^0/\text{Ha}), \quad \langle \theta_{s'} \rangle_t \text{Ha}^{1/5} \sim g(\text{Re}^0/\text{Ha}), \quad \langle \Delta x_r \rangle_t \sim h(\text{Re}^0/\text{Ha}) \quad (3.1)$$

The fact that the lower values of Ha ($\text{Ha}=13.5$ and less noticeably $\text{Ha}=18$) match these scalings imperfectly certainly indicates that these are valid in the limit of large Ha and breakdown at lower Ha , where electromagnetic effects are less intense and regimes are not asymptotic in this sense anymore.

3.4. Analysis of the bifurcations

In this section we analyse the nature of bifurcations that occur at the transition to unsteady flow regimes "III" and "IV" (Sec. 3.2). To this end, we determine the absolute value of amplitude A_i and frequency f_i at the saturation level ($dA_i(t)/dt = 0$) of corresponding base oscillations $A_i(t) \sin(2\pi f_i t + \phi_i^v)$ (with phasing ϕ_i^v and $i \in \{1, 2\}$), depending on the strength of the forcing I (or expressed non-dimensionally by Re^0). In order to obtain a reasonable representation of the evolution of the instability we refined our experimental procedure (Sec. 2.6). It means that we decreased the step size of injected electric current to $0.01A$ within the range $I_c \pm 0.05 A$ where I_c denotes the critical forcing where any transition occurs. Once $I_c + 0.05A$ is reached, a possible hysteresis around I_c was sought

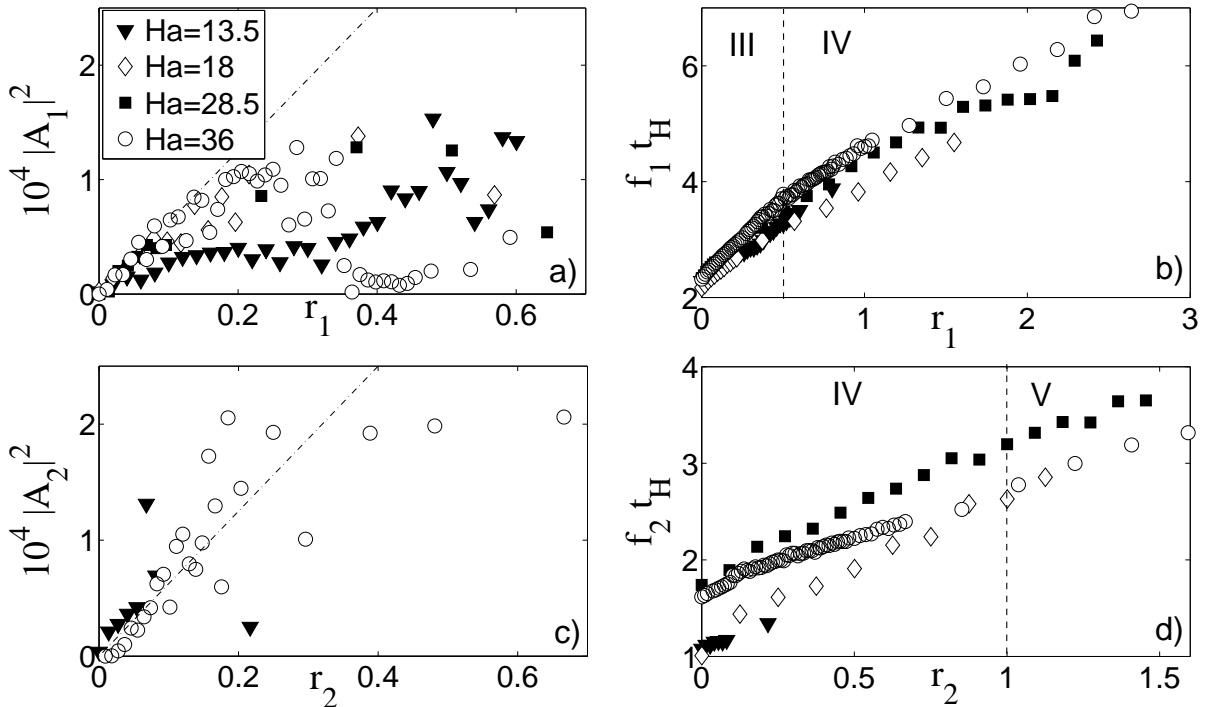


Figure 3.10.: Analysis of the bifurcations based on times series of $\phi_w(t)$ measured near the box centre at $x = -0.4375R$, $y = -0.4375R$ and $z = 0$. (a) square of the amplitude A_1 of mode 1 vs. r_1 . (b) frequency f_1 of mode 1 vs. r_1 . (c) square of the amplitude A_2 of mode 2 vs. r_2 . (d) frequency f_2 of mode 2 vs. r_2 . Oscillation amplitudes A_i and frequencies f_i are normalised by $B_z U_0 a$ and the Hartmann friction time t_H^{-1} respectively.

by decreasing the current in the same steps. This helps us to find out whether observed bifurcations are of supercritical or subcritical nature (*e.g* [16, 34]). Note that the analysis thereafter is based on time-dependent electric potentials $\phi_w(t)$ measured near the centre of the container at $x = -0.4375R$, $y = -0.4375R$ and $z = 0$, however, it was checked that time series obtained at other locations (x, y and $z \in \{0; a\}$) yielded qualitatively similar

results.

The evolution of the stationary amplitude $|A_1|$ of mode 1 with fundamental frequency f_1 versus the critical parameter $r_1 = \text{Re}^0/\text{Re}_{III}^0 - 1$ is reported on Fig. 3.10a (recall that values of Re^0 are dimensionless representations of the forcing I). It is found to follow a square root function in the region of small parameters $r_1 < 0.15$. Since it was also no hysteresis observed at the transition, this indicates a supercritical bifurcation or *Hopf*-bifurcation. According to [34], the weakly non-linear evolution of the amplitude of the perturbation $|A_1|$ can be described by the *Landau* equation in the region $r_1 < 0.15$ as follows:

$$\frac{d}{dt}|A_1|^2 = 2\sigma_1|A_1|^2 - l_1|A_1|^4 + \mathcal{O}(|A_1|^6), \quad \text{with } \sigma_1 > 0 \quad (3.2)$$

where σ_1 denotes the growth rate of the instability. l_1 is the *Landau* constant and measures the nonlinear saturation in the perturbation growth ([34]). Values of A_1 in Fig. 3.10a are obtained at the saturation level of the instability and the amplitude of the oscillation is stationary. In short, in regimes that satisfy $d(|A_1|^2)/dt = 0$. This implies that (3.2) can be modified into:

$$|A_1|^2 \simeq \frac{2\sigma_1}{l_1} = \frac{2k_1}{l_1}r_1 \quad (3.3)$$

Again, l_1 is the *Landau* constant and k_1 is a constant too ([34]). We have determined the ratio k_1/l_1 for $0 < r_1 < 0.15$ by interpolating the set of points $A_1(r_1)$ in Fig. 3.10a with a square root function. It yielded $k_1/l_1 \simeq 3 \times 10^{-4}$ for all values of Ha , but $\text{Ha} = 13.5$ as this case departs from the asymptotic curve and exhibits stronger saturation (see Fig. 3.10a). Also, related base frequencies f_1 increase linearly for small r_1 as a function of Re^0 and seem to saturate for higher r_1 as the flow approaches regime IV (Fig. 3.10b). Furthermore, since sets of points related to frequencies f_1 obtained for different *Hartmann* numbers almost collapse to a single curve when scaling them with the *Hartmann* friction time $\tau_H = (1/2)(a^2/(\nu\text{Ha}))$ indicates that the frequency f_1 increases monotonically with Ha at the onset of regime "III".

The second bifurcation at $\text{Re}^0 = \text{Re}_{IV}^0$ results in a spectrum with two base frequencies f_1 and f_2 and subsequent linear combinations of the form $m_1f_1 + m_2f_2$ with $(m_1, m_2) \in \{-2, -1, 0, 1, 2\}^2$ as in [7] and [40] (Fig. 3.9b). As for mode 1, the fundamental frequency f_2 of mode 2 increases linearly with the critical parameter $r_2 = \text{Re}^0/\text{Re}_{IV}^0 - 1$, but the slope seems to depend weakly on Ha (Fig. 3.10d). No saturation was detected for $0 < r_2 < 1.5$ but it may well occur for higher forcing. As $A_1(r_1)$, $A_2(r_2)$ follows a square root function according to $|A_2|^2 \simeq 2\sigma_2/l_2 = 2k_2r_2/l_2$, without any measurable hysteresis. An interpolation of $A_2(r_2)$ for $0 < r_2 < 0.15$ yields also $k_2/l_2 \simeq 3 \times 10^{-4}$ (Fig. 3.10c) and one can also conclude to the supercritical nature of the bifurcation to regime IV.

Lastly, since f_1 and f_2 seem to be two independent base frequencies it points to two-

frequency quasi-periodicity at the onset of regime "IV" (*e.g.* [49, 25]). As for period-doubling or intermittency, quasi-periodicity can appear in the sequence of transition scenarios in dynamical systems that yield to chaotic behaviour. In this context, quasi-periodicity does not mean that the flow motion is almost periodic. It rather implies that a time series of a flow related quantity can be decomposed into parts which themselves are periodic, but their periods are incommensurate and the ratio of corresponding frequencies f_2/f_1 would yield an irrational number. However, because of the limit in precision when determining frequencies f_1 and f_2 we can only suppose the presence of quasi-periodicity. In order to prove it one would need to use other techniques like for instance *Poincare*-mapping ([1, 27]). *Poincare*-mapping provide a better tool to identify particular flow characteristics like quasi-periodicity. Though interesting and important, applying such techniques to our experimental data would have gone beyond the scope of the present work.

3.5. Appearance of three-dimensionality

In this section we show how and under which form three-dimensionality appears for all cases of Ha studied, using elements presented in Sec. 2.2.3. Since the arrangement of probes in this experiment does not provide a visualisation of iso- ϕ contours we distinguish between weak and strong three-dimensionality only from correlations between electric potential gradients $\nabla\phi_w(x, y, 0, t)$ and $\nabla\phi_w(x, y, a, t)$ obtained at the bottom and top *Hartmann* walls respectively. Correlations built on electric potential gradients $\partial_y\phi_w(x, 0, z, t)$ are thereafter denoted as C_2 , while those correlations built on fluctuations only $\partial_y\phi'_w(x, 0, z, t) = \partial_y\phi_w(x, 0, z, t) - \langle\partial_y\phi_w(x, 0, z)\rangle_t$ are called C'_1, C'_2 (recall that indices $(\cdot)_1$ and $(\cdot)_2$ denote the type of correlation function defined by (2.6)). At this point, we should emphasize that correlation factors C'_1, C'_2 and C_2 can be influenced by the presence of $\simeq 2\mu\text{V}$ peak to peak noise (see appendix A). This is especially the case in steady flow regimes "I" and "II" where signals are weak and the ratio $r_{S/N}$ between the effective amplitude (RMS) of the signal and that of the noise, respectively, is small. For very slow fluid motion this may induce an error on the correlations of about 20% in the case of $\text{Ha} = 36$. The error however progressively decreases if the flow intensity increases and is already not more than 5% when the flow changes into the unsteady regime "III".

The variations of spatially averaged correlations $\langle C_i \rangle$ and $\langle C'_i \rangle$ with Re^0 are depicted on Figs. 3.11a, 3.11c and 3.11d for all values of Ha studied here (note that the average is made from local correlations $C_i(x, 0)$ and $C'_i(x, 0)$ obtained along the diameter $y = 0$ for $x \in [-0.8125R, 0.8125R]$). When $\text{Ha} = 36$ and $\text{Ha} = 28.5$, the correlation factor $\langle C_2 \rangle$ is nearly unity for all investigated regimes and one can conclude that the flow is very close to quasi two-dimensionality. This also justifies plotting profiles of velocities and velocity fluctuations in Figs. 3.2a, 3.2c and 3.4 for $\text{Ha} = 36$ instead of profiles of $\nabla\phi_w$ as relations (2.4) from Sec. 2.2.2 are valid.

For $\text{Ha} = 18$, $\langle C_2 \rangle$ seems to be slightly below unity even for very high signal to noise ratios $r_{S/N}$, indicating some small three-dimensionality. For $\text{Ha} = 13.5$, this effect is more substantial, and one sees that three-dimensionality is always present. This certainly explains why the case $\text{Ha} = 13.5$ departs from all the others in the scaling laws found in Sec. 3.3. Since flow fluctuations are about one order of magnitude smaller than the mean flow in all observed regimes "I" - "V" (Figs. 3.2a, 3.2b), the correlation $\langle C_2 \rangle$ mostly reflects the presence of three-dimensionality in the mean flow, in particular its weak form. It shows however less how signals between bottom and top plate are correlated in phase and frequency which would provide information on the appearance of strong three-dimensionality as defined in Sec. 2.2.3. A refined picture can therefore be obtained when inspecting spatially averaged correlations $\langle C'_1 \rangle, \langle C'_2 \rangle$ based on fluctuations $\partial_y\phi'_w(x, 0, z, t)$ only (Figs. 3.11c, 3.11d).

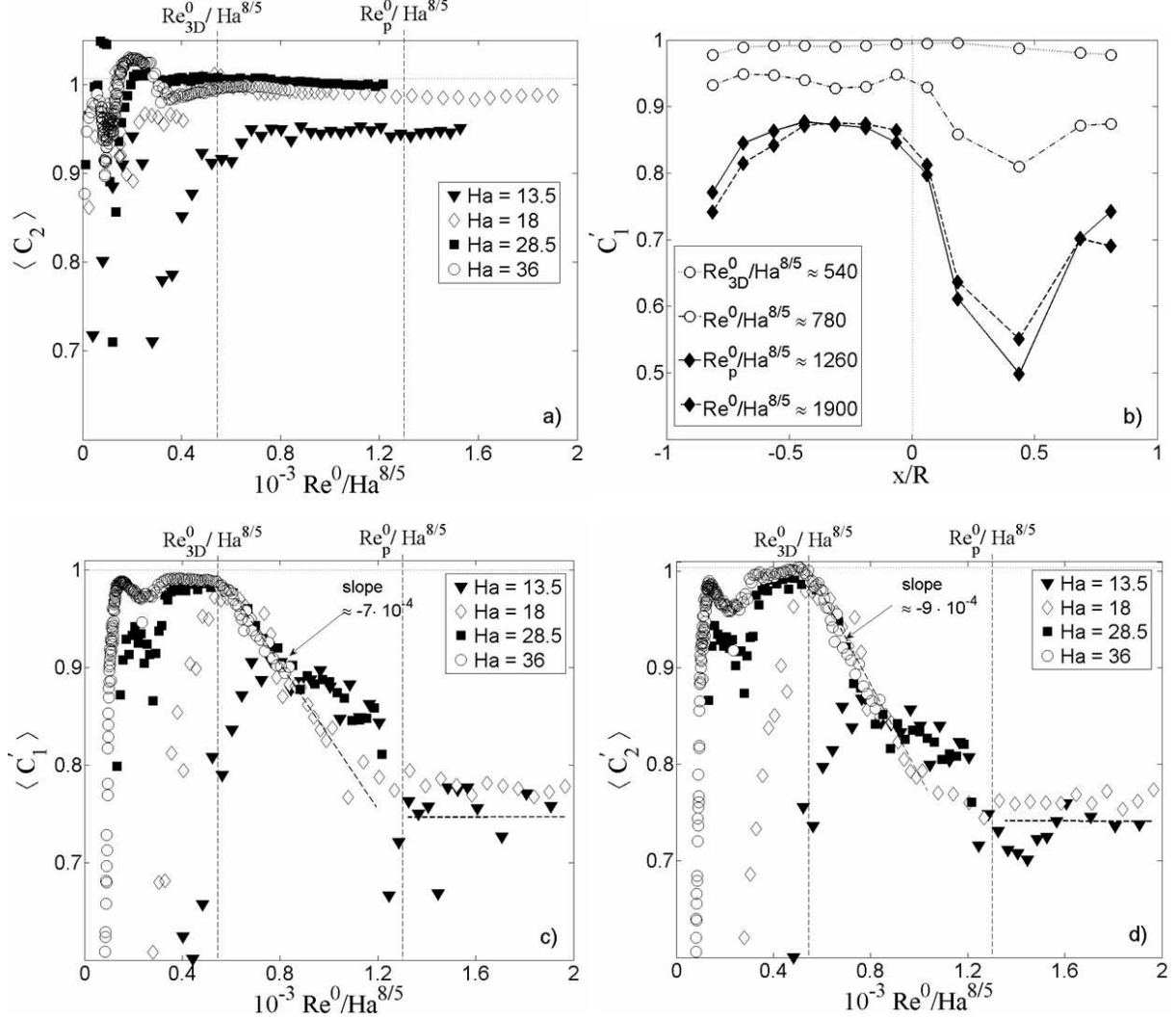


Figure 3.11.: Correlations of electric potential gradients $\nabla\phi_w(x, 0, z, t)$ as both profile and spatial averaged quantities along the diameter $y = 0$ for $x \in [-0.8125R, 0.8125R]$. (a) $\langle C_2 \rangle$ built on $\partial_y\phi_w(x, 0, z, t)$ vs. $Re^0/\text{Ha}^{8/5}$. (b) profile of C'_1 built on fluctuations $\partial_y\phi'_w(x, 0, z, t)$. (c) $\langle C'_1 \rangle$ built on fluctuations $\partial_y\phi'_w(x, 0, z, t)$ vs. $Re^0/\text{Ha}^{8/5}$. (d) $\langle C'_2 \rangle$ built on fluctuations $\partial_y\phi'_w(x, 0, z, t)$ vs. $Re^0/\text{Ha}^{8/5}$.

Both $\langle C'_1 \rangle$ and $\langle C'_2 \rangle$ are weak near the onset of unsteadiness where the amplitude of fluctuations and the ratio $r_{S/N}$ is small. They increase for higher forcing to a value of about unity and remain almost constant for $Re^0 \leq Re_{3D}^0$ (some small deviation can be again related to the presence of noise). Correlations in this flow regime are indeed close to unity at all locations (x, y) along the centerline, thus indicating quasi two-dimensionality (Fig. 3.11b). Furthermore, the fact that $\langle C'_1 \rangle \simeq \langle C'_2 \rangle$ tells us that flow fluctuations are strongly correlated in phase, frequency and amplitude which implies that they are subject to neither weak nor strong three-dimensionality.

This behaviour changes drastically at the critical value $Re^0 = Re_{3D}^0$. Both $\langle C'_1 \rangle$ and $\langle C'_2 \rangle$ linearly decrease for $Re^0 > Re_{3D}^0$ while $\langle C_2 \rangle$ remains almost constant (see Figs. 3.11a,

3.11c and 3.11d). This indicates the presence of three-dimensional vortices in the otherwise quasi two-dimensional flow. It can be seen from the profile in Fig. 3.11b that these three-dimensional structures are mostly located in the region $x > 0$ where vortices are strongly accelerated by the mean flow. Furthermore, since $\langle C'_2 \rangle$ decreases more strongly than $\langle C'_1 \rangle$, one can conclude to less intense fluctuations on the top *Hartmann* wall and to weak three-dimensionality that appears under the form of differential rotation along the field $B_0 \mathbf{e}_z$ at the scale of corresponding vortices (Sec. 2.2.3). A similar weakly three-dimensional effect that however appears in the core flow has been identified by [54] and [47] where the presence of *Hartmann* walls led almost two-dimensional vortices assume a *barrel* or *cigar* shape. The decrease in $\langle C'_2 \rangle$ also tells us that the flow in these structures is not only slower on the top plate than on the bottom plate, but also shifted in phase and frequency. In other words, the overall flow field $\mathbf{u}(x, y, z, t)$, even though mostly quasi two-dimensional, is not strictly of the form $\mathbf{u}_\perp(x, y, t)f(z)$ anymore as it exhibits strong three-dimensionality in its fluctuating part (Sec. 2.2.3).

It is noteworthy that for $\text{Ha} \geq 28.5$, Re_{3D}^0 is much larger than Re_V^0 so three-dimensionality appears well into turbulent flow regime V, whereas regimes I, II, III, IV are strictly quasi two-dimensional. Also, Re_{3D}^0 scales approximately as $\text{Ha}^{8/5}$, except for the lower values of Ha , $\text{Ha}=18$ and $\text{Ha}=13.5$. In these cases, the region of influence of the noise is extended as signals are weaker, so one can't tell whether the plateau $\langle C'_1 \rangle \simeq \langle C'_2 \rangle \simeq 1$ is reached for $\text{Re}^0 < \text{Re}_{3D}^0$. On the other hand, for these low values of Ha , higher values of $\text{Re}^0/\text{Ha}^{8/5}$ could be reached and a new regime appears at $\text{Re}^0 = \text{Re}_p^0$, where both $\langle C'_1 \rangle$ and $\langle C'_2 \rangle$ stop decreasing and stay constant for all $\text{Re}^0 > \text{Re}_p^0$ (see Fig. 3.11c and 3.11d). This behaviour can be due to residual viscous friction, that transports momentum along $\hat{\mathbf{e}}_z$. Furthermore, since the electric current is injected at the bottom plate, the motion near the top plate is mostly be induced by the motion near the bottom so they cannot be totally uncorrelated. However, whether the second plateau would extend when $\text{Re}^0 \rightarrow \infty$ can not be answered here.

Lastly one should mention that [28]'s numerical simulations also show the appearance of *Ekman* pumping because of local fluid rotation just above the *Hartmann* layer (Sec. 1.2.3). Figs. 3.5 (right column) illustrate that the related velocity component $u_z(x, y)$ is larger where horizontal velocity gradients are important as strong fluid sources and sinks appear in the core flow. It should be stressed that values of $u_z(x, y)$ could not be measured experimentally as it requires difficult bulk measurements which were not performed in the frame of this work.

3.6. Hartmann layer friction

The results presented in Sec. 3.2 show that the flow changes completely in nature and intensity at the onset of regime "V" where $\text{Re}_V^0 = \text{Re}^0$. This indicates a sudden reallocation of energy which can not be related to the appearance of three-dimensionality in the core flow at Re_{3D}^0 since $\text{Re}_{3D}^0 > \text{Re}_V^0$ (Figs. 3.1, 3.11). It may however indicate a variation in the *Hartmann* layer friction which could indeed occur when the flow inside the *Hartmann* layer changes from a laminar into a turbulent state (Sec. 1.2.2). In order to further check this property we use thereafter in this section elements in the spirit of [45]'s experimental investigation on the destabilisation of the *Hartmann* layer.

Our experiment is not made for flow measurements within the very thin *Hartmann* layer nor for a global measurement of the dissipation as obtained in the experiment of [45]. We can however obtain a rough measure of the fraction of the injected energy that is

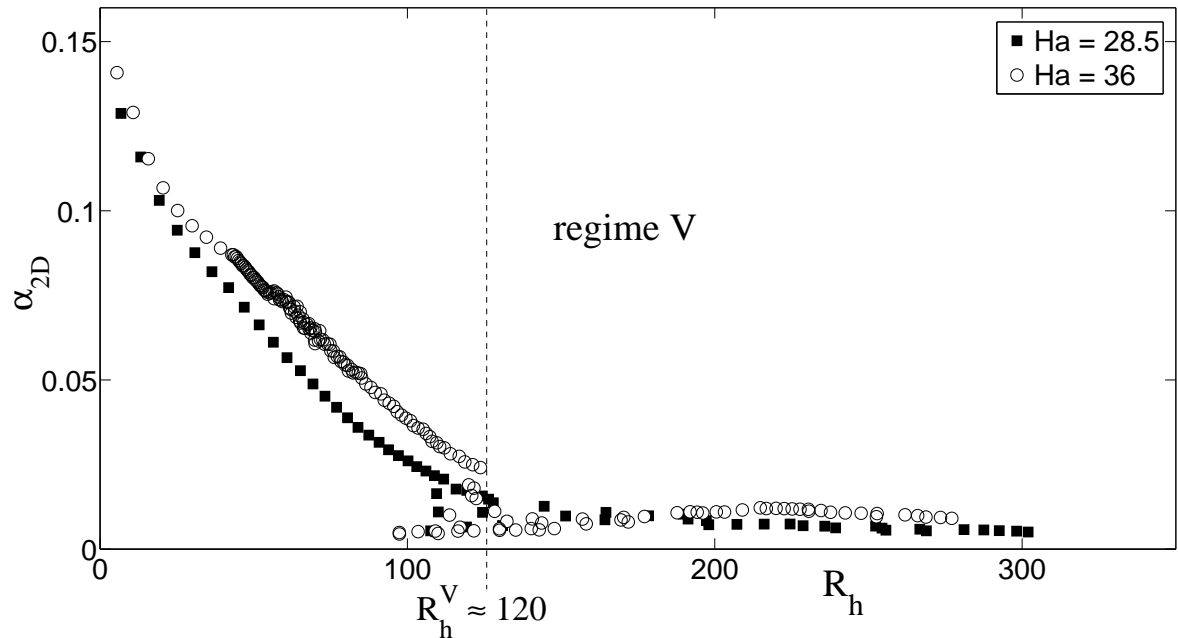


Figure 3.12.: $\alpha_{2D} = (\tilde{u}_x^M/U_0)^2$ vs. $R_h = \tilde{u}_x^M(\delta/\nu)$ for $\text{Ha} = 28.5$ and $\text{Ha} = 36$. Note that \tilde{u}_x^M and R_h drops strongly at the onset of regime "V" and increases again within regime "V".

passed on to the almost quasi two-dimensional flow for $\text{Ha} \geq 28.5$ by monitoring the evolution of $\alpha_{2D} = (\tilde{u}_x^M/U_0)^2$ vs. the Reynolds number $R_h = \tilde{u}_x^M(\delta/\nu)$ (recall that \tilde{u}_x^M is the maximum velocity in the profile along the diameter $y = 0$ (Fig. 3.2a)). In this regard α_{2D} is analogous to the friction factor F defined in [45] in the sense that it represents a ratio between a velocity built on the forcing and a measured velocity (here \tilde{u}_x^M). Also, as in [45], R_h is built on the *Hartmann* layer thickness as well as on a velocity derived from measurements of electric potentials and it controls the transition from a laminar to

a turbulent *Hartmann* layer. [45] however measure their voltage across the whole channel which gives them an average flow velocity, whereas our measurement corresponds to the maximum velocity in the driving jet along $\hat{\mathbf{e}}_x$. But in a sense, [45]'s and our R_h reflect the same physics, except that ours is local while [45]'s is global.

The idea of using α_{2D} is to show that the energy not transmitted to $(\tilde{u}_x^M)^2$ is either dissipated or transmitted to the residual three-dimensional part of the otherwise mostly quasi-two-dimensional flow. In short, a change in the *Hartmann* friction should reflect on the evolution of α_{2D} .

Figure 3.12 presents the evolution of α_{2D} vs. R_h for $Ha = 28.5$ and $Ha = 36$. For R_h lower than the critical value $R_h^V \simeq 120$ where the transition to flow regime "V" occurs, α_{2D} decreases almost linearly with R_h . Since the flow is close to quasi two-dimensionality in this regime, this essentially reflects joule dissipation in the *Hartmann* layers (or *Hartmann* layer friction). For $R_h > R_h^c = R_h^V$, α_{2D} suddenly drops. Here, the flow is still close to quasi two-dimensionality as $Re^0 < Re^{3D}$ (see Fig. 3.11). This suggests that the extra dissipation might come from a brutal change in the *Hartmann* layer friction, triggered by a transition from a laminar to a turbulent *Hartmann* layer. It may certainly be objected that the critical value $R_h^c \simeq 120$ is well below $R_h^c \simeq 380$ found in recent experimental ([45]) and numerical ([33]) studies on rectangular duct flows. This however might be related to the fact that local fluid rotation $\omega_z \mathbf{e}_z$ present above the boundary layer give the latter the properties of a *Hartmann-Boedwadt* layer which is indeed much less stable than a simple *Hartmann* layer as in [45, 33] (Sec. 1.2.2). Furthermore, our forcing mechanism is not the same as in [45] and therefore triggers a different flow. While the flow in [45]'s experiment is expected to be steady when the *Hartmann* layer destabilises, the flow in the present work, although still close to quasi two-dimensionality, is already strongly turbulent, because of instabilities generated in the side layers (see Sec. 3.2).

For $R_h \gg R_h^V$, α_{2D} decreases almost linearly with R_h but with a gentler slope than at low R_h (Fig. 3.12). For these values of R_h , $Re^0 > Re_{3D}^0$ so three-dimensional perturbations are also present that generate some additional Joule dissipation in the core flow on the top because of the dissipation in the turbulent *Hartmann* layer.

3.7. Conclusion

We have performed an experiment where a vortex pair confined by a circular wall was created by injecting electric current into a thin layer of liquid metal perpendicular to an homogeneous magnetic field \mathbf{B} . Such a flow is known to be almost quasi two-dimensional as physical quantities hardly vary along the field lines, except in the thin *Hartmann* boundary layers at the walls perpendicular to the field \mathbf{B} (see [64, 54]). Electric potential measurements at these walls have been used to determine part of the mostly two-dimensional flow field outside the *Hartmann* layers. Flow visualisations provided by [28]’s numerical simulations based on the shallow water model of [54] and performed for parameters similar to those in the experiments helped us to interpret different regimes spanned by the system when the electric current is increased. It was shown that the system undergoes a transition to quasi-2D turbulence through a sequence of supercritical bifurcations that [28] found to bear important similarities to those observed in the wake of a circular cylinder ([15]). Firstly, two recirculating regions appear behind the initial vortex pair as the boundary layer on the circular wall separates in two symmetric points (regime ”II”). Secondly the separated boundary layer becomes unstable and vortices shed and are sucked into the jet between these initial vortices (regime ”III”). When the forcing Re^0 is increased, the flow quickly changes into the chaotic regime ”IV”, as the shed vortices are re-injected into the main flow making the latter more unstable. Although flow characteristics in the cylinderwake are similar at the onset of regime ”IV”, [28] found that Re^0 spans a much larger interval in the previous regime ”III” compared to the one for the flow inside cylindrical container. Further insight into the analogy between these two systems could be obtained by investigating their properties as dynamical systems. Such a task was undertaken by [40] who has identified a clear scenario for the transition to turbulence of a single vortex in a square box from two-dimensional DNS. It is worth mentioning that the frequency spectra and dynamical behaviour found in the present study strongly resembles that found in theirs.

At higher injected electric current we have identified another transition in the quasi two-dimensional flow patterns where the velocity profile along the centre diameter becomes almost symmetric (regime ”V”). This regime was beyond the validity range of [54]’ numerical model so [28] could not provide exact flow patterns. Experimentally we noticed, however, a drastic drop at $Re_0 = Re_0^V$ exactly, in the slope of $\alpha_{2D} = (\tilde{u}_x^M/U_0)^2$ vs R_h , R_h being the Reynolds number based on the thickness of the *Hartmann* layer, that points to a likely transition to turbulence in this region.

Finally, we have checked the two-dimensionality of the system by calculating correlations between electric potential gradients measured on the same magnetic field line, on the top and bottom *Hartmann* walls enclosing the fluid layer. It turns out that for $Ha \geq 28.5$ the main flow is very close to quasi two-dimensionality in all investigated regimes as correla-

tions are nearly unity. This justifies interpreting electric potential gradients measured at the walls as velocities just outside the *Hartmann* layer according to (2.4). When these correlations are based on the flow fluctuations only, a sudden decrease appears well into regime "V" which we could show is due to both flow structures subject to differential rotation along the field \mathbf{B} , but still extending from the bottom to the top *Hartmann* wall (*weak* three-dimensionality), and flow structures that are disrupted across the fluid layer height (*strong* three-dimensionality) . This provides the first evidence of a transition between quasi two-dimensionality and three-dimensionality in forced, wall-bounded liquid metal MHD flows. Since this transition occurs well into regime V for $\text{Ha} \geq 28.5$, this also allows us to be certain that regimes "I", "II", "III" and "IV" are strictly quasi two-dimensional and reflect two-dimensional dynamics. Clearly though, experiments performed in our second experiment refine our understanding of such a flow transition mechanism as it is particularly designed to study the appearance of three-dimensional in wall-bounded MHD flows (Sec. 2.5 and Chap. 4).

Chapter 4

Experiment on the appearance of
three-dimensionality

4. Experiment on the appearance of three-dimensionality

In this chapter we single out the mechanism that explains the appearance of three-dimensionality in wall bounded magnetohydrodynamic (MHD) flows where the magnetic *Reynolds* number Rm is smaller than unity (Sec. 1.1). The results that we present here are obtained from measurements on the experiment described in Sec. 2.5. It should further be noted that the main content of this chapter is published in [29].

4.1. Introduction

Magnetohydrodynamic (MHD) flows intrinsically tend to two-dimensionality. They share this feature with stratified flows and rotating flows such as those which appear in atmospheres and oceans. The mechanisms responsible for this two-dimensionalisation are fairly well understood. In stratified flows, the relaxation of iso-density surfaces generates waves that transport momentum across them [50]. This role is played by inertial waves in rotating flows [22]. In MHD flows where the flow of an electrically conducting fluids is subject to a magnetic field, the tendency to two-dimensionalisation along the field lines results from the effect of the *Lorentz* force (Sec. 1.2.1). When this effect is dominant, flows confined between walls can become quasi two-dimensional, as boundary layers still develop along the walls. These boundary layers are called *Hartmann* layers in MHD, sometimes also *Hartmann-Bodewdt* (or *Hartmann-Ekman*) if the fluid rotates above the boundary layer (Sec. 1.2.2).

How three-dimensionality appears in such flows is however much less understood, although crucial since it determines both turbulent and transport properties of these flows. Examples range from the dynamics of oceans and atmospheres which are stratified and rotating, to liquid metal heat exchangers and the casting of liquid metals (MHD). In rotating and in MHD flows, some weak three-dimensionality is known to be induced by local rotation in the bulk of the flow generating *Ekman* recirculations (Sec. 1.2.3). These recirculations leads to velocity variations along the rotation direction of the magnetic field [2, 54, 62]. In

MHD, [64]’s heuristic theory also suggested that small scale vortices should disrupt into strongly three-dimensional ones under the effect of inertia (Sec. 1.3.2). Recent numerical simulations of ideal strictly two-dimensional MHD flows without *Hartmann* walls have indeed shown that strong three-dimensionality appeared brutally when three-dimensional perturbations became unstable, and sometimes led to two-dimensional/ three-dimensional intermittency [74, 71]. In wall-bounded MHD flows however, the question when and under which form (weak/ strong) three-dimensionality appears has remained unsolved, ever since it was raised in the 60’s when the anisotropic properties of these flows started to be systematically investigated [39]. In this chapter we bring an experimental answer to it by analysing square arrays of vortices rotating along a strong magnetic field in a cubic container, in the spirit of [62]’s experiment.

Thereafter in Sec. 4.2 we firstly present flow phase diagrams and related flow states in steady and slightly unsteady flow regimes. And secondly, we explain when and how three-dimensional inertial forces in these flow regimes induce a weak (differential rotation) and strong (disruption) form of three-dimensionality in individual flow structures. The appearance of weak and strong three-dimensionality in chaotic/turbulent flow regimes is singled out in Sec. 4.3 and refined in Sec. 4.4 where we give an important law that describes quantitatively how inertial effects select strongly three-dimensional flow fluctuations from the flow related frequency spectrum.

Lastly we shall remind the reader of our experimental setup described in Sec. 2.5. The experiment features a liquid metal filled cubic container of inner measure $L = 0.1$ subject to the constant magnetic field $B_0 \mathbf{e}_z$. The flow is generated by injecting constant electric current I from one *Hartmann* wall, through either $n = 100$ or $n = 16$ electrodes, arranged in a 10×10 or 4×4 square lattice of step $L_i = 0.01\text{m}$ or $L_i = 0.03\text{m}$. The electrodes are alternately connected to either pol of a DC power supply. For low electric currents I and high magnetic field strengths B_0 this generates a base flow of respectively 100 or 16 cylindrical, quasi two-dimensional vortices of size $L_i \times L$ rotating alternatively along \mathbf{e}_z in a square array. The flow is controlled by the amount of the injected current I and the strength B_0 of the imposed magnetic field, respectively measured non-dimensionally by the *Reynolds* number $\text{Re}^0 = 4I/(n\pi\nu(\sigma\rho\nu)^{1/2})$ with $\text{Re}^0 \in [0, 1.3 \times 10^5]$ and the *Hartmann* number $\text{Ha} = LB_0[\sigma/(\rho\nu)]^{1/2}$ with $\text{Ha} \in [364, 18220]$. Different flow states are identified from local measurements of the electric potential $\phi_w(t)$, on two identical sets of 196 electric potential probes embedded in top and bottom *Hartmann* wall respectively. The presence of three-dimensionality is determined by comparing these sets.

4.2. Observed flow states

In this section we report flow states that appear when the flow forcing measured non-dimensionally by the *Reynolds* number Re^0 is increased. For all *Hartmann* numbers Ha and lattice spacings (or vortex injection scale) $L_i \in \{0.01, 0.03\}\text{m}$, the flow follows the same sequence of regimes: at low Re^0 it is made of an array of steady vortices that follows the geometry of the forcing. When Re^0 reaches a critical value of $Re^0(Ha)$ the flow becomes unsteady. Steady and unsteady flow regimes in the (Ha, Re^0) parameter space are reported thereafter for lattice spacings $L_i = 0.01\text{m}$ and $L_i = 0.03\text{m}$ on the phase diagrams in Figs. 4.1, 4.5 and Fig. 4.8 respectively. In both figures a "high" Ha and a "low" Ha range clearly stand out. The "high" Ha range corresponds to regimes where the transition from steady to unsteady flow states is controlled by the same parameter $R_h^0 = Re^0/Ha$ for all cases of Ha , while the "low" Ha range comprises regimes where values of R_h^0 depend on Ha . Lastly, we would like to remark that we also observed some unexpected instability behaviour in the region of very high Ha for the larger injection scale $L_i = 0.03\text{m}$.

4.2.1. Flow states forced through 10×10 electrodes ($L_i = 0.01\text{m}$)

Thereafter we present flow states observed around the transition to unsteadiness for $Ha \gtrsim 7500$ and $Ha < 7500$, respectively denoted as "high" Ha and "low" Ha range in Fig. 4.1. Related contours of iso- ϕ_w (iso-electric-potential) are visualised in the centre region of both *Hartmann* walls in an area of $30 \times 30\text{mm}^2$ spanned by $x \in [30, 60]\text{mm}$ and $y \in [40, 70]\text{mm}$ (see area enclosed by the green, doted line in Fig. 2.22). In this region, electric potential ϕ_w is measured locally on a dense grid of 121 electric potential probes. Finally note that critical *Reynolds* numbers Re_I^0 , Re_{II}^0 defined thereafter are not related to those used in Sec. 3.2.

Flow states observed for high Ha ($Ha \gtrsim 7500$)

In the steady regime $Re^0 < Re_I^0(Ha)$, contours of iso- ϕ_w lines at the bottom and top *Hartmann* walls represent the expected square array of steady alternately rotating vortices. Each vortex has the transverse length scale $l_\perp \simeq L_i = 0.01\text{m}$ and parallel length scale $l_\parallel \simeq L = 0.1\text{m}$ as can be seen from Fig. 4.1a. Since iso- ϕ_w patterns in Fig. 4.1a are barely distinguishable from one another it indicates that the flow is very close to quasi two-dimensionality. This is also confirmed by time-averaged profiles of local electric potential gradients $\langle \partial_y \phi_w(x, y/L = 0.5, 0, t) \rangle_t$ and $\langle \partial_y \phi_w(x, y/L = 0.5, z/L = 1, t) \rangle_t$ obtained along the center line $y/L = 0.5$ at the bottom and top wall respectively (see black dashed line in Fig. 4.1a). These profiles are almost identical as can be seen from Fig. 4.4a. Since quasi two-dimensionality implies that relations (2.4) are valid, profiles of $\langle \partial_y \phi_w \rangle_t$ in Fig. 4.4a

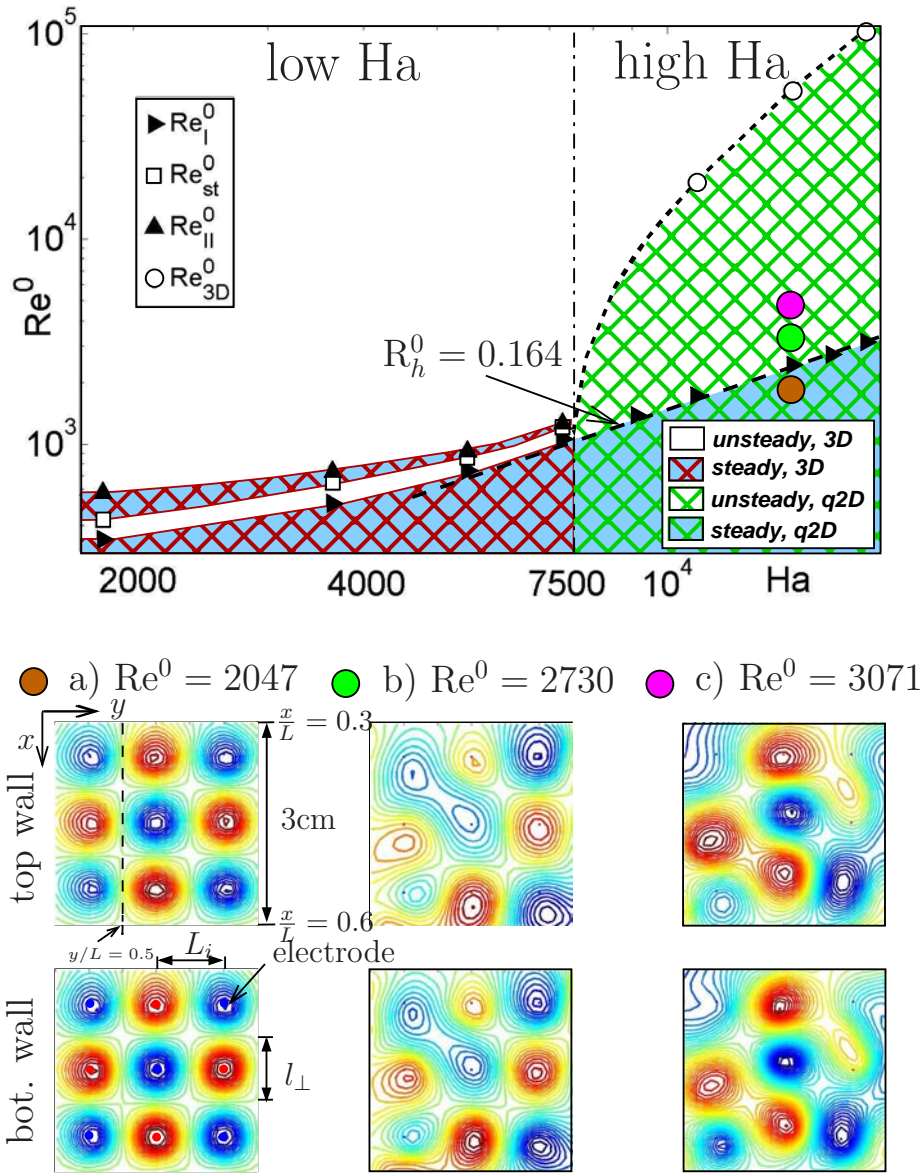


Figure 4.1.: Phase diagram for flows forced through an array of 10×10 injection electrodes which corresponds to the injection scale $L_i = 0.01\text{m}$. It gives critical *Reynolds* numbers $\text{Re}_I^0(\text{Ha})$, $\text{Re}_{st}^0(\text{Ha})$, $\text{Re}_{II}^0(\text{Ha})$ and $\text{Re}_{3D}^0(\text{Ha})$ vs. Ha and shows snapshots of iso- ϕ_w lines, obtained at the centre of bottom and top Hartmann walls (area enclosed by green dashed line in Fig. 2.22). It should be emphasized that Re_{3D}^0 represents the non-dimensional injected electric current at the transition between nearly quasi two-dimensional and strongly three-dimensional, turbulent flow regimes (*resp.* regime I and regime II in Fig.4.11). The snapshots show iso- ϕ_w contours for $\text{Ha}= 14580$, representing quasi-two-dimensional flow regimes: a) steady flow regimes ($\text{Re}^0 < \text{Re}_I^0$), b) flow regimes at the transition to unsteadiness ($\text{Re}^0 \gtrsim \text{Re}_I^0$), c) chaotic flow regimes ($\text{Re}^0 > \text{Re}_I^0$). Note that blue and red colours indicate the vortex rotation in clockwise and anti-clockwise direction respectively.

could be also interpreted as velocity profiles just outside the *Hartmann* layer. The profiles show that the absolute value of the velocity along \mathbf{e}_x would be highest in the centre between the axes of two counterrotating vortices.

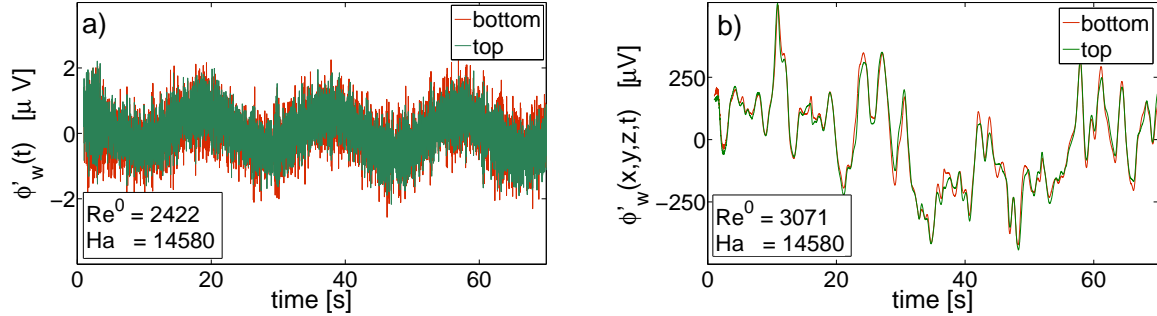


Figure 4.2.: Time evolution of electric potential fluctuations $\phi'_w(t) = \phi_w(t) - \langle \phi_w(t) \rangle_t$ obtained at $(x/L = 0.5875, y/L = 0.5125)$ at both bottom and top *Hartmann* wall for $\text{Ha} = 14580$. (a) periodic oscillation at the transition to unsteadiness, $\text{Re}_I^0 = \text{Re}^0 = 2422$. (b) chaotic/turbulent flow regime for $\text{Re}^0 = 3071 > \text{Re}_I^0$. Note that signals taken at other locations yield similar results.

For forcing $\text{Re}^0 \gtrsim \text{Re}_I^0(\text{Ha})$ this flow becomes unsteady. Accordingly, a periodic oscillation appears in the time-dependent signal of recorded electric potentials $\phi_w(t)$ (Fig. 4.2a). This results into a fundamental frequency f in the frequency spectrum that scales with Ha according to $f \sim \text{Ha}^{1/2}$ (Fig. 4.3).

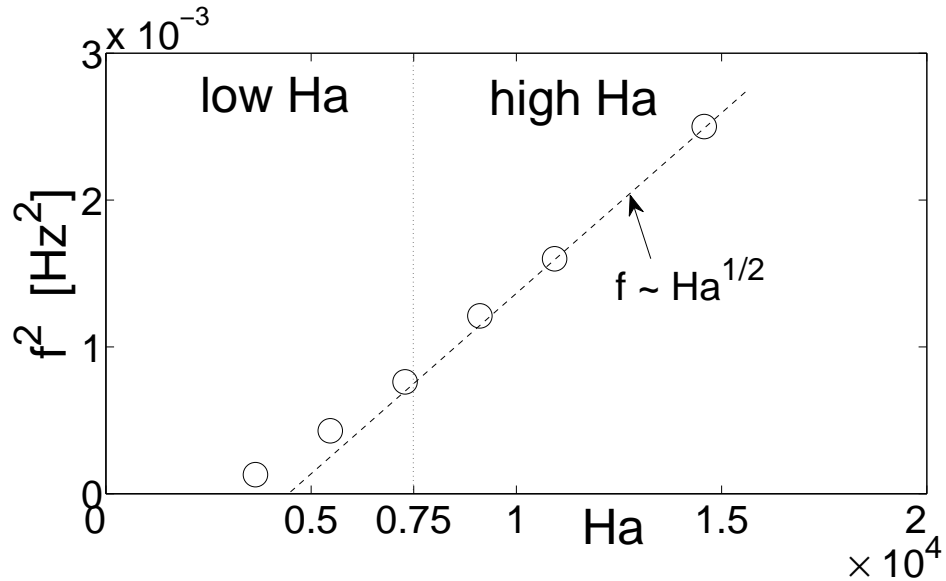


Figure 4.3.: *Hartmann* number Ha vs. fundamental frequency f that appears at the destabilisation of the 10×10 vortex array at Re_I^0 . In the high Ha region ($\text{Ha} \gtrsim 7500$) f increases according to the law $f \sim \text{Ha}^{1/2}$.

These oscillations correspond to the connection and disconnection of iso- ϕ lines from adjacent co-rotating vortices which points to the periodic formation of quasi two-dimensional vortex pairs (Fig. 4.1b). [62] experimentally and [69] analytically show that the vortex pairing process is indeed the main mechanism that appears when an initial steady, square array of circular vortices destabilises. For higher forcing $Re^0 > Re_I^0$, the flow be-

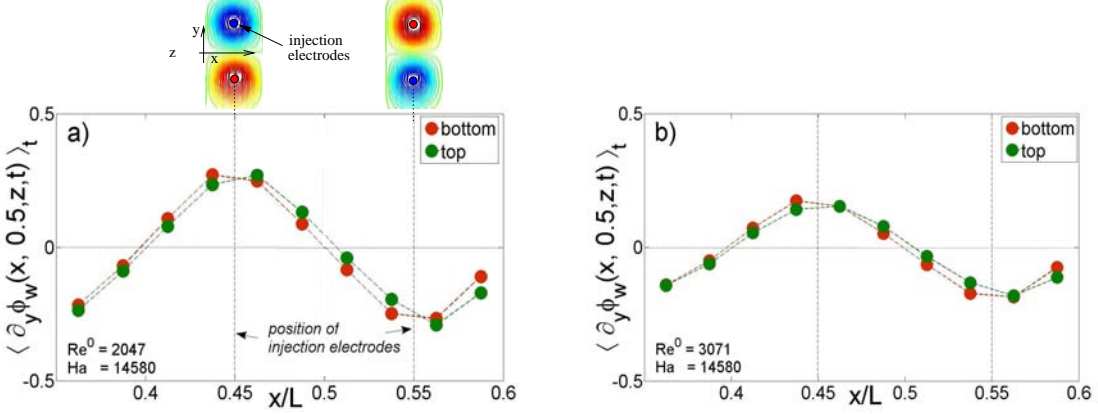


Figure 4.4.: Time averaged profiles of electric potential gradients $\langle \partial_y \phi_w(x, 0.5, 0) \rangle_t$ and $\langle \partial_y \phi_w(x, 0.5, L) \rangle_t$ along the centerline $y/L = 0.5$ (see Fig. 4.1a) and normalized by $U_0 B_0$, obtained at the bottom and top Hartmann wall respectively. Left: steady flow regime $Re^0 = 2047$. Right: chaotic flow regime $Re^0 = 3071$.

comes chaotic, then turbulent (Fig. 4.2b)), but the contours of iso- ϕ_w as well as profiles of $\langle \partial_y \phi_w(t) \rangle_t$ at bottom and top walls remain almost identical (Figs. 4.1c, 4.4b), still indicating quasi-two-dimensionality.

The physics in the high Ha range is therefore dominated by the effect of the *Lorentz* force. It makes individual vortices of typical transverse size $l_\perp \simeq L_i$ over the time $\tau_{2D}(L_i) = \rho/(\sigma B_0^2)(L/L_i)^2$ quasi two-dimensional before three-dimensional inertial effects can affect them (related time scales τ_{2D} are given in Table 2.4). In this regime, almost no electric current density remains in the bulk so that the flow experiences most of its dissipation due to linear friction exerted by either *Hartmann* layers over the *Hartmann* damping time $\tau_H = L^2/(2\nu Ha)$ (Sec. 1.2.3 and Table 2.4 for related time scales τ_H). This also implies that the dynamics of the flow in the high Ha range should depend only on one non-dimensional control parameter R_h^0 which is defined according to (1.69) as:

$$R_h^0 = \frac{Re_I^0(Ha)}{Ha} = 2 \frac{\tau_H}{\tau_{U_0}(L_i)} \left(\frac{L_i}{L} \right)^2. \quad \text{with} \quad \tau_{U_0}^{-1}(L_i) = \frac{U_0}{L_i} = 2 \frac{2I}{n\pi\sqrt{\sigma\rho\nu}L_i^2} \quad (4.1)$$

That R_h^0 does control the flow dynamics in the high Ha range is confirmed as we found that the 10×10 quasi two-dimensional vortex array destabilised when it reached the

critical value $R_h^0 = \text{Re}_I^0(\text{Ha})/\text{Ha} = 0.164$ (Fig. 4.1). In fact, R_h^0 in (4.1) is a local control parameter since it is built on the amount of electric current locally injected per electrode $2I/n$. It describes therefore the flow dynamics of a local quasi two-dimensional vortex created above the corresponding injection electrode. R_h^0 does however not explain whether the walls parallel to the imposed field $B_0\mathbf{e}_z$ have an influence on the vortex dynamics and its destabilisation or not.

In Sommeria's experiment on the destabilisation of a 6×6 quasi-two-dimensional vortex array though ([62]), the corresponding stability control parameter R_h^S is built on the total amount of the electric current I and describes the global flow dynamic. This also implies that the influence of the walls parallel to the magnetic field $B_0\mathbf{e}_z$ should reflect on the value of R_h^S . Applied to the geometry of our experiment R_h^S is defined as:

$$R_h^S = \left(R_h^0 \frac{n\pi}{16} \right)^{1/2} \quad (4.2)$$

[62] found that his steady 6×6 array of vortices, each with dimension $l_\perp \simeq l_\parallel \simeq 0.02\text{m}$ destabilised when R_h^S reaches the critical value $R_h^S = 1.78$. Interestingly, even though the vortices in our 10×10 array have with $l_\perp \simeq 0.01\text{m}$ and $l_\parallel \simeq 0.1\text{m}$ different dimensions we found that they destabilise at $R_h^S = 1.8$, very close to the value $R_h^S = 1.78$ for [62]'s 6×6 vortex array. Since both critical values are apparently almost identical one might think that the presence of the side walls affects the destabilisation of the 6×6 and 10×10 vortex array, if at all, similarly. Also important to notice is that thanks to comparable sets of measurements on both *Hartmann* walls, we have been able to verify [62]'s assumption of quasi-two-dimensionality in both steady and unsteady flow regimes.

Finally we should remark that no hysteresis has been observed around the transition at $\text{Re}^0 = \text{Re}_I^0$. However, in contrary to our small experiment we can not clearly conclude to a supercritical nature of the instability (Sec. 3.4). The reason is that the strongly chaotic behaviour for slightly higher forcing $\text{Re}^0 > \text{Re}_I^0$ precluded us from tracking the evolution of the amplitude of the first unstable mode with base frequency f versus the critical parameter $\text{Re}^0/\text{Re}_I^0 - 1$.

Flow states observed for intermediate Ha ($3500 < \text{Ha} < 7500$)

Flow states observed around the destabilisation of the 10×10 vortex array for intermediate Ha are significantly different to those observed for high Ha . In this Ha range, *Lorentz* forces are weaker so that vortices generated in the vicinity of the bottom *Hartmann* wall need longer times $\tau_{2D}(L_i)$ to extend up to the top *Hartmann* wall (Table 2.4). This implies that three-dimensional inertial effects become more important.

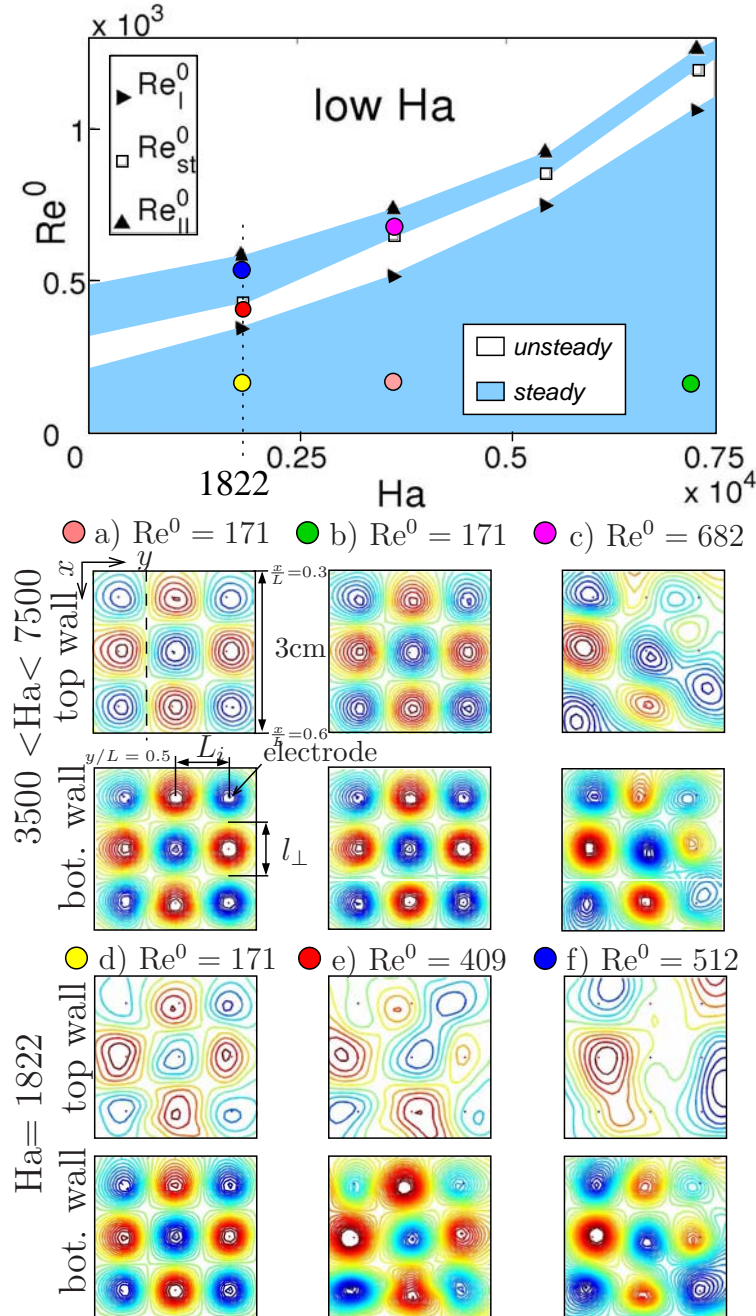


Figure 4.5.: Top: magnification of the low Ha region of the stability diagram in Fig. 4.1. Bottom: related snapshots of iso- ϕ_w contours for $3500 < Ha < 7500$ and $Ha=1822$. Weak three-dimensionality under the form of differential rotation along the axis of individual vortices is present for all Ha and in all regimes separated by critical parameter Re_I^0 , Re_{st}^0 and Re_{II}^0 . Also strong three-dimensionality appears for $Ha=1822$: firstly, under the form of partial vortex pairing for $Re^0 \gtrsim Re_I^0$ and, secondly, under the form of steady *Giraffe*-like vortices for $Re_{st}^0 < Re^0 < Re_{II}^0$ (Sec. 4.2.1).

In the steady regime where $\text{Re}^0 < \text{Re}_I^0(\text{Ha})$, both bottom and top contours of iso- ϕ_w still exhibit the topology of a square lattice of vortices. The intensity of ϕ_w and the flow however, is significantly lower in the vicinity of the top wall (Fig. 4.5a,b). This can be also seen from corresponding profiles of electric potential gradients $\langle \partial_y \phi_w(t) \rangle_t$ in Figs. 4.6a,b. In other words, weak three-dimensionality under the form of differential rotation at the scale of each vortex is present. Weak in this sense implies too that the structures that are affected by this type of three-dimensionality still extend from the bottom to the top *Hartmann* wall, without disruption of iso- ϕ surfaces in the core flow along the field lines $B_0 \mathbf{e}_z$ (Sec. 2.2.3). Since differential rotation is a direct consequence of more significant three-

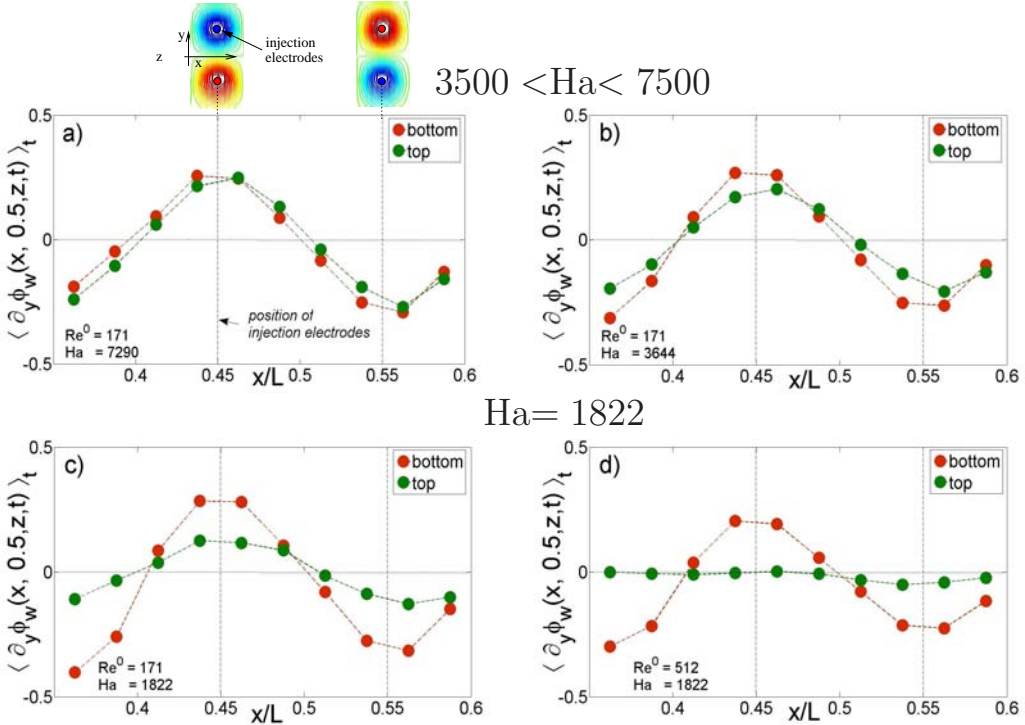


Figure 4.6.: Time averaged profiles of electric potential gradients $\langle \partial_y \phi_w(t) \rangle_t$ along the centerline $x, y/L = 0.5$ obtained on both top and bottom *Hartmann* wall (see also Fig. 4.5a) and normalized by $U_0 B_0$, obtained at the bottom and top *Hartmann* wall respectively. Top: steady flow regimes where $\text{Re}^0 = 171$, for a) $\text{Ha} = 7290$ and b) $\text{Ha} = 3644$. Bottom: steady flow regimes where $\text{Ha} = 1822$, for c) $\text{Re}^0 = 171$ and d) $\text{Re}^0 = 512$.

dimensional inertial effects in the intermediate Ha range one understands intuitively that it appears progressively from high to lower values of Ha (Figs. 4.5a,b,d and Figs. 4.6a,b,c). Weak three-dimensionality that appears under the form of differential rotation in individual vortices has been also observed in our small experiment where it is reflected in the stronger decrease of the correlation factor $\langle C'_2 \rangle$ compared to $\langle C'_1 \rangle$ for forcing $\text{Re}^0 > \text{Re}_{3D}^0$ (Sec. 3.5).

In this low Ha range, the transition to unsteadiness at $\text{Re}^0 = \text{Re}_I^0(\text{Ha})$ is no longer con-

trolled by $R_h^0 = 2\tau_H/\tau_{U_0}(L_i)(L_i/L)^2 = 0.164$, indicating a non-asymptotic regime that is less dominated by the *Lorentz* force (Fig. 4.1). Vortex pairing however is still observable for $\text{Re}^0 \gtrsim \text{Re}_I^0(\text{Ha})$, and flows near bottom and top walls remain topologically identical at all time, even though some differential rotation is present. As for regimes where $\text{Ha} \gtrsim 7500$, the first unstable mode is periodic, but its frequency f no longer scales with $\text{Ha}^{1/2}$ (Fig. 4.3).

For $\text{Re}^0 > \text{Re}_I^0(\text{Ha})$, the flow becomes more chaotic, but, remarkably, stabilises again when $\text{Re}^0 = \text{Re}_{st}^0(\text{Ha})$. In this regime, iso- ϕ_w lines in Fig. 4.5c show paired vortices at bottom and top walls, although the flow is less intense near the latter, than near the former. In short, this second steady regime is characterized by the presence of weakly 3D, steady vortex pairs. This flow destabilises again at $\text{Re}^0 \gtrsim \text{Re}_{II}^0(\text{Ha}) > \text{Re}_{st}^0(\text{Ha})$ where the vortex pairing process resumes, but more erratically. Related time series of iso- ϕ_w contours obtained at the bottom and top *Hartmann* wall show that their topology remains the same, however the merging and disconnecting of iso- ϕ lines between co-rotating vortices is more irregular.

"Giraffe"-like flow structures for lowest Ha= 1822

In the previous subsection it has been shown how inertial effects induce three-dimensionality in flows that are less dominated by the effect of the *Lorentz* force. It is therefore not surprising that three-dimensionality manifests itself most spectacularly in the case of lowest *Hartmann* number studied here, $\text{Ha}= 1822$, creating yet another set of remarkable, novel flow structures.

In steady flow regimes where $\text{Re}^0 < \text{Re}_I^0(\text{Ha})$ the flow is still made of a square array of 10×10 vortices. Each vortex is subject to weak three-dimensionality in the form of differential rotation, as observed in flow regimes where $3500 < \text{Ha} < 7500$. The vortex rotation rate near the top *Hartmann* wall however is even less intense, indicating stronger differential rotation in individual vortices (see Fig. 4.5d and Fig. 4.6c).

At the transition to the first unsteady regime $\text{Re}^0 = \text{Re}_I^0(\text{Ha})$ though, oscillations in the flow field are erratic, rather than periodic as for cases $\text{Ha} > 3500$. Furthermore, these fluctuations are stronger near the top *Hartmann* wall than near the bottom *Hartmann* wall. Corresponding contours of iso- ϕ_w in Fig. 4.5e are topologically not equivalent anymore, indicating the appearance of strong three-dimensionality, on the top of weak-three dimensionality (Sec. 2.2.3). The iso- ϕ_w contours show that the vortex pairing process in this regime is indeed only apparent near the top *Hartmann* wall. This in turn indicates that the top-end of vortices merge, while their bottom ends remain disjoint and almost steady in the vicinity of the bottom *Hartmann* wall. In other words, strong three-dimensionality appears as partial vortex pairing along the magnetic field lines $B_0\mathbf{e}_z$. This also implies

that the horizontal velocity field is not of the form $\mathbf{u}_\perp(x, y)f(z)$ anymore (Sec. 2.2.3). Not surprising, strong three-dimensionality becomes even more blatant when Re^0 and therefore the effect of inertia is further increased. At $\text{Re}^0 = \text{Re}_{st}^0(\text{Ha})$ where the flow re-stabilises as for intermediate *Hartmann* numbers $3500 < \text{Ha} < 7500$, this results into remarkable, steady flow structures. These structures still display the mostly regular 10×10 iso- ϕ_w pattern at the bottom *Hartmann* wall, indicating the typical square array of alternately rotating vortices with transverse size $l_\perp \approx L_i$. Corresponding iso- ϕ_w lines on the top *Hartmann* wall show an almost regular pattern too, but related vortices are about twice as large ($l_\perp \approx 2L_i$) and arranged in a 5×5 array (Fig. 4.5f, recall again that contours of iso- ϕ_w are plotted in the centre region of both *Hartmann* walls covering an area of $30 \times 30\text{mm}^2$). Furthermore, these large vortices clearly rotate more slowly than the small ones in the vicinity of the bottom *Hartmann* wall, implying that the strongly three-dimensional flow structures between top and bottom *Hartmann* walls are subject to weak three-dimensionality too (Fig. 4.6d).

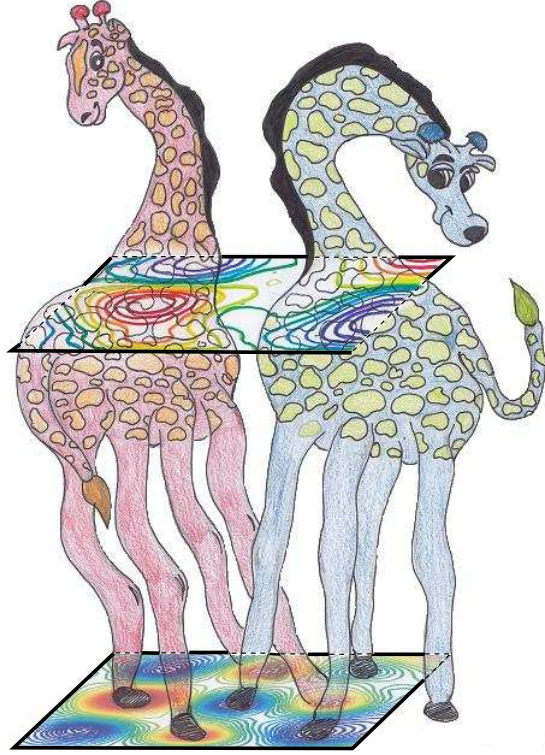


Figure 4.7.: Caricature of strongly three-dimensional and steady flow structures that appear for lowest values of Ha . The connection between the 10×10 vortex array and 4×4 vortex array obtained at the bottom and top *Hartmann* wall might be pictured as the appearance of *Giraffe*-like flow structures.

In order to be able to explain how the 10×10 vortex array connects to the 5×5 vortex array it would require the visualisation of the flow between top and bottom *Hartmann* wall. This however is not possible here so that we prefer to keep the picture of these steady, strongly three-dimensional flow structures rather simple for now, and even caricature-like

for amusement. This means that we term the connection between 10×10 and 5×5 vortex array as the formation of *Giraffe*-like vortices. Each of these *Giraffes* is "standing" on the bottom *Hartmann* wall with its feet "made" from sets of four, co-rotating vortices which connect to one single vortex in the vicinity of the top *Hartmann* wall forming the *Giraffe*'s corpus (Fig. 4.7).

At $\text{Re}^0 = \text{Re}_I^0(\text{Ha})$, this flow destabilises again resulting in periodic oscillations that quickly become chaotic at slightly higher forcing.

4.2.2. Flow states forced through 4×4 electrodes ($L_i = 0.03\text{m}$)

The flow states that undergoes the 4×4 vortex array are mostly similar to those of the 10×10 vortex array. Individual vortices in the 4×4 base flow however have a transverse size of $l_{\perp} \simeq L_i$ which is 3 times larger than in the 10×10 vortex array. Again, a region of low Ha and a region of high Ha clearly stands out, but this time for ranges of $\text{Ha} \lesssim 1450$ and $\text{Ha} \gtrsim 1450$ respectively. Furthermore, we encountered rather unexpected instability behaviour when $\text{Ha} \geq 3640$. Lastly one should notice that flow patterns presented thereafter are obtained from local electric potential measurements at top ($z = L$) and bottom ($z = 0$) *Hartmann* wall in an area of $60 \times 60\text{mm}^2$ spanned by $x \in [20, 80]\text{mm}$ and $y \in [20, 80]\text{mm}$ (area enclosed by the cyan, dotted line Fig. 2.22).

Flow states similar to the 10×10 forcing geometry for $\text{Ha} < 3640$

In this section we firstly describe the phase diagram of the 4×4 vortex base flow for the range $\text{Ha} < 3640$, where a high and low Ha region clearly stand out again (Fig. 4.8). And secondly, we point to similarities of related flow states to those that appear when the base flow is made of a 10×10 vortex array (Sec. 4.2.1). It should be noted that values of the critical parameter Re_I^0 used thereafter to distinguish between steady and unsteady flow regimes are different to those given in Sec. 4.2.1.

For $\text{Re}^0 < \text{Re}_I^0(\text{Ha})$ the flow is steady and contours of iso- ϕ_w obtained at the top and bottom *Hartmann* wall are topologically identical (Fig. 4.8a, b). They indicate a 4×4 array of alternatively rotating, almost quasi two-dimensional vortices, each with dimension $l_{\perp} \simeq L_i = 0.03\text{m}$ and $l_{\parallel} \simeq L$. In the region of low *Hartmann* numbers though, the flow is clearly less intense in the vicinity of the top *Hartmann* wall, thus indicating the presence of weak three-dimensionality that appears under the form of differential rotation in individual vortices (Fig. 4.8b). In fact, similar observations have been made in steady regimes when the flow is forced through the 10×10 electrode array (Sec. 4.2.1). The range of high Ha in Fig. 4.8 however extends to much smaller values of Ha than in the 10×10 case. This implies that the larger vortices in the 4×4 array are less prone to

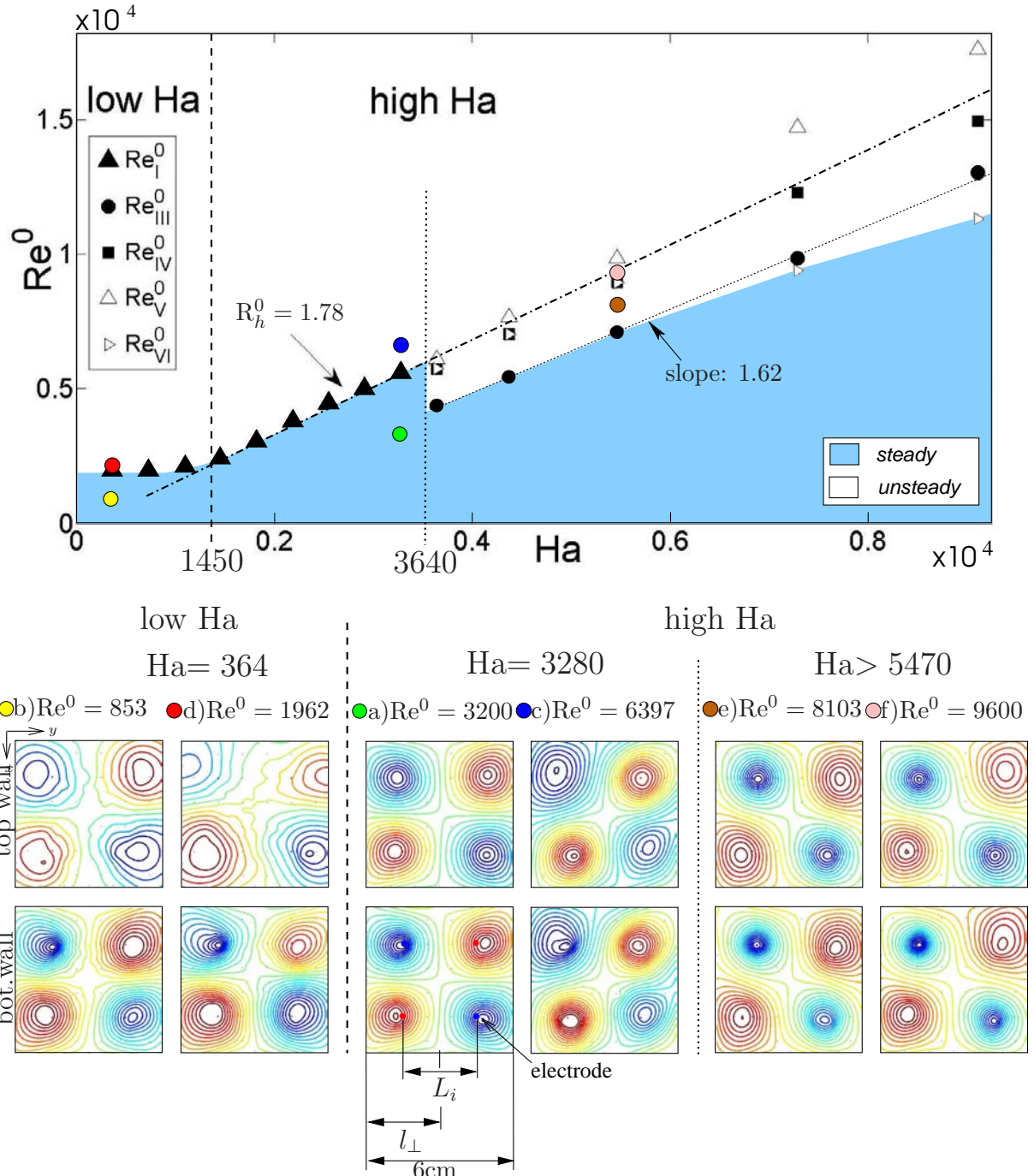


Figure 4.8.: Phase diagram for $L_i = 0.03\text{m}$ giving the critical *Reynolds* numbers $Re_I^0(\text{Ha})$, $Re_{III}^0(\text{Ha})$, $Re_{IV}^0(\text{Ha})$, $Re_V^0(\text{Ha})$ and $Re_{VI}^0(\text{Ha})$ vs. Ha and snapshots of iso- ϕ_w lines, obtained at the bottom and top *Hartmann* walls. Flow regimes in low and high Ha regions when $\text{Ha} < 3640$ are similar to those found for $L_i = 0.01\text{mm}$ (Fig. 4.1). The sudden change in the flow state for $\text{Ha} > 3640$ should be regarded with some reservation as the physical meaning of this behaviour is unclear. Note again that blue and red colours indicate the vortex rotation in clockwise and anti-clockwise direction respectively.

three-dimensional inertial effects.

The vortex array destabilises at the critical forcing $\text{Re}_I^0(\text{Ha})$ as a periodic oscillation of base frequency f_I appears in the spectrum of recorded electric potentials $\phi_w(x, y, z, t)$ (Fig. 4.8 and Fig. 4.9a). f_I varies with Ha , but we could not obtain a clear dependency like the $f \sim \text{Ha}^{1/2}$ law found for fundamental frequencies at the destabilisation of the 10×10 array of quasi two-dimensional vortices. Related time series of iso- ϕ_w contours however show periodic connection and disconnection of iso- ϕ_w lines in high Ha regimes ($1450 \leq \text{Ha} \leq 3640$). This points again to the formation of quasi two-dimensional vortex pairs (Fig. 4.8c, [62, 69]). The corresponding local control parameter $R_h^0 = \text{Re}_I^0(\text{Ha})/\text{Ha}$ has the value 1.78 (note that the local parameter $R_h^0 = 1.78$ found here should not be mistaken for the global parameter $R_h^S = 1.78$ given in Sec. 4.2.1 for the 10×10 vortex array). Since this value is about 10times larger than the control parameter $R_h = 0.164$ in the case of the 10×10 vortex array it indicates that the larger quasi two-dimensional vortices in the 4×4 array are more stable against two-dimensional inertial effects. Although less obvious, it seems that the parallel walls have a stabilising effect on these larger vortices too as the related global control parameter R_h^S (4.1) has the value 2.36 and is clearly greater than those found for an array of 6×6 and 10×10 quasi two-dimensional vortices ([62] and Sec. 4.2.1 respectively).

In the low Ha regime and for the lowest case $\text{Ha} = 364$ though, the destabilisation of the already weakly three-dimensional vortex array seem to be affected by strong three-dimensional inertial effects. Although less clear, one might think that contours of iso- ϕ_w obtained at both *Hartmann* walls are topologically not equivalent anymore (Fig. 4.8d). While bottom iso- ϕ_w contours still indicate the square array of 4×4 vortices, the contours obtained at the top seem to show paired vortices. In other words, we think that these observations again point to strong three-dimensionality in form of partial vortex pairing as observed for the 10×10 vortex array for $\text{Ha} = 1822$. The reason why this effect occurs for the 4×4 vortex array only at much lower $\text{Ha} = 364$ possibly relates to the scale-dependent *Lorentz* force which makes vortices with large l_\perp over a shorter time $\tau_{2D}(l_\perp)$ quasi two-dimensional than vortices with small l_\perp (1.40).

In Sec. 4.2.1 we have also demonstrated that three-dimensional inertial effects might be responsible for flow re-stabilisation and even can create steady, strongly three-dimensional *Giraffe*-like structures. Although neither of these interesting effects could be rediscovered in the low Ha range of the 4×4 vortex array it does not mean that they could not exist. It is rather possible that we have missed them since we did not increase the forcing Re^0 much above the critical value Re_I^0 . It would therefore be important to perform further measurements in this regard.

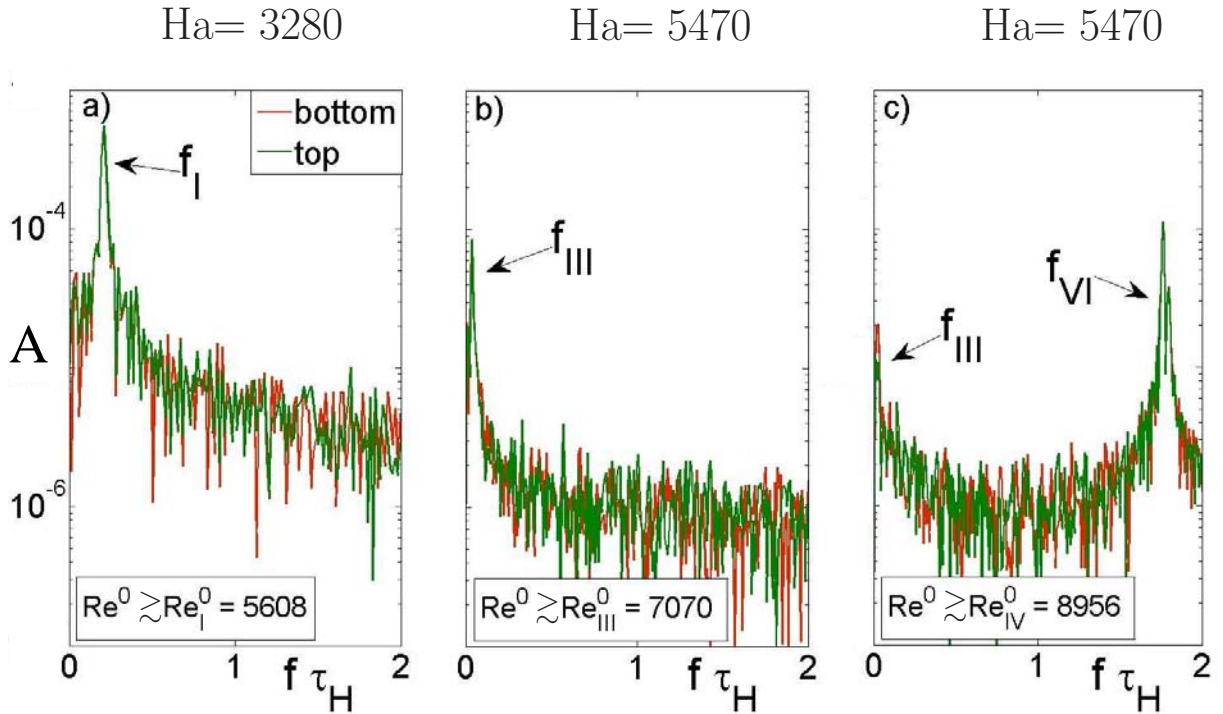


Figure 4.9.: Spectra of time-dependent electric potential $\phi_w(x, y, z, t)$ at parameters a) $Re^0 \gtrsim Re_I^0$ and $Ha = 3280$, b) $Re^0 \gtrsim Re_{III}^0$ and $Ha = 5470$, c) $Re^0 \gtrsim Re_{IV}^0$ and $Ha = 5470$. These spectra are obtained along the same magnetic field line $B_0\mathbf{e}_z$ at top and bottom Hartmann wall, on electric potential probes that are located near the centre of the walls (note that spectra obtained at other location yield qualitatively similar results). The amplitude A of oscillations with fundamental frequency f_I , f_{III} and f_{VI} is normalised by $Re^0\nu B_0 = 4\Gamma_0 B_0$ with $\Gamma_0 = I/(n\pi(\sigma\nu\rho)^{1/2})$ and $n = 16$. Again, the appearance of the fundamental frequencies f_{VI} for regimes where $Ha > 3640$ has to be regarded with reservation as the physical meaning is unclear. This observation requires further experimental validation.

Peculiar flow states for $Ha > 3640$

In the high Ha range $1450 < Ha < 3640$, the initially steady flow of 4×4 quasi two-dimensional vortices destabilises through periodic formation of vortex pairs at $R_h^0 = 1.78$. For even higher $Ha > 3640$ however, the phase diagram Fig. 4.8 changes abruptly and the overall picture becomes peculiar. Even if we are not able to give a clear physical interpretation related to these unexpected observations, we still present them, also pointing to the fact that they would need further, important experimental investigation.

Lastly, one should notice that indexes of critical values Re_{III}^0 , Re_{IV}^0 , Re_V^0 defined thereafter are not related to those used in Sec. 3.2 to distinguish between different flow regimes in the shallow cylindrical container.

For $Re^0 < (\min|Re_{III}^0, Re_{VI}^0|)$ the flow is steady (Fig. 4.8). Related contours of iso- ϕ_w

show the same topology at the top and bottom *Hartmann* wall as in steady regimes when $1450 < \text{Ha} < 3640$, thus indicating the 4×4 array of quasi two-dimensional vortices (Fig. 4.8a).

At $\text{Re}^0 \gtrsim \text{Re}_{III}^0(\text{Ha})$, periodic, quasi two-dimensional vortex pairing sets in (see Fig. 4.8 and related flow patterns in Fig. 4.8e). Accordingly, corresponding spectra of recorded electric potentials $\phi_w(x, y, z, t)$ exhibit a clear peak at fundamental frequency f_{III} (Fig. 4.9b). These observations are indeed similar to those that have been observed when the 4×4 vortex array destabilises at $\text{Re}_I^0(\text{Ha})$ for $1450 < \text{Ha} < 3640$. But, although $\text{Re}_{III}^0(\text{Ha})$ lays on a line with slope 1.62, not very different to the value 1.78 observed for $\text{Re}_I^0(\text{Ha})$, it is shifted to a lower value than $\text{Re}_I^0(\text{Ha})$, by ΔRe^0 of order or 2000 (Fig. 4.8). In other words, the quasi two-dimensional flow destabilises at much lower rotation rate of individual vortices in the 4×4 array when $\text{Ha} > 3640$ than for the range $1450 < \text{Ha} < 3640$.

The vortex pairing process continues mostly periodically with fundamental frequency f_{III} until it almost stops for $\text{Re}^0 \geq \text{Re}_{IV}^0$ (Fig. 4.8). Accordingly, the amplitude of the corresponding oscillation $A(f_{III})$ obtained at the top and bottom *Hartmann* wall is very small (Fig. 4.9c). Related times series of iso- $\phi_w(t)$ contours show merged iso- ϕ_w lines on top and bottom *Hartmann* wall, indicating almost quasi-two-dimensional and nearly stabilised vortex pairs (snapshot in Fig. 4.8f). In this flow regime one observes also periodic oscillations of higher fundamental frequency $f_{VI} > f_{III}$ and amplitude $A(f_{VI}) > A(f_{III})$ in time-dependent signals $\phi_w(x, y, z, t)$ (Fig. 4.9c). In fact, these "high" frequency oscillations occur for each set of Ha in the range $\text{Ha} > 3640$ when the forcing Re^0 reaches the critical value $\text{Re}_{VI}^0(\text{Ha})$. Fig. 4.8 further shows that $\text{Re}_{VI}^0(\text{Ha}) \approx \text{Re}_{IV}^0(\text{Ha})$ when $3640 < \text{Ha} \lesssim 4740$, but $\text{Re}_{VI}^0(\text{Ha}) < \text{Re}_{IV}^0(\text{Ha})$ and even $\text{Re}_{VI}^0(\text{Ha}) < \text{Re}_{III}^0(\text{Ha})$ for $\text{Ha} \gtrsim 4740$. In other words, electric potential oscillations with "high" frequency f_{VI} can not exclusively be linked to the appearance of almost steady vortex pairs.

At $\text{Re}^0 = \text{Re}_V^0$ the vortex pairing process resumes and the flow quickly becomes chaotic for slightly higher forcing $\text{Re}^0 > \text{Re}_V^0$.

As already mentioned, the reader should regard the above presented observations with some reservation, as we do in fact. The sudden change in the instability behaviour compared to cases where $\text{Ha} < 3640$ indeed raises many questions. Up to now, we neither have a physical explanation why the 4×4 vortex array destabilises at much lower forcing than expected nor can we relate the appearance of "high" frequency oscillations to any physical effect with certainty. One may however speculate that these oscillations correspond to small, quickly rotating vortices that have been generated in the vicinity of the side walls due to boundary layer separation as in our other experiment (Sec. 3.2). In order to confirm this and to be able to explain the overall instability behaviour in this Ha region one would need to perform further important experimental and numerical work.

4.3. Appearance of three-dimensionality in chaotic and turbulent flow regimes

In this section we firstly explain how we obtain relevant quantities that characterize the appearance of weak and strong three-dimensionality in flow regimes that are chaotic or turbulent. And secondly, using these quantities we describe the link between inertia and the appearance of three-dimensionality.

4.3.1. Quantities that characterize the appearance of three-dimensionality

To single out the mechanism that explains the appearance of three-dimensionality in chaotic or turbulent flow regimes we use spatially averaged correlations $\langle C'_1 \rangle$ and $\langle C'_2 \rangle$ based on local electric potential gradients and the *true* interaction parameter $N_t(L_i)$ (1.39) built on the injection scale L_i . Thereafter we explain how we obtain sets of these quantities for injection scales $L_i \in \{0.01, 0.03\}$ m, *Reynolds* numbers $Re^0 \in [0, 1.3 \times 10^5]$ and *Hartmann* numbers $Ha \in \{1092, 1822, 3644, 7290, 10930, 14580, 18220\}$.

Spatially averaged correlations $\langle C'_1 \rangle$ and $\langle C'_2 \rangle$

In order to quantify the appearance of three-dimensionality and to distinguish between weak and strong three-dimensionality we apply the correlation functions C_1 and C_2 as defined in Sec. 2.2.3, to time dependent electric potential gradients obtained at the bottom ($z = 0$) and top ($z = L$) *Hartmann* wall at locations (x, y) . Since the mean flow is negligible compared to flow fluctuations in chaotic or turbulent flow regimes, the correlations C_1 and C_2 are built on fluctuations of the electric potential gradient $\nabla \phi'_w(x, y, t) = \nabla \phi_w(x, y, t) - \langle \nabla \phi_w(x, y, t) \rangle_t$, more precisely on local gradients $\partial_y \phi'_w(x, y, t)$ (note that correlations built on $\partial_x \phi'_w(x, y, t)$ yield quantitatively similar results). Accordingly we term these correlations C'_1 and C'_2 . In order to get a more global representation of three-dimensionality we determine their spatial averages $\langle C'_1 \rangle$ and $\langle C'_2 \rangle$ which are built on correlations locally obtained on the 10×10 grid of measurement points located in the centre of the *Hartmann* wall (Fig. 2.22). Our flow forcing mechanism however induces intrinsically some three-dimensionality in the vicinity of individual injection electrode as can be seen from Fig. 4.10. Since we do not know how this local phenomenon might affect our analysis on the global appearance of three-dimensionality, we excluded correlations obtained close to individual injection electrodes from spatial averages $\langle C'_1 \rangle$ and $\langle C'_2 \rangle$ (for more details read caption of Fig. 4.10).

Lastly one should mention that the ratio $r_{S/N}$ between the effective amplitude (RMS) of fluctuations $\partial_y \phi'_w$ and that of the noise is of the order of 10^2 in chaotic flow regimes.

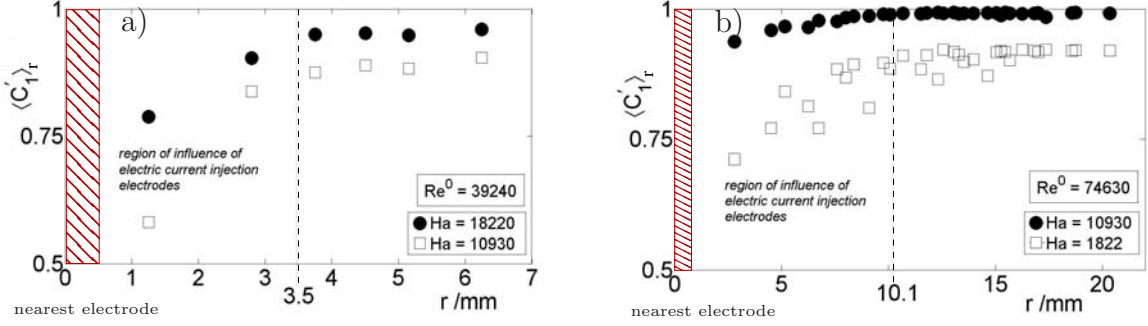


Figure 4.10.: Spatially averaged correlations $\langle C'_1(r) \rangle_r$ vs. distance r to an injection electrode. Values of $\langle C'_1(r) \rangle_r$ are built on correlations obtained at the 10×10 grid of electric potential probes in the centre of the *Hartmann* wall (Fig. 2.22), at fixed distances $r \in [0, 6.25]\text{mm}$ and $r \in [0, 20.35]\text{mm}$ from individual injection electrodes for: a) forcing geometry 10×10 , $\text{Re}^0 = 39240$ and $\text{Ha} \in \{18220, 10930\}$ and b) forcing geometry 4×4 , $\text{Re}^0 = 74630$ and $\text{Ha} \in \{10930, 1822\}$ respectively. Correlations obtained at measurement points less than 3.5mm or 10.1mm from individual electrodes, for forcing geometry 10×10 or 4×4 respectively, are excluded from spatial averages $\langle C'_1 \rangle$, $\langle C'_2 \rangle$ and $\langle C'_1(f_p) \rangle$. This eliminates the local influence of the flow forcing mechanism on the global appearance of three-dimensionality analysed in Sec. 4.3.2 and Sec. 4.4 respectively.

This implies that the error on local correlations C'_1 and C'_2 is not larger than 1% (see appendix A).

The true interaction parameter N_t

To assess the link between inertia and the appearance of three-dimensionality we plot spatially averaged correlations $\langle C'_1 \rangle$ and $\langle C'_2 \rangle$ thereafter in Fig. 4.11 against the true interaction parameter $N_t(L_i)$ which is built on the injection scale L_i . According to (1.39) $N_t(L_i)$ reads:

$$N_t(L_i) = \frac{\sigma B_0^2 L_i}{u' \rho} \left(\frac{L_i}{L} \right)^2 = \frac{\text{Ha}^2}{\text{Re}} \left(\frac{L_i}{L} \right)^4 = \frac{\tau_{u'}(L_i)}{\tau_{2D}(L_i)}. \quad (4.3)$$

$N_t(L_i)$ measures the relative influence of *Lorentz* to inertial forces in vortices with transverse length scale $l_\perp = L_i \in \{0.01, 0.03\}\text{m}$. The quantity u' in the *Reynolds* number $\text{Re} = u' L_i / \nu$ and the vortex turnover time $\tau_{u'}(L_i) = L_i / u'$ in (4.3) is a typical velocity built on the spatial average of local RMS's of corresponding moduli $|\partial \phi'_w(x, y, 0, t)| = (\partial_x \phi'^2_w(t) + \partial_y \phi'^2_w(t))^{1/2}$ obtained at the bottom *Hartmann* wall:

$$u' = \frac{\langle \langle |\partial \phi'_w(t)|^2 \rangle_t^{1/2} \rangle}{B_0}. \quad (4.4)$$

To get u' , we firstly determine local values of $|\partial\phi'_w(x, y, 0, t)|$ by interpolating between measurement points of the 10×10 grid in the centre region (Fig. 2.22) to obtain a 20×20 grid with spacing 1mm between points in the region spanned by $x = [37.5 \ 57.5]\text{mm}$ and $y = [42.5 \ 62.5]\text{mm}$. And secondly, we calculate the corresponding spatial average to get the quantity $\langle\langle|\partial\phi'_w(t)|^2\rangle_t^{1/2}\rangle$.

4.3.2. Appearance of three-dimensionality

In this section we single out the mechanism that explains how the subtle interplay between inertial and *Lorentz* forces produces weak and strong three-dimensionality in chaotic and turbulent flow regimes. To this end, we plot spatially averaged correlations $\langle C'_1 \rangle$, $\langle C'_2 \rangle$ vs. the *true* interaction parameter $N_t(L_i)$ in Fig. 4.11. At this point it is also important to recall again that values of $\langle C'_1 \rangle$ below unity reflect strong three-dimensionality, while $\langle C'_2 \rangle$ is smaller than unity whenever either weak or strong three-dimensionality is present (Sec. 2.2.3).

Remarkably, the correlation diagram in Fig. 4.11 shows that all measurement points collapse into two single curves for $\langle C'_1(N_t(L_i)) \rangle$ and $\langle C'_2(N_t(L_i)) \rangle$. This proves that either form of three-dimensionality (weak and strong) we detect here is exclusively of inertial nature. Both $\langle C'_1 \rangle$ and $\langle C'_2 \rangle$ decreases with decreasing $N_t(L_i)$ as stronger inertia gives rise to perturbations that are less effectively damped by the *Lorentz* force. Fig. 4.11 however shows that $\langle C'_2 \rangle < \langle C'_1 \rangle$ for all values of $N_t(L_i)$. This implies that the flow is always less intense in the vicinity of the bottom than on the top *Hartmann* wall, thus indicating again the presence of weak three-dimensionality that appears under the form of differential rotation in individual vortices.

The dynamics of this weakly three-dimensional flow however, is still mostly two-dimensional when $\langle C'_1 \rangle \simeq 1$. This is the case in regime I of the correlation diagram in Fig. 4.11, in the range of high values of $N_t(L_i)$. Accordingly, the topology of contours of iso- ϕ_w at the bottom ($z = 0$) and top ($z = L$) *Hartmann* wall are almost identical and corresponding power spectral density (PSD) of electric potential gradients $\partial_y\phi'_w$ overlap over the full frequency range (Fig. 4.11d). Towards the transition between regime I and regime II in Fig. 4.11, $N_t(L_i)$ approaches values close to unity and $\langle C'_1 \rangle$ noticeably decreases, indicating the appearance of strong three-dimensionality. Since the correlation factor $\langle C'_1 \rangle$ is about 0.93 at this transition and still very close to unity, the appearance of strong three-dimensionality remains small and the flow is still nearly quasi two-dimensional. Although small, the appearance of strong three-dimensionality at the transition between those regimes can be clearly seen when inspecting related topologies of iso- ϕ_w contours. They are not identical anymore and one clearly identifies small structures of size l_\perp that are generated near the

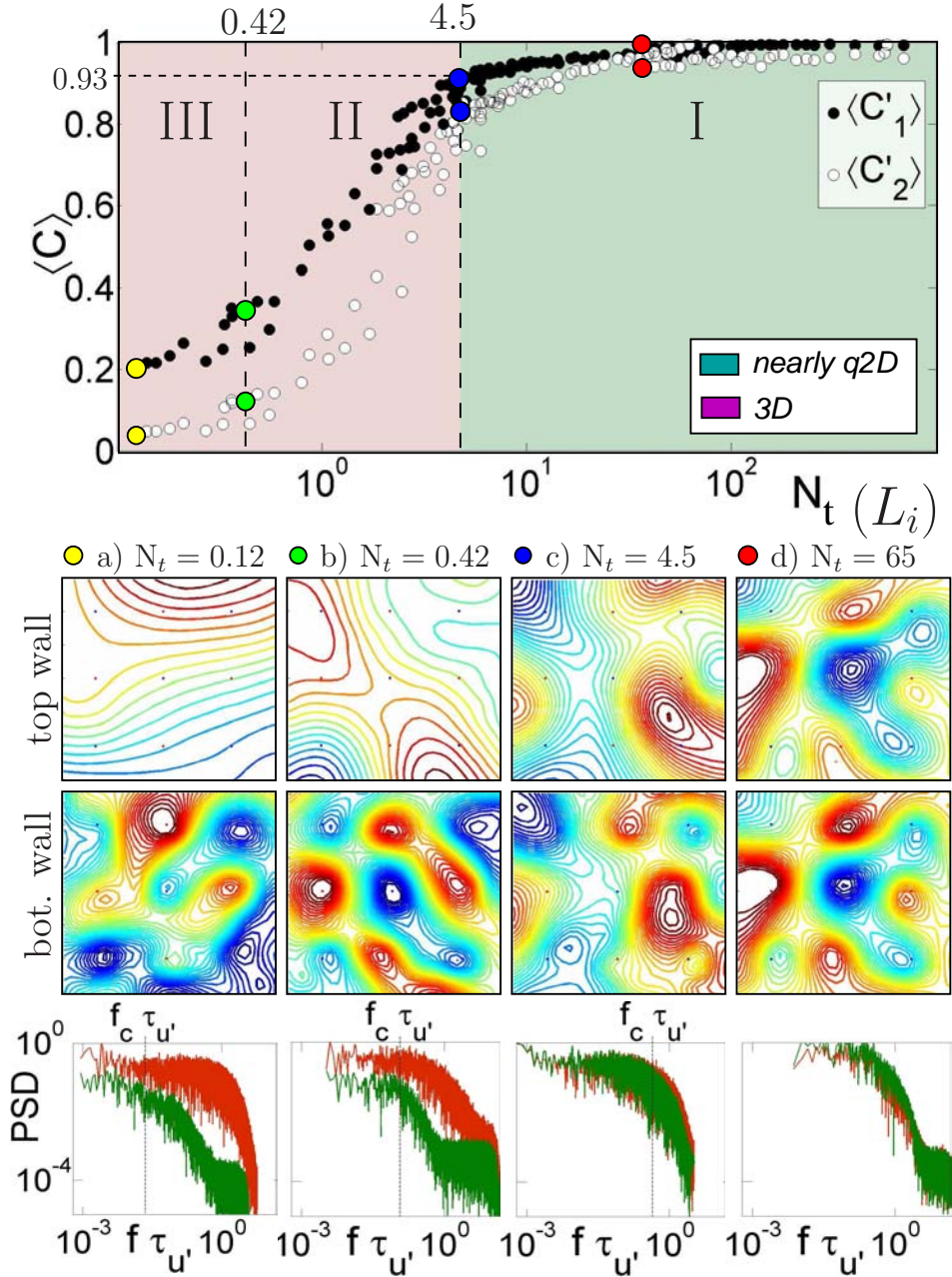


Figure 4.11.: Top: Spatially averaged correlations $\langle C'_1 \rangle$ and $\langle C'_2 \rangle$ vs. the true interaction parameter $N_t(L_i) = \text{Ha}^2/\text{Re} (L_i/L)^4$ where the Reynolds number $\text{Re} = u'L_i/\nu$ is based on the typical velocity u' obtained at the bottom Hartmann wall and the injection scale $L_i \in \{0.01, 0.03\}$ m. Bottom: snapshots of iso- lines, (a)-(d) and corresponding Power Spectral Density of $\partial_y \phi_w'$ at bottom (red) and top (green) Hartmann wall, normalized by $(U_0 B_0)^2$. Attention should be paid too to the threshold between nearly quasi two-dimensional flow regimes ("I") and strongly three-dimensional flow regimes ("II") that is defined where $\langle C'_1 \rangle \approx 0.93$. It is marked by the curve $\text{Re}_{3D}^0(\text{Ha})$ in the (Ha, Re^0) parameter space in Fig. 4.1 for $L_i = 0.01$ m. It should further be noted that labels "I", "II" and "III" have nothing in common with those used to distinguish between flow regimes in our small experiment in Sec. 3.2.

bottom *Hartmann* wall but do not extend to the top *Hartmann* wall (Fig. 4.11c). Larger vortices however remain nearly quasi two-dimensional as they are almost not affected by three-dimensional inertia (Fig. 4.11c). This suggests defining a critical or *cutoff* vortex size l_{\perp}^c which separates smaller, strongly three-dimensional vortices from larger, mostly quasi two-dimensional ones. Because of the great precision with which time dependent electric potential gradients $\partial_y \phi_w$ are recorded, it is however easier to identify a related *cutoff* frequency f_c that separates slow, almost quasi two-dimensional, large scale fluctuations from fast, small scale, strongly three-dimensional ones (see the PSD in Fig. 4.11c). In regime II where $0.42 \lesssim N_t(L_i) \lesssim 4.5$, $\langle C'_1 \rangle$ and $\langle C'_2 \rangle$ almost abruptly decreases with $N_t(L_i)$ Fig. 4.11. This is clearly different to the evolution of $\langle C'_1 \rangle$ and $\langle C'_2 \rangle$ in regime I and one identifies a threshold that separates regime I from II. This threshold is plotted in the (Ha, Re^0) parameter space at the non-dimensional injected electric current Re_{3D}^0 in Fig. 4.1, for injection scale $L_i = 0.01\text{m}$. Contours of iso- ϕ_w in Figs. 4.11c,b in this regime II illustrate that the strong decrease of $\langle C'_1 \rangle$ and $\langle C'_2 \rangle$ is induced by larger and larger structures that are strongly three-dimensional as the *Lorentz* force becomes less and less efficient against three-dimensional inertia. Accordingly, the cutoff frequency f_c shifts toward lower frequencies in the spectrum Fig. 4.11b.

A last regime, regime III, has been identified for $N_t(L_i) < 0.42$ where signals are almost uncorrelated. Three-dimensionality still increases when $N_t(L_1)$ decreases, though more slowly than in the previous regime II. Related PSD in Fig. 4.11a show that strongly three-dimensional inertia progressively contaminates the lowest frequency range so that f_c becomes very small. Accordingly, contours of iso- ϕ_w in Fig. 4.11a illustrate that almost no structure extends to the top *Hartmann* wall so hardly any flow is remaining there. In other words, the flow in the cubic container is mostly three-dimensional and quasi two-dimensionality might appear only in vortices that are larger than the box size L .

In summary, one may picture the transition from a mostly quasi two-dimensional flow to a strongly three-dimensional flow through sequent regimes I, II and III by the appearance of strong three-dimensionality in vortices with transverse size l_{\perp} that is, respectively smaller than the injection scale L_i , about the injection scale L_i and larger than the injection scale L_i .

4.4. Frequency-selective strong three-dimensionality

In Sec. 4.3.2 we have identified a cutoff frequency f_c which is related to a critical vortex size l_\perp^c that distinguish between vortices of size l_\perp that are strongly three-dimensional ($l_\perp \lesssim l_\perp^c$) and those that are mostly quasi two-dimensional ($l_\perp \gtrsim l_\perp^c$). Accordingly, f_c separates slow, nearly quasi two-dimensional fluctuations from fast, strongly three-dimensional ones in the spectrum (Fig. 4.11a-c). In this section we single out the link between this frequency selective strong three-dimensionality and inertia by plotting $f_c(L_i)$ against the true interaction parameter $N_t(L_i)$ for injection scales $L_i \in \{0.01, 0.03\}$ m. It should be noted that related values of $f_c(L_i)$ are obtained using the technique explained in appendix B.

Fig. 4.12 shows that the link between frequency selective strong three-dimensionality and inertia satisfies the law,

$$f_c \simeq 1.7\tau_w^{-1}N_t^{2/3 \pm 0.03}(L_i), \quad (4.5)$$

to a great precision.

This important law provides a clear estimate for the minimum frequency f_c of fluctuations in the flow that are strongly three-dimensional. It is also in the spirit of [64]'s heuristic law that gives the condition for the minimum vortex size l_\perp^c that is still quasi two-dimensional in a *Hartmann* wall-bounded, turbulent flow (Sec. 1.3.2). Using (1.98) and the superscript $()^c$ instead of $()^{q2D}$, [64]'s law writes expressed in terms of the true interaction parameter $N_t(L_i)$:

$$l_\perp^c >> L_i N_t^{-1/3}(L_i). \quad (4.6)$$

Since we could not determine l_\perp^c from our measurements because of the limit in spatial resolution it still remains an interesting and important task for future work to prove the above heuristic law of [64] experimentally.

Fig. 4.12 shows too that cutoff frequencies f_c could be obtained for all values of the true interaction parameter $N_t(L_i)$, even in flow regimes where $N_t(L_i)$ is large and signals are almost fully correlated (see regime I in Fig. 4.11). Firstly, this points to the high precision with which values of f_c are determined using the frequency-filter-technique explained in the appendix B. And Secondly, even more important, it indicates that strongly three-dimensional fluctuations appear not abruptly, but, like weak three-dimensionality, progressively when inertial forces becomes increasingly more significant compared to the *Lorentz* force. However, whether the latter finding is a general physical mechanism at the transition between quasi two-dimensional and strongly three-dimensional flows needs further experimental and numerical confirmation.

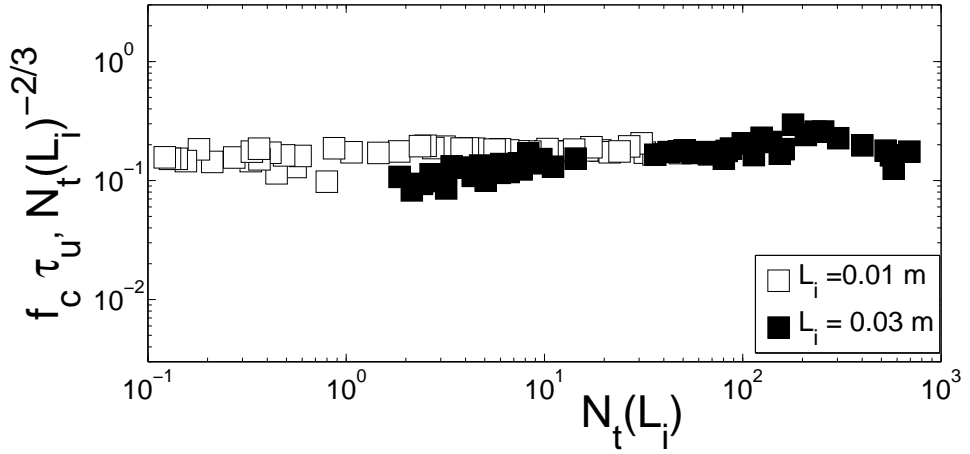


Figure 4.12.: Cutoff frequency f_c , normalized by the injection scale turnover frequency $\tau_{u'}^{-1}(L_i)$ vs. $N_t(L_i)$

Lastly, since the state of turbulent fluctuations, either strongly three-dimensional or quasi-two-dimensional depends only on $N_t = \tau'_u(l_\perp)/\tau_{2D}(l_\perp)$, and therefore on the times scales $\tau_{u'}$ and τ_{2D} , a similar law to our experimental law $f_c \sim N_t^{2/3}$ should hold too in other, non-MHD flows with a tendency to two-dimensionality, albeit with a different expression for τ_{2D} ([29]).

4.5. Conclusion

We performed a magnetohydrodynamic (MHD) experiment to single out the mechanism that explains how and under which form three-dimensionality appears from initially quasi two-dimensionally, in flows bounded by physical walls. Answering this fundamental question is crucial not only from the scientific point of view, but bears too critical consequences in practical situations: in liquid metal heat exchangers or metal casting processes, for instance, where three-dimensional flows are preferable to quasi two-dimensional ones to enhance heat and mass transport and favour homogeneous mixing.

Our experiment was purposely designed to create individual vortices of size l_{\perp} that can either assume a quasi two-dimensional or a three-dimensional state, depending on whether their two-dimensionalisation time $\tau_{2D}(l_{\perp})$ is much smaller or comparable *resp.* larger to their inertial time scale $\tau_U(l_{\perp})$.

The flow in a liquid metal filled, cubic container subject to the magnetic field $B_0 \mathbf{e}_z$ was forced by injecting constant electric current I from one wall perpendicular to $B_0 \mathbf{e}_z$ (*Hartmann* wall) through electrodes arranged in a square array with spacing L_i and alternatively connected to either pol of a DC power supply. For strong fields B_0 and weak electric current I this forcing is known to produce a base flow of a steady, quasi two-dimensional vortex array with individual vortices of size $l_{\perp} \approx L_i$ rotating in alternate direction along \mathbf{B} ([62]). Depending on the strength of I and B_0 , respectively expressed non-dimensionally by the *Hartmann* number Ha and *Reynolds* number Re^0 , the flow undergoes different states in which weak and strong three-dimensionality in individual flow structures of size l_{\perp} appeared too, always when corresponding three-dimensional inertial forces become of comparable strength with the *Lorentz* force ($\tau_{2D}(l_{\perp}) \gtrsim \tau_U(l_{\perp})$). Electric potentials ϕ_w measured locally on either *Hartmann* walls monitor both flow characteristics outside thin *Hartmann* layers that shape along the *Hartmann* wall and the appearance of three-dimensionality.

For high Ha and in steady regimes we found that the flow assumes the expected square array of quasi two-dimensional, alternatively rotating vortices [62]. For all values of Ha in that range this flow destabilises at the same critical parameter $R_h^0 = \text{Re}^0 / \text{Ha} = cst.$ into typical, periodic vortex pairing that occurs along the field \mathbf{B} over the full container height ([62, 69]). For low Ha however, three-dimensional inertial forces are more significant so that the steady vortex array is not strictly quasi two-dimensional anymore, but subject to a weak form of three-dimensionality that appears as differential rotation in individual vortices. The vortex pairing process still occurs over the full box height when this weakly three-dimensional vortex array destabilises, but at critical parameters $R_h^0(\text{Ha})$ that depends on Ha . For very small Ha though, we identified the appearance of strong three-

dimensionality as the pairing process at critical parameters $R_h^0(\text{Ha})$ appears only partially along the field \mathbf{B} . Remarkably in this low Ha range, at forcing slightly higher than critical values of $R_h^0(\text{Ha})$ the vortex pairing process stops abruptly resulting into either steady, weakly three-dimensional vortex pairs for intermediate Ha or, most spectacularly, in the appearance of steady, strongly three-dimensional, *Giraffe*-like structures for a very small Ha.

To quantify the appearance of weak and strong three-dimensionality in chaotic and turbulent flow regimes we analysed correlations of fluctuations of electric potential gradients $\partial_y \phi'_w(t)$, between pairs of measurement points aligned opposite each other on top and bottom *Hartman* wall. How either form of three-dimensionality are linked to inertial forces was singled out by plotting spatially averaged correlations against [68]'s true interaction parameter $N_t(L_i)$ built on vortices with size $l_\perp = L_i$. This showed us that the effect of inertia induced always weak three-dimensionality under the form of differential rotation in individual vortices, but progressively less towards large values of $N_t(L_i)$. Strong three-dimensionality in individual vortices with $\tau_{2D}(l_\perp) \gtrsim \tau_U(l_\perp)$ occurs also less towards large $N_t(L_i)$. This indicates that the critical vortex size l_\perp^c that separates small, strongly three-dimensional vortices ($l_\perp \lesssim l_\perp^c$) from large, mostly quasi two-dimensional ones ($l_\perp \gtrsim l_\perp^c$) increases also with $N_t(L_i)$. A related cutoff frequency $f_c(N_t)$ has been identified from corresponding spectra of fluctuations $\partial_y \phi'_w(t)$ separating respectively fast, strongly three-dimensional fluctuations from large, mostly quasi two-dimensional ones. The link between inertial forces and this frequency-selective strong three-dimensionality could be quantified by the important law $f_c \sim N_t^{2/3}$, in the spirit of [62]'s heuristic law $l_\perp^c \sim N_t^{-1/3}$. The law $f_c \sim N_t^{2/3}$ may also apply to other flows with tendency to two-dimensionality such as stratified and rotating flows which appear in atmospheres and oceans.

General conclusion

The physics of magnetohydrodynamic (MHD) that imposes tendency to two-dimensionality in liquid metal flows is of general interest. Since rotating or stratified flows in geophysics and astrophysics have the same tendency, it helps understanding them by studying fundamental MHD problems at the laboratory scale. MHD effects are important too in practical applications involving molten metal like in the steel casting industry or in the blankets of future nuclear fusion reactors. In all these situations it is crucial, but often unclear when and under which form inertial forces induce three-dimensionality as well as how flows are affected by the presence of walls.

In this dissertation we addressed the above key issues by performing two MHD laboratory experiments at the fundamental level. Both experiments featured a liquid metal flow subject to a homogeneous magnetic field $B_0\mathbf{e}_z$ and bounded by physical walls. In the smaller one of these experiments the flow was confined by the walls of a shallow, cylindrical container of height 0.005m and the field $B_0\mathbf{e}_z$ pointed along the cylinder axis. This design favours quasi two-dimensional flows, hence flows that are invariant everywhere across the shallow fluid layer (*i.e* along $B_0\mathbf{e}_z$), except in thin *Hartmann* layers that develop along the walls orthogonal to the field (*Hartmann* walls).

Unlike this experiment aimed mostly at quasi two-dimensional flows, our other, larger experiment was designed not shallow but cubic with inner edge 0.1m, to promote the appearance of three-dimensionality too. In both experiments, the liquid metal was forced by injecting DC electric current locally, through electrodes that are embedded in one *Hartmann* wall. This created a base flow made of a vortex pair in our small and a square array of vortices in our large scale experiment as in [62]. Flow characteristics at different intensities of the forcing and magnetic field as well as the appearance of three-dimensionality were determined by measuring the electric potential ϕ_w on the *Hartmann* walls that confined the liquid metal from the top and from the bottom. In this dissertation we distinguish between a weak and a strong form of three-dimensionality. Weak three-dimensionality implies that corresponding flow structures are almost strictly quasi two-dimensional but subject to differential rotation along $B_0\mathbf{e}_z$, whilst strongly three-dimensional flow structures do not anymore extend from the bottom to the top wall.

The mostly quasi two-dimensional flow in the shallow container was found to undergo a sequence of supercritical bifurcations to turbulence, triggered by boundary layer separation from the circular wall at the back of the initial vortex pair. Interestingly, subsequent flow regimes bore also some analogies to those that appear in flows around a cylindrical

obstacle [28]. To shed more light into these analogies however, it calls now for further experimental and theoretical analysis. This applies also to observations made at the onset of the last identified flow regime "V" where the turbulent flow, still mostly quasi two-dimensional, brutally changed its character and experienced a sudden extra dissipation. We suggested that the extra dissipation might be linked to the transition from a laminar to a turbulent *Hartmann* layer. Furthermore, we provided first evidence for the appearance of weakly and strongly three-dimensional flow structures in the otherwise mostly quasi two-dimensional flow by calculating correlations between fluctuations of the electric potential gradient $\partial_y \phi'_w$ obtained on the same magnetic field line, on top an bottom *Hartmann* walls.

At this point we shall recall again that we initially aimed at using this experiment for test purposes only. But thanks to its further important development we could use it too to study the above interesting MHD effects.

The main task of this dissertation was however to clarify experimentally how the interplay between inertia and the *Lorentz* force induces three-dimensionality in complex, wall-bounded MHD flows where the presence of *Hartmann* layers precludes strict two-dimensionality. We answered this important question by analysing a vortex array in a cubic container where we controlled the strength of inertia and Lorentz force respectively by the intensity of the forcing and the imposed magnetic field $B_0 \mathbf{e}_z$. If the intensity of the latter was high, the forcing produced nearly quasi two-dimensional vortices in steady and slightly unsteady regimes similar to what [62] observed. However, in regimes where the field $B_0 \mathbf{e}_z$ was small, the *Lorentz* force could not maintain quasi two-dimensionality. Accordingly, inertial forces induced weak and strong three-dimensionality in individual vortices, manifesting itself most spectacularly in the appearance of steady, *Giraffe*-like flow structures (Fig. 4.7). The link between inertia and the appearance of three-dimensionality in chaotic and turbulent flow regimes was even more subtle. Simply speaking, the effect of inertia selected small, quickly rotating flow structures by making them both weakly and strongly three-dimensional, whilst large, slowly rotating flow structures remained nearly quasi two-dimensional as mostly controlled by the effect of the Lorentz force. In this regard probably most importantly, we could quantify this selecting mechanism by a related cut-off frequency f_c that separates quasi two-dimensional from strongly three-dimensional flow fluctuations in the frequency spectrum according to the law $f_c \sim N_t(L_i)^{2/3}$, N_t being the true interaction parameter based on the vortex injection scale L_i ([68]).

The above results indeed show that "only" by the use of electric potential measurements on either *Hartmann* walls we were able to propose an excellent, experimental answer to the question of how three-dimensionality appears in wall-bounded MHD flows. The shape of corresponding three-dimensional flow structures between the two *Hartmann* walls remained however unclear so that this opens now the scope for further research. To assess

this issue and to refine our picture of the appearance of three-dimensionality it requires important bulk measurements, to obtain velocities $\mathbf{u}_\perp(z)$ and $u_z \mathbf{e}_z$. Intrusive electric potential measurements for instance, or too acoustic waves emitted by ultrasound probes ([9]) could provide these three-dimensional information of the flow. Corresponding measurement systems may be implemented in a new side plate that, because of the modularity of the experiment, can be swapped easily with another one previously used in the set-up. Before however performing such difficult bulk measurements one may already shed some light into flow region between either *Hartmann* walls by analysing recorded sets of electric potentials measured on walls parallel to the imposed field $B_0 \mathbf{e}_z$ (Fig. 2.22). This might give some insight into the shape of flow structure near the wall outside the parallel layer.

Lastly we shall recall that the results of both the small scale and the large experiment have been recently published in "Experiment on a confined electrically driven vortex pair" [28] and "Appearance of three-dimensionality in wall-bounded MHD flows" [29] respectively.

Bibliography

References

- [1] H. D. I. Abarnel. *Analysis of Observed Chaotic Data*. Springer Verlag, 1996.
- [2] R. A. D. Akkermans, A. R. Cieslik, L. P. J. Kamp, R. R. Trieling, H. J. H. Clercx, and van Heijst G. J. F. The three-dimensional structure of an electromagnetically generated dipolar vortex in a shallow fluid layer. *Phys. Fluids*, 20:116601, 2008.
- [3] T. Alboussiere, V. Uspenski, and R. Moreau. Quasi-2d MHD turbulent shear layers. *Exp. Therm. and Fluid Science*, 20:19–24, 1999.
- [4] A. Alemany, R. Moreau, P. Sulem, and U. Frish. Influence of an external magnetic field on homogeneous MHD turbulence. *J. Mec.*, 18:277–313, 1979.
- [5] O. V. Andreev and Yu. B. Kolesnikov. MHD instabilities at transverse flow around a circular cylinder in an axial magnetic field. *3. Int. Conf. on Transf. Phen. in Magnetohydrodynamics and Electroconducting Flows*, pages 205–210, 1997.
- [6] G. K. Batchelor. Computation of the energy spectrum in homogeneous two-dimensional turbulence. *Phys. Fluids Suppl. II*, 12:233, 1969.
- [7] P. Bergé, Y. Pomeau, C. Vidal, and David Ruelle. *Order within chaos: towards a deterministic approach to turbulence*. John Wiley & Sons Inc, 1984.
- [8] G. G. Branover. Resistance of magnetohydrodynamic channels. *Magnetohydrodynamics*, 3:1–11, 1967.
- [9] D. Brito, H. C. Nataf, P. Cardin, J. Aubert, and J. P. Masson. Ultrasonic doppler velocimetry in liquid gallium. *Exp. Fluids*, 31:653–663, 2001.
- [10] P. A. Davidson. The role of angular momentum in the magnetic damping of turbulence. *J. Fluid Mech.*, 336:123–150, 1997.
- [11] P. A. Davidson and A. Pothérat. A note on Bodewadt-Hartmann layers. *Eur. J. Mech /B*, 21:541–559, 2002.

- [12] P.A. Davidson. *An Introduction to Magnetohydrodynamics*. Cambridge University Press, 2001.
- [13] P.A. Davidson. *Turbulence: An Introduction for Scientists and Engineers*. Oxford University Press, 2004.
- [14] R Doering and J. D. Gibbons. *Applied Analysis of the Navier-Stokes equation*. Cambridge University Press, 1995.
- [15] V. Dousset and A. Pothérat. Numerical simulations of a cylinder wake under a strong axial magnetic field. *Phys. Fluids*, 20, 2008.
- [16] P. G. Drazin. *Hydrodynamic Stability*. Cambridge University Press, 1981.
- [17] J. M. Nguyen Duc. Instabilité et turbulence dans des écoulements bidimensionnels MHD. *These de Doctorat de l'Institut National Polytechnique de Grenoble*, 1988.
- [18] J. M. Nguyen Duc, P. Caperan, and J. Sommeria. Experimental investigation of the two-dimensional inverse energy cascade. *Current Trends in Turbulence Research of Progress in Astronautics and Aeronautics, A.I.A.A.*, 112:78–86, 1988.
- [19] M. Faraday. Experimental researches in electricity. *Phil. Trans.*, 15:175, 1832.
- [20] Deutschen Institut fr Normung e.V. DIN. *Thermocouples -Part 1: Reference tables (DIN EN 60584-1)*. Beuth, 1996.
- [21] M. Frank, L. Barleon, and U. Müller. Visual analysis of two-dimensional magnetohydrodynamics. *Phys. Fluids*, 13:2287–2295, 2001.
- [22] H. P. Greenspan. *The Theory of Rotating Fluids*. Cambridge University Press, 1969.
- [23] J. Hartmann. Theory of the laminar flow of an electrically conductive liquid in a homogeneous magnetic field. *K. Dan. Vidensk. Selsk. Mat. Fys. Medd.*, 15(6):1–28, 1937.
- [24] J. Hartmann and F. Lazarus. Experimental investigations on the flow of mercury in a homogeneous magnetic field. *K. Dan. Vidensk. Selsk. Mat. Fys. Medd.*, 15(7):1–45, 1937.
- [25] R. C. Hilborn. *Chaos and nonlinear dynamics: an introduction for scientists and engineers*. Oxford University Press, 2000.
- [26] J. C. R. Hunt and W. E. Williams. Some electrically driven flows in magnetohydrodynamics. part 1. theory. *J. Fluid Mech.*, 31:705–722, 1968.

- [27] H. Kantz and T. Schreiber. *Nonlinear Time Series Analysis*. Cambridge University Press, 1997.
- [28] R. Klein and A. Pothérat. Experiment on a confined electrically driven vortex pair. *Phys. Rev. E*, 79:016304, 2009.
- [29] R. Klein and A. Pothérat. Appearance of three-dimensionality in wall-bounded mhd flows. *Phy. Rev. Let.*, 104:034502, 2010.
- [30] A. Kljukin and A. Thess. Direct measurements of the stream-function in a quasi-two-dimensional liquid metal flow. *Exp. in Fluids*, 25:298–304, 1998.
- [31] A. N. Kolmogorov. On degeneration of isotropic turbulence in an incompressible viscous liquid. *Comptes Rendus (Doklady) de l'Academie des Sciences de l'U.R.S.S.*, 31:538–540, 1941b.
- [32] R. H. Kraichnan. Inertial ranges in two-dimensional turbulence. *Phys. Fluids*, 10:1417–1423, 1967.
- [33] D. S. Krasnov, E. Zienicke, O. Zikanov, T. Boeck, and A. Thess. Numerical study of the instability of the Hartmann layer. *J. Fluid. Mech.*, 504:183–211, 2004.
- [34] L. D. Landau and E. M. Lifshitz. 1959. Pergamon Press, Fluid mechanics.
- [35] M. Lesieur. *Turbulence in fluids*. Kluwer Academic, 1990.
- [36] R. J. Lingwood and T. Alboussiere. On the stability of the Hartmann layer. *Phys. Fluids*, 11:2058–2068, 1999.
- [37] K. Messadek and R. Moreau. An experimental investigation of MHD quasi two-dimensional shear flows. *J. Fluid Mech.*, 456:137–159, 2002.
- [38] K. Messadek and R. Moreau. On the measurement of the Hartmann layer thickness in a high magnetic field. *Phys. Fluids*, 16:3243–3246, 2004.
- [39] H.K. Moffatt. On the suppression of turbulence by a uniform magnetic field. *J. Fluid Mech.*, 28:571–592, 1967.
- [40] D. Molenaar, H. J. H. Clercx, and G. J. F. van Heijst. Transition to chaos in a confined two-dimensional fluid flow. *Phy. Rev. Let.*, 95:104503, 2005.
- [41] R. Moreau. On magnetohydrodynamic turbulence. *Proc. of Symp. on turbulence of fluid and plasma, Polyt. Inst. of Brooklyn*, 359, 1968.
- [42] R. Moreau. *Magnetohydrodynamics*. Kluwer Academic Publisher, 1990.

- [43] R. Moreau. MHD turbulence at the laboratory scale: Established ideas and new challenges. *Appl. Scient. Research*, 58:131–147, 1998.
- [44] P. Moresco and T. Alboussiere. Weakly nonlinear stability of Hartmann boundary layers. *Eur. J. Mech /B*, 22:345–353, 2003.
- [45] P. Moresco and T. Alboussiere. Experimental study of the instability of the Hartmann layer. *J. Fluid. Mech*, 504:167–181, 2004.
- [46] P. Moresco and T. Alboussiere. Stability of boedwadt-Hartmann layers. *Eur. J. Mech /B*, 23:851–859, 2004.
- [47] B. Mueck, C. Guenther, U. Mueller, and L. Buehler. Three-dimensional MHD flows in rectangular ducts with internal obstacles. *J. Fluid Mech.*, 418:265–295, 2000.
- [48] J. Ohkitani. Log corrected energy spectrum and attractor dimension in two-dimensional turbulence. *Phys. Fluids A*, 1:451–452, 1989.
- [49] E. Ott. *Chaos in Dynamical Systems*. Cambridge University Press, 1993.
- [50] J. Paret, D. Marteau, O. Paireau, and P. Tabeling. Are flows electromagnetically forced in thin stratified layers two dimensional? *Phys. Fluids*, 9:3102–3104, 1997.
- [51] J. Paret and P. Tabeling. Experimental observation of the two-dimensional inverse energy cascade. *Phy. Pev. L.*, 79:4162–4165, 1997.
- [52] R. Pelster, R. Pieper, and I. Huettl. Thermospannungen- viel genutzt und fast immer falsch erklaert! *Physik und Didaktik in Schule und Hochschule*, 4:10–22, 2005.
- [53] A. Pothérat and T. Alboussiere. Small scales and anisotropy in low Rm magnetohydrodynamic turbulence. *Phys. Fluids*, 15:3170–3180, 2003.
- [54] A. Pothérat, J. Sommeria, and R. Moreau. An effective two-dimensional model for MHD flows with transverse magnetic field. *J. Fluid Mech.*, 424:75–100, 2000.
- [55] A. Pothérat, J. Sommeria, and R. Moreau. Numerical simulations of an effective two-dimensional model for flows with a transverse magnetic field. *J. Fluid Mech.*, 534:115–143, 2005.
- [56] P.H. Roberts. *Introduction to Magnetohydrodynamics*. Longmans, London, 1967.
- [57] M. A. Rutgers. Forced 2d turbulence: Experimental evidence of simultaneous inverse energy and forward enstrophy cascades. *Phy. Pev. L.*, 81:2244–2247, 1998.

- [58] D. Schmitt, T. Alboussiere, D. Brito, P. Cardin, N. Gagniére, D. Jault, and H. C. Nataf. Rotating spherical couette flow in a dipolar magnetic field: experimental study of magneto-inertial waves. *J. Fluid Mech.*, 604:175–197, 2008.
- [59] U. Schuhmann. Numerical simulation of the transition from three- to two-dimensional turbulence under a uniform magnetic field. *J. Fluid Mech.*, 74:31–58, 1975.
- [60] J. A. Shercliff. *The Theory of Electromagnetic Flow Measurement*. Cambridge University Press, 1962.
- [61] J. A. Shercliff and W. H. Heiser. A simple demonstration of the Hartmann layer. *J. Fluid Mech.*, 22:701–707, 1965.
- [62] J. Sommeria. Experimental study of the two-dimensional inverse energy cascade in a square box. *J. Fluid Mech.*, 170:139–168, 1986.
- [63] J. Sommeria. Electrically driven vortices in a strong magnetic field. *J. Fluid Mech.*, 189:553–569, 1988.
- [64] J. Sommeria and R. Moreau. Why, how and when, MHD turbulence becomes two-dimensional. *J. Fluid Mech.*, 118:507–518, 1982.
- [65] D. Sous, N. Bonneton, and J. Sommeria. Turbulent vortex dipoles in a shallow water layer. *Phys. Fluids.*, 16:2886–2898, 2004.
- [66] B. Sreenivasan. *Evolution of inertial flow structures in the presence of a magnetic field*. PhD thesis. Ph.d. dissertation, Department of Engineering, University of Cambridge, December 2000.
- [67] B. Sreenivasan and T. Alboussiere. Evolution of a vortex in a magnetic field. *Eur. J. Mech. B-Fluids*, 419:403–421, 2000.
- [68] B. Sreenivasan and T. Alboussiere. Experimental study of a vortex in a magnetic field. *J. Fluid Mech.*, 464:287–309, 2002.
- [69] A. Thess. Instabilities in two-dimensional spatially periodic flows. part ii: Square eddy lattice. *Phys. Fluids A*, 4:1396–1407, 1992.
- [70] A. Thess, D. Krasnov, T. Boeck, E. Zienicke, O. Zikanov, P. Moresco, and T. Alboussière. Transition to turbulence in the Hartmann boundary layer. In: *GAMM-Mitteilungen*, 30:125–132, 2007.
- [71] A. Thess and O. Zikanov. Transition from two-dimensional to three-dimensional magnetohydrodynamic turbulence. *J. Fluid Mech.*, 579:383–412, 2007.

- [72] M.M. Zdravkovich. *Flow around circular cylinders. Vol. 1: Fundamentals.* Oxford University Press, 1997.
- [73] M.M. Zdravkovich. *Flow around circular cylinders. Vol. 2: Applications.* Oxford University Press, 2003.
- [74] O. Zikanov and A. Thess. Direct numerical simulations of forced MHD turbulence at low magnetic reynolds number. *J. Fluid Mech.*, 358:299–333, 1998.

Own publications

- [1.] R. Klein and A. Pothérat. Experiment on a confined electrically driven vortex pair. *Phys. Rev. E*, 79:016304, 2009.
- [2.] R. Klein and A. Pothérat. Appearance of three-dimensionality in wall-bounded MHD flows. *Phy. Rev. Let.*, 104:034502, 2010.
- [3.] R. Klein and A. Pothérat. Quasi-2d/3d transition in forced, wall-bounded MHD flows-low Rm. In *UK MHD 2009, Coventry (United Kingdom)*, June 2009.
- [4.] R. Klein and A. Pothérat. Experiment on MHD-Turbulence at low magnetic Reynolds number Rm. In *7th PAMIR International Conference on Fundamental and Applied MHD, Giens (France)*, September 2008.
- [5.] R. Klein and A. Pothérat. Experiment on MHD-Turbulence at low magnetic Reynolds number Rm. In *UK MHD 2008, Salford (United Kingdom)*, June 2008.
- [6.] R. Klein and A. Pothérat. Experiment on confined Q2D MHD-Vortex pair. In *WMHD08: MHD fundamentals from liquid metals to astrophysics, Brussels (Belgium)*, April 2008.
- [7.] R. Klein and A. Pothérat. Experiment: Confined Q2D MHD-Vortex pair. In *ICIAM07: 6th Int. Congress on Industrial and Applied Mathematics, Zurich (Switzerland)*, July 2007.
- [8.] R. Klein and A. Pothérat. Experiment on MHD Turbulence under low magnetic Reynolds number. In *MTLM2007: 2nd International Workshop on Measuring Techniques for Liquid Metal Flows, Dresden (Germany)*, April 2007.
- [9.] R. Klein and A. Pothérat. Experiment on MHD Turbulence under low magnetic Reynolds number. In *51th IWK, Ilmenau (Germany)*, September 2006.

- [10.] R. Klein and A. Pothérat. Experiment on MHD Turbulence under low magnetic Reynolds number. In *EUROMECH Colloquim on Fluid Flows in High Magnetic fields, Ilmenau (Germany)*, March 2006.

Appendices

A. Influence of noise on signal correlations

Three-dimensionality in chaotic and turbulent flow regimes is quantified using the correlation functions $C_1(S_T(t), S_B(t))$ and $C_2(S_T(t), S_B(t))$ as shown in Sec. 2.2.3. Though filtered to attenuate background electronic noise, signals $S_T(t)$ and $S_B(t)$ still contain noise of about $\simeq 2\mu\text{V}$ peak to peak which is mostly internal noise generated by the measurement system. The noise induces an error in values of $C_1(S_T(t), S_B(t))$ and $C_2(S_T(t), S_B(t))$ which we shall estimate thereafter.

Measured signals $S_T(t)$ and $S_B(t)$ can be decomposed as follows:

$$S_T(t) = S_T^0(t) + N_T(t) \quad \text{and} \quad S_B(t) = S_B^0(t) + N_B(t) \quad (\text{A.1})$$

where $S_T^0(t)$ and $S_B^0(t)$ are flow related, time-dependent quantities while $N_T(t)$ and $N_B(t)$ represent the noise captured in signals obtained at the bottom and top respectively. Combining (A.1) with (2.6) yields respectively:

$$\begin{aligned} C_1 &= \frac{\sum_{i=0}^k [S_B^0(t_i) + N_B(t_i)][S_T^0(t_i) + N_T(t_i)]}{\sqrt{\sum_{i=0}^k [S_B^0(t_i) + N_B(t_i)]^2 \sum_{i=0}^n [S_T^0(t_i) + N_T(t_i)]^2}} \quad \text{and,} \\ C_2 &= \frac{\sum_{i=0}^k [S_B^0(t_i) + N_B(t_i)][S_T^0(t_i) + N_T(t_i)]}{\sum_{i=0}^k [S_B^0(t_i) + N_B(t_i)]} \end{aligned} \quad (\text{A.2})$$

In the following we restrict our analysis to the correlation function C_1 , but the same approach applies also to the function C_2 .

We assume here that flow related quantities and the noise generated by the measurement system are intrinsically not correlated to each other. This implies that for large enough

number of measurement samples $\sum_{i=0}^k S_B^0(t_i)N_B(t_i) \asymp \sum_{i=0}^k S_T^0(t_i)N_T(t_i) \asymp \sum_{i=0}^k S_B^0(t_i)N_T(t_i) \asymp$
 $\sum_{i=0}^k S_T^0(t_i)N_B(t_i) \asymp 0$ and (A.2) modifies into:

$$C_1 = \frac{\sum_{i=0}^k S_B^0(t_i)S_T^0(t_i) + \sum_{i=0}^k S_B^0(t_i)S_T^0(t_i)}{\sqrt{(1 + \alpha_T + \alpha_B + \alpha_T\alpha_B)\sum_{i=0}^k (N_B(t_i))^2 \sum_{i=0}^k (N_T(t_i))^2}} \quad (\text{A.3})$$

where $\alpha_T = \sum_{i=0}^k (N_T(t_i))^2 / \sum_{i=0}^k (S_T^0(t_i))^2$ is the ratio between the effective amplitude (RMS) of the noise and the signal respectively near the top wall and, accordingly

$\alpha_B = \sum_{i=0}^k (N_B(t_i))^2 / \sum_{i=0}^k (S_B^0(t_i))^2$ the ratio near the bottom wall. Using Taylor series the term $1/\sqrt{(1 + \alpha_T + \alpha_B + \alpha_T\alpha_B)}$ can be approximated to $(1 - (\alpha_T + \alpha_B + \alpha_T\alpha_B)/2)$, and, since $\alpha_T\alpha_B \ll \alpha_T, \alpha_B$ relation (A.3) can be simplified into:

$$C_1 = \left(\frac{\sum_{i=0}^k S_B^0(t_i)S_T^0(t_i)}{\sqrt{\sum_{i=0}^k (S_B^0(t_i))^2 \sum_{i=0}^k (S_T^0(t_i))^2}} + \frac{\sum_{i=0}^k N_B(t_i)N_T(t_i)}{\sqrt{\sum_{i=0}^k (S_B^0(t_i))^2 \sum_{i=0}^k (S_T^0(t_i))^2}} \right) \left(1 - \frac{\alpha_B + \alpha_T}{2} \right) + \mathcal{O}\left(\alpha_T^2, \alpha_B^2, \alpha_T\alpha_B\right) \quad (\text{A.4})$$

where the first term on the right denotes the signal correlation $C_1^0(S_B^0(t), S_T^0(t))$ that is unaffected by the noise. The second term in (A.4) quantifies the correlation between the noise. Since cross channel noise is a well known effect in electronics we can not exclude this effect from our analysis. When further simplifying relation (A.4) and dropping second order terms it yields:

$$C_1 = C_1^0 \left(1 - \frac{\alpha_B + \alpha_T}{2} + \frac{\sum_{i=0}^k N_B(t_i)N_T(t_i)}{\sum_{i=0}^k S_B^0(t_i)S_T^0(t_i)} \right) \quad (\text{A.5})$$

Accordingly, when applying the above approach also to $C_2(S_T(t), S_B(t))$ one finds:

$$C_2 = C_2^0 \left(1 - \alpha_B + \frac{\sum_{i=0}^k N_B(t_i) N_T(t_i)}{\sum_{i=0}^k S_B^0(t_i) S_T^0(t_i)} \right) \quad (\text{A.6})$$

The last two terms in the brackets in relations (A.5) and (A.6) correspond to the relative error on correlations C_1 and C_2 induced by the presence of noise. On the one hand, C_1 and C_2 are affected by "signal to noise" ratios $r_{S/N} = 1/\alpha_B$ and $r_{S/N} = 2/(\alpha_B + \alpha_T)$ respectively. If $r_{S/N}$ is small, for instance $r_{S/N} = 5$, it induces a maximal error of about 20% in the correlation factor, provided that the noise itself is uncorrelated and the third term in relations (A.5) and (A.6) vanishes. On the other hand, if the noise $N_T(t_i)$ and $N_B(t_i)$ between channels is correlated it would artificially increases the correlation between signals $S_T(t)$ and $S_B(t)$.

B. Determination of the cutoff frequency f_c

In Sec. 4.3.2 we have identified a *cutoff* frequency f_c that separates quasi two-dimensional fluctuations from strongly three-dimensional ones (Fig. 4.11c, Fig. 4.11b and Fig. 4.11a). In this section we explain how we obtain f_c for a given true interaction parameter $N_t(L_i)$.

In order to calculate f_c precisely, we firstly apply a low-pass filter with variable cut-off frequency f_p in the range $\in [0.01, 20]\text{Hz}$, to time series of local electric potential gradients $\partial_y \phi'_w(x, y, 0, t)$ obtained at the bottom *Hartmann* wall. This gives us a set of frequency filtered signals $\partial_y \phi'^{\text{filt}}_w(x, y, 0, t, f_p)$ (note that for each set we vary f_p in steps $\Delta f_p \in [0.01, 0.1] \text{ Hz}$). Secondly, for each value of f_p we calculate the local correlation factor $C'_1(f_p)$ between the frequency filtered signal $\partial_y \phi'^{\text{filt}}_w(x, y, 0, t, f_p)$ and the unfiltered signal obtained along the same magnetic field line on the top *Hartmann* wall $\partial_y \phi'_w(x, y, L, t)$ (recall again that the correlation function C'_1 quantifies the appearance of strong three-dimensionality). We then spatially average local functions $C'_1(f_p)$ taking the same measurement points on which spatial averages $\langle C'_1 \rangle$ and $\langle C'_2 \rangle$ in Sec. 4.3.2 are based on (see also explanations to Fig. 4.10). This gives us the more global function $\langle C'_1(f_p) \rangle$ shown for $N_t(L_i) = 0.12$ and $N_t(L_i) = 692$ in Fig. B.1 and Fig. B.2 respectively. The cutoff frequency f_c corresponds to the value of f_p where the function $g(f_p) = \langle C'_1(f_p) \rangle$ is maximum. Power Spectral Density of related frequency filtered and unfiltered quantities plotted in Figs. B.1a, b, c, d show indeed that this maximum evaluates f_c very well. For low-pass filter frequencies $f_p < f_c$, strongly three-dimensional but also fraction of quasi-two-dimensional fluctuations are removed from the spectrum of $\partial_y \phi'^{\text{filt}}_w(x, y, 0, t, f_p)$ (Fig. B.1b). Accordingly, the value of the corresponding correlation factor $\langle C_1(f_p) \rangle$ is small (Fig. B.1). The function $\langle C_1(f_p) \rangle$ increases with increasing f_p and reaches a maximum at $f_p \approx f_c$ where the spectrum of $\partial_y \phi'^{\text{filt}}_w(x, y, 0, t, f_p)$ contains quasi-two-dimensional fluctuations only (Fig. B.1c). When further increasing the filter cutoff frequency in the range $f_p > f_c$, one progressively adds strongly three-dimensional fluctuations to the bottom signal $\partial_y \phi'^{\text{filt}}_w(0, t, f_p)$ and therefore the correlation factor $\langle C_1(f_p) \rangle$ decreases.

The above described technique applies still to flow regimes where the interaction parame-

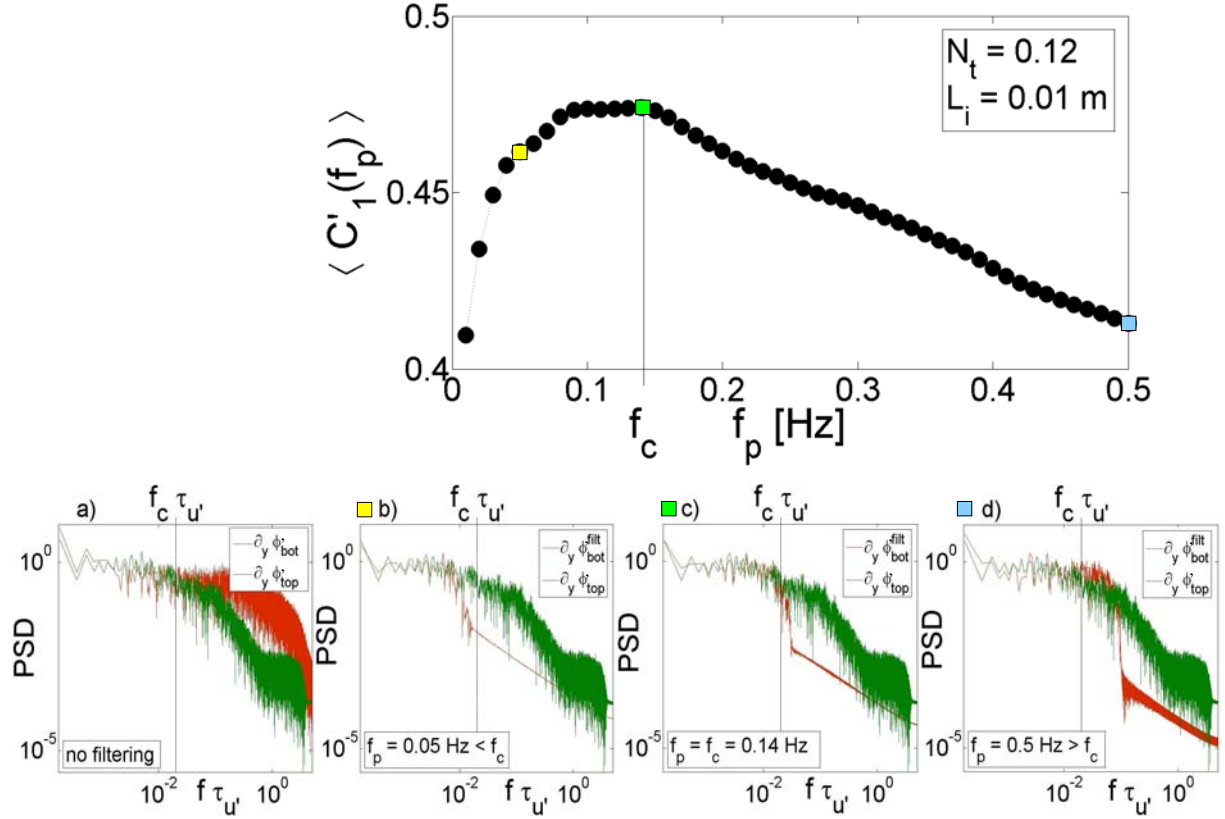


Figure B.1.: Determination of the cutoff frequency f_c . Top: spatially averaged correlation function $\langle C'_1(f_p) \rangle$ vs. cutoff frequency of the filter f_p for our smallest $N_t(L_i = 0.01\text{m}) = 0.12$. $\langle C'_1(f_p) \rangle$ is built on local correlations between frequency filtered bottom signals $\partial_y \phi_w^{\text{filt}}(x, y, 0, t, f_p)$ and corresponding unfiltered top signals $\partial_y \phi_w'(x, y, L, t)$. Bottom: Power Spectral Density of unfiltered top signals and related bottom signals: a) unfiltered. b) filtered with $f_p < f_c$. c) filtered with $f_p = f_c = 0.14\text{Hz}$. d) filtered with $f_p > f_c$. The flow related cutoff frequency f_c corresponds to the maximum of the function $\langle C'_1(f_p) \rangle$. Note that weak three-dimensionality that appear under the form of differential rotation in individual vortices can not be noticed as corresponding spectra are normalized by their largest frequencies in the spectrum)

ter $N_t(L_i)$ is high. Flow fluctuations in such regimes are mostly quasi two-dimensional over the full range of the frequency spectrum and the fraction of strongly three-dimensional ones is almost negligible. Although the maximum of the function $C'_1(f_p)$ is less noticeable in such regimes, we could still identify a flow related cutoff frequency f_c , even for our highest $N_t(L_i) = 692$ (Fig. B.2).

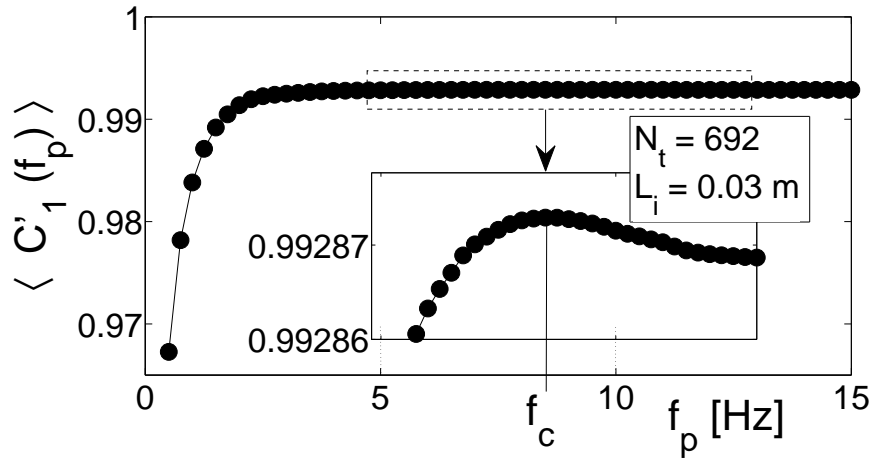


Figure B.2.: Determination of the the cutoff frequency f_c . Spatially averaged correlation function $\langle C'_1(f_p) \rangle$ vs. cutoff frequency of the filter f_p for our highest $N_t(L_i = 0.03\text{m}) = 692$. Our precise analysis allows us to identify a cutoff frequency f_c , although the strongly three-dimensional part of the spectrum of flow fluctuations is almost negligible.

C. Article: Experiment on a confined electrically driven vortex pair

Article published in *Physical Review E*, 79:016304, 2009.

Experiment on a confined electrically driven vortex pair

R. Klein^{*} and A. Pothérat

Coventry University, Priory Street, Coventry CV1 5FB, United Kingdom

A. Alferenok

Moscow Power Engineering Institute, Institute of Electrical Engineering, Krasnokazarmennaya Street 14, 111250 Moscow, Russia

(Received 15 July 2008; published 13 January 2009)

An experimental study of the transition to turbulence in a confined quasi-two-dimensional magnetohydrodynamic flow is presented. A pair of counterrotating vortices is electrically driven in the center of a thin horizontal liquid metal layer, enclosed in a cylindrical container and subject to a homogeneous vertical magnetic field. When the forcing is increased, the pair is displaced away from the center. Boundary layer separations from the circular wall appear that trigger a sequence of supercritical bifurcations. These are singled out in numerical calculations based on our previously developed shallow water model as well as in the experiment, and these bifurcations are shown to resemble those observed in flows past a cylindrical obstacle. For the highest forcing, the flow then ends up in a turbulent regime where the dissipation increases drastically, which we could relate to a possible transition from a laminar to a turbulent Hartmann boundary layer. Finally we show the first experimental evidence of a transition to three-dimensionality in liquid metal magnetohydrodynamics (MHD) by comparing velocity measurements on either horizontal sides of the layer as we find that columnar vortex wobble for a high enough forcing.

DOI: 10.1103/PhysRevE.79.016304

PACS number(s): 47.32.C-, 47.27.Cn, 47.20.Ib

I. INTRODUCTION

We are interested in the transition to turbulence induced by the presence of a wall in quasi-two-dimensional flows. In applications, boundaries are often responsible for the development of turbulence. Their role is, for example, crucial in the dynamics of wings or flying objects where boundary layer separations initiate vortex shedding and subsequent turbulent patterns that, in turn, determine lift and drag forces. The complexity of these flows makes them difficult to investigate experimentally and very costly to tackle numerically. In this regard, quasi-two-dimensional flows in simpler configurations allow us to easily reproduce some elementary properties of the transitions phenomena that occur in real configurations and to understand the two-dimensional part of their dynamics. This is why a large number of studies have been dedicated to the very generic quasi-two-dimensional separated flow past a circular cylinder (see Refs. [1–3] for a review of numerical work on boundary-generated two-dimensional turbulence). These flows are, to a large extent, determined by how single vortices or vortex pairs interact with walls so it is essential to understand the dynamics of such a reduced system. There has been a number of studies around this theme and one can cite two that are closest to our purpose: Ref. [4] demonstrated some elegant visualization of the vortex-wall interaction in liquid metal magnetohydrodynamic (MHD) flows and Ref. [3] recently performed numerical simulations of a forced vortex at the center of a square box. They exhibit a transition to turbulence through a sequence of supercritical bifurcations that leads to a chaotic, then turbulent state, as in the case of the cylinder wake. In

the present work, we aim at reproducing such a boundary induced transition to turbulence experimentally and analyze it, by studying a forced vortex pair confined in a circular domain.

Since a purely two-dimensional flow cannot be achieved experimentally, we wish to put a particular emphasis on the measure of residual three-dimensional effects and their consequences on the quasi-two-dimensional flow. To this end, we study a flow in a thin layer of liquid metal under an externally imposed, transverse magnetic field, as in Ref. [4]. This offers a simple way of reproducing a flow with two-dimensional dynamics. In such a laboratory scale configuration, the feedback action of the flow onto the magnetic field is neglected in the frame of the quasi-static approximation (Ref. [5]). The main effect of the Lorentz force is then to damp velocity variations along the magnetic field lines. If this transverse magnetic field is strong enough, the resulting flow is quasi-two-dimensionality in the sense that physical quantities do not vary across the layer except in the vicinity of the walls that confine it, where so-called Hartmann boundary layers develop because of the nonslip condition (see, for instance, Ref. [6]). Because of this particular flow structure, several small but important laboratory MHD experiments have been built where a layer of liquid metal held between two parallel planes is used to obtain an experimental realization of quasi-two-dimensional flows. Among them, Ref. [7] has provided an experimental evidence of the two-dimensional inverse energy cascade that characterizes two-dimensional turbulence. References [8,9] experimentally and Ref. [10] numerically have studied the quasi-two-dimensional wake of a circular cylinder and identified the usual regimes found in the hydrodynamic case. In none of these studies, however, was the actual limit of the quasi-two-dimensionality assumption examined, although more general studies have proposed theoretical scenarios for the transition between quasi-two-dimensional and three-dimensional flows

^{*}Also at: Applied Mathematics Research Centre, Coventry University.

(see Refs. [11,12]). This question is crucial in order to quantify the relevance of MDH flows in thin layers to two-dimensional flows. We shall therefore address it by calculating the correlations between velocities measured on either side of the fluid layer, just outside of the Hartmann layers as in Ref. [13] where the progressive elongation of a single pulsed vortex subject to a magnetic field was measured. This will allow us to determine whether the observed flow properties are influenced by three-dimensional effects or not.

Our experiment features an horizontal shallow fluid layer enclosed in a cylindrical container in a vertical magnetic field imposed by permanent magnets. A pair of counterrotating vortices is generated by injecting constant electric current through two point electrodes embedded in one of the horizontal, electrically insulating walls as in Refs. [7,4]. The flow characteristics are identified for different values of magnetic field \mathbf{B} and injected current I . This is done using both numerical simulations from the shallow water model of Ref. [14] and local measurements of electric potential to determine the velocity just outside of the Hartmann layers (e.g., Ref. [15]). We first present numerical calculations and the main flow patterns in Sec. II. In Sec. III A, we describe the experimental setup and the measurement techniques. The experimentally observed flow regimes are presented in Sec. III C and compared to the regimes found numerically in Sec. II. In Sec. III E, we characterize the bifurcations observed at the transition between these flow regimes. Finally we discuss the presence of three-dimensional effects in all observed flow regimes in Secs. III F and III G.

II. THEORY

A. Basic equations

The configuration of interest is that of a liquid metal (viscosity ν , density ρ , and electric conductivity σ) in a cylindrical container of height $a=5$ mm and radius $\tilde{R}=20$ mm plunged in a steady homogeneous magnetic field \mathbf{B} directed along the cylinder axis so that $\mathbf{B}=B_z\hat{\mathbf{e}}_z$. The walls of the container are electrically insulating and the flow is driven by connecting the two poles of a current generator to two metallic electrodes (diameter $d_e=1$ mm) embedded in the bottom plate at locations $(0,d,0)$ and $(0,-d,0)$ (see Fig. 6), where the origin is taken at the center of the bottom plate of the container. It is known from Ref. [11] that when the magnetic field is strong enough, the flow is invariant along the magnetic field lines, except near the wall orthogonal to the field where Hartmann layers with an exponential velocity profile develop. The Lorentz force then acts indirectly on the flow by shaping those layers, which in turn exert a linear friction on the resulting quasi-two-dimensional flow. The flow is now well described by two-dimensional motion equations obtained by averaging the full three-dimensional equations along the magnetic field lines, as in Ref. [11]. This model will thereafter be referred to as SM82. In the present cylindrical geometry, the high curvature of the streamlines, however, induces some strong inertial effects that disturb this simplified picture: Ref. [14] has indeed shown that strong rotation triggers a local Ekman pumping that leads to impor-

tant velocities along the magnetic field lines. Although quasi-two-dimensionality may still be achieved in the sense that the horizontal velocities in the core flow are still invariant along the magnetic field lines, these secondary flows lead to a significant redistribution of the flow's momentum that can drastically change the global dissipation. Reference [14] has further proposed a refinement of the SM82 model, denoted PSM, that accounts locally for these secondary flows through higher order nonlinear terms, and that we shall apply to our problem. In nondimensional variables, the PSM equations that govern the evolution of quantities averaged spatially along $\hat{\mathbf{e}}_z$ between the two Hartmann walls located at $z=0$ and $z=a$ yield

$$\nabla_{\perp} \cdot \mathbf{u}_{\perp} = 0, \quad (1)$$

$$\begin{aligned} & (\partial_t + \mathbf{u}_{\perp} \cdot \nabla_{\perp}) \mathbf{u}_{\perp} + \nabla_{\perp} p - \frac{N}{Ha^2} \nabla_{\perp}^2 \mathbf{u}_{\perp} \\ & = -2 \frac{N}{Ha} \mathbf{u}_{\perp} + \frac{2}{Ha N} \left(\frac{7}{36} \mathcal{D}_{\mathbf{u}_{\perp}} + \frac{1}{8} \partial_t \right) \mathbf{u}_{\perp} \cdot \nabla_{\perp} \mathbf{u}_{\perp} + \mathbf{f}, \end{aligned} \quad (2)$$

where the operator $\mathcal{D}_{\mathbf{u}_{\perp}}$ is defined as

$$\mathcal{D}_{\mathbf{u}_{\perp}} : \mathbf{F} \mapsto \mathcal{D}_{\mathbf{u}_{\perp}} \mathbf{F} = (\mathbf{u}_{\perp} \cdot \nabla_{\perp}) \mathbf{F} + (\mathbf{F} \cdot \nabla_{\perp}) \mathbf{u}_{\perp}. \quad (3)$$

Quantities averaged along $\hat{\mathbf{e}}_z$ are by definition dependent only on x and y . The corresponding Nabla operator ∇_{\perp} is two-dimensional and carries the subscript $(\)_{\perp}$. Similarly, the same subscript on a vector indicates components perpendicular to the magnetic field only. All quantities have been further normalized using the dimensional quantities U_0 and a as reference velocity and distance. Furthermore, the superscript on observed quantities such as velocities, velocity fluctuations, and distances, thereafter presented in the experimental part Sec. III denotes a dimensional quantity (e.g., $R=\tilde{R}/a$ as the dimensionless counterpart of \tilde{R}). The square of the Hartmann number $Ha=aB_z\sqrt{\sigma/(\rho\nu)}$ and the interaction parameter $N=\sigma B_z^2 a/(\rho U_0)$ represent the ratio of the Lorentz forces to viscous and inertial forces, respectively, so both are required to be larger than unity for the PSM model to be valid.

Out of the two additional terms that appear in the right-hand side of Eq. (2), the first one is linear and results from the friction induced by the Hartmann layer on the two-dimensional flow. The associated dimensional Hartmann damping time $t_H=(1/2)(a^2/\nu)(1/Ha)$ strongly decreases with B_z , indicating the nature of the magnetohydrodynamic (MHD) effect: when the magnetic field increases, the Hartmann layer becomes thinner thus inducing a stronger friction on the flow. The other additional terms are nonlinear and result from the redistribution of momentum due to local Ekman pumping. The model also provides the expression of the dimensionless velocity u_z along the field lines just outside the Hartmann layer (for a mathematically rigorous definition of this concept, see Refs. [16,17]):

TABLE I. Nondimensional parameters and related time step in cases calculated numerically.

regime	I		II			III	IV								
Re^0	216	2164	4328	6494	7576	8116	8658	9740	10822	11904	12986	15152	17316	21644	28138
Re^M	89.8	846	1567	2250	2580	2740	2898	3245	3573	3894	4188	4768	5281	6122	7174
R_δ^{num}	0.5	4.9	9.1	13.1	15	15.9	16.9	18.9	20.8	22.6	24.4	27.7	30.7	25.6	41.7
N_v	137.2	13.7	6.9	4.6	3.9	3.7	3.4	3.0	2.7	2.5	2.3	2.0	1.7	1.4	1.1
Δt	0.05	0.01	0.005	0.01/3	0.01/3	0.01/3	0.0025	0.0025	0.002	0.002	0.002	0.002	0.001	0.001	0.001

$$u_z(z=0) = -\frac{5}{6} \frac{a^2}{\tilde{R}^2 \text{Ha}} \frac{1}{N_v} \nabla_{\perp} \cdot [(\mathbf{u}_{\perp} \cdot \nabla_{\perp}) \mathbf{u}_{\perp}], \quad (4)$$

where $N_v = N\tilde{R}/a \geq 1$ is the interaction parameter based on the horizontal scale. The ratio $u_z/\|\mathbf{u}_{\perp}\|$ gives a good indication as to where Ekman pumping is important. $u_z > 0$ ($u_z < 0$) indicates that fluid is expelled from (injected in) the Hartmann layers to (from) the core flow. Some detailed accounts of this effect are presented in Refs. [14,18,19].

The forcing \mathbf{f} results from the interaction of the electric current injected at the electrodes with the external magnetic field, which, by virtue of the Hartmann layer theory is equivalent to imposing a vorticity along $\hat{\mathbf{e}}_z$, proportional to the injected current. Following Refs. [7,14], the forcing imposed on the flow by an electric current I injected through an electrode of diameter d_e , with the center located at \mathbf{r}_e expresses dimensionally as

$$\mathbf{f}(\mathbf{r}) = \frac{\Gamma}{t_H} \frac{\mathcal{H}\left(\|\mathbf{r} - \mathbf{r}_e\| - \frac{d_e}{2}\right)}{\|\mathbf{r} - \mathbf{r}_e\|} \hat{\mathbf{e}}_{\theta}, \quad (5)$$

where $\Gamma = I/(2\pi\sqrt{\sigma\rho\nu})$ is the total circulation induced by the current injection at one electrode and \mathcal{H} is the Heaviside step function. $\hat{\mathbf{e}}_{\theta}$ denotes the azimuthal direction with respect to the center of the electrode. Since the nondimensional forcing \mathbf{f} that appears in Eq. (2) is induced by the two electrodes with opposite polarities, respectively, located at $\mathbf{r}_e^+ = d\hat{\mathbf{e}}_y$ and $\mathbf{r}_e^- = -d\hat{\mathbf{e}}_y$, it can be written in nondimensional form as

$$\mathbf{f}(\mathbf{r}) = \frac{\tilde{R} N}{a \text{Ha}} \left(\frac{\mathcal{H}\left(\|\mathbf{r} - \mathbf{r}_e^+\| - \frac{d_e}{2}\right)}{\|\mathbf{r} - \mathbf{r}_e^+\|} \hat{\mathbf{e}}_{\theta}^+ - \frac{\mathcal{H}\left(\|\mathbf{r} - \mathbf{r}_e^-\| - \frac{d_e}{2}\right)}{\|\mathbf{r} - \mathbf{r}_e^-\|} \hat{\mathbf{e}}_{\theta}^- \right), \quad (6)$$

where $\hat{\mathbf{e}}_{\theta}^+$ ($\hat{\mathbf{e}}_{\theta}^-$) again points in the azimuthal direction with respect to the electrode located at \mathbf{r}_e^+ (\mathbf{r}_e^-). This suggests $U_0 = 2\Gamma/d$ as a reference velocity *a priori* with the corresponding Reynolds number $\text{Re}^0 = U_0 \tilde{R} / \nu$ and underlines the fact that the ratio of two-dimensional inertial effects to the Lorentz force is measured by $(\tilde{R}/a)(N/\text{Ha})$, rather than the interaction parameter N . Similarly, since U_0 is derived from the forcing only, and ignores all types of dissipation present in the flow [viscous, Hartmann layer friction, effect of three-dimensional (3D) recirculations], it is clearly larger than the true flow velocity, albeit of the same order of magnitude. A more realistic Reynolds number Re^M based on the maximum

velocity along $\hat{\mathbf{e}}_x$ and therefore calculated *a posteriori* is therefore given alongside Re^0 in Table I that can be used as an *a priori* control parameter.

Finally, a nonslip boundary condition is applied at the impermeable wall located at $\|\mathbf{r}\| = R$. Note that Eq. (2) implies that this wall is electrically insulating.

Before proceeding with the numerical resolution of the PSM equation presented in this section, it is worth recalling that this model is a shallow water approximation [such as those widely used in geophysical flows (see Ref. [20])], obtained by integration of the full Navier-Stokes equations along the magnetic field. This integration is performed by approximating the velocity profile in the z direction at order 2 for the small parameters Ha^{-1} and N_v^{-1} . At this order, the Hartmann layer is assumed laminar and the three-dimensional velocity field $\mathbf{u}_{\text{Ha}}(x, y, z, t)$ within the Hartmann layer expresses as

$$\mathbf{u}_{\text{Ha}}(x, y, z, t) = \mathbf{u}^{\text{core}}(x, y, t) f(z), \quad (7)$$

where $f(z)$ represents both the two-dimensional flow in the core with the velocity field $\mathbf{u}^{\text{core}}(x, y, t)$ and the classical exponential velocity profile in the laminar Hartmann layer. In the PSM model, however, this profile is modified to account for inertial effects of order N_v^{-1} (see Ref. [6]), while the horizontal velocity outside these layers is invariant in the z direction. Since $f(z)$ is obtained from assumptions in the limit of small Ha^{-1} and N_v^{-1} , the model is free from artificial modelling but also implies that it becomes imprecise when either of the parameters Ha^{-1} or N_v^{-1} becomes of order 1. Reference [21] has shown that for $N < 1$, the secondary flows due to local Ekman pumping are overestimated (note that values of N_v for our simulations are given in Table I).

The validity of the model of Ref. [14] is further affected depending on whether the Hartmann layer is laminar or turbulent. From the form of Eq. (7), three important cases can be distinguished.

(a) If the velocity field $\mathbf{u}^{\text{core}}(x, y, t)$ becomes turbulent while $f(z)$ remains unaffected, the flow is in a quasi-two-dimensional turbulent state, but still with a laminar Hartmann layer and the PSM model from Ref. [14] remains valid.

(b) If the Hartmann layer becomes turbulent, the function $f(z)$ takes a different form although the core flow outside the layer may still be two-dimensional, as observed by Ref. [22]. In this case the PSM model breaks down as it cannot account for a turbulent Hartmann layer profile nor for the transition between a laminar and a turbulent Hartmann layer. This transition happens at the critical Reynolds number $R_\delta = \text{Re}^M / \text{Ha}$

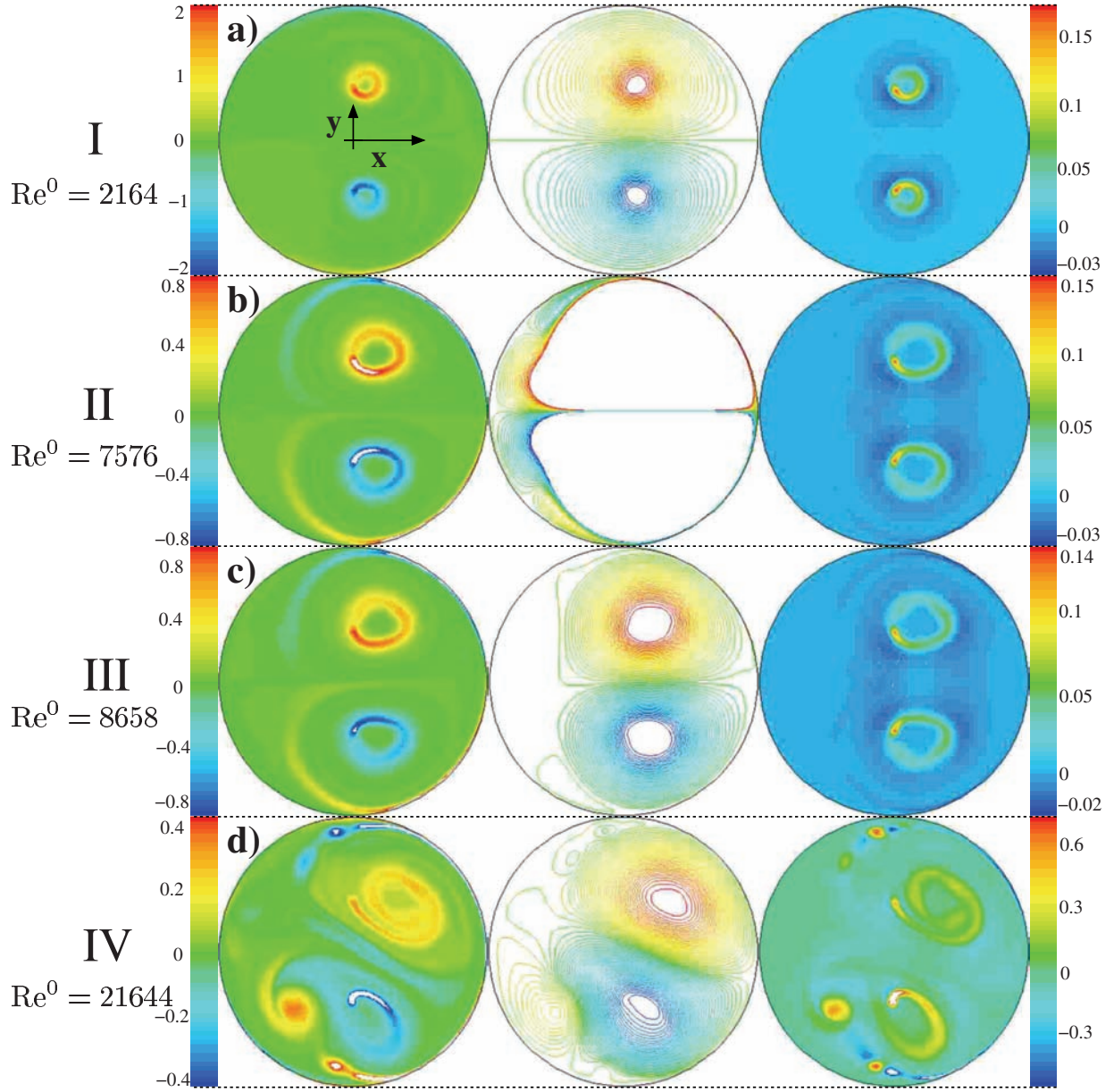


FIG. 1. (Color online) Snapshots of equilibrium and quasi-equilibrium states in all flow regimes for $\text{Ha}=43$ obtained from numerical simulations. Contours of vorticity normalized by U_0/a (left column), streamlines (center column), contours of vertical velocity as given by Eq. (4), normalized by U_0 (right column). (a) Regime I, (b) regime II, (c) regime III, (d) regime IV.

in the case of a channel flow (see Ref. [23]). In the present simulations, however, R_δ^{num} remains an order of magnitude below this critical value (see Table I).

(c) If the flow is in a state of full three-dimensional turbulence, the velocity field may not take the form of Eq. (7) anymore. In spite of the above limitations, the PSM model is better suited to our goal of finding the main flow patterns than three-dimensional direct numerical simulations for several distinct reasons: on the top of its simplicity and natural precision at high Ha and N_v , PSM removes the necessity of meshing the very thin Hartmann layers and also eliminates

the coupling between velocity and electric potential that is inherent to the 3D MHD equations. The resolution of these coupled equations demands special care indeed, in order to be accurately resolved (see Refs. [24,25]).

B. Numerical model

We shall now solve the system (2) numerically, in order to visualise the different flow states when the electric current is increased. Velocity profiles recorded along diameter $y=0$ will then be compared to the measurements from the experi-

ment in Sec. III in order to help identify the regimes found experimentally, as no global flow visualization is possible in our setup. The comparison can, however, only remain qualitative as wall roughness present in the experiment is not modeled in the numerical simulation. The latter is expected to stabilize the flow and to shift the transitions between quasi-two-dimensional flow regimes identified in this section further. Since the initial problem has been reduced to a two-dimensional one thanks to the PSM model, we are now left with the task of solving the unsteady equations (2) on a disk of radius R . To this end, we use the numerical method and mesh described and tested in Ref. [19], where a numerically similar problem to ours is considered, but with a different forcing. Also, compared to theirs, our numerical system now uses a third instead of a second order spatial discretization, which slightly improves precision, especially on the unstructured part of the mesh. All computations are performed for $\text{Ha}=43$ with the fluid initially at rest and with the injected current I (hence Re^0) set to a constant value. The calculation runs until the total energy of the flow is stable over a time much longer than t_H or than all remaining oscillations. Averaged quantities reported thereafter are then computed over a time interval of several times t_H . Table I summarizes the different cases we have simulated.

C. General aspect of the flow

When the forcing is increased from $I=0$, the final flow state goes through a sequence of bifurcations that can be seen from the contours of vorticity and streamlines represented on Fig. 1. We shall now describe these globally, whereas local quantities such as velocity profiles are reported together with experimental results in Sec. III.

At very low forcing, i.e., at low Re^0 , the flow essentially consists of two steady counterrotating vortices, antisymmetric about the $\hat{\mathbf{e}}_x$ axis and centred slightly to the right of the electrode axis [Fig. 1(a)]. The distance between the axis of their centers and that of the electrodes results from the balance between their mutual influence that tends to imprint a motion toward $x>0$, and the influence of the circular wall. Each of these vortices presents a sharp vorticity maximum located away from the vortex centre that corresponds to a free shear layer in the shape of a ring. This first steady regime will be denoted “I” thereafter and the corresponding Re^0 are displayed in Table I.

For slightly higher values of Re^0 , the flow remains steady but the boundary layers located along the cylinder wall or side layers separate in two symmetric locations behind the vortices so a small counterrotating recirculation appears behind each of the initial vortices [Fig. 1(b)]. These two anti-symmetric recirculation regions are analogous to those in duct flows past a cylindrical obstacle with an homogeneous magnetic field oriented along the cylinder axis, as studied by Ref. [10]. Unlike these, however, those from the present problem remain apart from each other as the main flow reattaches to the cylinder wall. The length of the recirculation region along the wall, however, increases with Re^0 . By analogy with Ref. [10], we will call this second steady flow regime “regime II” (see Table I).

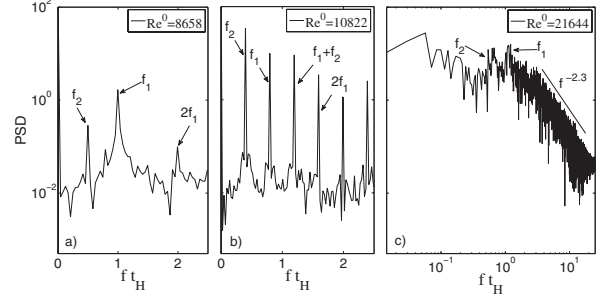


FIG. 2. Power density spectra obtained from $u(0,t)$ for $\text{Ha}=43$. Energy and frequencies are normalized by $U_0^2/2$ and t_H^{-1} , respectively. (a) $\text{Re}^0=8658$, regime III. (b) $\text{Re}^0=10\,822$, regime IV. (c) $\text{Re}^0=21\,644$, regime IV. Note that for $\text{Re}^0=8658$ the flow is nearly in regime IV, however, the amplitude of the corresponding oscillation with frequency f_2 remains small.

For higher Re^0 a new regime (regime III, see Table I) appears where the separated boundary layers at the back of the vortices destabilize. Vortices form there and grow along the layer until they are released in the stream between the two electrodes, resulting in the appearance of a low frequency f_1 in the oscillations of the velocity field see [Figs. 1(c) and 2(a)]. This shedding process is reminiscent of that in the Von Kàrmàn street behind a cylindrical obstacle (see Refs. [1,10]), but differs from it in two ways: first, at the forcing for which this phenomenon first appears, vortices are released almost simultaneously and not in turn. This synchronization is, however, lost at slightly higher forcing. Second, two very weak additional vortices are released along the centerline in the direction $x<0$. The frequency spectrum of $|u_x^2(0,t)+u_y^2(0,t)|$ that characterizes this regime exhibits strong peaks for the fundamental frequency f_1 of vortex shedding as well as for the higher harmonic $2f_1$ [Fig. 2(a)].

A further flow regime, called regime IV (see Table I) is found when a lower base frequency f_2 appears in the frequency spectrum [see Fig. 2(b)]. In this regime, the central vorticity rings are strongly disrupted and exhibit both short and long wave instabilities. Also, vortices that shed in the direction $x<0$ become stronger so the global picture is that of a strongly chaotic flow. Interestingly, Ref. [10] also pointed out the appearance of a lower frequency in the regime he calls IV, where the Von Kàrmàn street is disrupted by vortices generated due to boundary layer separation at the duct side walls. The periodic Von Kàrmàn street regime they find, however, spans a much larger interval of Re^0 . The reason is that in our case, the vortex shedding process is immediately disturbed by the reinjection of shed vortices in the main stream, whereas the flow around the cylinder has to reach much higher velocities for shed vortices to produce some boundary layer separation at the duct walls.

Further regime changes at higher forcing are much more difficult to detect as the flow becomes fully turbulent. At $\text{Re}^0=21644$, the spectrum exhibits the $|u_x^2(0,t)+u_y^2(0,t)| \sim f^{-2.3}$ power law in the mid range [see Fig. 2(c)]. A spatial energy spectrum can be deducted from these frequency spectra by defining the wave number sequence as $k=f|u(0,t)|$. Since at this location, the flow is dominated by a strong jet in

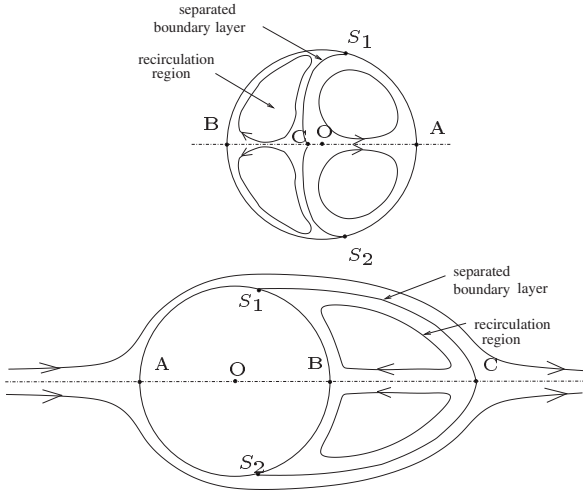


FIG. 3. Steady flows and flows with separations within (top) and outside (bottom) a cylinder. A, B, and C are stagnation points, S_1 and S_2 are separation points.

the direction $\hat{\mathbf{e}}_x$, $k_x \sim f|\langle u(0,t) \rangle|$, where $\langle u(0,t) \rangle$ is the time average from $u(0,t)$. This implies that $|u_x^2(0,t) + u_y^2(0,t)| \sim k_x^{-2.3}$. For $Re^0 = 21\,644$ and $Re^0 = 28\,138$ (Table I) which are the highest in our numerical simulations, however, one can expect the secondary flows to be slightly overestimated as N_v comes close to unity (see Ref. [21]).

D. Similarities with the flow around a cylinder

To further investigate the similarity between the present flow and the duct flow past a cylinder under axial magnetic field studied by [10], we define the base pressure coefficient $C'_{pb} = (p_A - p_C)/[\rho(\tilde{u}_x^M)^2]$ where \tilde{u}_x^M is a dimensional quantity and denotes the maximum velocity of \tilde{u}_x along the diameter $\tilde{y}=0$ (p_A as well as p_C refer to the pressure at stagnation points A and C, respectively, as displayed in Fig. 3). Its variation as a function of $Re^M = \tilde{u}_x^M \tilde{R}/\nu$ (see Table I for values of Re^M) and Re for fixed Ha is shown in Fig. 4(a) for a

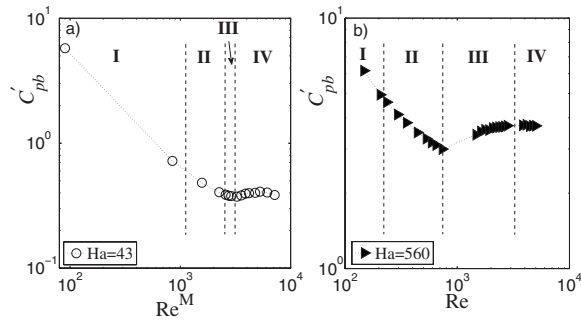


FIG. 4. Base pressure coefficients C'_{pb} in flow regimes I, II, III, and IV obtained from numerical simulations. (a) C'_{pb} vs Re^M for the flow within a cylinder for $Ha=43$. (b) C'_{pb} vs Re for a flow past a cylinder for $Ha=560$ (see Ref. [10]). Re is built on average velocity at the duct inlet.

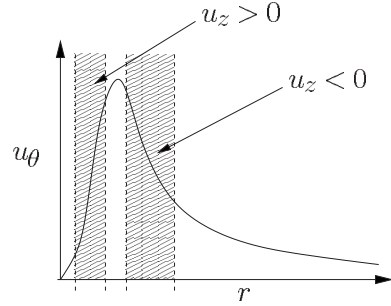


FIG. 5. Typical profile of an electrically driven vortex (see, for instance, Refs. [4,14]). A strong flow from the Hartmann layers to the core appears in vortex core, while a strong reverse flow takes place in the high velocity region just outside the core

flow within the cylinder and for a flow past the cylinder in Fig. 4(b) (found by Ref. [10]), respectively. For the latter, the Reynolds number Re is built on average velocity at the duct inlet. Although only high Hartmann results are available from Ref. [10], the evolution of C'_{pb} is similar between both problems throughout regimes I to III [see Figs. 4(a) and 4(b)]. In particular, C'_{pb} decreases in the steady regime and increases in the unsteady regime. Evolutions of C'_{pb} for flows that are well in regime III and thereafter in regime IV differ but this might be due to the effect of three-dimensional recirculations which become dominant since N_v approaches unity in the cases calculated here. These recirculations are known to significantly increase the dissipation in concave parallel layers (see Refs. [14,19]) and can therefore be expected to influence C'_{pb} strongly. They are, however, suppressed at such high values of N_v such as those from Ref. [10].

E. Effect of the Ekman recirculations

The third column from Fig. 1 shows the contours of $u_z(x,y)$ calculated from Eq. (4). This equation implies that this quantity is larger where horizontal velocity gradients are more important as strong fluid sources and sinks appear in the core flow. The associated horizontal transport of angular momentum can drastically increase the viscous dissipation, in particular where boundary layers are involved, as shown in Ref. [19].

A further effect is that vortices are surrounded by regions where the fluid plunges into the Hartmann layers, as also shown by the three-dimensional numerical simulations of Ref. [26] in the non-MHD case. This can be understood by considering an axisymmetric clockwise vortex, centered at the origin, with typical profile shown on Fig. 5. Then, Eq. (4) implies that $u_z(r) \sim 1/r \partial_r u_\theta^2$. Near the vortex center, the velocity must be zero so $u_\theta \sim r^\alpha$ with $\alpha > 0$ and $u_z(r) \sim 2\alpha r^{2\alpha-1}$. This means that a strong Ekman pumping is present there with $u_z > 0$. Further out, the velocity is high but decreases as $u_\theta \sim r^\alpha$, with $\alpha < 0$ this time, so a surrounding region with strong vertical velocities toward the Hartmann layers must exist just outside the vortex core.

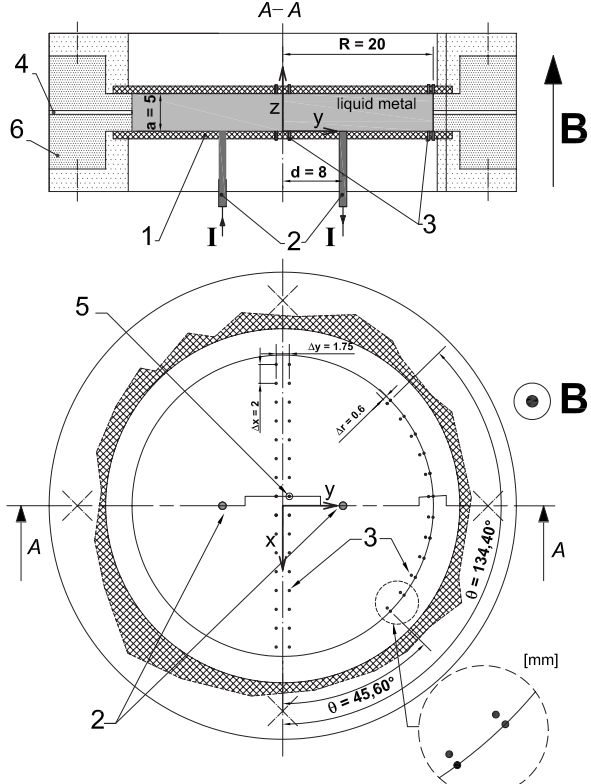


FIG. 6. Experimental apparatus. Top: cross section of the cylindrical container, bottom: top view of the bottom plate. (1) Electric board, (2) electric current injection electrodes (diameter $d_e=1$ mm), (3) electric potential probes, (4) inlet and outlet to fill cavity with GaInSn, (5) reference probe for electric potential measurements, (6) plexiglas hollow cylinder. $\Delta\tilde{x}=2.5$ mm, $\Delta\tilde{y}=1.75$ mm, and $\Delta\tilde{z}=0.6$ mm are the distances between the potential probes.

III. EXPERIMENT

A. Experimental setup and measurement techniques

The main experimental apparatus (Fig. 6) is made of a closed cylindrical container with radius $\tilde{R}=20$ mm and height $a=5$ mm, where all walls are electrically insulating. The cavity is hermetically filled with GaInSn, a metal alloy liquid at room temperature (electric conductivity $\sigma=2.3 \times 10^6$ S/m, density $\rho=6440$ kg/m³, viscosity $\nu=4 \times 10^{-7}$ m²/s). The top and bottom plates of thickness 1.5 mm are made of fiber-reinforced epoxy FR4, which is a standard material for electronic boards.

Once filled, the apparatus is centered inside the gap between two sets of identical permanent magnets (surface 120×100 mm). Magnetic fields of $B_z=0.09$ T, $B_z=0.12$ T, $B_z=0.19$ T, and $B_z=0.24$ T with maximum inhomogeneity of 10% along $\hat{\mathbf{e}}_y$, 4% along $\hat{\mathbf{e}}_x$, and 1% along $\hat{\mathbf{e}}_z$ over the fluid domain, are achieved by adjusting the gap width.

The flow is forced by injecting constant electric current I through two copper electrodes (diameter $d_e=1$ mm) fitted flush to the bottom wall at $(0, d, 0)$ and $(0, -d, 0)$ and with $d=8$ mm. Both electrodes are connected to a regulated DC

TABLE II. Characteristic Hartmann friction time t_H and Hartmann number Ha .

B [T]	0.09	0.12	0.19	0.24
$t_H = \frac{a^2}{2\nu} \frac{1}{Ha}$ [s]	3.3	1.75	1.1	0.85
$Ha = aB \sqrt{\frac{\sigma}{\rho\nu}}$	13.5	18	28.5	36

power supply, providing electric currents in the range $I \in [0-20A]$ with a maximum ripple 0.5×10^{-3} A.

Electric potential ϕ is measured locally thanks to two symmetric sets of 56 potential probes (diameter $\phi d_{pr} = 0.25$ mm) embedded in the top and bottom wall, respectively, at locations sketched on Fig. 6. The two sets are aligned exactly opposite each other along the $\hat{\mathbf{e}}_z$ axis. The measured signals are typically of the order of $10 \mu\text{V}$ and must therefore be amplified by a high precision, low-noise system. We use a 112 multichannel single ended amplifier system with gain 111 and integrated 24 bit A/D converter for every channel, that measures each electric potential with respect to one electric potential probe (reference probe), located near the box center (see Fig. 6). All signals are simultaneously recorded at a sampling rate of 128 Hz, for which the peak to peak noise is about $2 \mu\text{V}$.

As, e.g., noticed by Refs. [15,7], the electric current density in the core flow $\|\mathbf{j}^{\text{core}}\|$ is small in quasi-two-dimensional and even weakly three-dimensional flows so Ohm's law in the core flow can be approximated by $-\nabla\phi^{\text{core}} + \mathbf{u}^{\text{core}} \times \mathbf{B} \approx 0$, to a precision of the order of $\frac{\|\mathbf{j}^{\text{core}}\|}{\sigma}$. Since the variation of electric potential across the boundary layer is $O(\delta/a)$, with $\delta = \frac{a}{Ha}$ as the Hartmann layer thickness, the electric potential field in the core is nearly that measured at the Hartmann wall, to this same precision. Combining these two arguments leads to $-\nabla\phi_{\text{wall}} + \mathbf{u}^{\text{core}} \times \mathbf{B} \leq O(\max|\frac{\delta}{a}, \frac{\|\mathbf{j}^{\text{core}}\|}{\|\mathbf{u}^{\text{core}} \times \mathbf{B}\|}|)$. As long as $\frac{\delta}{a} \ll 1$ and $\frac{\|\mathbf{j}^{\text{core}}\|}{\|\mathbf{u}^{\text{core}} \times \mathbf{B}\|} \ll 1$, the velocity just outside the Hartmann layer can be deduced from probes embedded in the wall and, respectively, distant by $\Delta\tilde{x}$ and $\Delta\tilde{y}$ from one another by Fig. 6:

$$\begin{aligned} \tilde{u}_x &= -\frac{1}{B_z} \left(\frac{\tilde{\phi}_{\text{wall}}(\tilde{x}, \tilde{y} + \Delta\tilde{y}) - \tilde{\phi}_{\text{wall}}(\tilde{x}, \tilde{y})}{\Delta\tilde{y}} \right), \\ \tilde{u}_y &= \frac{1}{B_z} \left(\frac{\tilde{\phi}_{\text{wall}}(\tilde{x} + \Delta\tilde{x}, \tilde{y}) - \tilde{\phi}_{\text{wall}}(\tilde{x}, \tilde{y})}{\Delta\tilde{x}} \right). \end{aligned} \quad (8)$$

In order to take advantage of Eq. (8), the probes have been placed so as to obtain profiles of velocities \tilde{u}_x and \tilde{u}_y along the diameter $\tilde{y}=0$ (Fig. 6). Velocity profiles $\tilde{u}_\theta(\tilde{r}, \theta, t)$ near the side walls at $\tilde{r}=19.7$ mm for $\theta \in [45.6^\circ, 134.4^\circ]$ (see Fig. 6) are measured in the same way, however using $\Delta\tilde{r}=0.6$ mm as radial spacing between probes. Finally it is important to notice that even if the Hartmann layer becomes turbulent, its thickness δ remains very thin (see Ref. [27]) so the assumption $\frac{\delta}{a} \ll 1$ is still valid. Furthermore, the core flow above a turbulent Hartmann layer also remain two-

dimensional, provided the turn-over time l_\perp/u of turbulent vortices, of size l_\perp and spinning velocity u , remains large compared to the time of two-dimensionalization $\frac{\rho \cdot a^2}{\sigma B^2 l_\perp^2}$ (see Refs. [11,22]). This suggests that Eq. (8) remains valid, even when the Hartmann layer becomes turbulent. Finally, in order for three-dimensionality to spoil the validity of Eq. (8), the current in the core would have to be $O(\mathbf{u}^{\text{core}} \times \mathbf{B})$. This only occurs in strongly three-dimensional flows so the method presented here also applies to weakly three-dimensional flows, albeit with a larger error than in quasi-two-dimensional flows.

Electric potentials, measured on potential probes aligned exactly opposite each other along the $\hat{\mathbf{e}}_z$ axis, allow us to derive the velocity correlations between points located just outside the Hartmann layer on either wall. A velocity correlation coefficient lower than one indicates that the flow is three-dimensional in the sense that the velocity varies along the magnetic field lines outside the Hartmann layer.

B. Experimental procedure

Starting at $I=0A$, the electric current is first increased in steps of $0.1A$ up to the maximum value of $I=10A$. If a bifurcation is found at critical electric current I_c , the step size is reduced to $0.01A$ within the range $I_c \pm 0.05A$. Once $I_c + 0.05A$ is reached, a possible hysteresis around I_c is sought by decreasing the current in the same steps. The electric current I is expressed under nondimensional form through the Reynolds number Re^0 that measures the forcing (see Sec. II A). For each forcing we wait several times the Hartmann friction time t_H until the flow is fully developed and start then recording time dependent electric potentials over at least $10t_H$ (Table II). Quantities averaged in time in the established flow regime are denoted $\langle \cdots \rangle$ thereafter.

This procedure is repeated for four different values of magnetic field strength B_z , which correspond to nondimensional Hartmann numbers Ha presented in Table II. Ha as well as Re^0 are then the two control parameters in this experiment. Thus, critical values Re_{III}^0 , Re_{IV}^0 , Re_{V}^0 , and Re_{3D}^0 mentioned thereafter, are in fact functions of the Hartmann number as shown in Fig. 7.

C. Flow regimes identified from velocity profiles

For weak forcing, such that $Re^0 < Re_{\text{II}}^0$, the flow is steady and the corresponding profile of u_x [marked by “I” in Fig. 8(a)] along the diameter $y=0$ is almost symmetric about $x=0$, with $u_x > 0$ everywhere. In this regime, the point of maximum velocity u_x^M is, however, located at $x^M > 0$, x^M being small and increasing with Re^0 [Fig. 9(a)]. Velocities $u_\theta(r=0.985R, \theta, t)$, measured near the cylinder wall, are anticlockwise orientated and almost azimuthal, without any sign reversal (Fig. 10). In the numerical simulations (Sec. II C) this type of profile is typical from regime I [Fig. 11(a)], and the location of the maximum velocity u_x^M along the diameter $y=0$ corresponds to the position of the initial vortex pair.

For $Re^0 \geq Re_{\text{II}}^0$, the flow changes to a second steady state (regime II), where the velocity profile $u_\theta(r=0.985R, \theta, t)$ first

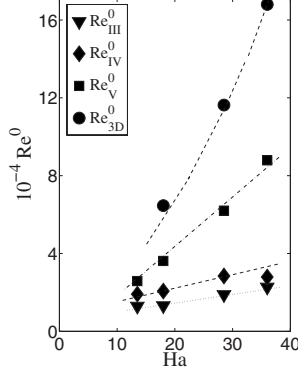


FIG. 7. Critical Reynolds numbers vs Hartmann number. Re_{III}^0 : transition from the steady flow regime to the periodic flow regime. Re_{IV}^0 : transition from the periodic flow regime to the flow regime with two base frequencies. Re_{V}^0 : transition to the flow regime where the profile of u_x almost becomes symmetric again. Re_{3D}^0 : transition to three-dimensionality (see Sec. III F).

exhibits a change of sign at angle θ_s , (Fig. 10), that corresponds to the separated boundary layer found in Sec. II C. When the forcing is further increased, the flow still remains steady and θ_s is displaced along the wall in clockwise direction [Fig. 9(c)]. This displacement also coincides with the increase of x^M , which indicates that it is a consequence of the displacement of the initial vortex pair in the $x > 0$ direction.

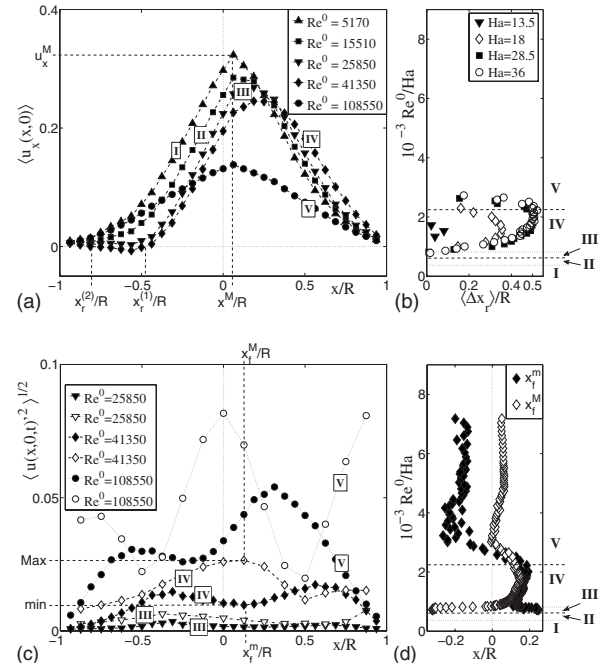


FIG. 8. Time averaged quantities. (a) Velocity profiles $\langle u_x(x,0) \rangle$ for $Ha=36$. (b) Width of recirculating region $\langle \Delta x_r \rangle = \langle x_r^{(1)} - x_r^{(2)} \rangle$ vs Re^0/Ha . (c) r.m.s. of velocity fluctuations $\langle u'(x,0,t) \rangle$ along the diameter $y=0$ for $Ha=36$. Black markers: $\langle u'_x(x,0,t)^2 \rangle^{1/2}$, white markers: $\langle u'_y(x,0,t)^2 \rangle^{1/2}$. (d) x_f^m and x_f^M vs Re^0/Ha for $Ha=36$. The corresponding flow regimes are indicated as I, II, III, IV, and V.

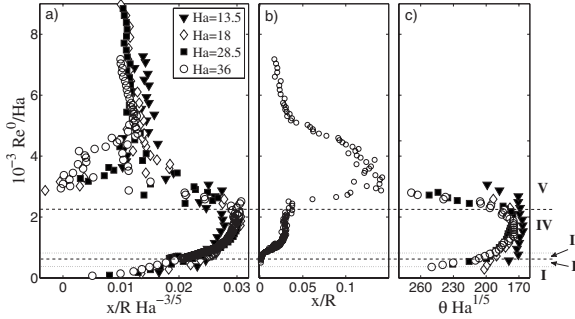


FIG. 9. (a) $\langle x^M \rangle$ vs Re^0/Ha . (b) Standard deviation $\sigma(x^M)$ vs Re^0/Ha for $\text{Ha}=36$. (c) $\langle \theta_s' \rangle$ vs Re^0/Ha .

The zone of positive azimuthal velocity for $\theta > \theta_s'$, in Fig. 10 therefore characterizes the antisymmetric counterrotating recirculation regions that appear behind each of the two initial vortices because of the separated boundary layer (see Sec. II C).

The unsteady flow regime sets in at $\text{Re}^0 = \text{Re}_{\text{IV}}^0$ [“III” in Fig. 8(a)]. It results in a periodic oscillation in $\phi(x, y, t)$ and is characterized by strong peaks with base frequency f_1 and further harmonics $2f_1$ and $3f_1$ in the frequency spectrum. Corresponding spectra, recorded from measurements on the top plate at $x = -0.4375R$ and $y = -0.04375R$ are shown on Fig. 12(a) (power spectra taken from potential measurements at other locations yield qualitatively similar results). Accordingly, x^M and θ_s' are time-dependent and when the forcing is intensified, $\langle x^M \rangle$ and the standard deviation $\sigma(x^M) = \langle [x^M(x, 0, t) - \langle x^M(x, 0) \rangle]^2 \rangle^{1/2}$ increase. Also, $\langle \theta_s' \rangle$ is displaced along the circular wall in the $\theta < 0$ direction [see Fig. 9(c)]. The good qualitative agreement between numerical and experimental mean velocity profiles, as well as the r.m.s. of velocity fluctuations $\mathbf{u}'(x, 0, t)$, with $u_x(x, 0, t)' = u_x(x, 0, t) - \langle u_x(x, 0) \rangle$ and $u_y(x, 0, t)' = u_y(x, 0, t) - \langle u_y(x, 0) \rangle$, proves that these measurements characterize the vortex shedding regime found in numerical simulations [Figs. 11(a) and 11(b) and Figs. 8(a) and 8(c), respectively]. This also explains the presence of maxima at $x < 0$ in the profiles III of $\langle u_x'(x, 0, t)^2 \rangle^{1/2}$ and $\langle u_y'(x, 0, t)^2 \rangle^{1/2}$ plotted along the diameter $y=0$, as they correspond to the location where the shed vortices impact onto the centerline [see Figs. 11(b) and 8(c)].

For $\text{Re}^0 = \text{Re}_{\text{IV}}^0$, a second base oscillation f_2 , with $f_2 < f_1$, appears in the frequency spectrum of $\phi(x, y, t)$. The spectrum

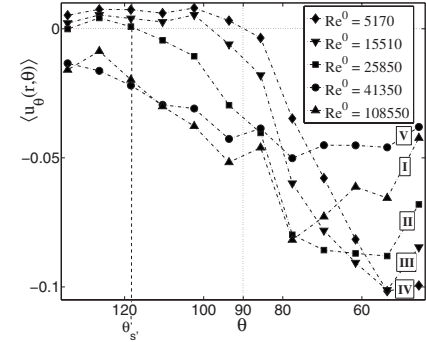


FIG. 10. Time averaged velocity profiles $\langle u_\theta(r=0.985R, \theta) \rangle$ along the circular box side wall for $\text{Ha}=36$. Note that the precise determination of θ_s' is limited by the number of measurement points along the side wall and a low signal to noise ratio.

is then seen to be extended as further frequency peaks occur for Re^0 slightly higher than Re_{IV}^0 [Fig. 12(b)] and exhibits a $A \sim f^{-2.3}$ power law for $\text{Re}^0 \gg \text{Re}_{\text{IV}}^0$ [Fig. 12(c)]. This equates to regime IV identified in the numerical simulations as here again, the time averaged profiles of velocity as well as r.m.s. profiles of velocity fluctuations, obtained numerically and experimentally are in good qualitative agreement [see Figs. 11(a) and 11(b) and Figs. 8(a) and 8(c), respectively]. In this regime, a clear maximum in the profiles of $\langle u_y'(x, 0, t)^2 \rangle^{1/2}$ appears in the region $x > 0$ at x_f^M [Fig. 8(c)], roughly at the location x^M where $u_x = u_x^M$ [Fig. 8(a)]. It is due to the two initial vortices starting to oscillate and periodically crossing the centerline $y=0$. Furthermore, the vorticity carried by shed vortices induces a flow of negative mean velocity in the $x < 0$ region on the centerline and the width of this region $\langle \Delta x_r \rangle = \langle x_r^{(1)} - x_r^{(2)} \rangle$ increases with the forcing as the associated return flow intensifies [see Figs. 8(a) and 8(b)]. Once sucked into the stream between the two oscillating vortices located at $x > 0$, these shed vortices are strongly squeezed and stretched along $\hat{\epsilon}_r$. This points to the minimum in the profile $\langle u_x'(x, 0, t)^2 \rangle^{1/2}$ at x_f^m [see Fig. 8(c)]. Since this stretching is directly induced by the two initial vortices, the evolution of x_f^m follows that of x_f^M with increasing forcing, until these two points clearly separate, which marks the end of regime IV.

A last change of flow regime has been detected at $\text{Re}^0 = \text{Re}_{\text{V}}^0$, where all quantities are brutally altered. $\langle \Delta x_r \rangle$ drastically shrinks [Fig. 8(b)] and negative velocity components

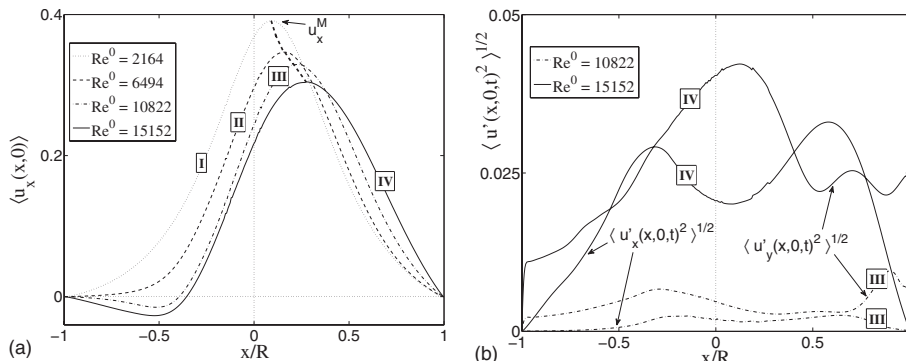


FIG. 11. Time averaged quantities obtained from numerical simulations for $\text{Ha}=43$. (a) Velocity profiles $\langle u_x(x, 0) \rangle$. (The thick dashed line indicates the shift of the vortex pair toward $x > 0$ with increasing Re^0 .) (b) $\langle u'_x(x, 0, t)^2 \rangle^{1/2}$ and $\langle u'_y(x, 0, t)^2 \rangle^{1/2}$ along the diameter $y=0$.

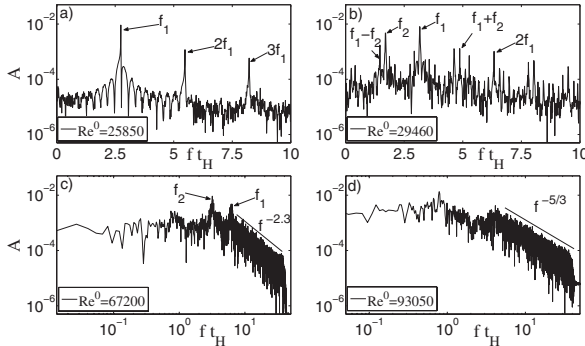


FIG. 12. FFT of recorded time-dependent signal $\phi(x=-0.4375R, y=-0.04375R, t)$ for $Ha=36$. (a) Periodic flow (regime III). (b) Two base frequency flow (regime IV). (c) Chaotic or turbulent flow in flow regime IV. (d) Chaotic or turbulent flow in flow regime V. Oscillation amplitudes A and frequencies f_i are normalized by $B_z U_0 a$ and the Hartmann friction time t_H^{-1} , respectively.

vanish completely along the diameter $y=0$, resulting in a profile of $\langle u_x \rangle$ that is almost symmetric about $x=0$ [Fig. 8(a)]. Accordingly, the average $\langle x_M \rangle$ rapidly drops to the vicinity of $x=0$ at first, increases again and then slightly decreases for higher forcing. Also, the averaged point of sign reversal along the circular wall $\langle \theta_s' \rangle$ is displaced in anti-clockwise direction, thus following the displacement of $\langle x^M \rangle$. For $Re^0 \gg Re_V^0$, very strong velocity fluctuations make the detection of θ_s' in the profile $u_\theta(r=0.985R, \theta, t)$ impossible.

Figures 12(c) and 12(d) show that the amplitude of all measured frequencies raises significantly above that from previous regimes. According to Ref. [3] this indicates a transition to a spectrum with a broad continuous component, thus implying that the flow in regime V is turbulent. This regime is also characterised by the emergence of a new peak frequency much lower than f_2 , as well as a $A \sim f^{-5/3}$ inertial range.

D. Scaling laws based on R_h

The critical values $Re_{\text{III}}^0, Re_{\text{IV}}^0, Re_{\text{V}}^0$ that correspond to the transitions between the regimes identified in the previous section are shown on Fig. 7. With the exception of the case $Ha=13.5$, all critical Reynolds numbers scale as Ha , indicating that they may be governed by a single parameter $R_h = Re^0/Ha$. In order to further check this property, all Re^0 -dependent quantities have been plotted against R_h instead of Re^0 [see Figs. 8(b), 9(a), and 9(c)]. It clearly appears that any set of curve describing a topological quantity ($\langle x^M \rangle, \langle \theta_s' \rangle, \langle \Delta x_r \rangle$) can be merged into a single one, provided they are, respectively, scaled as

$$\begin{aligned} \frac{\langle x^M \rangle}{Ha^{3/5}} &\sim f(Re^0/Ha), \quad \langle \theta_s' \rangle Ha^{1/5} \sim g(Re^0/Ha), \\ \langle \Delta x_r \rangle &\sim h(Re^0/Ha). \end{aligned} \quad (9)$$

The fact that the lower values of Ha ($Ha=13.5$ and less noticeably $Ha=18$) match these scalings imperfectly certainly

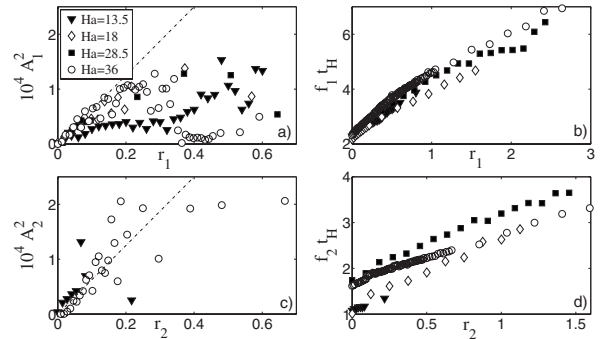


FIG. 13. Nature of bifurcations. (a) Square of the amplitude A_1 of mode 1 vs r_1 . (b) Frequency f_1 of mode 1 vs r_1 . (c) Square of the amplitude A_2 of mode 2 vs r_2 . (d) Frequency f_2 of mode 2 vs r_2 . Oscillation amplitudes A_i and frequencies f_i are normalized by $B_z U_0 a$ and the Hartmann friction time t_H^{-1} , respectively.

indicates that these are valid in the limit of large Ha and breakdown at lower Ha , where three-dimensional effects are present, as will be seen in Sec. III F. The relevance of R_h as governing parameter in quasi-two-dimensional MHD flows has been pointed out long ago (see Refs. [4,7]) in flows dominated by Hartmann friction. It is, however, remarkable that this parameter keeps its relevance in the present case where strong three-dimensional recirculations due to some local Ekman pumping are present. This certainly indicates that the extra global dissipation induced by these remains small compared to the Hartmann friction and that they essentially alter the local shape of individual vortices. Velocity profiles across any of them (which are not available in the experiment) may indeed not follow an universal law expressed in terms of R_h only, as in the case of Sommeria's isolated vortex in Ref. [4], where local recirculations affect the vortex core only.

E. Nature of the bifurcations at $Re^0=Re_{\text{III}}^0$ and $Re^0=Re_{\text{IV}}^0$

We have analyzed the nature of the bifurcation at $Re^0 = Re_{\text{III}}^0$ by plotting the amplitude A_1 of mode 1 with fundamental frequency f_1 versus the critical parameter $r_1 = Re^0/Re_{\text{III}}^0 - 1$ on Fig. 13(a). It is found to follow a square root function. This, together with the fact that no hysteresis at transition to regime III was observed, indicates a supercritical bifurcation. The corresponding coefficients from the Landau theory (see Refs. [28,29]) can be extracted by interpolating $A_1(r_1)$ as

$$|A_1| \simeq \sqrt{\frac{2k_1 r_1}{l_1}} = \sqrt{\frac{2\sigma_1}{l_1}}, \quad (10)$$

where σ_1 is the exponential growth rate, $k_1 = \text{const}$ and l_1 measures the nonlinear saturation in the perturbation growth. For $0 < r_1 < 0.15$, the interpolation of $A_1(r_1)$ with a square root function yields $k_1/l_1 \simeq 3 \times 10^{-4}$ for all values of Ha , but $Ha=13.5$ [see Fig. 13(a)]. Here again, the case $Ha=13.5$ departs from the asymptotic curve and exhibits stronger saturation. Also, the related base frequency f_1 increases linearly for small r_1 as a function of Re^0 and seems to saturate for

higher r_1 as the flow approaches regime IV [Fig. 13(b)]. Furthermore, the frequency f_1 at the onset of regime III increases monotonically with Ha . The second bifurcation at $\text{Re}^0 = \text{Re}_{\text{IV}}^0$ results in a spectrum with two base frequencies f_1 and f_2 and subsequent linear combinations [Fig. 12(b)] of the form $m_1 f_1 + m_2 f_2$ with $(m_1, m_2) \in \{-2, -1, 0, 1, 2\}^2$ as in Refs. [30,3]. As for mode 1, the fundamental frequency f_2 of mode 2 increases linearly with the critical parameter $r_2 = \text{Re}^0/\text{Re}_{\text{IV}}^0 - 1$, but the slope seems to depend weakly on Ha [Fig. 13(d)]. No saturation was detected for $0 < r_2 < 1.5$ but it may well occur for higher forcing. As $A_1(r_1), A_2(r_2)$ follows a square root function without any measurable hysteresis. An interpolation of $A_2(r_2)$ for $0 < r_1 < 0.15$ yields also $k_2/l_2 \approx 3 \times 10^{-4}$ [Fig. 13(c)], and one can conclude to the supercritical nature of the bifurcation to regime IV as well.

F. Measure of three-dimensionality

The three-dimensionality of the flow is measured by the correlation between values of quantity $V_T(t)$ and $V_B(t)$, taken at the same location (x, y) at top and bottom plate, respectively. Two different types of correlation functions are used:

$$C_1 = \frac{\sum_{i=0}^n V_B(t)V_T(t)}{\sqrt{\sum_{i=0}^n V_B^2(t)\sum_{i=0}^n V_T^2(t)}} \quad \text{and} \quad C_2 = \frac{\sum_{i=0}^n V_B(t)V_T(t)}{\sum_{i=0}^n V_B^2(t)}, \quad (11)$$

where n is the number of samples over which C_1 and C_2 are calculated. C_1 quantifies how much phase and frequency are correlated, regardless of signal amplitudes. C_2 is the more usual correlation function, that incorporates the signal amplitude. Correlations based on the velocity component $u_x(x, 0, t)$ are denoted C_2 thereafter.

Correlations built on velocity fluctuations $u'_x(x, 0, t) = u_x(x, 0, t) - \langle u_x(x, 0) \rangle$ are denoted by C'_1 and C'_2 . At this point, it should be stressed that the correlation factor can be influenced by the presence of $\approx 2 \mu\text{V}$ peak to peak noise, especially in regimes I and II where the signals are weak, and the ratio $r_{S/N}$ between the amplitude of the signal and that of the noise, respectively, is small. For example, $r_{S/N} \approx 5$ for $\text{Re}^0 = 5170$ and $\text{Ha} = 36$. This induces an error of $\approx 10\%$ in the correlation factor C_2 . This deviation from $C_2 \approx 1$, however, quickly decreases for higher values of Re^0 , as $r_{S/N}$ becomes much larger. Consequently, this error is already as small as $\approx 0.25\%$ and hence negligible when the flow changes to regime III.

The variations of C_i and C'_i with Re^0 are depicted on Figs. 14(a), 14(c), and 14(d) for several values of Ha . When $\text{Ha} = 36$ and $\text{Ha} = 28.5$, the velocity correlation C_2 is nearly unity for all investigated regimes and one can conclude that the flow is very close to quasi-two-dimensionality. For $\text{Ha} = 18$, C_2 seems to be slightly below unity even for very high $r_{S/N}$'s, indicating some small three-dimensionality. For $\text{Ha} = 13.5$, this effect is more substantial, and one sees that three-dimensionality is always present. This certainly explains why the case $\text{Ha} = 13.5$ departs from all the others in the scaling

laws found in the previous section. The picture turns out to be a little more refined when inspecting the correlations based on the velocity fluctuations [Figs. 14(c) and 14(d)]. Both C'_1 and C'_2 are weak near the onset of unsteadiness as fluctuations and hence the $r_{S/N}$ is small. They eventually increase to a value of about unity and remain almost constant for $\text{Re}^0 \leq \text{Re}_{3D}^0$. Here again, the small deviation is due to the presence of noise. However, correlations close to unity at all locations (x, y) along the centerline [Fig. 14(b)] indicate quasi-two-dimensionality in this flow regime. Furthermore, the fact that $C'_1 \approx C'_2$ tells us that the velocity fluctuations are strongly correlated in phase, frequency and amplitude.

This behavior changes drastically at the critical value $\text{Re}^0 = \text{Re}_{3D}^0$ (values for Re_{3D}^0 are given on Fig. 7). Both C'_1 and C'_2 linearly decrease for $\text{Re}^0 > \text{Re}_{3D}^0$ while C_2 remains almost constant [see Figs. 14(a), 14(c), and 14(d)]. This indicates the presence of three-dimensional vortices even though the mean flow remains quasi-two-dimensional. It can be seen from the profiles of velocity correlations in Fig. 14(b) that these three-dimensional structures are mostly located in the region $x > 0$ where vortices are strongly accelerated by the mean flow. Furthermore, since C'_2 declines more strongly than C'_1 , one can conclude to a smaller amplitude of the velocity fluctuations on the top plate. The decrease in C'_2 also tells us that the flow in these structures is not only slower on the top plate than on the bottom plate, but also shifted in phase and frequency. In other words, the quasi-two-dimensional columnar vortices start wobbling.

It is noteworthy that for $\text{Ha} \geq 28.5$, Re_{3D}^0 is much larger than Re_v^0 so three-dimensionality appears well into turbulent flow regime V, whereas regimes I, II, III, IV are strictly quasi-two-dimensional. Also, Re_{3D}^0 scales approximately as $\text{Ha}^{8/5}$, except for the lower values of Ha , $\text{Ha} = 18$ and 13.5 . In these cases, the region of influence of the noise is extended as signals are weaker, so one can not tell whether the plateau $C'_1 \approx C'_2 \approx 1$ is reached for $\text{Re}^0 < \text{Re}_{3D}^0$. On the other hand, for these low values of Ha , higher values of $\text{Re}^0/\text{Ha}^{8/5}$ could be reached and a new regime appears at $\text{Re}^0 = \text{Re}_p^0$, where both C'_1 and C'_2 stop decreasing and stay constant for all $\text{Re}^0 > \text{Re}_p^0$ [see Fig. 14(c) and 14(d)]. This behavior can be due to residual viscous friction and local Ekman pumping at the scale of each vortex, that transports momentum along $\hat{\mathbf{e}}_z$. Furthermore, since the electric current is injected at the bottom plate, the motion near the top plate is mostly induced by the motion near the bottom so they cannot be totally uncorrelated.

G. Hartmann layer friction

Our experimental setup does not allow for measurements made directly within the Hartmann layer nor for a global measurement of the dissipation as obtained in the experiment of Ref. [23]. We can, however, obtain a rough measure of the fraction of the injected energy that is passed on to the quasi-two-dimensional flow in the jet along the diameter $y = 0$ by monitoring the evolution of $\alpha_{2D} = (\tilde{u}_x^M/U_0)^2$ vs R_δ (we recall that \tilde{u}_x^M is the maximum velocity in the time averaged velocity profile [see Fig. 8(a)]). In this regard α_{2D} is analogous to the friction factor F defined in Ref. [23] in the sense that it

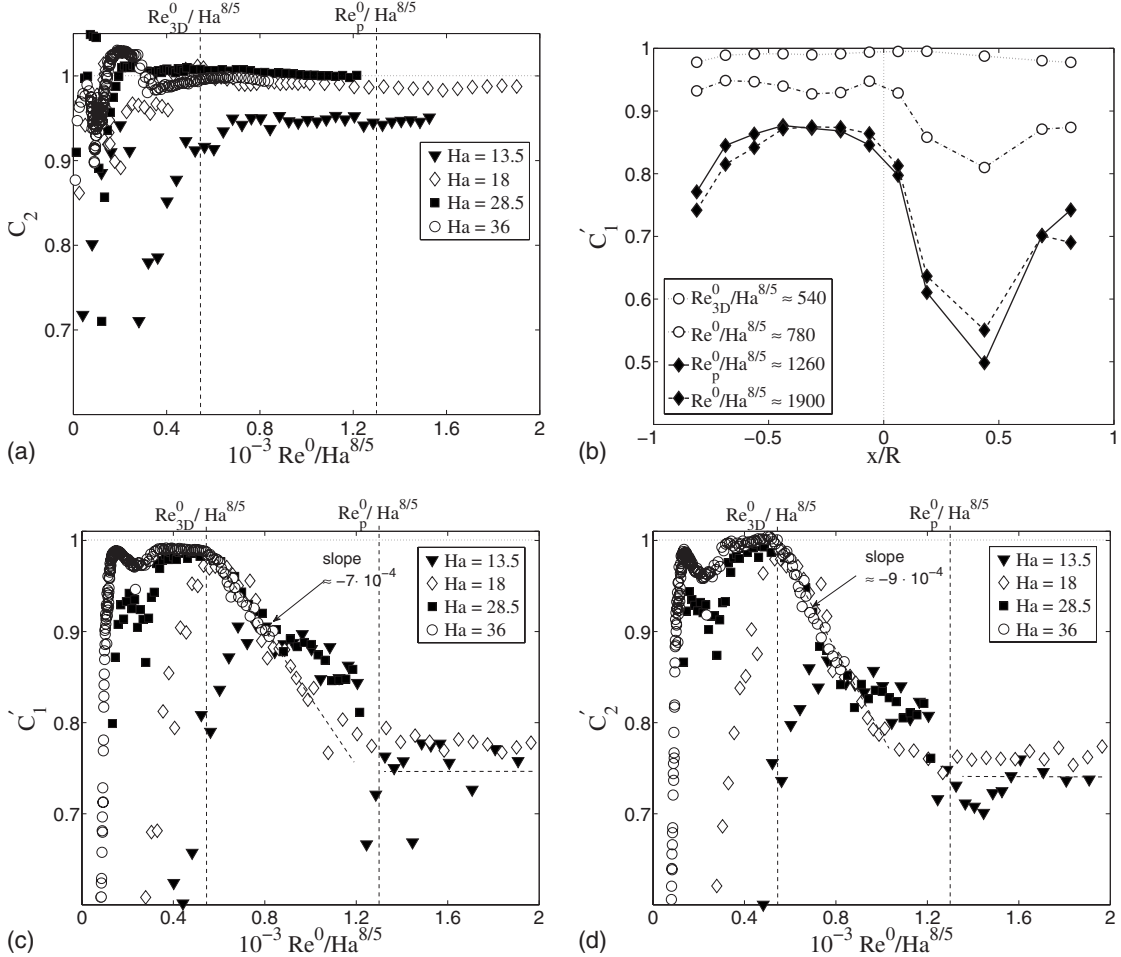


FIG. 14. Correlations averaged along the diameter $y=0$ for $x \in [-0.8125R, 0.8125R]$ and vs $\text{Re}^0/\text{Ha}^{8/5}$. (a) C_2 . (b) Profile of C'_1 along the diameter $y=0$. (c) C'_1 . (d) C'_2 .

represents a ratio between a velocity built on the forcing and a measured velocity (here \tilde{u}_x^M). Also, as in Ref. [23] R_δ represents the Reynolds number based on the Hartmann layer thickness as well as on a velocity derived from measurements of electric potentials, and it controls the transition from a laminar to a turbulent Hartmann layer. Reference [23], however, measure their voltage across the whole channel, which gives them an average flow velocity whereas our measurement corresponds to the maximum velocity in the driving jet along $\hat{\mathbf{e}}_x$. In this sense both R_δ 's reflect the same physics, except that ours is local while that in Ref. [23] is global.

The energy not transmitted to $(\tilde{u}_x^M)^2$ is either dissipated or transmitted to the three-dimensional part of the flow so a change in the Hartmann friction should reflect on the evolution of α_{2D} .

Figure 15 presents the evolution of α_{2D} vs R_δ . For $\text{Ha} = 28.5$ and 36 , and R_δ lower than the critical value for the transition to regime V ($R_\delta^V \approx 120$), α_{2D} decreases almost linearly with R_δ . Since the flow is close to quasi-two-dimensionality in this regime (see Figs. 7 and 14), this es-

sentially reflects joule dissipation in the Hartmann layers (or Hartmann friction). For $R_\delta > R_\delta^V$, α_{2D} suddenly drops (see Fig. 15). Here, the flow is still quite close to quasi-two-dimensionality as $\text{Re}^0 < \text{Re}^{3D}$ (see Fig. 14). This suggests that the extra dissipation might come from a brutal change in

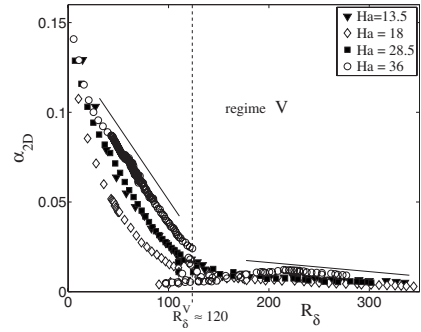


FIG. 15. $\alpha_{2D} = (\tilde{u}_x^M/U_0)^2$ vs $R_\delta = \tilde{u}_x^M(\delta_{\text{lam}}/\nu)$ for all Ha . Note that \tilde{u}_x^M and therefore R_δ drops strongly at the onset of regime V for $\text{Ha}=18, 28.5$, and 36 , and increases again within regime V.

the Hartmann layer friction, triggered by a transition from a laminar to a turbulent Hartmann layer. It may certainly be objected that the critical value $R_\delta \approx 120$ is well below $R_\delta \approx 380$ found in recent experimental (see Ref. [23]) and numerical (see Ref. [22]) studies on rectangular duct flows. This, however, might be related to the fact that our forcing mechanism is not the same as in Ref. [23] and therefore triggers a different flow. While the flow in the experiment of Ref. [23] is expected to be steady when the Hartmann layer destabilizes, the flow in the present work, although still close to quasi-two-dimensionality, is already strongly turbulent, because of instabilities initialised in the side layers. The presence of a complex turbulent flow in the vicinity of the measurement points introduces uncontrolled perturbations that are absent in the idealized configurations cited above. On the top of this several other factors such as wall roughness (see Ref. [23]) as well as a large number of potential probes on the Hartmann walls could generate additional disturbances and also lead to a destabilization of the Hartmann layer for lower R_δ than in Ref. [23].

For $R_\delta \gg R_\delta^V$, α_{2D} decreases almost linearly with R_δ again for all Ha but with a gentler slope than at low R_δ (see Fig. 15). For these values of R_δ , $Re^0 > Re_{3D}^0$ so three-dimensional perturbations are also present that generate some additional Joule dissipation in the core flow on the top of the dissipation in the turbulent Hartmann layer.

IV. CONCLUSION

We have performed an experiment where a vortex pair confined by a circular wall was created by injecting electric current into a thin layer of liquid metal perpendicular to an homogeneous magnetic field. Such a flow is known to be almost quasi-two-dimensional as physical quantities hardly vary along the field lines, except in the fine Hartmann boundary layers at the top and bottom plates (see Refs. [11,14]). This allowed us to perform numerical simulations based on the shallow water model of Ref. [14], that accounts for moderate Ekman pumping locally. In the experiment, electric potential measurements have been used to determine part of the two-dimensional velocity field. Both methods were cross checked in order to identify the different regimes spanned by the system when the electric current is increased. It was shown that the system undergoes a transition to turbulence through a sequence of supercritical bifurcations that are very similar to those observed in the wake of a circular cylinder (see Ref. [10]). First, two recirculating bubbles appear behind the initial vortex pair as the boundary layer on the circular wall separates in two symmetric points (regime II). Secondly the separated boundary layer becomes unstable and

vortices are shed and are sucked in the jet between these initial vortices (regime III). Unlike a cylinder wake where shed vortices are released downstream, vortices are reinjected into the main flow making it more unstable, so the flow quickly becomes chaotic as the forcing is increased (regime IV). Further insight into the analogy between these two systems could be obtained by investigating their properties as dynamical systems. Such a task was undertaken by Ref. [3] who has identified a clear scenario for the transition to turbulence of a single vortex in a square box from two-dimensional direct numerical simulation. It is worth mentioning that the frequency spectra found in the present study strongly resembles that found in theirs.

At higher injected electric current, we have identified another transition in the quasi-two-dimensional flow patterns where the velocity profile along the center diameter becomes almost symmetric (regime V). This regime was beyond the validity range of our numerical model so the exact flow patterns remain unclear. We noticed, however, a drastic drop at $Re_0 = Re_0^V$ exactly, in the slope of $\alpha_{2D} = (\tilde{u}_x^M/U_0)^2$ vs R_δ , the Reynolds number based on the thickness of the Hartmann layer, that points to a likely transition to turbulence in this region.

Finally, we have checked the two-dimensionality of the system by calculating correlations between velocities measured on the same magnetic field line, on the top and bottom walls enclosing the fluid layer. It turns out that for $Ha \geq 28.5$ the flow is very close to quasi-two-dimensionality in all investigated regimes as correlations are nearly unity. When these correlations are based on the velocity fluctuations only, a sudden decrease appears well into regime V which we could show is due to columnar vortices not only having different rotation rates at the top and bottom plates, but also wobbling. This provides the first evidence of a transition between quasi-two-dimensional and three-dimensional turbulence in forced liquid metal MHD flows. Since this transition occurs well into regime V for $Ha \geq 28.5$, this also allows us to be certain that regime I, II, III, and IV are strictly quasi-two-dimensional and reflect two-dimensional dynamics. Clearly though, further experiments in a larger box are needed, where a higher number of measurement points as well as a measurements in the bulk of the flow should help determine the mechanisms of this transition to three-dimensionality.

ACKNOWLEDGMENTS

Finally, the authors would like to express their gratitude to the Deutsche Forschungsgemeinschaft for their support (Grant No. PO1210/4-1).

-
- [1] M. Zdravkovich, *Flow Around Circular Cylinders* (Oxford University Press, Oxford, 1997), Vol. 1.
[2] M. Zdravkovich, *Flow Around Circular Cylinders* (Oxford University Press, Oxford, 2003), Vol. 2.
[3] D. Molenaar, H. J. H. Clercx, and G. J. F. van Heijst, Phys. Rev. Lett. **95**, 104503 (2005).
[4] J. Sommeria, J. Fluid Mech. **189**, 553 (1988).
[5] P. Roberts, *Introduction to Magnetohydrodynamics* (Long-

- mans, London, 1967).
- [6] R. Moreau, *Magnetohydrodynamics* (Kluwer Academic Publisher, Dordrecht, 1990).
 - [7] J. Sommeria, *J. Fluid Mech.* **170**, 139 (1986).
 - [8] O. V. Andreev and Y. B. Kolesnikov, in *3rd International Conference on Transfer Phenomena in Magnetohydrodynamics and Electroconducting Flows, Aussois, France*, pp. 205–210 (1997).
 - [9] M. Frank, L. Barleon, and U. Müller, *Phys. Fluids* **13**, 2287 (2001).
 - [10] V. Dousset and A. Pothérat, *Phys. Fluids* **20**, 017104, (2008).
 - [11] J. Sommeria and R. Moreau, *J. Fluid Mech.* **118**, 507 (1982).
 - [12] P. A. Davidson, *J. Fluid Mech.* **336**, 123 (1997).
 - [13] B. Screenivasan and T. Albuissiere, *J. Fluid Mech.* **464**, 287 (2002).
 - [14] A. Pothérat, J. Sommeria, and R. Moreau, *J. Fluid Mech.* **424**, 75 (2000).
 - [15] A. Kljukin and A. Thess, *Exp. Fluids* **25**, 298 (1998).
 - [16] S. Kaplun, *Z. Angew. Math. Phys.* **9**, 111 (1954).
 - [17] A. Pothérat, J. Sommeria, and R. Moreau, *Phys. Fluids* **14**, 403 (2002).
 - [18] P. Dellar, *J. Fluid Mech.* **515**, 197 (2004).
 - [19] A. Pothérat, J. Sommeria, and R. Moreau, *J. Fluid Mech.* **534**, 115 (2005).
 - [20] J. Pedlosky, *Geophysical Fluid Dynamics* (Springer Verlag, Berlin, 1987).
 - [21] P. A. Davidson and A. Pothérat, *Eur. J. Mech. B/Fluids* **21**, 541 (2002).
 - [22] D. S. Krasnov, E. Zienicke, O. Zikanov, T. Boeck, and A. Thess, *J. Fluid Mech.* **504**, 183 (2004).
 - [23] P. Moresco and T. Albuissiere, *J. Fluid Mech.* **504**, 167 (2004).
 - [24] L. Leboucher, *J. Comput. Phys.* **150**, 181 (1999).
 - [25] M. Ni, R. Munipalli, P. Huang, N. B. Morley, and M. A. Abdou, *J. Comput. Phys.* **227**, 205 (2007).
 - [26] M. P. Satin, A. W. Cense, R. Verzicco, H. J. H. Clercx, and G. J. F. van Heijst, *Phys. Fluids* **13**, 1932 (2001).
 - [27] R. J. Lingwood and T. Albuissiere, *Phys. Fluids* **11**, 2058 (1999).
 - [28] P. G. Drazin, *Hydrodynamic Stability* (Cambridge University Press, Cambridge, 1981).
 - [29] L. D. Landau and E. M. Lifshitz, *Fluid Mechanics* (Pergamon Press, Oxford, 1959).
 - [30] P. Bergé, Y. Pomeau, C. Vidal, and D. Ruelle, *Order Within Chaos: Towards a Deterministic Approach to Turbulence* (Wiley, New York, 1984).

D. Article: Appearance of three-dimensionality in wall-bounded MHD flows

Article published in *Physical Review Letters*, 104:034502, 2010.

Appearance of Three Dimensionality in Wall-Bounded MHD Flows

R. Klein and A. Pothérat

Applied Mathematics Research Centre, Coventry University, Priory Street, Coventry CV1 5FB, United Kingdom

(Received 3 August 2009; revised manuscript received 16 November 2009; published 21 January 2010)

We characterize experimentally how three dimensionality appears in wall-bounded magnetohydrodynamic flows. Our analysis of the breakdown of a square array of vortices in a cubic container singles out two mechanisms: first, a form of three dimensionality we call *weak* appears through differential rotation in individual 2D vortices. Second, *strong* three dimensionality characterized by vortex disruption leads on the one hand to a remarkable vortex array that is both steady *and* 3D, and, on the other hand, to scale-selective breakdown of two dimensionality in chaotic flows. Most importantly, these phenomena are entirely driven by inertia, so they are relevant to other flows with a tendency to two dimensionality, such as rotating, or stratified flows in geophysics and astrophysics.

DOI: 10.1103/PhysRevLett.104.034502

PACS numbers: 47.65.-d, 47.27.Cn, 47.32.cd

When a strong magnetic field is applied to an electrically conducting flow, the variations of all physical quantities are damped along it so the flow tends to two dimensionality. Broadly speaking, 2D magnetohydrodynamic (MHD) flows, like other 2D flows, tend to favor large, long-lived structures while fine, highly dissipative structures are the hallmark of 3D flows. Knowing the 2D or 3D nature of MHD and other flows is therefore key to understanding their behavior and global properties. This important question of fundamental physics also bears critical consequences in practical situations: in liquid metal heat exchangers or steel casting processes for instance, 3D turbulent flows are preferable to 2D flows to enhance heat and mass transport and favor homogeneous mixing. By contrast, in laboratory experiments, physicists use magnetic fields to artificially reproduce 2D flows [1]. Nevertheless, in all these problems, it is crucial but unclear, whether three dimensionality is present or not, and under which form. [2] clarified the “two dimensionalization” mechanism for a given MHD flow structure, of size l_{\perp} and velocity U , by discovering that the Lorentz force diffused the momentum along a magnetic field $B\mathbf{e}_z$ over a length l_z , in a typical time $\tau_{2D}(l_{\perp}) = \tau_j(l_z/l_{\perp})^2$ [σ and ρ are the fluid conductivity, density and $\tau_j = \rho/(\sigma B^2)$ is the Joule dissipation time that characterizes the Lorentz force]. The structure’s inertia, on the other hand, increases with its turnover frequency $\tau_U(l_{\perp})^{-1} = U/l_{\perp}$, and can induce three dimensionality when the latter becomes comparable to τ_{2D}^{-1} . Such inertia-induced 3D effects can occur in any 2D flow. [1,3] proved, for instance, that the meridional Ekman recirculations that drive a strong upward flow in tornadoes’ eyes, acted alike in wall-bounded MHD flows. In tornadoes, indeed as in atmospheres, oceans and all rapidly rotating flows, the tendency to two dimensionality arises from the propagation of inertial waves along the rotation direction [4,5], so the same struggle between this tendency and inertia as in MHD flows determines the appearance of three dimensionality. Stratified flows too, where two dimensionality is

driven along the density gradient, exhibit an analogous behavior [6]. Understanding how three dimensionality appears in MHD flows therefore bears some relevance to apparently remote problems such as weather forecast, predicting pollutant advection in the atmosphere, or describing some astrophysical flows. To this day though, although the mechanisms that favor two dimensionality are fairly well understood, most studies of the breakdown of two dimensionality have focused either on strictly 2D vortices, [7,8], or on single vortices or vortex pairs [9,10]. The mechanisms that ignite three dimensionality in more complex, wall-bounded flows, where boundary layers that develop along walls precludes strict two dimensionality, pose an open question. In this Letter, we propose an experimental answer to it: we prove that boundaries across the direction of two dimensionality allow inertia to sustain local differential rotation in nearly 2D structures. We also single out how the subtle interplay between inertia and the Lorentz force leads to stationary 3D flows that no model has foreseen, and to a scale-selective breakdown of two dimensionality in chaotic flows.

The principle of our experiment follows that of [1] in which a quasi 2D flow was produced by applying a constant homogeneous magnetic field across a square, shallow container made of electrically insulating walls and filled with liquid metal. The flow was termed “quasi 2D” to reflect its assumed invariance everywhere across the layer (i.e., along $B\mathbf{e}_z$), except in *Hartmann* boundary layers that develop along the walls orthogonal to the field, called *Hartmann walls*. Unlike this earlier experiment aimed at quasi 2D flows, our container is not shallow, but cubic with inner edge $L (= l_z) = 0.1$ m, so as to feature longer two-dimensionalization times τ_{2D} and thereby obtain 3D flows. The homogeneous field is directed along \mathbf{e}_z too, so the two Hartmann walls are parallel to the $(\mathbf{e}_x, \mathbf{e}_y)$ plane. The flow entrainment relies on the MHD equivalent of the tornado mechanism: in the same way these are triggered by a vertical flow due to ocean evaporation, columnar vortices

of rotation axis \mathbf{e}_z are driven in MHD flows by injecting electric current locally at one Hartmann wall only. 100 current injection electrodes are thus mounted flush at the bottom Hartmann wall only, with all or 16 of them, arranged in a 10×10 or 4×4 square lattice of step $L_i = 0.1L$ or $L_i = 0.3L$, alternately connected to either pole of a dc current generator. Hence, our base quasi 2D flow, obtained for low current and high magnetic field, is a square array of 100 or 16 cylindrical, quasi 2D vortices of axis \mathbf{e}_z , each of size $L_i \times L$, that rotate in alternate directions. Three dimensionality is monitored by measuring the electric potential ϕ at two sets of 121 points, covering two $(3 \text{ cm})^2$ squares, respectively located on top and bottom Hartmann walls and aligned exactly opposite each other along \mathbf{e}_z [10]. Since the electric potential is known not to vary across the very thin Hartmann layers, a quasi 2D flow would yield identical measurements on these two sets, while any difference between the two would betray 3D behavior. Furthermore, with the electric potential at a wall being proportional to the stream function just outside the Hartmann layer [11], our system provides a direct visualization of the flow patterns near either Hartmann walls. This allows us to visually identify quasi 2D structures. The flow is controlled by the injected current per electrode I (measured nondimensionally by a Reynolds number $Re^0 = 2I/[\pi\nu(\sigma\rho\nu)^{1/2}]$) and by the externally imposed magnetic field intensity, measured by the Hartmann number $Ha = LB[\sigma/(\rho\nu)]^{1/2}$. We track three dimensionality in established flows of increasingly high Re^0 in the interval $[0, 1.3 \times 10^5]$, for fixed values of Ha in [1092, 18220].

Regions of steady and unsteady flow regimes in the (Ha, Re^0) plane are reported on the stability diagram for $L_i = 0.1L$ on Fig. 1. A region of high magnetic field ($Ha \gtrsim 7500$) and a region of low magnetic field ($Ha < 7500$) clearly stand out. The physics of highest magnetic field regimes is essentially dominated by the very small values of τ_j , so that even our highest forcing produced a flow where all vortices had a turnover time $\tau_U(l_\perp) > \tau_{2D}(l_\perp)$. Corresponding flow patterns near the top and bottom Hartmann walls are identical at all times, which establishes their quasi two dimensionality [Figs. 1(a) and 1(b)]. In such flows, hardly any electric current remains in the bulk and the Lorentz force essentially acts on the flow by controlling the thickness of the Hartmann boundary layers $\delta_{Ha} = L/Ha$. These, in turn, exert a friction of characteristic time $\tau_H = \tau_j Ha$ on all quasi 2D flow structures [2]. Since τ_H is Ha times longer than τ_j , the flow stability is determined by τ_H/τ_U . Indeed, it can be seen from Fig. 1 (top) that when the parameter $R_h = Re^0/Ha = \tau_H/\tau_U(L_i)$ exceeds the same critical value of $Re_I^0/Ha = 0.164$ for all $Ha \geq 7500$, then 2D inertia destabilizes the array of alternately rotating vortices [Fig. 1(a)] into periodically oscillating quasi 2D vortex pairs [Fig. 1(b)]. For higher Re^0 , the flow becomes chaotic, and even turbulent, but still remains

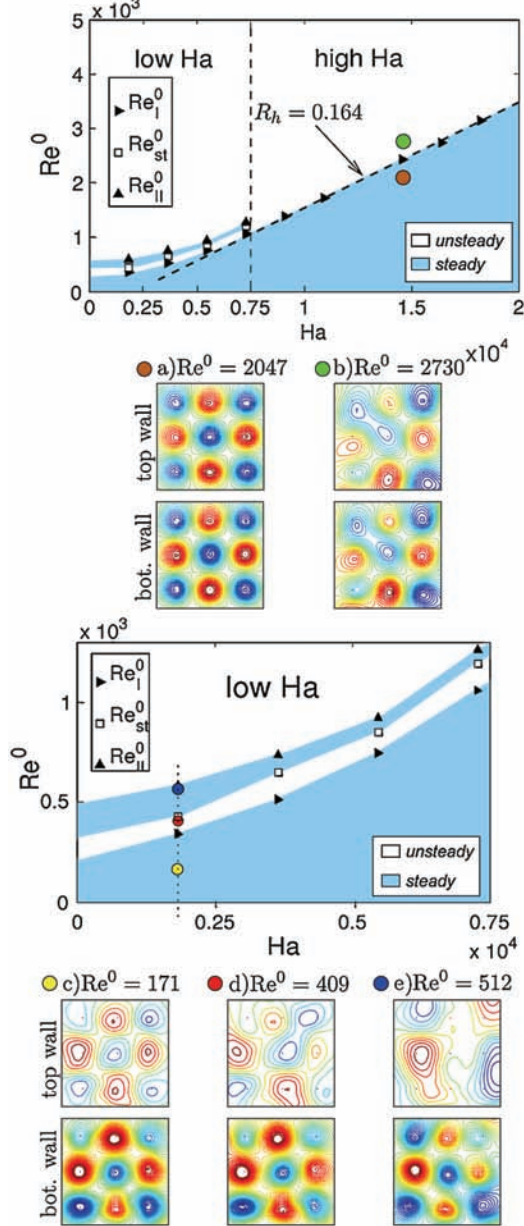


FIG. 1 (color online). Top: stability diagram giving critical Reynolds numbers $Re_I^0(Ha)$, $Re_{st}^0(Ha)$ and $Re_{II}^0(Ha)$ vs. Ha and snapshots of iso- ϕ lines, at the bottom and top Hartmann walls at $Re^0 \leq Re_I^0$ and $Re^0 \geq Re_I^0$ for $Ha = 1.458 \cdot 10^4$, for which the flow is quasi 2D. Bottom: magnification of the top diagram in the low Ha region and snapshots of iso- ϕ lines, at the bottom and top walls at $Ha = 1822$, for which the flow is 3D.

quasi 2D. This same instability and subsequent chaotic regimes were observed by [1] in a shallow container, but our results prove that the structures the author identified were indeed quasi 2D.

The above scenario changes significantly at lower fields ($\text{Ha} < 7500$), for which $\tau_{2D}(L_i)$ is of the order of $\tau_U(L_i)$, even at low forcing. The first visible consequence is that although the steady base flow patterns near the bottom and top walls remain topologically identical, the flow is less intense near the top wall [Fig. 1(c)], implying that each columnar vortex in the array undergoes some differential rotation. We call *weak* this first manifestation of three dimensionality, as the structures it affects still extend from the bottom to the top wall without disruption of iso- ϕ surfaces. Iso- ϕ contours in different (\mathbf{e}_x , \mathbf{e}_y) planes along $B\mathbf{e}_z$ are therefore homothetic. In fact, this phenomenon appears progressively when inspecting base flows from high to low values of Ha . In the intermediate range $3500 < \text{Ha} < 7500$, periodically oscillating vortex pairs still appear at $\text{Re}^0 = \text{Re}_{II}^0(\text{Ha})$, even though each of them is subject to differential rotation. A further novelty in this range of fields is that the flow stabilizes again when $\text{Re}^0 = \text{Re}_{st}^0(\text{Ha}) > \text{Re}_I^0(\text{Ha})$. This second steady regime is made of weakly 3D, steady vortex pairs. It destabilizes again as oscillating vortex pairing resumes much more erratically at $\text{Re}^0 = \text{Re}_{II}^0(\text{Ha}) > \text{Re}_{st}^0(\text{Ha})$.

Until now, weak MHD three dimensionality had only been predicted theoretically and numerically by [3, 12], but not observed experimentally. These authors proved that 2D inertia-induced electric eddy currents between Hartmann layers and the bulk, that caused differential rotation and led columnar vortices to assume a 3D *barrel*-like shape. Weak three dimensionality is therefore a direct consequence of the presence of Hartmann walls.

Not unsurprisingly, three dimensionality manifests itself most spectacularly at the lowest magnetic field ($\text{Ha} = 1822$), where τ_{2D} is highest. Compared to the intermediate field range, the pairing process at $\text{Re}^0 \gtrsim \text{Re}_I^0$ is only apparent on the top wall where the top end of vortices merge, while their bottom ends remain disjoint and nearly steady in the vicinity of the bottom wall [Fig. 1(d)]. This topological difference between flows near top and bottom Hartmann walls implies that vortices merge only partially across the container, as their reconnection does not take place everywhere along \mathbf{e}_z . We term this type of three dimensionality as *strong*, as opposed to the weak one, as it implies a disruption of iso- ϕ surfaces along \mathbf{e}_z and the flows in different (\mathbf{e}_x , \mathbf{e}_y) planes are not topologically equivalent anymore. Strong three dimensionality becomes even more blatant when the flow restabilizes at $\text{Re}^0 = \text{Re}_{st}^0$. In this second steady regime, while the 10×10 array of vortices is still visible near the bottom wall, it connects in the bulk to a quite regular array of 5×5 alternately rotating vortices, visible near the top wall [Fig. 1(e)]. At $\text{Re}^0 = \text{Re}_{II}^0$, this flow destabilizes again through periodic oscillations that become chaotic at slightly supercritical forcing.

Unlike weak three dimensionality, strong three dimensionality appears through partial vortex pairing, a mechanism that is not *a priori* related to the presence of

Hartmann walls. This second effect, and the even more spectacular fact that it can lead to steady 3D vortex arrays had not been predicted theoretically, so its dynamics now calls for theoretical analysis in MHD and other 2D flows.

We now turn our attention towards the last unsteady regime ($\text{Re}^0 > \text{Re}_{II}^0$ for $\text{Ha} \leq 7500$ and $\text{Re}^0 > \text{Re}_I^0$ for $\text{Ha} > 7500$), where we shall quantify the presence of weak and strong three dimensionality. Since flow visualizations are not as revealing in these regimes, we shall instead analyze the correlations of the fluctuations of electric potential gradients $\partial_y \phi'$ around their time average, between pairs of measurement points aligned opposite each other on bottom and top Hartmann walls (denoted by subscripts b and t , respectively). Weak and strong three dimensionality are identified by comparing two types of correlations

$$C'_1 = \frac{\sum_{t=0}^T \partial_y \phi'_b(t) \partial_y \phi'_t(t)}{\sqrt{\sum_{t=0}^T \partial_y \phi'^2_b(t) \sum_{t=0}^T \partial_y \phi'^2_t(t)}},$$

$$C'_2 = \frac{\sum_{t=0}^T \partial_y \phi'_b(t) \partial_y \phi'_t(t)}{\sum_{t=0}^T \partial_y \phi'^2_b(t)},$$

where T is the duration of our recorded signals. Values of C'_1 below unity reflect strong three dimensionality only, while C'_2 differs from unity whenever either weak or strong three dimensionality is present. To assess the link between inertia and three dimensionality, we have plotted the variations of spatial averages $\langle C'_1 \rangle$ and $\langle C'_2 \rangle$ against the *true* interaction parameter $N_t = \tau_{u'}/\tau_{2D}(L_i)$ [13], that measures the relative influence of Lorentz to inertial forces in vortices at the injection scale ($\tau_{u'} = L_i/U_{\text{RMS}}$ is a turnover time built on a typical RMS of velocity fluctuations $U_{\text{RMS}} = \langle \langle \partial_y \phi'_b \rangle_t^{\text{RMS}} \rangle / B$, as in [10]). First, the fact that all our measurement points collapse into two single curves $\langle C'_1 \rangle(N_t)$ and $\langle C'_2 \rangle(N_t)$ proves that the three dimensionality we detect is exclusively of inertial nature. Second, since $\langle C'_2 \rangle(N_t) < \langle C'_1 \rangle(N_t)$ for all N_t , weak three dimensionality is always present, albeit in minute amounts at high B . This supports [3]'s theoretical prediction that the *barrel* effect exists whenever inertia is present in the flow, and vanishes at high N_t . Also, the increase of correlations with N_t is in line with [14] who found analytically that in the absence of inertia, the correlation length along the field increased with B .

More light is shed on the precise variations of $\langle C'_1 \rangle(N_t)$ and $\langle C'_2 \rangle(N_t)$ by inspecting the power spectral density from signals acquired at points aligned opposite each other on either Hartmann walls, and corresponding snapshots of the flow patterns on Figs. 2(a)–2(d). In the high N_t regime where $\langle C'_2 \rangle < \langle C'_1 \rangle \lesssim 1$, both spectra overlap over the whole frequency spectrum: the dynamics of vortices of all sizes is therefore 2D to a very good approximation. [Fig. 2(d)].

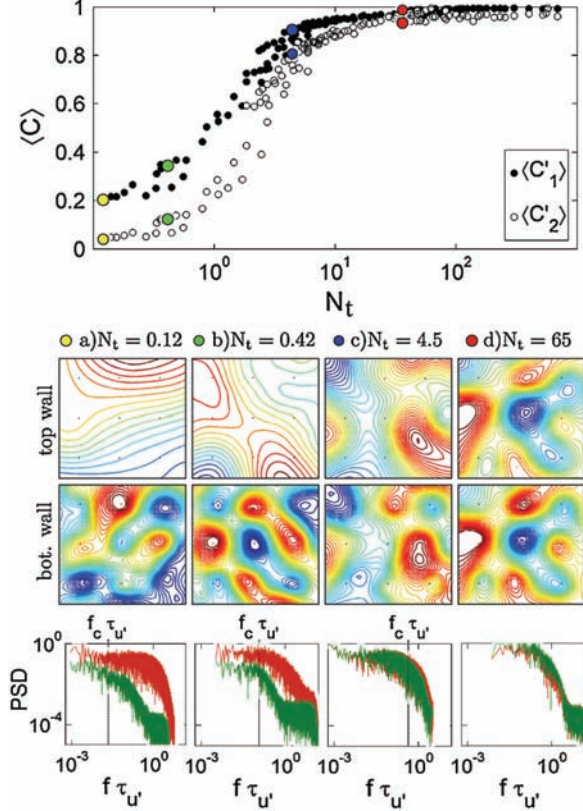


FIG. 2 (color online). Top: Spatially averaged correlations $\langle C'_1 \rangle$ and $\langle C'_2 \rangle$ vs. true interaction parameter N_t . Bottom: snapshots of iso- ϕ lines, (a)–(d) and corresponding power spectral density of $\partial_y \phi(x, y, t)$ at bottom (red) and top walls (green).

The sharp drop of both correlations at intermediate N_t is initiated by a loss of energy in the smaller scales near the top wall [Fig. 2(c)]. Structures of the corresponding size are generated near the bottom wall but because of their large aspect ratio L/l_\perp , the Lorentz force takes a longer time $\tau_{2D}(l_\perp)$ to diffuse their momentum up to the top wall, than it does for larger structures. When this time exceeds their turnover time $\tau_U(l_\perp)$, inertial effects disrupt them before they can reach the top wall, so they become 3D. Larger vortices, on the other hand, have a smaller aspect ratio, a shorter $\tau_{2D}(l_\perp)$, so they remain essentially quasi 2D. A cutoff scale, identified by a frequency $f_c(N_t)$ in the spectra, separates vortices that are “wide” enough to be quasi 2D from the smaller, 3D ones. When N_t decreases, $f_c(N_t)$ decreases as three dimensionality contaminates larger and larger scales [Fig. 2(b)], until even the largest structures become 3D and hardly any flow remains near the top wall [Fig. 2(a)].

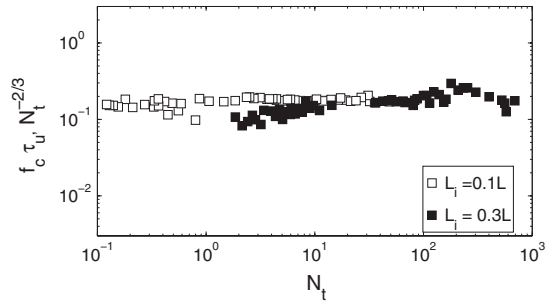


FIG. 3. Cutoff frequency f_c , normalized by the large scale eddy turnover frequency $\tau_{u'}^{-1}$, vs N_t .

We have calculated f_c precisely, by seeking the maximum of the function $g(f_p) = \langle C'_1(f_p) \rangle$, obtained by applying a low-pass filter of variable cutoff frequency f_p to $\partial_y \phi_b'(t)$ when calculating C'_1 . Figure 3 shows that for both $L_i = 0.1L$ and $L_i = 0.3L$, f_c satisfies $f_c \approx 1.7\tau_{u'}^{-1}N_t^{0.67}$ to a great precision, over the whole range of control parameters Ha and Re⁰. This general law gives a clear estimate for the minimum frequency of vortices that are affected by 3D inertial effects, in the spirit of the heuristic law $k_{3D} \sim N_t^{1/3}$ given by [2] for the minimum transverse wavelength of 3D vortices. Furthermore, since this scale-selective breakdown process depends on $\tau_{u'}$ and τ_{2D} only, a similar law should hold in other flows with a tendency to two dimensionality, albeit with a different expression of τ_{2D} .

We are grateful to the Electroheat group from Ilmenau University for lending us their Magnet and to the Deutsche Forschungsgemeinschaft for funding this work (Grant No. PO1210/4-1).

- [1] J. Sommeria, J. Fluid Mech. **170**, 139 (1986).
- [2] J. Sommeria and R. Moreau, J. Fluid Mech. **118**, 507 (1982).
- [3] A. Pothérat *et al.*, J. Fluid Mech. **424**, 75 (2000).
- [4] H. P. Greenspan (Cambridge University Press, Cambridge, England, 1969).
- [5] R. Akkermans *et al.*, Phys. Fluids **20**, 116601 (2008).
- [6] J. Paret *et al.*, Phys. Fluids **9**, 3102 (1997).
- [7] O. Zikanov and A. Thess, J. Fluid Mech. **358**, 299 (1998).
- [8] A. Thess and O. Zikanov, J. Fluid Mech. **579**, 383 (2007).
- [9] D. Sous *et al.*, Phys. Fluids A **16**, 2886 (2004).
- [10] R. Klein, A. Pothérat, and A. Alferenok, Phys. Rev. E **79**, 016304 (2009).
- [11] A. Kljukin and A. Thess, Exp. Fluids **25**, 298 (1998).
- [12] B. Mück *et al.*, J. Fluid Mech. **418**, 265 (2000).
- [13] B. Sreenivasan and T. Alboussière, J. Fluid Mech. **464**, 287 (2002).
- [14] G. Rüdiger, Astron. Nachr. **295**, 275 (1974).